MOLECULAR STRUCTURE AND CRYSTALLIZATION OF LONG *N*-ALKANES IN LIPID MEMBRANES

Dissertation

zur Erlangung des Doktorgrades der Naturwissenschaften
(Dr. rer. nat.)

der

Naturwissenschaftlichen Fakultät II
Chemie, Physik und Mathematik

der Martin-Luther-Universität
Halle-Wittenberg

vorgelegt von

Frau Anika Wurl

Erstgutachter: Prof. Dr. Kay Saalwächter
Zweitgutachter: Prof. Dr. Alfred Blume
Drittgutachter: Prof. Dr. Daniel Huster

Datum der öffentlichen Verteidigung: 10.07.2024

Abstract

The interactions between purely hydrophobic molecules and lipid membranes are integral to a number of biophysical problems such as the formation of lipid droplets or the delivery of hydrophobic drugs by lipid nanoparticles. In order to better understand the fundamental behaviour of hydrophobic chains in lipid membranes, a model system consisting of linear n-alkanes and different phospholipid bilayers is investigated. n-Alkane lengths range from 10 to 30 carbons. Particular focus is placed on the effect of chain length on mixing behaviour, molecular arrangement and crystallizability of n-alkanes inside the membranes. Using a combination of different solid-state nuclear magnetic resonance (NMR) techniques, molecular dynamics (MD) simulations, X-ray scattering, differential scanning calorimetry (DSC), and cryogenic transmission electron microscopy (cryo-TEM), the model systems are described with a high level of molecular detail.

Zusammenfassung

Die Wechselwirkungen zwischen hydrophoben Molekülen und Zellmembranen spielen eine zentrale Rolle in verschiedenen biophysikalischen Prozessen, wie z.B. der Bildung von Lipidtröpfen oder dem Transport von hydrophoben Wirkstoffen mithilfe von Lipid-Nanopartikeln. Diese Arbeit untersucht das Verhalten langkettiger, hydrophober Moleküle in Lipidmembranen anhand eines Modellsystems bestehend aus linearen n-Alkanen und verschiedenen Phospholipiden. Die gewählten n-Alkane haben Kettenlängen von 10 bis 30 Kohlenstoffatomen. Ein besonderes Augenmerk liegt auf der Auswirkung von Kettenlänge auf das Mischungsverhalten, die molekulare Struktur und die Kristallisation von n-Alkanen in Lipid-Doppelschichten. Durch die Kombination verschiedener Methoden der Festkörper-Kernmagnetresonanzspektroskopie mit Molekulardynamik-Simulationen, Röntgenstreuung und Kalorimetrie werden die untersuchten Systeme ausführlich charakterisiert.

Contents

Chapter 1

Introduction

Long, purely hydrophobic molecules appear in a number of biologically relevant contexts, such as the packaging of hydrophobic drugs by lipid nanoparticles [1–3] or the formation of lipid droplets which is aided by triglycerides and other neutral lipids [4–6]. In recent years, the interactions between synthetic polymers and cellular membranes have received increasing attention. For many years now, plastic pollution has been recognized as a global problem [7, 8]. Consequently, numerous studies have been conducted to determine explicit effects of plastic ingestion on marine life, showing that micro- and nano-plastic particles can indeed be found in many marine organisms and may affect metabolism, behaviour and reproduction [9–14]. Most plastic materials in use today contain hydrophobic polymers such as polyethylene, polystyrene, or polycaprolactone. It stands to reason that these polymers may enter the hydrophobic core of cellular membranes when ingested, in order to not be dispersed in an aqueous environment. This hypothesis, as well as the widespread use of polymers in drug delivery systems, has motivated a number of computational studies aimed at characterizing the partition of purely hydrophobic molecules into lipid membranes [15–19]. These and other [20, 21] studies have repeatedly shown that different hydrophobic molecules accumulate inside the hydrophobic core of lipid membranes.

Surprisingly, even though there is a large number of computational studies, experimental evidence proving the accumulation of long, hydrophobic polymers in lipid membranes is rare. In one study, squalane was found to enter the lipid membrane core of DOPC/DOPG membranes [22]. More recently, Bochicchio et al. discussed the effects of polystyrene 25-mers on DPPC membrane dynamics, thermal and mechanical properties using a combination of experimental techniques and computer simulations [19]. In particular, they reported on the existence of a threshold concentration of PS above which phase separation occurs. The comparatively small number of experimental studies may be partly related to the fact that it is challeng-

ing to mix long, purely hydrophobic chains with lipid membranes. In contrast to amphiphilic or polyphilic molecules, hydrophobic molecules often induce pore formation in the membranes, or they phase separate [23]. Even linear *n*-alkanes, the most (chemically) simple hydrophobic chains, are difficult to insert into lipid bilayers. Previous studies by Pope et al. [24, 25] suggest that *n*-alkanes longer than approximately 18 carbons do not mix with bilayers consisting of 1,2-dimiristoyl-*sn*-glycero-3-phosphatidylcholine (DMPC) or 1,2-dipalmitoyl-*sn*-glycero-3-phosphatidylcholine (DPPC). They did however observe a certain chain-length dependence, i.e. longer *n*-alkanes could be incorporated to larger amounts when the lipid acyl tail length was increased to 18 carbons (1,2-distearoyl-*sn*-glycero-3-phosphatidylcholine, DSPC). Moreover, Pope et al. compared the amounts of *n*-alkane that could be incorporated for different alkane lengths in terms of mole fraction. It is likely that the miscibility of *n*-alkanes with lipid membranes is limited by alkane volume fraction relative to the volume of the hydrophobic membrane region instead. However, to this date, no systematic studies investigating the mixing behaviour of longer *n*-alkanes with lipid membranes have been conducted. It might be expected that such studies would show similar results to nematic solvents diluted with flexible chains (including *n*-alkanes): In those mixtures, phase separation into nematic and isotropic phases has been observed, and the concentration of the flexible chains in the nematic phase decreased with chain length [26–28].

Successfully performing a systematic investigation of the miscibility of *n*-alkanes with different chain lengths inside various lipid bilayers would be extremely beneficial: If longer *n*-alkanes can be shown to mix with the lipid membranes, these mixtures will present a perfect model system for studying the molecular arrangement of other long, hydrophobic molecules in lipid membranes. In this way, one can obtain new, valuable information regarding the interactions between hydrophobic molecules and cellular membranes, advancing the understanding of e.g. lipid-droplet formation.

Furthermore, if longer hydrophobic molecules can indeed be incorporated into the hydrophobic region of a lipid membrane, it is of interest to determine whether those molecules can crystallize inside the lipid membrane environment (without being expelled). On one hand, the characterization of polymer crystallization in different confinement geometries has been the goal of material scientists for many years [29–32]. The 1-dimensional confinement realized by lipid bilayers is substantially different from the confinement of polymer melts (or solutions) in thin films, micelles, or block-copolymer geometries (where, in the latter case, the crystallizing molecules are anchored to at least one interface). Instead, the lipid membrane resembles a 2-dimensional, anisotropic solution featuring a gradient of molecular order. Thus, studying the crystallization of hydrophobic chains inside lipid bilayers is interesting from a fundamental point of view, and may pave the way for the design of new

lipid-based materials. On the other hand, crystallization inside a membrane environment is highly relevant from a biophysical perspective. Various drugs show crystal polymorphism and the crystal properties are often related to the stability and performance of a drug [33]. Moreover, such drugs can potentially crystallize inside their carrier nanoparticles [33–35] or in a biological environment [36]. Naturally, in order to properly control crystallization behaviour in a lipid environment, it is essential to understand it in detail. However, currently we still lack understanding of allegedly simple systems such as the crystallization of *n*-alkanes in a lipid bilayer. While the molecular arrangement of shorter *n*-alkane chains in lipid membranes has been studied in great detail (see chapter 2.2.3), in all those studies only *n*-alkanes in the liquid state were considered. In fact, to the best of my knowledge, no studies addressing the crystallizability of hydrophobic, chain-like molecules in a lipid bilayer environment exist. Answering the fundamental question of whether hydrophobic chains can crystallize inside lipid membranes will not only further the understanding of drug crystallization in lipid/polymer nanoparticles, but may also help to identify the role of triglycerides in lipid-droplet formation, or assess the effect of crystalline nanoplastic particles on cell membranes.

1.1 Scope of the thesis

This thesis aims to fill current gaps in our understanding of the interactions between hydrophobic molecules and lipid membranes via the characterization of a model system: linear *n*-alkanes in phospholipid bilayers. In particular, the miscibility, molecular arrangement and crystallizability of *n*-alkanes inside lipid membranes are studied as a function of hydrophobic chain length. In order to achieve a high level of molecular detail, this thesis combines different solid-state nuclear magnetic resonance (NMR) techniques with molecular dynamics (MD) simulations. Additional experimental techniques such as x-ray scattering, differential scanning calorimetry (DSC) or cryogenic transmission electron microscopy (cryo-TEM) are employed to answer specific questions.

Three linear alkanes of different chain length are studied, namely *n*-decane (C10), *n*-eicosane (C20) and *n*-triacontane (C30), with chain lengths of 10, 20 and 30 carbons, respectively. First, the miscibility of these *n*-alkanes with bilayers consisting of either DMPC or DPPC is investigated. The results are presented in paper I [37]. Thereby, the relevance of the chain length of both alkanes and lipids is studied systematically. In addition, the effect of sample hydration on the miscibility and molecular structure of the mixtures is highlighted. MD simulations proved to be a valuable tool to help interpret the experimental results, however some discrepancies between experimental and simulated order parameters were observed. Thus, in paper II [38], the potential

of two different MD force fields, CHARMM36 and Slipids, to model longer *n*-alkanes was examined. In this context it was also tested if MD simulations performed for a range of *n*-alkane concentrations can result in an even better understanding of the miscibility of *n*-alkanes and lipids, and reveal features which might be obscured by sample preparation difficulties in experiments.

Finally, paper III [39] explores if *n*-eicosane and *n*-triacontane can crystallize inside different phospholipid membranes. In addition to DMPC and DPPC, this investigation also includes unsaturated phospholipids, namely 1-palmitoyl-2-oleoyl-*sn*-glycero-3-phosphocholine (POPC) and 1,2-dioleoyl-*sn*-glycero-3-phosphocholine (DOPC). Again, the effect of hydrocarbon chain length and acyl tail composition on *n*-alkane crystallizability is determined. Then, the crystallization process of C30 in DMPC membranes is examined in detail, comparing temperature dependence, phase sequence and crystallization kinetics to bulk C30.

In summary, this thesis provides an unprecedented characterization of the molecular structure and crystallization of long *n*-alkanes (C20 and C30) in phospholipid membranes.

Chapter 2

Scientific background

This chapter aims to provide a detailed overview of the physical concepts discussed in this thesis. In order to appreciate the effects of foreign molecules on lipid membranes, it is essential to first review the structural features and properties of common lipid assemblies. Subsequently, the phase behaviour of linear alkanes will be discussed, before turning towards alkane crystallization both in bulk and under confinement. Experimental techniques used to study lipid/alkane systems will be summarized in chapter 3, and principles of molecular dynamics (MD) simulations are described in chapter 4.

2.1 Phospholipids

Biological membranes contain numerous components such as proteins, sterols, and various types of lipids. Phospholipids in particular are a major building block of the lipid membranes surrounding cells and cell compartments, and are thus frequently used to model cellular membranes. They uphold the bilayer structure of cell membranes and are also important for protein function and energy metabolism [6, 40–45]. The molecular structure of a common diacyl-glycerophospholipid, 1-palmitoyl-2-oleoyl-*sn*-glycero-3-phosphocholine (POPC) is shown in Figure 2.1. This type of lipid consist of a so-called headgroup which is connected to two acyl tails via a glycerol backbone. Many phospholipids found in the cell membranes of humans, animals and plants are such diacyl-glycerophospholipids, including phosphatidylcholines (PC), -ethanolamines (PE), -serines (PS), -glycerols (PG) or -inositols (PI) [46, 47], which differ in the nature of their headgroups. PC and PE in particular make up a large part of the lipid pool of eukaryotic cell membranes, but specialized membranes may contain significant amounts of other phospholipids. For example, up to about 20 % of phospholipids of the inner mitochondrial membrane are cardiolipins [48], which contains two phosphate groups and a total of four acyl

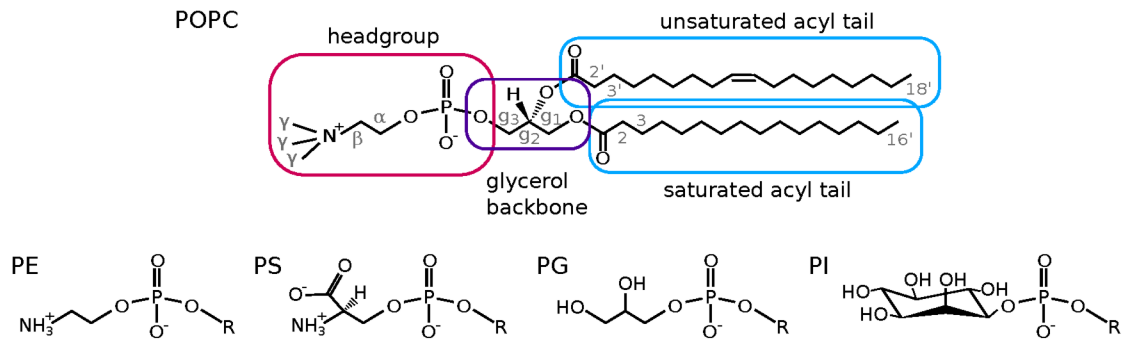

Figure 2.1: Chemical structure of diacyl-glycerophospholipids. These lipids consist of a headgroup containing the phosphate group, a glycerol backbone, and two acyl tails shown here for the lipid POPC. Carbon labels as used in this thesis are added in gray. The headgroup structures of PE, PS, PG and PI lipids are included below, where the label R shows the connection to glycerol backbone and acyl tails.

tails.

In addition to distinct headgroups, the structure of the lipid acyl tails also varies across different phospholipid species: Acyl tail lengths usually vary between 16 and 20 carbons (though shorter and longer chains can also be found), and the tails may contain multiple double bonds. In some cases, such as for POPC, phospholipids may also have asymmetric acyl tails, i.e. the two tails have different lengths and degrees of saturation. The nature of both the lipid headgroup and tails has remarkable effects on the structure and phase behaviour of phospholipid assemblies, as will be discussed in the following sections.

2.1.1 Lipid self-assembly

Phospholipids are amphiphilic molecules, meaning they consist of both a hydrophobic and a hydrophilic moiety – i.e. the hydrocarbon tails and headgroup, respectively. Therefore, in an aqueous environment, phospholipids self-assemble to form various structures such as micelles and vesicles. The self-assembly process is thereby governed by thermodynamics, i.e. interaction free energies, which depend on the lipid geometry as formulated and summarized in detail by Israelachvili et al. [49, 51, 52]. While entropy generally favours assemblies consisting of as few as possible lipid molecules, different opposing forces act between lipids, and between lipid and water molecules, permitting the formation of aggregates [51, 53]: On one hand, attractive hydrophobic forces favour a close packing of the lipid acyl tails. On the other hand, repulsive forces such as electrostatic and steric repulsion, or hydration forces, favor a certain separation of individual molecules. These repulsive forces are particularly relevant for phospholipids with non-zero headgroup charges, and can be modified further by the addition of ions to the solvent. Israelachvili et al. showed

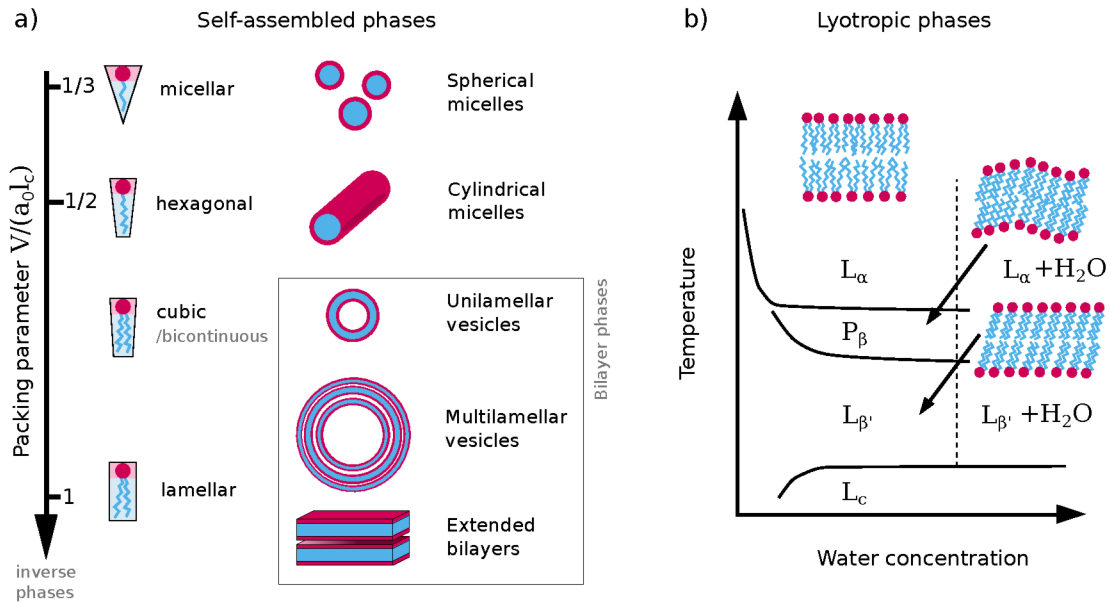

Figure 2.2: Lipid phases. a) Relation between the packing parameter and self-assembled lipid structures. This thesis focuses on bilayer phases (box). b) Qualitative phase diagram showing the lyotropic phases of DPPC (at ambient pressure). Figure adapted from references [49] and [50].

that these opposing forces result in a minimum of the interaction free energy at a certain optimal headgroup area a_0, which is dependent on the strength of the individual forces [49]. By combining a_0 with lipid-specific geometrical constraints, i.e. hydrocarbon chain volume V and maximum length l_c, they define a so-called packing parameter $V/(a_0 l_c)$. This packing parameter predicts whether the amphiphilic molecules will form spherical or cylindrical micelles, vesicles, or extended bilayers as shown in Figure 2.2a. However, extended bilayers have energetically unfavorable edges and, if $V/(a_0 l_c)$ is only very slightly different from 1.0, high line tensions and spontaneous curvature force these bilayers to form large vesicles instead [49, 54]. Compared to surfactants with a single acyl tail, diacyl-phospholipids have a large hydrophobic volume and usually cannot form micelles. Instead, in water these lipids generally assemble into vesicles [49, 51, 52], or so-called multi-lamellar vesicles (MLVs), depending on the sample preparation method [55]. MLVs feature multiple spherical lipid bilayers and can reach up to 20 μm in diameter [56]. On the other hand, uni-lamellar vesicles are classified into small uni-lamellar vesicles (SUVs, <100 nm in diameter), large uni-lamellar vesicles (LUVs, 100 nm-1 μm) and giant uni-lamellar vesicles (GUVs, >1 μm) [56, 57]. It has been discussed that MLVs have a lower free energy than uni-lamellar vesicles [55], which would explain why phospholipids form SUVs only upon sonication [58].

The considerations that were presented in this section are valid for fluid hydrocarbon tails. For a complete picture, the next section discusses effects of hydration and temperature on acyl tail structure in PC lipid bilayers.

2.1.2 Lyotropic phases of PC lipids

Self-assembled phospholipid bilayers in water exhibit lyotropic mesomorphism, that is to say they adopt distinct phases as a function of both temperature and hydration. At atmospheric pressure, PC lipids form bilayer phases [46, 50], although a number of other phases have been observed in the very low hydration regime [59, 60]. Since bilayer phases are highly relevant for cellular membranes, those phases present the main focus of this thesis. As an example, the qualitative phase diagram of 1,2-dipalmitoyl-*sn*-glycero-3-phosphatidylcholine (DPPC) is sketched in Figure 2.2b [50, 60]. DPPC contains two 16-carbon long, saturated acyl tails and exhibits a phase behaviour that is representative for such lipids [59, 61]. The relevant lyotropic phases are commonly referred to as (hydrated) crystalline phase (L_c), gel phase (L_β, $L_{\beta'}$), rippled phase ($P_{\beta'}$) and liquid-crystalline phase (L_α). Increasing the amount of water in lamellar phases results in an increased separation of the individual bilayers. A limit to this swelling process is reached at a certain water concentration, e.g. at 27 water molecules per DPPC lipid in the L_α phase [61]. Higher hydration levels are commonly referred to as the excess-water limit.

The crystalline phase is sometimes referred to as the sub-gel phase and is characterized by extended, frozen hydrocarbon chains [62–64]. Upon increasing temperature, a transition into the so-called gel-phase is observed [65]. In the gel phase, positional long-range order is retained; the hydrocarbon tails are extended and arranged on a (distorted) hexagonal lattice [59, 61, 66]. However, they are now able to rotate around their long axis [59]. One distinguishes two types of gel-phases, the L_β and $L_{\beta'}$ phases. For DPPC and other PC lipids with saturated acyl tails of equal length, only the $L_{\beta'}$ phase appears. In contrast to the L_β phase, the $L_{\beta'}$ phase exhibits a chain tilt, i.e. the hydrocarbon chains are tilted away from the bilayer normal by about 30-35 ° [59, 66, 67]. Smith et al. have noted that the $L_{\beta'}$ phase can in fact be divided into three distinct phases, which vary in the direction of chain tilt [68]. The transition from the gel to the ripple phase is termed pretransition. The ripple phase is named after the periodic ripples distorting the lamellar structure of the $L_{\beta'}$ phase [59, 61, 66, 69]. The pretransition is only observed at water concentrations above approx. 17-20 wt% [60, 61]. Finally, the highest-temperature transition is the so-called main transition, which is associated with the melting of the lipid acyl chains. In the L_α phase, the lipid acyl tails are fluid-like and highly disordered [59]. One often hears the term trans-gauche isomerization mentioned in this context, referring to the fact that the dihedral angles in the acyl tails are able to easily shift between the trans and gauche states (see chapter 4.1.1 and paper III for details). In the case of DPPC, the main transition occurs between the $P_{\beta'}$ and the L_α phase. However, the main transition may also refer to the transition between gel and liquid-crystalline phases in lipids or mixtures that do not form a rippled

phase. The main transition temperatures T_{m} of PC lipids generally increase with acyl tail length, due to increased van-der-Waals interactions between longer acyl tails [50, 70]. Similarly, unsaturation lowers the phase transition temperature since double bonds induce kinks in the hydrocarbon chains, destabilizing the gel-phase. Moreover, in unsaturated lipids the gel-phase is in fact the L_β phase, and the $P_{\beta'}$ phase disappears.

Lipids with different headgroups or special tail structures may form non-bilayer phases under certain conditions. The most well-known, and biologically relevant, example of these are probably the (inverted) hexagonal phases formed by PE lipids [71–74]. However, such phases are not discussed further in this thesis.

For completeness, it should be mentioned that phase separation can occur when different lipid species are mixed [75, 76], and heterogeneity is an important feature of biological membranes [77, 78]. Moreover, new phases can be formed in lipid mixtures when cholesterol is present [79–81]: Mixtures consisting of one phospholipid species with saturated acyl tails, one with unsaturated tails, and cholesterol (e.g. DPPC/DOPC/Cholesterol) form a cholesterol-rich, liquid-ordered phase (L_o), and show phase-coexistence at certain concentrations and temperatures. The L_o phase exhibits high (orientational) ordering reminiscent of gel phases, but long-range translational disorder characteristic of fluid phases [79].

2.1.3 The C-H bond order parameter

As mentioned in the previous section, hydrocarbon tails of lipids in the L_α phase are highly disordered. However, the degree of disorder depends on temperature [59, 82], hydration [83], lipid composition [84], or the presence of other chemical species in the membrane [85]. It has become common practice to evaluate the effects of such perturbations by measuring C-H bond order parameters, S_{CH}. The order parameter of a given C-H bond in a lipid bilayer is defined as the time- and ensemble-averaged orientation of this bond with respect to the lipid bilayer normal:

$$S_{\mathrm{CH}} = S_{\mathrm{mn}} = \frac{1}{2}\langle 3\cos^2\theta_{\mathrm{mn}} - 1\rangle \quad .$$

Here, the indices "m" and "n" refer to the axis of the C-H bond $\boldsymbol{m}$, and the bilayer normal $\boldsymbol{n}$, respectively (see Figure 2.3a). Due to ensemble averaging, the order parameter can not provide any information on bond dynamics and is therefore a purely structural quantity. S_{CH} can be positive or negative, depending on the average angle θ_{mn}. For the lipid acyl tails, the order parameter is usually negative since the C-H bonds lie perpendicular to the bilayer normal [82, 86]. If the C-H bond undergoes isotropic motion, S_{CH} will average to zero.

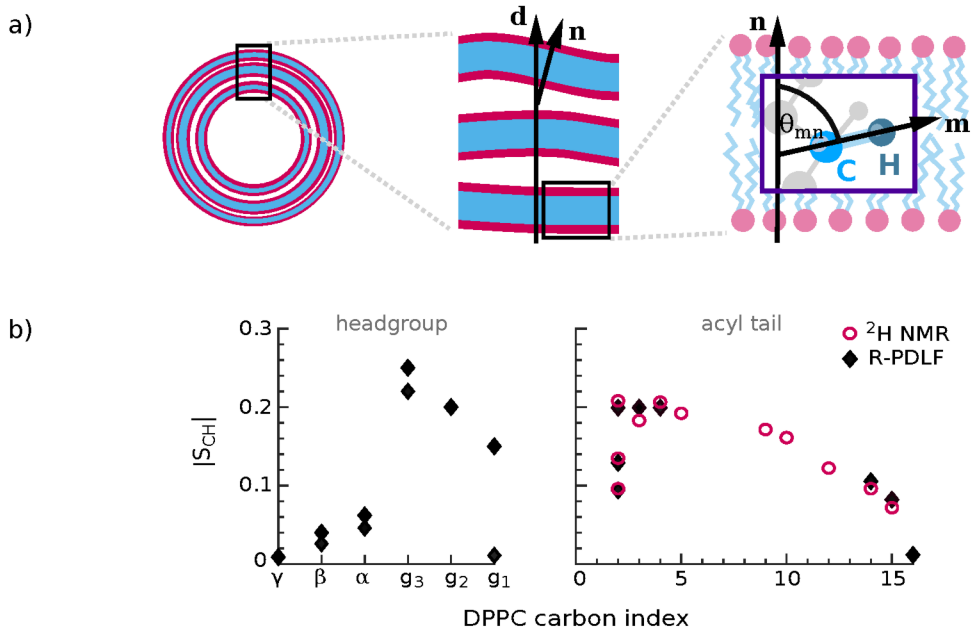

Figure 2.3: The C-H bond order parameter. a) Molecular orientations in lipid MLVs. Segments of MLVs can often be treated as separate bilayer stacks defined by a common director $\boldsymbol{d}$. If bilayer undulations are present, the bilayer normal $\boldsymbol{n}$ is tilted with respect to $\boldsymbol{d}$. The relevant angle for calculating the S_{CH} is θ_{mn}, between $\boldsymbol{n}$ and the C-H bond vector $\boldsymbol{m}$. b) Absolute order parameters of liquid-crystalline DPPC, measured by different NMR techniques. ^{2}H NMR results (57°C) were taken from reference [82], and R-PDLF results (60°C) from paper II. Carbon indices are defined in Figure 2.1.

Generally, effects of orientation and motion on the C-H bond order parameter can not be disentangled easily. For example, a C-H bond with a fixed angle $\theta_{\mathrm{mn}} = 54.74°$ would result in an order parameter of zero, but the same is true for a C-H bond exhibiting isotropic reorientation. However, one can assume that the order parameter is closer to zero if the C-H bond samples a wider range of angles θ_{mn}. Larger absolute values of S_{CH} then indicate bonds that are restricted to a small range of angles θ_{mn}. This assumption helps to understand the order parameter profile along a lipid molecule, depicted in Figure 2.3b: The glycerol backbone is a relatively rigid group that is fixed at the interface between the hydrophilic and hydrophobic regions of the bilayer. Due to the restricted mobility of these C-H bonds, they have comparatively large (absolute) order parameters. The acyl tails are connected to the glycerol backbone and extend straight into the bilayer center. Therefore the C-H bonds on the first few carbons of the acyl tails are also highly ordered. Only towards the end of the acyl tails does the ordering decrease [82]: The free end of the lipid tail allows for more flexibility of the final carbon-carbon and carbon-proton bonds. Since the orientation of a C-H bond is affected by the dihedral rotations of all the C-C bonds connecting this C-H bond to the glycerol backbone, trans-gauche isomerization can lead to notable re-orientations towards the end of the acyl tail. This also explains why unsaturated tails are more disordered than

fully saturated tails. C=C double bonds introduce "kinks" in the acyl chain which reduce the packing efficiency of the tails and generate free volume for (other) tails to fold into.

2.2 Linear alkanes (*n*-alkanes)

2.2.1 Thermotropic phases and crystallization

The thermotropic phase behaviour of linear alkanes is quite complex and strongly depends on *n*-alkane length [87]. Still, certain similarities to the lipid phases described in chapter 2.1.2 can be found. At low temperatures, *n*-alkanes shorter than approx. 150-200 carbons form crystals of extended hydrocarbon chains in all-trans configuration. The exact crystal structure then depends on the number of alkane carbons (nC) [87, 88]: Even-numbered *n*-alkanes crystallize in triclinic (nC $\leq$ 26), monoclinic (26 $\leq$ nC $\leq$ 36) or orthorhombic (nC = 38, 40, 44, 46, 50 or 60) structures, while odd-numbered *n*-alkanes form orthorhombic crystals. One noteworthy feature of the triclinic and monoclinic alkane crystals is that the all-trans chains are tilted with respect to the methyl-group planes. For some *n*-alkanes, a number of solid-solid phase transitions can be observed at low temperatures [87]. At higher temperatures, an order-disorder transition takes place. In certain cases, this is a transition to a rotator phase. Rotator phases are adopted by odd- and even-numbered *n*-alkanes longer than 17 and 20 carbons, respectively, prior to actual melting [87, 89–92]. These rotator phases are similar to the lipid gel phase in that they exhibit positional long range order while the molecules are able to oscillate/rotate around their long axis (hence the name rotator phases). Five distinct rotator phases have been identified (R_I-R_V), and the sequence of rotator phases occurring in various *n*-alkanes has been summarized by Dirand et al. [87], and Cholakova and Denkov [92]. Figure 2.4a shows the rotator phase sequence for several even *n*-alkanes upon cooling, as determined by Sirota et al. [90]. Importantly, this plot does not provide any information on the phase sequence in odd-alkanes, which may be quite different. The different rotator phases are all hexagonal phases, but vary in terms of lattice distortion, chain tilt (direction), and layer stacking as sketched in Figure 2.4b. Rotator phases are also formed upon cooling from the melt, during the crystallization process [93]. Upon cooling it is possible to observe transient and meta-stable rotator phases for some shorter, even-numbered *n*-alkanes such as hexadecane or eicosane [94]. While meta-stable rotator phases persist indefinitely at a fixed temperature once formed, transient phases will eventually transition to the stable crystal form.

The melting temperatures of *n*-alkanes strongly depend on chain length, similar to those of the lipid acyl tails [95]. Just above the melting temperature, *n*-alkanes

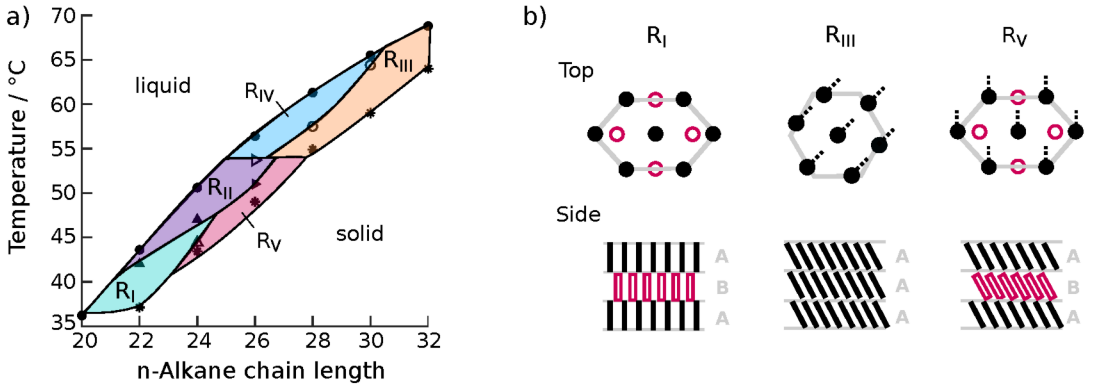

Figure 2.4: *n*-Alkane phases. a) Phase sequence of even *n*-alkanes upon cooling as determined by (and adapted from) Sirota et al. [90]. The boundaries of the rotator phase regions were added manually to guide the eye and should not be used to predict the phase sequence of odd *n*-alkanes of similar chain length. b) Structure of selected rotator phases as seen from the top and from the side, adapted from references [90–92]. Open symbols show the location of the second layer of molecules. Dotted lines in the top-view show the direction of chain tilt with respect to the neighboring chains.

with nC between 15 and 50 exhibit so-called surface freezing [96–99]. In such alkane melts a single layer of ordered chains exists at the *n*-alkane-air interface. This frozen layer has been found to persist up to approx. 3 °C above the melting temperature, depending on chain length. The structure of this ordered layer is also dependent on chain length: For nC < 44, the layer has a (distorted) hexagonal structure similar to the rotator phases, with either tilted ($30 \leq$ nC < 44) or untilted ($16 \leq$ nC < 30) chains. For longer alkanes, the surface layer is of a crystalline nature. The presence of a frozen surface layer at the freezing temperature can also explain the negligible hysteresis between rotator phase melting and crystallization [93, 100]. In bulk *n*-alkanes, the liquid-to-rotator transition during cooling occurs pretty much at the same temperature as the melting of the rotator phase during heating. On the other hand, the rotator-to-crystal transition supercools a few degrees (particularly for even *n*-alkanes) [90, 91]. The supercooling (or undercooling) $\Delta T = T_\mathrm{m} - T_\mathrm{c}$ generally refers to the difference between the crystallization and (equilibrium) melting temperature.

The crystallization of liquid bulk *n*-alkane can be described by classic theories of nucleation and crystal growth [101–103]. Nucleation is the process of the formation of small crystal nuclei, which occur spontaneously due to density and conformation fluctuations or are induced by the presence of impurities and surfaces. These two possibilities are termed homogeneous and heterogeneous nucleation, respectively. Since small impurities and surface-frozen layers are present in most alkane melts, heterogeneous nucleation is observed in most experiments. Then, rotator phase nuclei are formed prior to the transition to the low-temperature crystal phase. It is possible to create spaces that are sufficiently small to be free of impurities and lacking

an alkane-air interface by droplet techniques [31, 104, 105]. Thus, homogeneous nucleation can be studied (see section 2.2.2 for more details).

A crystal nucleus has to reach a certain size to become stable and continue to grow into a crystal. This is because the free energy ΔG of a nucleus is the sum of (positive) interfacial energy ΔG_s and (negative) bulk free energy ΔG_b [101]. It has been found that a cylindrical model is most suitable to describe n-alkane nuclei [103, 106]:

$$\begin{aligned}\Delta G &= \Delta G_\mathrm{s} + \Delta G_\mathrm{b} \\ &= 2\pi(r^2\sigma_\mathrm{e} + rmd\sigma_\mathrm{s}) - \pi\Delta S\Delta T r^2 md\end{aligned} \tag{2.1}$$

Here r and m are the radius and height of the nucleus in number of molecules, d is the n-alkane length, $\sigma_\mathrm{e/s}$ is the interfacial energy per area at the end/side of the cylindrical nucleus, ΔS is the entropy of melting per unit volume and $\Delta T = T_\mathrm{m} - T$ is the undercooling below the equilibrium melting temperature [103]. The resulting energy landscape of ΔG features a saddle point at a given nuclei radius and height, defining the critical size necessary for a nucleus to become stable. If nucleation is considered as an activated process, the value of ΔG at a given nucleus size defines the related activation energy that needs to be overcome.

For n-alkanes of medium chain length, a nucleus consists of a small number of crystallized/rotator-phase molecules, aligned in parallel. Notably, it was discussed that the methyl groups of the hydrocarbon chains initially may not be aligned in one plane [103, 107, 108]. Instead, misalignment of the methyl groups is considered to promote further growth of the crystallites by increasing the number of ways in which new chains can attach to an existing crystallite and by facilitating the formation of additional crystal layers. Experimental evidence suggests that crystalline n-alkane molecules possess a certain amount of mobility which permits re-arrangements of the crystal and slowly perfects the misaligned lamellae [107, 109, 110].

2.2.2 Confined crystallization

The effect of confinement on the crystallization of n-alkanes has been studied in a number of different geometries. 1-dimensional confinement has been investigated for example between mica-plates or in thin films bordered by different surfaces [111–115], 2-dimensional confinement is most often realized by nanoporous matrices [116–122], and 3-dimensional confinement can be studied when n-alkanes are enclosed in (emulsion) droplets [105, 123–126] or polymeric nanoparticles [127, 128]. The effects of different confinement geometries were recently summarized by Cholakova and Denkov [92].

Since one-dimensional confinement of n-alkanes is usually investigated on, or in

between, different surfaces, interfacial interactions and energies strongly influences the alkane orientation and phase behaviour in these systems [113–115, 129]. Also, alkane surface crystallization plays a much larger role. In alkane monolayers at solid-air interfaces for example, surface crystallization completely defines the alkane phase behaviour, and both rotator and crystalline phase structure are different from bulk *n*-alkane [111]. Alkane melting was shown to be dependent on film thickness, with thinner films crystallizing at lower temperatures [130]. At alkane-polymer interfaces, the *n*-alkane phase state was shown to affect the motions of interfacial polymer segments [131]. In this thesis (paper III), a fundamentally different type of one-dimensional confinement is studied. By inserting *n*-alkanes into lipid membranes, the alkanes are not only confined to the membrane interior, but also dissolved in an anisotropic solvent with a gradient of molecular order.

The effects of confinement in nanopores on *n*-alkane crystallization depend on pore geometry and material [118, 122], but exhibit a number of general aspects as discussed in references [116–122]. If the nanopores have sufficiently small diameters (below $\approx 200-300\,\mathrm{nm}$), the confined *n*-alkane exhibits notably reduced phase transition temperatures. The magnitude of this effect is thereby related to the pore diameter, with smaller diameters resulting in a more pronounced depression. In 10 nm pores for example, melting occurred about 10-12°C below the bulk melting point. In addition, new rotator phases appeared in these systems, and transient rotator phases were stabilized for example in tetradecane (C14). The new rotator phases were of type R_I or R_{II}, i.e. with non-tilted chains, and their presence is thought to be connected to the fact that lamellar ordering is lost, or strongly reduced, inside pores of small diameters.

As mentioned in the previous section, confinement in droplets can lead to homogeneous nucleation if the droplet volume is small compared to the number of heterogeneities [103–106, 123, 132, 133]. The homogeneous crystallization temperatures of *n*-alkanes between 16 and 40 carbons in length were found to be about 14-17°C lower than the respective melting temperatures [103, 133]. Thus, homogeneous nucleation can usually be identified unambiguously. There is however some uncertainty regarding the relevance of rotator phases during homogeneous nucleation [103]. When homogeneous nucleation was observed in odd and even *n*-alkanes between 20 and 32 carbons in length, rotator phases were not detected during the crystallization process [104, 105, 132, 133]. Thus, it is expected that homogeneous nucleation results in direct crystallization from the melt, i.e. the structure of the initial nuclei is the same as in the low-temperature crystal phase. However, for shorter, odd *n*-alkanes (C15, C17 and C19), rotator phases have been observed during homogeneous nucleation [105, 123]. In these studies, the liquid-to-rotator transition temperature was reduced by 11-13°C compared to the bulk *n*-alkane transition, while the rotator-to-crystal transition temperature was only reduced by 6-7°C. It is therefore expected

that these *n*-alkanes homogeneously nucleate in the rotator phase, which then facilitates the formation of the final crystal phase. Similar to 1-dimensional confinement, the droplet surface or the interface between *n*-alkane and droplet shell can influence the crystallization behaviour. It was found that *n*-alkane chains can co-crystallize with the acyl tails of shell surfactant molecules similar to a surface freezing process, thus acting as seeds for heterogeneous nucleation [35, 124–126]. The freezing temperatures found for such cases of surface heterogeneous nucleation lie in between those measured for homogeneous and volume heterogeneous nucleation. The type of surfactant or microcapsule used to confine an *n*-alkane melt can also affect the structures adopted during the crystallization process. For example, rotator phases were only observed if surfactants had sufficiently long acyl tails [124, 126]. Alkane crystal morphology in sufficiently small droplets can be different from bulk [105, 134], rotator phases can be stabilized, and additional rotator phases may appear [135].

2.2.3 Short *n*-alkanes in lipid membranes

The organization of shorter *n*-alkanes (nC $\leq$16) in lipid membranes, as well as the effect of such *n*-alkanes on membrane properties, has been studied for several decades [136–140]. Many of the early studies had been motivated by the fact that short *n*-alkanes (up to C8) have anaesthetic properties [136, 141]. The molecular mechanisms behind the anaesthetic effect are still under debate, but may be related to the accumulation of short *n*-alkanes in the lipid bilayer center [142]. More recent studies on phospholipid/*n*-alkane mixtures focused on using *n*-alkanes as a model component for other hydrophobic chains in fundamental investigations of the effect of such molecules on phospholipid bilayers [143–148]. Since *n*-alkanes of various lengths are readily available, these molecules are particularly suitable for studying chain-length dependent effects.

Previous results regarding the effects of short *n*-alkanes on phospholipid bilayers can be summarized as follows. Calorimetric experiments showed that *n*-alkanes may either lower or raise the lipid main transition temperature T_{m}, depending on their length [140]. The addition of *n*-alkanes shorter than approximately 12 carbons results in a decrease of T_{m} for several biologically relevant phospholipids [24, 137, 143, 147, 149–152]. This observation was explained by short *n*-alkanes introducing disorder and causing a reduction in the van-der-Waals interactions in the lipid gel phase. Moreover, *n*-alkane order parameters of C6, C8 and C12 in DMPC are notably smaller than lipid acyl tail order parameters and decrease with decreasing alkane length, [24, 149, 153], demonstrating the high mobility of shorter alkanes. *n*-Alkanes of similar length as the lipid acyl tails, or even longer, have been shown to increase the hydrocarbon chain interactions and thus the lipid T_{m} [24, 137, 143, 146, 147, 149]. In addition to a shift of the main transition temperature, a slight

broadening of the transition region as well as the disappearance of the pretransition have been reported [137, 143, 146, 154]. Furthermore, the effect of different *n*-alkanes on the lipid T_m was found to depend on the nature of the lipid headgroup [143].

The addition of *n*-alkanes was also shown to affect the lipid bilayer bending modulus. The group of K. Saito reported that in the gel-phase, addition of *n*-tetradecane strongly increases the bending rigidity of DPPC bilayers due to denser chain packing [155]. On the other hand, they found that C10, C12 and C14 decreased the bending modulus of liquid-crystalline DPPC membranes by decreasing the coupling between the two bilayer leaflets [147].

Since both the phase behaviour and the mechanical properties of alkane-containing bilayers depend on the exact location of the *n*-alkane chains in the phospholipid membrane, the molecular arrangement of *n*-alkanes in lipid membranes has been discussed extensively. C6, C8 and C10 were found to significantly increase the thickness of gel- and liquid-crystalline bilayers of saturated phospholipids [136, 137, 156], and these short alkanes are thus suspected to accumulate to a large amount in the space between the two bilayer leaflets. C12, C14 and C16 on the other hand only increased the thickness of gel-state lipid bilayers considerably [137, 149, 156]. It was found that the thickness increase in these cases results from a removal of lipid acyl chain tilt [137, 146] and it was argued that longer *n*-alkanes align parallel to the lipid acyl chains. More recently, Usuda et al. published apparently contradicting results [147]. For liquid-crystalline DPPC bilayers, they observed an increase in bilayer thickness for C14, but not for C8, C10 or C12. Therefore, they concluded that longer molecules partition into the bilayer center and shorter *n*-alkanes disperse evenly. Usuda et al. explained the deviation from previous results by different *n*-alkane concentrations in the lipid membranes. Since e.g. McIntosh et al. [137] studied lipid membranes saturated with *n*-alkanes, their final alkane content (for the shorter *n*-alkanes) was likely higher than the constant mole fraction of 40 % studied by Usuda et al. Moreover, Gruen et al. had previously calculated that *n*-alkane location should depend on concentration, and an increasing accumulation of *n*-alkanes in the bilayer center should be observed for higher concentrations [157].

Finally, it has been noted that the addition of *n*-alkanes can result in the formation of non-bilayer lipid phases [140]. For example, *n*-alkanes ranging from C12 to C20 were found to decrease the bilayer-to-inverted hexagonal phase transition temperatures of different PE lipids [158, 159]. The *n*-alkane chains thereby preferentially partition into the interstitial space between the cylinders of the hexagonal phase [145, 159–161]. In addition, different *n*-alkanes could be shown to promote the formation of inverted hexagonal phases in PC lipids which do not originally exhibit non-bilayer phases [162, 163]. In some of these samples, at high hydration levels, the formation of an isotropic phase was also observed.

Chapter 3

Experimental methods

This chapter discusses the experimental techniques used in this thesis. A particular focus is placed on different types of solid-state nuclear-magnetic resonance (NMR) experiments, but X-ray scattering, cryogenic electron transmission microscopy (cryo-TEM) and differential scanning calorimetry (DSC) are also introduced briefly.

3.1 Solid-state NMR

NMR is the study of nuclear spin systems. The nuclear spin is an intrinsic property of atoms, and every nucleus with a nuclear spin quantum number I greater than zero can be observed by NMR. By combining strong magnetic fields and radio-frequency (RF) pulses it is possible to detect transitions between different spin states and to determine the chemical composition of a substance, or to study molecular structures and dynamics. This chapter summarizes a number of NMR techniques relevant for the study of lipid membrane systems. More fundamental concepts of NMR will not be discussed here since they are reviewed in a number of excellent textbooks (e.g. [164–167]). All explanations provided in this chapter are based on the books by M. Levitt [164] and M. Duer [165], as well as the review by Bärenwald et al. [168], unless noted otherwise.

In solid-state NMR, orientation-dependent interactions play a very important role. Their presence and magnitude can provide information on the (molecular) structure of the sample. Orientation-dependent interactions include the chemical shift anisotropy (CSA), homo- and heteronuclear dipolar coupling, as well as the quadrupolar coupling. As highlighted in the following sections, the orientation dependence of these interactions is often given by a second Legendre polynomial, e.g.

$$P_2(\cos\theta_{\mathrm{ml}}) = \frac{1}{2}(3\cos^2\theta_{\mathrm{ml}} - 1) \quad , \tag{3.1}$$

where θ_{ml} refers to the angle between the principal component of the interaction tensor, $\boldsymbol{m}$, and the laboratory frame $\boldsymbol{l}$ which is parallel to the main magnetic field $\boldsymbol{B}_0$. Importantly, in an NMR experiment, one generally observes a time average of the orientation-dependent interactions. As a consequence, sample structure and dynamics play an important role in determining which interactions affect the NMR spectrum, and to which degree.

A sample is isotropic if a single molecule can in principle sample all orientations θ_{ml} during the timescale of the NMR experiment (which depends on the strengths of the couplings involved but is often on the order of microseconds). This is the case for e.g. liquid n-alkanes or lipids in small vesicles which perform isotropic tumbling in water, and where lipids diffuse efficiently through the bilayer. For isotropic samples, the time average of equation 3.1 evaluates to zero:

$$\langle P_2(\cos\theta_{\mathrm{ml}})\rangle_{\mathrm{iso}} = \int_0^{\pi} \sin\theta_{\mathrm{ml}}\, P_2(\cos\theta_{\mathrm{ml}})\, d\theta_{\mathrm{ml}} = 0 \tag{3.2}$$

Here, the factor $\sin\theta_{\mathrm{ml}}$ corresponds to a 3-dimensional isotropic distribution of angles θ_{ml}. Evidently, orientation-dependent interactions can be neglected in isotropic systems, similar to solution NMR.

Lipid bilayer phases or solid n-alkanes however are anisotropic systems. While MLVs are usually spherical, they are large enough that a lipid molecule can not isotropically diffuse around an MLV on the timescale of the NMR experiment. Every lipid is therefore effectively confined to a finite region of the bilayer. That region is here referred to as a "bilayer slab". It can be described by its director $\boldsymbol{d}$, i.e. the average direction of the bilayer normales in a stack of lipid bilayers (see Figure 2.3a). A bilayer slab is oriented at an average angle θ_{dl} with respect to the main magnetic field, and the average orientation dependence may be written as

$$\langle P_2(\cos\theta_{\mathrm{ml}})\rangle_{\mathrm{aniso}} = \langle P_2(\cos\theta_{\mathrm{md}})\rangle P_2(\cos\theta_{\mathrm{dl}}) \quad . \tag{3.3}$$

Similarly, solid n-alkanes contain crystallites of various orientations θ_{dl} and it is customary to refer to the resulting, broad NMR lineshapes as powder- or Pake patterns.

Explicit examples of how anisotropic interactions in lipid/n-alkane systems can be used to determine molecular structure are provided in the following sections. First, static techniques making use of ^{31}P CSA and ^{2}H quadrupolar coupling are discussed. Then, the benefit of using high-resolution magic-angle spinning (MAS) ^{1}H and ^{13}C NMR is highlighted, and the principle of ^{13}C-^{1}H dipolar recoupling experiments is explained.

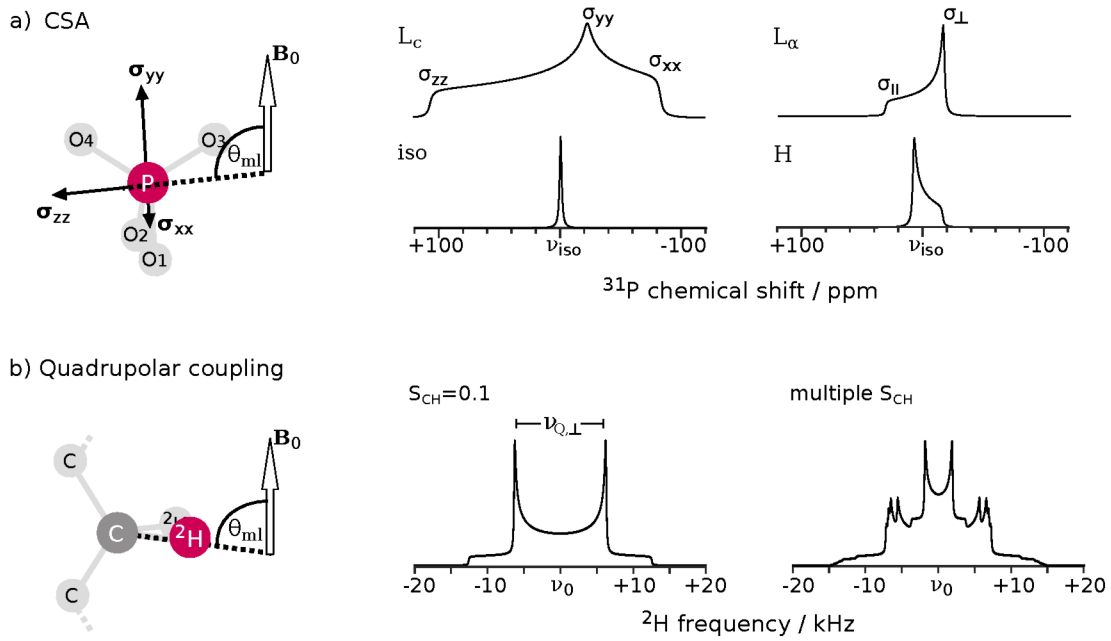

Figure 3.1: Orientation-dependent interactions in lipids and exemplary NMR spectra. a) ^{31}P-CSA tensor orientation, definition of θ_{ml}, and simulated ^{31}P NMR spectra. Left: Orientation of the eigenvectors $\boldsymbol{\sigma}_{zz}$, $\boldsymbol{\sigma}_{yy}$ and $\boldsymbol{\sigma}_{xx}$ in the phospholipid headroup, adapted from [58, 169] (length not to scale). The oxygen atoms O1 and O2 are connected to the glycerol backbone and headgroup, respectively. $\boldsymbol{\sigma}_{zz}$ and $\boldsymbol{\sigma}_{yy}$ are located in the O4-P-O3 plane. The angle ϕ is not defined in this sketch, making it valid only for $\eta = 0$. Right: Simulated spectra centered around ν_{iso} and calculated as described in the text, using the following settings. L$_c$: Equation 3.4, $\{\sigma_{zz}, \sigma_{yy}, \sigma_{xx}\} = \{108, -21, -81\}$ ppm, line-broadening of T_2=0.5 ms; L$_\alpha$: Equation 3.9, $\{\sigma_\perp, \sigma_\parallel\} = \{18, -30\}$ ppm, T_2=1 ms; H: Equation 3.10, $\{\sigma_\perp, \sigma_\parallel\} = \{18, -30\}$ ppm, T_2=1 ms; iso: $\nu_{cs} = \nu_{iso}$. b) Orientation of θ_{ml} for quadrupolar coupling in a C-^{2}H bond (in a hydrocarbon methylene group), and simulated ^{2}H spectra. The spectra were calculated using equation 3.13, T_2=2 ms, and order parameters of $S_{\mathrm{CH}} = 0.1$ ($\Delta\nu_{Q,\perp}$=12.5 kHz) and $S_{\mathrm{CH}} = \{0.03, 0.09, 0.105, 0.11, 0.115\}$, respectively. The latter values correspond to order parameters of liquid C10 in a DPPC membrane, as determined in paper II.

3.1.1 Static ^{31}P NMR

This section describes how ^{31}P chemical shift anisotropy can be used to distinguish between different lipid phases. ^{31}P has a nuclear spin of $I = 1/2$ and a natural abundance of about 100 %, making it a convenient nucleus for NMR investigations. In addition, the phosphorous in a lipid headgroup is isolated from other phosphorous nuclei. Thus, homonuclear dipolar couplings can be neglected and CSA is the dominant interaction at high fields, although it may still be beneficial to decouple ^{1}H-^{31}P dipolar interactions in order to obtain sharp spectra [58].

In general, chemical shift refers to a change of the effective magnetic field at the site of a nucleus due to shielding by the surrounding electron cloud. Since the local magnetic field defines the transition energy between the nuclear spin states, an NMR spectrum features peaks at distinct frequencies for nuclei in different chemical

environments (as illustrated in sections 3.1.4, 3.1.5 and e.g. Figure 3.2). In most cases, the molecular surroundings of a nucleus are not isotropic. Then, the electronic shielding varies depending on how a molecule is oriented with respect to the main magnetic field. This phenomenon is referred to as chemical shift anisotropy (CSA). The chemical shielding at the position of the nucleus is described by the symmetric chemical shielding tensor, or CSA tensor, $\boldsymbol{\sigma}$. In its principle axis system, $\boldsymbol{\sigma}$ is defined by the three eigenvalues σ_{zz}, σ_{yy} and σ_{xx} which correspond to the three basis vectors of a given molecular geometry. This is illustrated in Figure 3.1a for the ^{31}P nucleus in a phospholipid headgroup.

The dependence of the resonance frequency on molecular orientation in the presence of CSA is given by

$$\nu_{cs} = \nu_0 - \nu_0\sigma_{iso} - \frac{1}{2}\nu_0\Delta(3\cos^2\theta_{\mathrm{ml}} - 1 + \eta\sin^2\theta_{\mathrm{ml}}\cos 2\phi) \quad , \tag{3.4}$$

where ν_0 is the Larmor frequency in Hz, θ_{ml} is the angle between σ_{zz} and the main magnetic field $\boldsymbol{B}_0$, ϕ is the azimuthal angle, and Δ, σ_{iso} and η are defined as [165]:

$$\Delta = \sigma_{zz} - \sigma_{iso} \tag{3.5}$$

$$\sigma_{iso} = \frac{1}{3}(\sigma_{xx} + \sigma_{yy} + \sigma_{zz}) \tag{3.6}$$

$$\eta = \frac{\sigma_{xx} - \sigma_{yy}}{\Delta} \tag{3.7}$$

For lipids, it can be shown that phase structure strongly influences the shape of the ^{31}P NMR spectra [170]. Figure 3.1a shows exemplary spectral shapes corresponding to PC lipids in the L_c, L_α, isotropic or hexagonal phase. The origins of these different spectral shapes have been analyzed by J. Seelig [58], and can be summarized as follows. In crystalline bilayers (L_c), all three eigenvalues of $\boldsymbol{\sigma}$ are different. Additionally, lipid headgroup rotation and diffusion are extremely limited in this phase, and no averaging over different orientations takes place. Thus, the ^{31}P NMR spectra of L_c phases can be calculated using equation 3.4. In non-oriented bilayers (i.e. samples containing randomly oriented L_c bilayers as found in e.g. MLVs), all the different orientations θ_{ml} and ϕ can be found in the sample. As a consequence, the measured spectrum is a superposition of individual spectra corresponding to the different resonance frequencies $\nu_{cs}(\theta_{\mathrm{ml}}, \phi)$. The resulting L_c spectra of PC and PE lipids are about 190 ppm wide [169] and have a very characteristic powder-pattern lineshape featuring two edges at σ_{zz} and σ_{xx}, and a sharp feature at σ_{yy}.

In liquid-crystalline bilayers (e.g. L_α), lipids rotate around the axis of the bilayer

normal. Thus, the CSA tensor is partially averaged to a uniaxial tensor,

$$\bar{\boldsymbol{\sigma}} = \begin{pmatrix} \sigma_\perp & 0 & 0 \\ 0 & \sigma_\perp & 0 \\ 0 & 0 & \sigma_\parallel \end{pmatrix} \quad . \tag{3.8}$$

Using this tensor, equation 3.4 simplifies to

$$\nu_{cs} = \nu_0 - \nu_0\sigma_{iso} - \frac{2}{3}\nu_0\Delta\sigma P_2(\cos\theta_{\mathrm{dl}}) \quad , \tag{3.9}$$

with θ_{dl} being the angle between $\boldsymbol{B}_0$ and the bilayer director $\boldsymbol{d}$ (compare Figure 2.3a), and $\Delta\sigma = \sigma_\parallel - \sigma_\perp$. Across the whole sample, all possible values of θ_{dl} are present, and the spectrum is again a superposition of multiple resonance peaks. Since $\bar{\boldsymbol{\sigma}}$ only has two unique eigenvalues, the spectum features only two edges. The more perpendicular orientations thereby occur more often, and the edge with higher intensity can be assigned to $\sigma_\perp$. For PC lipids, $\Delta\sigma \approx -50$ to -40 ppm [170, 171], and acyl tail composition does not affect the headgroup motion significantly [171–174]. The characteristic shape of the ^{31}P spectrum of liquid-crystalline bilayers is retained to a certain degree in the gel- and rippled phases. However, corresponding spectra are somewhat broader, with $\Delta\sigma \approx -60$ to -50 ppm in PCs [169, 171, 173, 175]. The value of $\Delta\sigma$ depends on both the length of the lipid acyl tails as well as the exact temperature. The latter observation was explained by the fact that, while axial rotation remains possible in the $\mathrm{P}'_\beta/\mathrm{L}_\beta$ phases, it becomes progressively slower at lower temperatures, causing deviations from the theoretical line shape.

If small lipid vesicles are studied instead of MLVs, lipid diffusion around the vesicle surface and isotropic tumbling of vesicles in water cause averaging of θ_{dl} (identical to θ_{ml} in equation 3.2). Then, the ^{31}P spectrum of such lipid assemblies is reduced to a single, narrow peak at the isotropic chemical shift $\nu_{iso} = \nu_0(1 - \sigma_{iso})$ [58, 174, 176–178]. Under such conditions, static ^{31}P NMR also enables determination of the distribution of different lipid species across the two bilayer leaflets [174, 179].

In hexagonal phases on the other hand, motional averaging occurs around the circumference of the lipid "cylinders" (compare Figure 2.2a). Then, the corresponding symmetry axis $\boldsymbol{c}$ is parallel to these cylinders, and the resonance frequency is given by

$$\nu_{cs} = \nu_0 - \nu_0\sigma_{iso} + \frac{1}{3}\nu_0\Delta\sigma P_2(\cos\theta_{\mathrm{cl}}) \quad , \tag{3.10}$$

where θ_{cl} is the angle between $\boldsymbol{c}$ and $\boldsymbol{B}_0$. Assuming that the orientations θ_{cl} also follow an isotropic distribution, the expected NMR spectrum will be only half as wide as the spectrum of a bilayer phase, and inverted.

3.1.2 Static ^{2}H NMR

^{2}H NMR is a convenient method to study lipid membrane order parameters and has been around for many decades, starting with the works by e.g. Oldfield et al. [180], Seelig et al. [82, 86, 181, 182] and Stockton et al. [183] in the 1970's. This section summarizes the most important concepts of ^{2}H NMR for the determination of C-H (or, more accurately, C-^{2}H or C-D) bond order parameters and is mostly based on the work of J. Davis [184], in addition to references [164, 165, 185].

^{2}H has a nuclear spin of $I = 1$ and thus ^{2}H NMR is dominated by the quadrupolar coupling (Figure 3.1b). All nuclei with $I > 1/2$ have an electric quadrupole moment, i.e. the electric charge distribution of the nucleus is not a perfect sphere. This quadrupole moment interacts with the electric field gradient, $\boldsymbol{V}$, at the position of the nucleus. In it's principal axis system, $\boldsymbol{V}$ is diagonal with the three eigenvalues V_{xx}, V_{yy} and V_{zz}, where V_{zz} is the largest eigenvalue.

For ^{2}H in a C-D bond, $\boldsymbol{V}_{zz}$ is collinear to the bond vector, defining the angle θ_{ml} as shown in Figure 3.1b. The quadrupolar coupling constant $\chi = eV_{zz}Q/h$, with quadrupole moment Q, for ^{2}H in a C-D bond is about 167 kHz. This is a much smaller frequency than the ^{2}H Larmor frequency (e.g. 61.4 MHz at 9.4 T), and consequently it is sufficient to consider only the first-order terms of the quadrupolar Hamiltonian when calculating the effect of quadrupolar coupling on the NMR spectrum. For $I = 1$ one obtains three spin eigenstates with quantum numbers $m = \{-1, 0, +1\}$, and their energies given by

$$E_m = E_0 + \frac{3eV_{zz}Q}{4}[m^2 - \frac{2}{3}][P_2(\cos\theta_{\mathrm{ml}}) + \frac{1}{2}\eta_Q \sin^2\theta_{\mathrm{ml}} \cos 2\phi] \quad . \tag{3.11}$$

Note the similarity to equation 3.4. Further discussion will continue under the assumption that $\eta_Q = 0$. For liquid-crystalline lipids, this assumption is easily justified by the fast rotation of lipids about their long axis [86], see also section 3.1.1 on ^{31}P CSA. In the case of a rigid C-^{2}H bond (i.e. crystalline lipids and alkanes), ab-initio calculations [186] and ^{2}H NMR measurements on very short, solid n-alkanes [187] have also confirmed that η_Q is small enough to be neglected. However, the situation is more complicated in the gel- and rotator phases of lipids and alkanes, respectively, due to slow axial motions. The resulting ^{2}H spectra are quite broad, and are lacking distinctive features (except possibly the methyl group peaks, which benefit from sufficiently fast methyl group rotation even in the gel phase [85, 184, 188, 189]). It is not trivial to derive order parameters from such spectra and they are not considered further in this section.

For $\eta_Q = 0$, one can define

$$\Delta\nu_Q = \frac{3\chi}{2} P_2(\cos\theta_{\mathrm{ml}}) \quad , \tag{3.12}$$

and it becomes evident that the quadrupolar interaction shifts the Zeeman energy levels corresponding to $m = \pm 1$ by $+1/6\,\Delta\nu_Q$, and the energy level with $m = 0$ by $-1/3\,\Delta\nu_Q$ (compare equation 3.11). Thus, a ^{2}H quadrupolar spectrum shows two peaks at $\nu_0 \pm 1/2\,\Delta\nu_Q$, with a splitting of $\Delta\nu_Q$. Equation 3.12 states that the quadrupolar splitting $\Delta\nu$ is orientation dependent. Considering that NMR in fact measures the time averaged quantity $\langle\Delta\nu_Q\rangle$, this orientation dependence can be related to the C-D bond order parameter of lipid membranes, S_{CD} (or S_{CH}, equation 2.1). For a single C-D bond in a stack of lipid bilayers with director $\boldsymbol{d}$ and without membrane undulations (i.e. $\boldsymbol{d} \parallel \boldsymbol{n}$), equation 3.3 results in

$$\begin{aligned} \langle\Delta\nu_Q\rangle &= \frac{3\chi}{2} \langle P_2(\cos\theta_{\mathrm{md}})\rangle\, P_2(\cos\theta_{\mathrm{dl}}) \\ &= \frac{3\chi}{2}\, S_{\mathrm{CD}}\, P_2(\cos\theta_{\mathrm{dl}}) \end{aligned} \tag{3.13}$$

Similar to ^{31}P NMR, powder averaging over θ_{dl} needs to be considered. Thus the NMR spectrum is a superposition of resonance pairs, each with a certain splitting $\langle\Delta\nu_Q\rangle(\theta_{\mathrm{dl}})$. Such an exemplary powder pattern is shown in Figure 3.1b. Since the splitting related to $\theta_{\mathrm{dl}} = 90°$ is the most prominent, the order parameter is usually determined from the set of prominent horns separated by $\Delta\nu_{Q,\perp} = \langle\Delta\nu_Q\rangle(90°)$:

$$|\, S_{\mathrm{CD}}\,| = |\, -\frac{4}{3\chi}\,\Delta\nu_{Q,\perp}\,| \tag{3.14}$$

Using this method, only absolute order parameters can be obtained. However, it is possible to determine the sign of the order parameter using ^{13}C-^{1}H dipolar recoupling techniques which are discussed in chapter 3.1.6.

Usually, order parameters in a hydrocarbon chain vary along the chain. While it is possible to obtain selectively deuterated molecules, many studies make use of molecules that are deuterated in multiple positions. Then, the observed ^{2}H NMR spectrum will be a superposition of the individual powder spectra. An example for this is also included in Figure 3.1b. Similar to CSA, the quadrupolar coupling is averaged to zero in the case of isotropic systems. Then, $\langle\Delta\nu_Q\rangle = 0$ and the ^{2}H spectrum will only show a single, narrow peak at the Larmor frequency. Such spectra can be expected for example for liquid bulk *n*-alkanes, and thus static ^{2}H NMR is a useful tool to determine whether *n*-alkane molecules are mixed with lipid membranes, as shown in paper I.

It should be noted that so far only flat bilayers have been considered, where $\theta_{\mathrm{mn}} =$

θ_{md}. However, if membrane undulations are present, $\boldsymbol{d}$ is not necessarily parallel to $\boldsymbol{n}$, and

$$\langle P_2(\cos\theta_{\mathrm{md}})\rangle = S_{\mathrm{CD}} S_{\mathrm{nd}} \tag{3.15}$$

with [190]

$$S_{\mathrm{nd}} = \int_0^{\pi} P(\theta_{\mathrm{nd}}) P_2(\cos\theta_{\mathrm{nd}}) d\theta_{\mathrm{nd}} \quad . \tag{3.16}$$

$P(\theta_{\mathrm{nd}})$ then describes the probability distribution of angles θ_{nd}.

For spin $I = 1$ nuclei, the broad quadrupolar NMR spectrum is measured using the so-called quadrupolar echo, as opposed to a single 90° pulse. For a detailed discussion of the quadrupolar echo in terms of the spin-density matrix, the reader is referred to chapter 13.1.10 of M. Levitts book [164]. Suffice to say here that this echo sequence consists of two 90°-pulses separated by a delay τ, the second pulse being phase-shifted by 90°. It can be shown that the second pulse switches the satellite orders of the single-quantum coherences (which define the phase factor acquired during dephasing), resulting in refocusing of the quadrupolar interaction after the second pulse and an echo being observed at time 2τ.

3.1.3 Magic-angle spinning (MAS)

Even though anisotropic spin interactions provide useful information on sample structure, NMR spectra of satisfactory (isotropic) chemical shift resolution can only be obtained in the absence of such interactions. The following sections will show that this is particularly useful for ^{1}H and ^{13}C NMR experiments. Magic-angle spinning (MAS) allows averaging of orientation-dependent interactions to zero and is therefore an indispensable technique in solid-state NMR. During MAS, the sample is rotated at a sufficiently large frequency ω_{r} around an axis $\boldsymbol{r}$. For an anisotropic nuclear spin interaction whose orientation-dependence is defined by equation 3.1, the time-averaged orientation dependence under fast spinning can be written as

$$\langle P_2(\cos\theta_{\mathrm{ml}})\rangle = \langle P_2(\cos\theta_{\mathrm{mr}})\rangle P_2(\cos\theta_{\mathrm{rl}}) \quad , \tag{3.17}$$

where θ_{mr} and θ_{rl} denote the angles between the principle axis of the interaction tensor and the rotation axis, and between the rotation axis and the main magnetic field direction, respectively. If $\theta_{\mathrm{rl}} = \theta_{\mathrm{MA}} = 54.74°$, $P_2(\cos\theta_{\mathrm{rl}})$ is zero and consequently the time average of any orientation-dependent interaction proportional to $P_2(\cos\theta_{\mathrm{ml}})$ is also zero. However, this only holds if spinning is fast compared to the strength of the anisotropic coupling. For lipids in the L_α phase, ω_{r}=5 kHz is

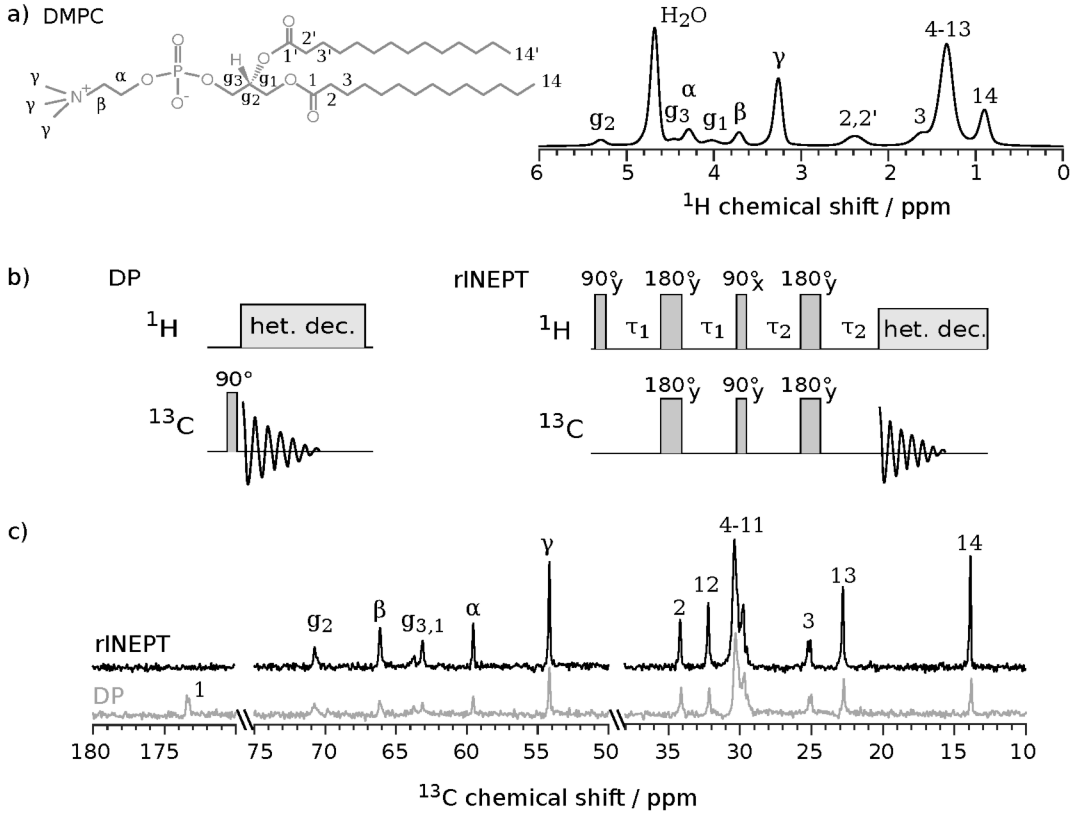

Figure 3.2: ^{1}H and ^{13}C MAS NMR of lipids. a) Assignment of lipid carbons and ^{1}H spectrum of DMPC in water, acquired at 35°C (i.e. in the L_α phase). Peak integration results in a water content of n_w=8.3±1.5. b) Pulse sequences of DP and the refocused INEPT technique. c) ^{13}C rINEPT and DP spectra for DMPC in water measured at 40°C. The two ^{13}C spectra were acquired using the same number of scans.

usually sufficient to obtain resolved spectra since molecular motion additionally decreases the strength of the relevant interactions. In some cases however, it may still be necessary to employ techniques for homo- or heteronuclear dipolar decoupling. Heteronuclear decoupling for ^{13}C NMR experiments is discussed in section 3.1.5.

3.1.4 ^{1}H-MAS NMR

^{1}H is an extremely convenient nucleus for NMR studies. ^{1}H has a spin of $I = 1/2$, has a natural abundance of close to 100 %, and is present in nearly every molecule. In addition, even single-pulse experiments (i.e. excitation by a 90°pulse and acquisition during the subsequent relaxation) can provide useful information on sample composition. Figure 3.2a shows the ^{1}H NMR spectrum of liquid-crystalline 1,2-dimyristoyl-*sn*-glycero-3-phosphatidylcholine (DMPC) in water, acquired under MAS and using a single-pulse excitation and one scan only. The assignment of the peaks is well known [191]. One can clearly identify the peaks related to the different protons in the lipid headgroup and glycerol backbone by their markedly different chemical

shifts. The protons in the middle of the acyl tails however are more difficult (or impossible) to distinguish. *n*-Alkanes are chemically identical to the lipid tails and thus their ^{1}H spectrum shows peaks at similar chemical shifts (carbon numbers 4 to 14 in the Figure, see also paper III).

The ^{1}H NMR spectrum shown in Figure 3.2a is quantitative, that is to say the intensity of a peak in the NMR spectrum is proportional to the number of corresponding protons in the sample. Thus ^{1}H NMR can be used to determine the amount of water in lipid/water mixtures by fitting the relevant peaks to the real part of a complex Lorentzian function,

$$I(\nu) = I_0 \frac{\lambda}{\lambda^2 + (\nu - \mu)^2} \quad , \tag{3.18}$$

where ν is the chemical shift frequency in Hz, μ is the position of the peak maximum, and λ and I_0 relate to the peak width and height, respectively. For example, nine protons per DMPC molecule contribute to the γ peak, but only two protons are connected to the α or β carbons each. Consequently, the area under the γ peak should always be 4.5 times larger than the α or β peak area. Similarly, the number of water molecules per lipid molecule, n_w, can be calculated from the relative area of the water peak. Using this method, the sample resulting in the spectrum shown in Figure 3.2a was found to have a water content of $n_w = 8.3 \pm 1.5$.

^{1}H NMR can also be used to differentiate between gel-phase and liquid-crystalline lipid bilayers, or to determine the lipid main transition temperature. In the gel phase the lipid acyl tails have a much lower mobility than in the liquid-crystalline phase. Thus homonuclear dipolar interactions are stronger, leading to shorter T_2 relaxation times and peak broadening [192, 193]. At MAS frequencies of 5 kHz, the broadening is strong enough that the peaks are hardly visible, and the integral of the ^{1}H acyl tail region (about 0-3 ppm) shows a step-wise change at the phase transition temperature [168, 194]. Paper III shows that this principle can also be applied to *n*-alkanes. In such cases, the measured ^{1}H intensity drops considerably when the *n*-alkanes enter the rotator or crystalline phase.

3.1.5 ^{13}C-MAS NMR

^{13}C NMR spectra acquired under MAS result in a better spectral resolution compared to ^{1}H NMR. The lipid peaks are distributed over a larger range of chemical shifts (Figure 3.2c) and thus it is easier to assign peaks to specific carbon atoms. Even more importantly, ^{13}C-^{1}H dipolar recoupling measurements can provide details on molecular structure and will be discussed in the following section.

^{13}C is also a spin-$^1/_2$ nucleus, however its natural abundance is only 1.1 %. The more

common isotope ^{12}C has a nuclear spin of zero and thus cannot be used for NMR experiments. Still, the low abundance of ^{13}C is advantageous since it guarantees that carbon homonuclear dipolar couplings can be neglected. However, even in fluid lipids, MAS frequencies of only 5 kHz are not sufficient to completely remove the ^{1}H-^{13}C dipolar coupling. In addition, the network of homogeneously coupled proton spins creates a time-dependence of the ^{13}C-^{1}H coupling, rendering MAS less efficient. Therefore it is necessary to perform heteronuclear decoupling during signal acquisition.

The most simple type of heteronuclear decoupling is the so-called high-power, continuous-wave decoupling. Here the ^{1}H spins are continuously irradiated with a high-power RF pulse. Irradiation at their resonance frequency induces transitions between the two I_z spin states. If these transitions are fast compared to the heteronuclear dipolar coupling strength, the ^{13}C nuclei are only affected by the time-averaged heteronuclear coupling to the protons, which is zero. Thus, effective heteronuclear decoupling is achieved. The main problem with this technique is that the high-power RF irradiation can lead to substantial sample heating. To avoid this problem, a number of other decoupling sequences which achieve a higher decoupling efficiency at the same RF power have been invented. Prominent examples include the TPPM [195, 196] or SPINAL [197] sequences which employ a variety of long pulses with varying phases and/or flip angles.

For lipid samples, direct polarization (DP) experiments, consisting of single-pulse excitation and acquisition under heteronuclear decoupling, result in reasonably large signal intensities (Figure 3.2b,c). Still, signal enhancement techniques can shorten the duration of an experiment significantly. When magnetization is for example transferred from ^{1}H to ^{13}C, the maximum signal enhancement possible is $|\gamma_{\mathrm{H}}/\gamma_{\mathrm{C}}| \approx 4$ (with γ being the gyromagnetic ratio). With regards to lipid bilayers, the most commonly used enhancement techniques are the refocused INEPT (rINEPT) [198] and cross polarization (CP) [199]. Both pulse sequences transfer magnetization from ^{1}H to the ^{13}C spins, but their efficiency strongly depends on the dynamics and C-H bond order parameters (i.e. dipolar couplings) in the system [200, 201]. An explanation of the relation between order parameters and dipolar coupling strength is given in section 3.1.6. Figure 3.2b shows the pulse sequence of the refocused INEPT technique. A comparison between rINEPT and DP spectra obtained from DMPC in the L_α is shown in Figure 3.2c. Clearly, the refocused INEPT produces notably higher signal intensities for most carbons. The difference in enhancement between different carbon peaks is due to the mechanism of the magnetization transfer. In the refocused INEPT experiment, magnetization is transferred via J-couplings. It was shown [200] that stronger dipolar couplings and the resulting increase in transversal relaxation rate significantly decrease the enhancement factor, and thus this technique is much more efficient for disordered bonds and fast dynamics. Considering the lipid order

parameter profile discussed in section 2.1.3 and figure 2.3, the signal increase from DP to INEPT is somewhat smaller for carbons between the glycerol backbone and the middle of the acyl tails. Still, INEPT is particularly well suited for lipids in the liquid-crystalline phase. At lower temperatures, or when ordering is increased by the addition of guest molecules, CP may result in better signal enhancement: CP performs best when order parameters are large and/or dynamics slow [200, 201]. This is because the CP magnetization transfer occurs via ^{1}H-^{13}C dipolar couplings. Such magnetization transfer between ^{1}H and ^{13}C spins is enabled by matching the Hartmann-Hahn condition, $|\gamma_{\mathrm{H}} B_1(^{1}\mathrm{H})| = |\gamma_{\mathrm{C}} B_1(^{13}\mathrm{C})|$. Under MAS, this condition is modified to $\omega_1^H - \omega_1^C = \pm n\omega_r, n = 1, 2$.

3.1.6 ^{13}C-^{1}H dipolar recoupling

^{13}C-^{1}H dipolar couplings provide information about the C-H bond order parameter, similar to static ^{2}H NMR techniques. In order to obtain structural information while simultaneously retaining the chemical shift resolution, so-called dipolar recoupling techniques have been designed. These pulse sequences re-introduce the heteronuclear dipolar interaction under MAS, and have two main advantages over ^{2}H NMR. First, measurements can be performed on standard molecules (without specific deuteration). Second, it is possible to unambiguously assign C-H bond order parameters to the correct carbons based on the ^{13}C isotropic chemical shifts. Certain recoupling techniques even allow the determination of the sign of S_{CH} [202]. In order to compare different recoupling techniques, it is beneficial to first review the effect of heteronuclear dipolar couplings on an NMR spectrum. Then, the concept of scaling factors is introduced and the advantages of the R-PDLF pulse sequence are discussed.

A ^{13}C spectrum in the presence of heteronuclear dipolar coupling takes the form of a Pake pattern, with horns separated by a splitting $\Delta\nu_{dd}$ that is a measure of the dipolar coupling strength. This shape is identical to the one obtained by quadrupolar coupling (with $\eta_Q = 0$, Figure 3.1b), however its origin is somewhat different: The magnetic moment of a nucleus, $\boldsymbol{\mu}$, creates a local magnetic field. If two spins, e.g. a ^{13}C and a ^{1}H spin are close in space, they experience the local magnetic field generated by the other spin. Then, the carbon transition frequency depends on the orientation of μ_{H} relative to μ_{C}, resulting in two resonances at

$$\nu_{dd} = \nu_0 \pm d_s \langle P_2(\cos\theta_{\mathrm{ml}}) \rangle \quad , \tag{3.19}$$

where θ_{ml} is the angle between the vector connecting the two spins and the main magnetic field, and d_s is the static coupling. The static dipolar coupling between two spins depends on their gyromagnetic ratios and the distance between them, and

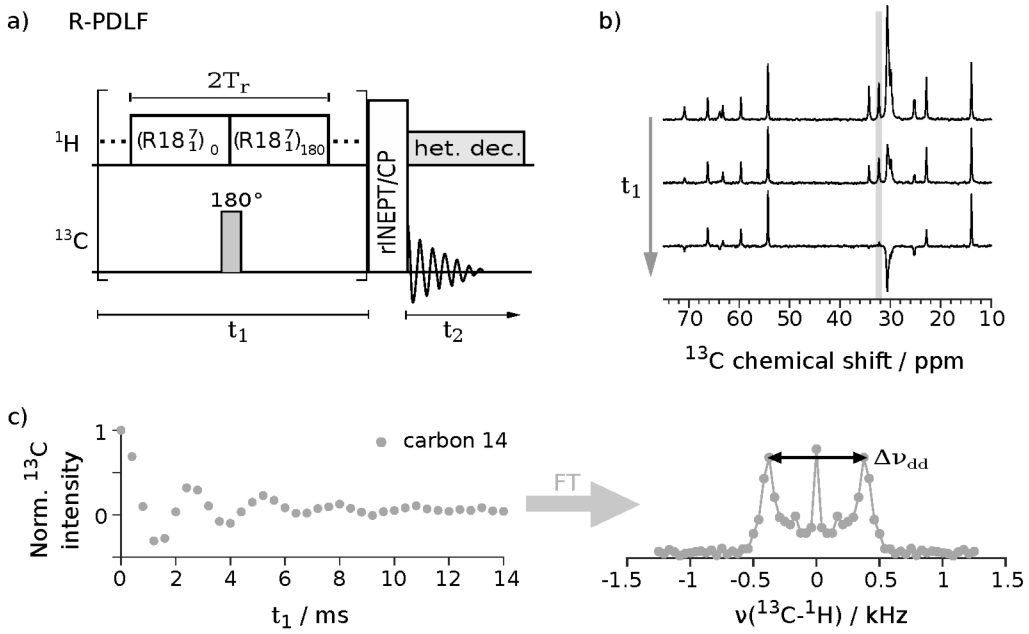

Figure 3.3: R-PDLF experiment. a) Pulse sequence of the R-PDLF experiment. b), c) Determination of order parameters via modulation of the ^{13}C intensities by ^{13}C-^{1}H dipolar coupling with t_1. Spectra of DPPC in water, acquired using rINEPT for magnetization transfer, are shown in b) for the first three values of t_1 (0, 0.4 and 0.8 ms; equal to $0\,T_r$, $2\,T_r$ and $4\,T_r$). The peak of carbon index 14 is highlighted, and the corresponding intensity modulation is shown in c) over the whole range of t_1. Fourier transform of the modulation yields a splitting $\Delta\nu_{dd}$ corresponding to a C-H bond order parameters of 0.111±0.006.

is approx. 21.5 kHz for a C-H bond [203]. In a crystalline solid, e.g. solid n-alkanes, averaging over different orientations θ_{ml} does not occur, and the spectrum is a superposition of resonance pairs. The orientation $\theta_{\mathrm{ml}} = 90°$ occurs most often, resulting in the characteristic powder-pattern line shape. The splitting between the two prominent horns then is $\Delta\nu_{dd} = 2d_sP_2(\cos 90°) = d_s$. In lipids and other anisotropic liquids the observed splitting is reduced by the factor $\langle P_2(\cos\theta_{\mathrm{md}})\rangle$ compared to the static splitting (see equation 3.3).

If dipolar recoupling techniques are used, the measured dipolar coupling is usually smaller than the true coupling by a factor k_d. If $d' = k_d\,\Delta\nu_{dd}$ is the coupling observed by a dipolar recoupling sequence, the following equation can be used to determine the C-H bond order parameter:

$$S_{\mathrm{CH}} = k_d^{-1}\frac{d'}{d_s} \tag{3.20}$$

The value of k_d depends solely on the type of recoupling technique used. It is important to select a sequence with a sufficiently large scaling factor, such that the splitting d' can still be resolved easily, even for the smallest expected order parameter.

One suitable option to measure C-H bond order parameters in lipids is the R-PDLF pulse sequence, depicted in Figure 3.3a [204, 205]. As is common for this kind of experiment, ^{13}C isotropic chemical shift evolution (during signal acquisition, t_2) and evolution under ^{13}C-^{1}H dipolar couplings (during t_1) are separated. Dipolar recoupling is achieved by type R18$_1^7$ recoupling blocks on the proton channel. These blocks each consist of eighteen 180° pulses, with alternating phases of 70° and -70°, spaced over exactly one rotor period T_r [203]. They simultaneously recouple the heteronuclear dipolar interactions and CSA, and decouple the ^{1}H-^{1}H homonuclear dipolar coupling. In order to remove CSA effects, an additional 180°-pulse is applied on the carbon channel at $t_1/2$, and the phases of the second half of R-blocks are all shifted by 180°. As the name suggests, R-PDLF is a PDLF ("proton-detected local field") technique. This means that the magnetization remains on the proton channel while ^{13}C-^{1}H coupling is active, in contrast to CDLF techniques ("carbon-detected local field"). PDLF techniques are thus particularly useful when the two protons in a CH_2 group have different order parameters. CDLF techniques such as FSLG-CP [205] or recoupled DIPSHIFT techniques [206, 207] can not distinguish these different order parameters since the effects of both protons on the carbon magnetization can not be separated. In order to retain this advantage of the R-PDLF experiment, the subsequent magnetization transfer should only occur between directly bonded protons and carbons. This is guaranteed by the refocused INEPT, or a CP with a sufficiently short contact time (see section 3.1.5). Then, during acquisition, the signal is only modulated by ^{13}C isotropic chemical shift since MAS averages out CSA, and heteronuclear decoupling removes residual ^{1}H-^{13}C interactions.

Figure 3.3b,c illustrates how to obtain order parameters from an R-PDLF measurement. The experiment is performed for a number of different t_1 values, each resulting in a ^{13}C spectrum. However, contrary to the spectrum shown in Figure 3.2c, the peak intensities are now modulated by the residual ^{13}C-^{1}H dipolar couplings. If these intensities are plotted versus t_1 for a selected peak, one observes a decaying oscillation. Stronger residual couplings, as found in the crowded spectral region and towards the glycerol backbone, correspond to larger frequency differences $\Delta\nu_{dd}$ and thus result in faster oscillations. This oscillation can be subjected to a Fourier transform to obtain a spectrum from which $\Delta\nu_{dd} = d'$ can be measured, as also shown in Figure 3.3c. S_{CH} is then calculated using equation 3.20 and a scaling factor of $k_d = 0.315$ [204]. This method was used in paper I, in order to determine the influence of *n*-alkane incorporation on lipid acyl tail ordering.

Instead of applying a Fourier transform, it can be advantageous to employ fitting techniques to determine the order parameters directly from the t_1-domain modulation [209, 210]. An example of time-domain fitting considering the spatial inhomogeneity of the RF field was highlighted in a recent publication by our group [208]: In order to resolve a splitting $\Delta\nu$ with sufficient accuracy, the longest time t_1 needs

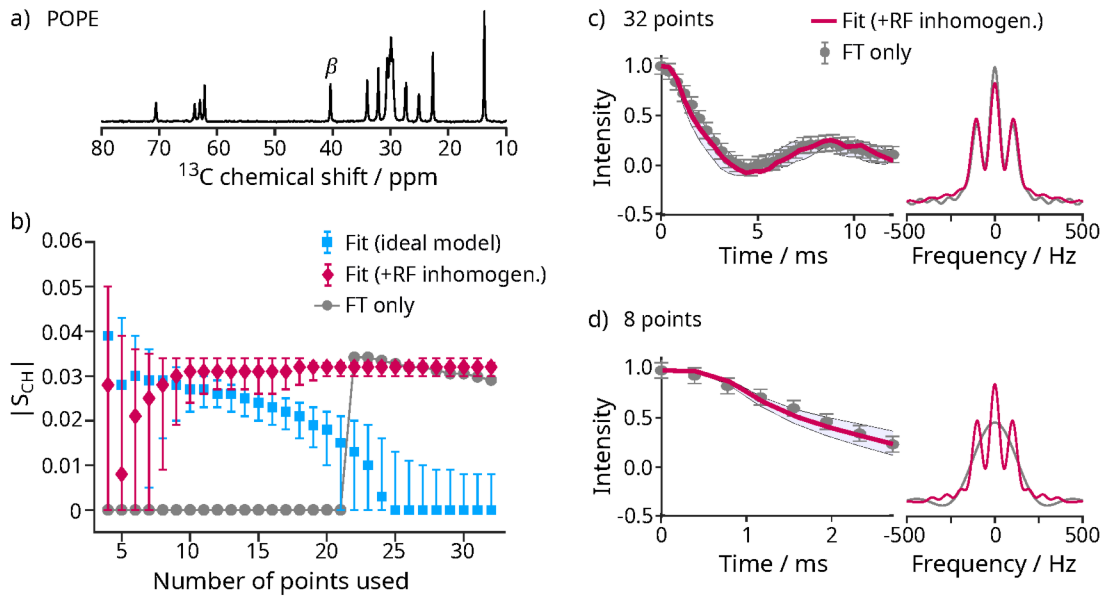

Figure 3.4: Time-domain fitting procedure including RF inhomogeneity; Figure adapted from reference [208][1]. a) ^{13}C refocused INEPT spectrum of POPE, b) C-H bond order parameter for the β carbon as a function of number of points in the time-domain, determined using the standard FT approach (gray), and employing the time-domain fitting technique with (red) and without (blue) accounting for RF inhomogeneity. c) Time-domain modulation with 32 points (gray) and Fit with RF inhomogeneity (red), and resulting frequency domain spectra using the two approaches. d) The same as c) but using only the first 8 points of the time-domain modulation.

to be longer than $0.5\,d'^{-1}$ [211] (ideally $t_{1,\max} \geq 4d'^{-1}$). If the modulation is a superposition of two different couplings with splittings d'_{A} and d'_{B}, the relevant coupling for determining $t_{1,\max}$ is $|d'_{\mathrm{A}} - d'_{\mathrm{B}}|$. Consequently, long times $t_{1,\max}$ are required to measure small order parameters or to separate multiple, similar order parameters for a single carbon index. Not only is the acquisition of many points t_1 very time-consuming, large t_1 values also result in significant heating of the sample due to RF irradiation. Time-domain fitting overcomes this problem, as shown in Figure 3.4. The standard FT approach provides accurate order parameters only when at least about 22 points are acquired in the time domain. Using the fitting procedure, the modulated intensity can be predicted for larger t_1 values and enables determination of $|S_{\mathrm{CH}}|$ for as few as 8 time-domain points. Importantly, the inhomogeneity of the RF field across the NMR sample [212] can obstruct the fitting process. In reference [208] we also showed that by simulating the time-domain modulation using a superposition of modulations corresponding to the different, measured RF frequencies across the sample, experimental data can be fitted reliably (Figure 3.4b).

[1]Published under the terms of the Creative Commons Attribution 4.0 License, which permits use and reproduction provided the original work is properly cited.

3.2 X-ray scattering

X-ray diffraction is widely used to determine the molecular structure of ordered phases, the most common example being the determination of unit cell parameters in crystalline systems. This example serves well to illustrate the basic concepts of X-ray diffraction/scattering experiments, and textbook knowledge is briefly summarized in the following. For further details and explanations the reader is referred to the book by W. H. de Jeu which this summary is based on [213].

If an x-ray beam is directed through a sample, the electrons present in the sample scatter the x-ray beam. Each atom then becomes the center of a radially scattered wave. If the sample exhibits structural order at length scales similar to the inverse x-ray wavelength $1/\lambda$, the scattered waves from various atoms interfere with each other. Then, scattering intensity can only be observed in the case of constructive interference. Consequently, the spacing of atoms with respect to each other, i.e. the crystal structure, defines the position of observable scattering reflections. Two conditions for observable reflections have been derived; The von-Laue condition states that the scattering vector $\boldsymbol{q} = \boldsymbol{k}_{\mathrm{out}} - \boldsymbol{k}_{\mathrm{in}}$ has to be equal to a lattice vector in so-called reciprocal space, $\boldsymbol{G}$, for scattered intensity to be observable. Here, $\boldsymbol{q}$ is defined by the wave vectors of the incoming and scattered waves, $\boldsymbol{k}_{\mathrm{in}}$ and $\boldsymbol{k}_{\mathrm{out}}$, respectively. The von-Laue condition is equivalent to the well-known Bragg equation,

$$2d\sin\theta = n\lambda \quad , \tag{3.21}$$

where d is the spacing of a given family of lattice planes, 2θ is the scattering angle, $n = 1, 2, 3, ...$, and λ is e.g. 0.1542 nm for the copper K_α line.

In crystalline powders, crystallites of different orientations can be found in the sample and one observes diffraction rings corresponding to distinct angles 2θ instead of individual reflections. It is common practice to perform angular averaging over this signal to obtain the scattering intensity $I(2\theta)$. Utilizing the relation between scattering angle and vector,

$$q = |\boldsymbol{q}| = \frac{4\pi}{\lambda}\sin\theta \quad , \tag{3.22}$$

one can instead plot $I(q)$, which is independent of wavelength. For crystals, $I(q)$ typically shows a series of sharp peaks. The spacing of these peaks can then be used to identify the type of the crystal lattice (e.g. hexagonal vs. different cubic lattices) and to determine the unit cell dimensions. Lamellar structures for example give rise to a series of equally spaced peaks.

The same principle can be applied to lipid multi-lamellar vesicles [214]. Of course,

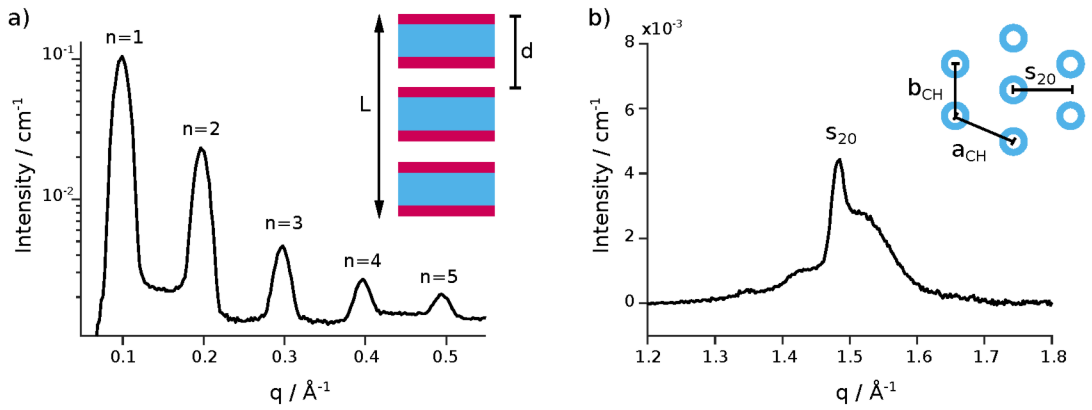

Figure 3.5: X-ray scattering intensities for DPPC in the $L_{\beta'}$ phase. a) Low-q range corresponding to the MLV bilayer structure, enabling calculation of the bilayer repeat distance d. b) High-q range indicating a distorted hexagonal unit cell with chain tilt for the acyl tail region.

gel-phase MLVs are very different from standard crystalline materials, but long range order persists in these systems and is reflected in the intensity profile $I(q)$. In lipid MLVs, two major "types" of order exist. First, the stacking of multiple bilayers in MLVs results in periodicity along the bilayer normal, i.e. along the director. In this case, d in equation 3.21 refers to the so-called repeat distance of the bilayers as defined in Figure 3.5a. A plot of the low-q region of $I(q)$ for a DPPC multilamellar vesicle is shown in the same figure (data from Figure 1 in paper III; note the similarity to DMPC in e.g. reference [215]). Here, DPPC is in the $L_{\beta'}$ phase. As mentioned above, lamellar order results in a characteristic intensity profile with equidistant peaks, and d can easily be determined by combining equations 3.21 and 3.22. Notably, the scattering peaks for DPPC are somewhat broad and the intensity decays towards higher orders n. This phenomenon is intensified in L_α bilayers (see e.g. paper I). To explain this observation, the liquid-crystal character of lipid bilayers needs to be considered [213, 214]. On one hand, MLVs consist of a finite number of stacked bilayers. This fact results in broadened peaks according to the relation

$$L = \frac{2\pi}{\Delta q} \quad , \tag{3.23}$$

where L refers to the size of the ordered domain (which is related to the number of stacked bilayers, see Figure 3.5a), and Δq is the full-width-at-half-maximum (FWHM) of a given peak. In addition, at high hydration, lipid bilayers are not perfectly planar, but are subject to local fluctuations and large-scale undulations. The increased disorder along the membrane director due to membrane undulations replaces true long-range order with quasi-long-range order, resulting in intensity loss for higher scattering orders n. Moreover, local disorder results in a broadening of the electron distribution along the bilayer normal, which also affects the peak

intensities. For lipid bilayers, the scattering intensity $I(q)$ is related to the bilayer structure by [216]

$$I(q) = S(q)|F(q)|^2 \quad , \tag{3.24}$$

where $S(q)$ is the (unit cell) structure factor, and $F(q)$ the so-called form factor. The form factor thereby is equal to the Fourier transform of the electron density, e.g.

$$F(q) = \int_{-d/2}^{d/2} \rho(z) \exp(iqz)\, dz \tag{3.25}$$

for the 1-dimensional case along the bilayer normal (z-coordinate). The correct determination of form factors is therefore essential for determining the electron density profile $\rho(z)$ of a lipid bilayer. Vice-versa, ρ affects $F(q)$ and therefore also $I(q)$.

In principle, only the magnitude (not the phase) of the complex value $F(q)$ is obtained from the measured scattering intensity. However, for lipid bilayers, the phase factors have been determined [216–219] and $\rho(z)$ can be obtained via inverse Fourier transformation of $F(q)$ [214, 216, 217, 220]. Using the electron density profile, it is possible to determine the average distance between the phosphorous planes of the two bilayer leaflets, $d_{\mathrm{P-P}}$, a quantity which is useful for comparing experimental results with computer simulations.

The second type of information that can be obtained from standard X-ray scattering experiments on lipid bilayers is related to the arrangement of the acyl chains. In gel-phase lipids, the acyl tails are highly ordered and thus a two-dimensional unit cell can be defined for the acyl tail region of a lipid bilayer [46]: For the $L_{\beta'}$ phase of DPPC for example, the high-q region of $I(q)$ shows a sharp peak with a shoulder at approximately $1.5\,\text{Å}^{-1}$ (Figure 3.5b). This peak position and shape is well known to indicate two-dimensional, distorted hexagonal chain packing with chain tilt. The sharp peak thereby corresponds to the distance $s_{20} \approx 4.20 - 4.25\,\text{Å}$, which results in distances $a_{\mathrm{CH}} \approx 4.80 - 4.86\,\text{Å}$ and $b_{\mathrm{CH}} \approx 4.65 - 4.70\,\text{Å}$ at 20°C [46, 59, 66, 215, 221]. When chain tilt is removed, for example by addition of cholesterol [222] or n-alkanes [137], the peak loses its shoulder and the chain packing becomes hexagonal [59, 223]. Thus, observation of the high-q peak can be useful to characterize the mixing of lipids with additives. An example showing the effect of adding the n-alkane C20 to DPPC bilayers is included in paper III.

3.3 Cryogenic transmission electron microscopy

Cryogenic transmission electron microscopy (cryo-TEM) provides high-resolution images of biological samples such as lipid vesicles and nanodiscs, membrane proteins or viruses [224–229]. Importantly, vitrification of the sample at cryogenic temperatures enables the study of biologically relevant structures with minimal perturbation of the native state. TEM requires a thin sample, which is imaged using an electron wave. This electron wave is scattered by electrostatic interactions with the nuclei in the sample, resulting in contrast between high- and low-density regions in the sample. A more detailed description of the different imaging mechanism and special considerations can be found e.g. in reference [230]. For lipid vesicles in water, the lipid bilayers are clearly visible due to the comparatively high density of the lipid headgroup region [231]. If resolution and image contrast are good, it is possible to identify both the headgroup- and hydrophobic region of the membranes. Examples of such images are shown in paper I or in references [224, 232, 233].

Since TEM requires a vacuum environment to minimize scattering of the electron beam outside of the sample, a rigid sample film has to be prepared [234]. For cryo-TEM, this film is prepared by vitrification of aqueous solutions [224, 234, 235]: A metal grid with hydrophilic surface coating, e.g. carbon coating, is wetted with the lipid suspension. When excess water is removed using blotting paper, the holes in the grid will be spanned by a thin film of the suspension. Vitrification is achieved by rapidly plunging the grid into liquid ethane or propane, which have a high thermal conductivity and sufficiently low freezing points. The sample grids then need to be stored at temperatures below approximately 135 K, the temperature at which vitrified water crystallizes to ice [236]. Since this "plunge-freezing" technique immobilizes biological systems in a native state, cryo-TEM enables for example the imaging of different membrane states. While liquid-crystalline lipid vesicles have a smooth surface, rippled and gel-phase bilayers can be identified by wavy surfaces or surfaces consisting of multiple planar sections, respectively [233, 237].

3.4 Differential scanning calorimetry

Differential scanning calorimetry (DSC) is a popular method to study phase transitions in soft-matter systems since it allows to measure heat capacities and transition enthalpies. Together with differential thermal analysis (DTA), DSC has been used to derive transition temperatures between lipid or *n*-alkane phases for decades, see e.g. references [56, 70, 91, 95, 238, 239]. This section summarizes the most relevant concepts of DSC based on the detailed explanations provided in references [240–242], unless otherwise noted.

Phase transitions such as melting, crystallization and transitions from/to the gel and rotator phase in lipids and n-alkanes are thermodynamic first-order transitions. Consequently, they can be easily identified and characterized by changes of thermodynamic quantities such as heat capacity or enthalpy. DSC allows to measure heat capacities in one of two slightly different ways, depending on the instrument: Heat flux DSC or power compensation DSC. Both modes compare the sample to a reference (which is often an empty aluminium pan), in order to determine the amount of heat absorbed or released by the sample during a thermal transition. In heat flux DSC instruments, sample and reference are heated (or cooled) in the same oven, and the temperature of each pan is recorded during the heating/cooling process. During a phase transition, the sample absorbs or generates heat, resulting in a temperature difference between sample and reference pan. This measured temperature difference is proportional to the heat absorbed/released by the sample. On the other hand, power compensation DSC which was used in this thesis (Paper III) relies on heating or cooling the sample and the reference in separate ovens. Instead of adding the same amount of heat per time to both pans, the heating power for the sample is changed based on the temperature difference measured between sample and reference. For example, once a sample reaches its melting temperature, additional heat is required to overcome the attractive forces between crystal molecules, and to melt the sample. Then, in order to keep the temperature of the sample the same as in the reference pan, the heating power for the sample pan needs to be increased compared to the reference power. The difference in heating power supplied to the two pans is then related to the heat absorbed by the sample.

Generally, the heat flow to/from the sample $\Phi = {}^{dQ}/_{dt}$ is recorded as a function of time or temperature and can easily be transformed into the heat capacity (at constant pressure) C_p by multiplication with the inverse heating/cooling rate β:

$$C_p = \frac{dQ}{dT} = \Phi \cdot \beta^{-1} \tag{3.26}$$

First order phase transitions are visible as a peak in the heat capacity, which yields information on the temperature range of the transition. Second-order phase transitions or the glass transition in polymers may also be observed as a step in the heat capacity curve. The actual amount of heat absorbed/produced by the sample during the transition, ΔH, is termed transition enthalpy or latent heat. It is obtained by integrating C_p with respect to temperature in the transition range:

$$\Delta H = \int_{T_1}^{T_2} C_p \, dT = \int_{t_1}^{t_2} \Phi \, dt \tag{3.27}$$

In this thesis, endothermic transitions (heat absorption by the sample, e.g. during melting) are shown as positive peaks, while exothermic transitions (heat production

as during crystallization) correspond to negative peaks/enthalpies. It is important to note that the phase transition temperatures determined by DSC often depend on the heating and cooling rates used during the experiment [243]. This effect can be understood by considering that a change in sample structure takes a certain amount of time to be realized. Thus, at higher rates, peaks may appear at later temperatures because the structural change "can not keep up" with the temperature change.

DSC can also be used to investigate crystallization kinetics. This is usually done by isothermal crystallization experiments, as described by Müller and Michell [244]. In this kind of experiment, the sample is first equilibrated at high temperature and then quickly cooled to certain temperature T_c below the melting temperature. This temperature is kept constant for the remaining duration of the experiment and the heat flow is recorded as a function of time. One can then determine the crystalline fraction as a function of time, $f(t)$, by

$$f(t) = \frac{\Delta H(t)}{\Delta H_{total}} \tag{3.28}$$

where ΔH_{total} refers to the total transition enthalpy. f increases due to two different processes: nucleation and crystal growth. This can lead to an interesting temperature dependence of the crystallization rate. At low T_c, molecular diffusion is decreased, making it harder for free chains to reach the site of a nucleus. At the same time however, nucleation is more efficient since nuclei are more likely to reach the critical size needed to become stable. As a consequence, the dependence of the crystallization rate on temperature can be used to identify which of the two effects is dominant, as was done in paper III. If, for example, the crystallization rate is faster at lower crystallization temperatures, molecular diffusion does not play a large role in that temperature range. It is important to note that equation 3.28 can also be used to calculate the fraction of converted molecules for any other thermal first-order transition. For example, this method was used in paper III to determine the amount of *n*-alkane in the rotator phase. However, if multiple transitions occur during the isothermal step, or not all molecules in the sample are subjected to the transition, this of course has to be taken into account.

Chapter 4

Molecular dynamics simulations

Often, the understanding of a system or process can be improved by performing computer simulations. For example, some quantities or properties of a system can be difficult to obtain experimentally. When systems are complex, simulations help to distinguish different effects from one another. Simulations also allow to predict the properties of systems that are particularly difficult, or impossible, to realize experimentally, either due to preparation issues or extreme environmental conditions. In biophysics, computer simulations have become an essential tool to supplement experiments [245], and have for example been used to predict peptide and protein structures [246–248], investigate lipid-protein interactions [44], or study lipid droplet formation [5].

4.1 General principles

Classic molecular dynamics (MD) simulations are based on Newton's equations of motion and thus present a deterministic simulation approach. This makes them substantially different from e.g. Monte Carlo simulations which are stochastic in nature. For the study of biomembranes it is often desirable to observe dynamic properties (e.g. time correlation functions) and thus MD is the simulation method of choice. General aspects of MD simulations are discussed in detail for example by J. M. Haile [249], M. P. Allen [250] and in the extensive reference manual of the GROMACS simulations software [251], and are summarized in this section. Since the GROMACS software [252–254] makes MD simulations easily accessible, this chapter highlights algorithms available in GROMACS in particular.

The aim of an MD simulation is to obtain the trajectory $\{\boldsymbol{r}^N(t), \boldsymbol{v}^N(t)\}$ with $\boldsymbol{r}^N = \{\boldsymbol{r}_1, \boldsymbol{r}_2, ..., \boldsymbol{r}_N\}$ for a system containing N particles. Then, various time-averaged, structural and thermodynamic quantities $A(\boldsymbol{r}^N(t), \boldsymbol{v}^N(t))$ can be derived from this

trajectory, according to

$$\langle A \rangle = \lim_{\tau \to \infty} \int_{t_0}^{t_0+\tau} A(\boldsymbol{r}(t), \boldsymbol{v}(t))\, dt \quad . \tag{4.1}$$

This includes for example kinetic energy, temperature, densities and order parameters. Newton's first law of motion states that a force acting on a particle is related to its mass and acceleration by

$$F(\boldsymbol{r}) = m\, \frac{d^2 \boldsymbol{r}}{dt^2} \quad . \tag{4.2}$$

Consequently, if one could accurately define all the forces acting on a single particle at a certain point in time t and space $\boldsymbol{r}$, one might calculate the position of the particle at time $t_0 + \Delta t$ by e.g. a truncated Taylor expansion, provided that the velocity $\boldsymbol{v}$ at time t is known and that the force remains constant during Δt:

$$\boldsymbol{r}(t + \Delta t) = \boldsymbol{r}(t) + \Delta t\, \boldsymbol{v}(t) + \Delta t^2\, \frac{\boldsymbol{F}(t)}{2m} \tag{4.3}$$

Clearly, if one considers a system of many thousands of particles, the forces will depend on the relative positions of the particles to each other and they can be expected to change continuously. However, if Δt is small, sufficiently realistic approximations of the complete trajectory can be obtained by these so-called finite-difference methods. The velocity Verlet algorithm and the leap-frog algorithm are popular examples of such methods for MD simulations. They are both adequately stable (i.e. the algorithms do not amplify errors during propagation for a suitable range of values Δt), and they only require updating the forces once per step Δt. As will be discussed further below, calculating the forces is computationally expensive and thus this should be done as seldom as possible. The leap-frog algorithm for example is based on calculating the positions and velocities at different time points according to the following set of equations:

$$\begin{aligned} \boldsymbol{v}(t + \frac{1}{2}\Delta t) &= \boldsymbol{v}(t - \frac{1}{2}\Delta t) + \Delta t\, \frac{\boldsymbol{F}(t)}{m} \\ \boldsymbol{r}(t + \Delta t) &= \boldsymbol{r}(t) + \Delta t\, \boldsymbol{v}(t + \frac{1}{2}\Delta t) \end{aligned} \tag{4.4}$$

Apart from estimating the total force on a particle, calculating the trajectory seems straightforward. However, there are a number of additional points that should be considered. First, the simulation algorithm requires a set of initial coordinates and velocities. Importantly, depending on the simulation settings, it is not guaranteed that the system will reach the expected (equilibrium) arrangement during the time of the simulation if the initial configuration is far from equilibrium. Starting velocities are usually chosen according to a Maxwell-Boltzmann distribution which defines the

probability of finding a certain velocity v at the desired simulation temperature T:

$$p(v) = \sqrt{\frac{m}{2\pi k_B T}} \exp\left(-\frac{mv^2}{2k_B T}\right) \tag{4.5}$$

Here, k_B is Boltzmann's constant.

So far, generic particles of a certain mass have been discussed. In MD simulations, particles are also defined by their charge and interaction potentials, as described in the force field (see following section). Since classic MD simulations do not consider quantum mechanical theories, the simulated particles should not be elementary particles, but rather atoms. However, in principle a particle may also refer to a select group of atoms such as methyl or methylene groups, or even the complete headgroup of a lipid molecule. These two cases are usually referred to as united-atom and coarse-grained simulations, respectively. In truly atomistic simulations, each atom is a unique particle and thus such simulations provide the most detailed representation of molecular structure. However, most observables (e.g. the C-H bond order parameter) can be calculated from united-atom simulations as well [255, 256]. It should be noted here that even atomistic MD simulations are not designed to describe excited electronic states, since electrons are inherently in the ground state.

Coarse-grained simulations also have certain advantages, the most important one being the fact that a reduced number of particles necessarily shortens the computation time and allows to simulate much larger systems or longer times. Thus, united-atom and coarse-grained simulations are often used to model phase transitions, large-scale structural changes and complex biological systems [15, 257, 258]. While larger systems can be simulated using coarse-graining, the simulated system is always of finite size. Clearly, if bulk substances are to be studied, a method to determine inter- and intramolecular forces near the system edges needs to be found in order to remove surface effects. This is achieved by introducing so-called periodic boundary conditions (pbc): The simulated system is always confined to a (cubic or rhombic) simulation box. Using pbc, this simulation box is surrounded by mirror images of itself in a space-filling manner. Now, any atom close to the box edge is effectively still surrounded by other atoms in all spatial directions, for the purpose of calculating forces. In addition, if an atom leaves the simulation box during a simulation step, at the same time the corresponding atom of a mirror image enters the box from the opposite site. Since atoms of the mirror image behave exactly as the original, mass and energy of the system are conserved with pbc.

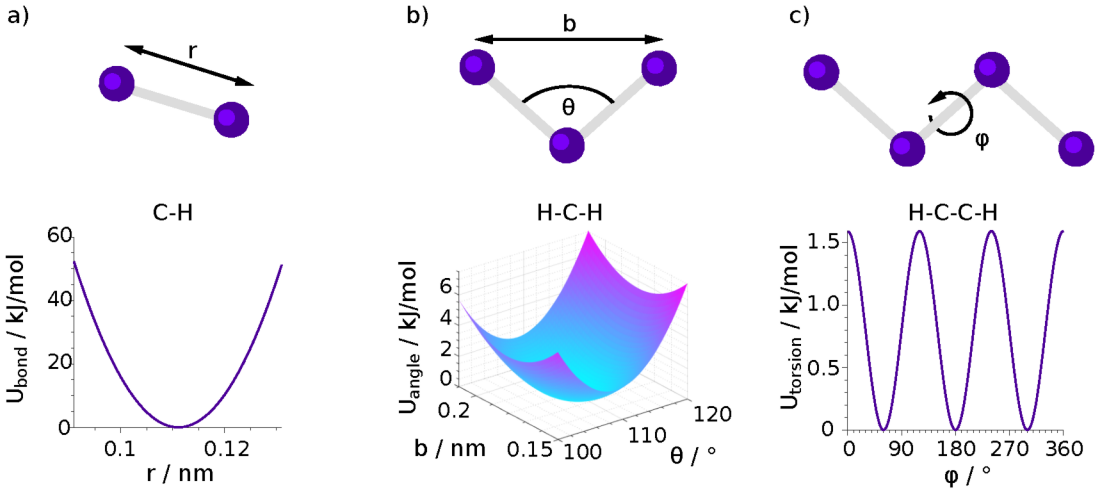

Figure 4.1: Bonded interaction potentials. a) Harmonic bond stretching and corresponding U_{bond} as defined in equation 4.8, using $k_r = 258571.2\,\text{kJ}\,\text{mol}^{-1}\,\text{nm}^{-1}$ and $r_0 = 0.1111\,\text{nm}$ (CHARMM36 methylene C-H bond potential). b) Bond-angle vibration and Urey-Bradley potential with $k_\theta = 297.064\,\text{kJ}\,\text{mol}^{-1}\,\text{rad}^{-1}$, $\theta_0 = 109.0°$, $k_b = 4518.72\,\text{kJ}\,\text{mol}^{-1}\,\text{nm}^{-1}$ and $b_0 = 0.1802\,\text{nm}$ (values corresponding to CHARMM36 methylene H-C-H angle). c) Dihedral angle orientation and potential according to equation 4.11, with $k_\phi = 0.79496\,\text{kJ}\,\text{mol}^{-1}\,\text{rad}^{-1}$, $\phi_0 = 0°$and $n = 3$ (e.g. CHARMM36 methylene H-C-C-H dihedral). All the calculated potentials are only valid for the shown sets of 2, 3 or 4 atoms, and do not include any summation of individual potentials.

4.1.1 Inter- and intramolecular forces

The force on a molecule i is given by the derivative of a potential function U:

$$\boldsymbol{F}_i = -\frac{\partial U}{\partial \boldsymbol{r}_i} \tag{4.6}$$

For atomistic MD simulations, U is generally defined as the superposition of various bonded and non-bonded interactions:

$$U = U_{\text{bond}} + U_{\text{angle}} + U_{\text{torsion}} + U_{\text{LJ}} + U_{\text{Coulomb}} \tag{4.7}$$

The form of these potentials, as well as the complete set of interaction parameters used to describe them, is referred to as the force field. Bonded interactions are represented by the first three terms of equation 4.7 and refer to potentials arising from the local conformation of a molecule. Commonly, the bonded interactions are separated into bond-, angle- and torsion-angle/dihedral contributions. For example, bond stretching can be described by a harmonic potential,

$$U_{\text{bond}} = \sum_{\text{bonds}} \frac{1}{2} k_r (r - r_0)^2 \quad , \tag{4.8}$$

where k_r is the force constant, r is the bond length, and r_0 is the equilibrium bond length (Figure 4.1a). Importantly, most atoms are bonded to more than one other atom, which is signified by the sum in the equation. Similarly, the potential of the bond-angle vibration may be defined as

$$U_{\text{angle}} = \sum_{\text{angles}} \frac{1}{2} k_\theta (\theta - \theta_0)^2 \tag{4.9}$$

or

$$U_{\text{angle}} = \sum_{\text{angles}} \frac{1}{2} k_\theta (\theta - \theta_0)^2 + \frac{1}{2} k_b (b - b_0)^2 \quad . \tag{4.10}$$

Here, equation 4.10 gives the Urey-Bradley potential for bond-angle vibrations which includes a correction term for bond-length fluctuations, as shown in Figure 4.1b. The periodic (proper) dihedral potential defines the trans ($\phi = 180°$) and gauche ($\phi = \pm 60°$) configurations of a molecule, and is often given by

$$U_{\text{torsion}} = \sum_{\text{dihedrals}} k_\phi (1 + \cos(n\phi - \phi_s)) \quad , \tag{4.11}$$

though other functional descriptions may be chosen [251]. Shown in Figure 4.1c is the dihedral potential for a single set of four atoms (e.g. a lipid methylene H-C-C-H sequence).

The non-bonded (or intermolecular) interactions are usually represented by the Lennard-Jones (LJ) and Coulomb potentials. The LJ potential combines short-range overlap repulsion and attractive van-der-Waals/long-range dispersion forces:

$$U_{\text{LJ}} = \sum_{i \neq j} 4\epsilon_{ij} \left(\left(\frac{\sigma_{ij}}{r_{ij}} \right)^{12} - \left(\frac{\sigma_{ij}}{r_{ij}} \right)^{6} \right) \tag{4.12}$$

The LJ potential is determined by the parameters ϵ and σ, defining the depth and position of the energy minimum of U_{LJ}, respectively. The sum has to be taken over all atom pairs $i \neq j$ in the system, but usually excludes bonded pairs, i.e. atoms up to three bonds apart, which is considered by the bonded interaction potential parameters. As will be discussed in section 4.2.1, so-called 1-4 interactions, i.e. interactions between pairs separated by exactly three bonds, are often specified separately in a force field. The calculation of dispersion forces has one major problem: The LJ potential only reaches zero at infinity. Clearly, calculating the forces between all possible atom pairs in the simulated system is computationally much too expensive (even when ignoring the issue of finite system size). However, simply ignoring contributions from pairs separated by larger distances will add a discontinuity which may ultimately result in a violation of energy conservation. The standard method to avoid this problem is the use of shifted or switched potentials/forces. For example,

in the case of force-switching, the absolute force between atoms i and j, $F^{LJ}(r_{ij})$, is modified according to

$$F^{LJ}_{\text{switch}}(r_{ij}) = \begin{cases} F^{LJ}(r_{ij}) & r_{ij} < r_{\text{switch}} \\ F^{LJ}(r_{ij}) + S(r_{ij}) & r_{\text{switch}} \leq r_{ij} < r_{\text{vdw}} \\ 0 & r_{\text{vdw}} \leq r_{ij} \end{cases} \tag{4.13}$$

where $S(r_{ij})$ is e.g. a third-degree polynomial which is smooth at the boundaries r_{switch} and r_{vdw}. Clearly, even though long-range dispersion forces are weak, disregarding them can result in errors. In recent years, an alternative long-range treatment for LJ dispersion forces has been developed based on the particle-mesh Ewald (PME) lattice-summation method [259–262]. PME is a well-known algorithm often used to account for long-range electrostatic interactions [263, 264]. While it can in principle be applied to any interaction for which the potential decays with $r^{-\alpha}$, $\alpha \geq 1$, adapting PME for the LJ dispersion forces has been challenging. Thus, it is not (yet) available for e.g. all the different lipid force fields.

The potential corresponding to the electrostatic interactions takes the form

$$U_{\text{Coulomb}} = \sum_{i \neq j} \frac{q_i q_j}{4\pi\epsilon_0 r_{ij}} \quad . \tag{4.14}$$

Here, $q_{i/j}$ are the partial atom charges, ϵ_0 is the vacuum permittivity and r_{ij} is the distance between two atoms i and j. Similar to the LJ potential, the Coulomb potential extends to large distances r_{ij}. It is common practice to consider long-range electrostatic interactions via the PME algorithm.

It should be noted that usually every atom/particle has a distinct partial charge. This point charge remains centered on the particle during the simulation and thus polarization effects can not be treated under normal circumstances. Specifically designed, polarizable force fields exist [265, 266], but are not discussed further here.

4.1.2 Temperature- and pressure coupling

Equilibrium MD simulations consider an isolated system of N molecules in a simulation box of volume V. Such simulations conserve energy, with total energy $E = E_{\text{kin}} + U$, resulting in a microcanonical (NVE) ensemble. However, experimentally measurable thermodynamic quantities are often formulated in the canonical (NVT) ensemble, at constant temperature T. This includes for example the heat capacity, which is defined via fluctuations of total energy,

$$C_V = \frac{1}{k_B T^2} \langle (E - \langle E \rangle^2) \rangle \quad . \tag{4.15}$$

In fact, a comparison with experimental results is usually most easy for NPT ensembles, since experiments are often conducted at constant ambient pressure. In order to perform MD simulations in an NVT or NPT ensemble, one makes use of temperature- and pressure coupling techniques. NVT ensembles are realized by temperature coupling algorithms alone, such as e.g. the Berendsen- [267], velocity-rescaling- [268] or Nosé-Hoover thermostats [269, 270]. The velocity-rescaling algorithm is an extension of the Berendsen thermostat; both rescale the velocities (e.g. kinetic energies) of all particles after each step Δt by a certain factor. As a result, the temperature deviation decays exponentially with simulation time. However, this simple rescaling approach results in incorrect sampling of the canonical ensemble, and thus computed quantities related to (energy) fluctuations such as the heat capacity may not be correct. The velocity-rescaling algorithm therefore adds a correction to the kinetic energy, such that a proper canonical ensemble is realized. The Nosé-Hoover thermostat does not rescale velocities, but instead introduces a friction coefficient into the equations of motion. This friction coefficient in turn has a time-dependent momentum which changes with the temperature deviation, resulting in an oscillatory approximation of the desired temperature. In NVE simulations, energy conservation is generally used for monitoring, and as an indicator for simulation errors. The temperature-coupling schemes presented here also allow the formulation of a conserved quantity that can be monitored instead of total energy.

For pressure coupling, the Berendsen barostat functions in the same manner as the respective thermostat [267], except using a reference pressure tensor instead of a reference temperature. Then, this reference pressure is approached exponentially with time by a continuous adjustment of the box dimensions and atom positions between simulation steps. However, again this algorithm does not provide the correct ensemble. An alternative is provided by the Parinello-Rahman pressure coupling [271, 272] which defines an equation of motion for the box dimensions, and also adjusts the particle velocities similarly to the Nosé-Hoover thermostat. In practice it can be beneficial to combine Berendsen pressure coupling during equilibration with Parinello-Rahman coupling during the production run.

4.1.3 Additional considerations

It is essential to find a suitable time step Δt that allows to capture even the fastest motions and does not obstruct energy conservation, but is also sufficiently large to enable efficient computing. Importantly, the atomic bond vibrations in organic substances generally have very high frequencies ($\nu \gtrsim k_\mathrm{B}T/h$), and thus they should be described by quantum mechanics rather than classic theories. Consequently, in MD simulations atom bonds are often constraint to certain bond length after each simulation step. Examples for such constraint algorithms are SHAKE [273],

SETTLE [274] or LINCS [275].

Finally, the total simulation time needs to be sufficiently long in order to accurately approximate the time-average given in equation 4.1. This time should approximately be longer than a few multiples of the correlation time corresponding to the property.

4.2 Lipid membrane simulations

Many simulations of biomembranes focus on describing the structure and dynamics of membrane proteins in their native environment. However, for such studies to provide realistic results it is essential to have an accurate representation of the membrane lipid environment. Moreover, the properties of different lipid types, and mixtures thereof, may strongly influence the behaviour of other membrane constituents. In order to accurately model lipid membranes with MD simulations, it is essential to use a suitable force field. This is becoming increasingly important as the simulated membranes become more and more complex [78, 257, 276].

4.2.1 Lipid force fields

Selecting the best lipid force field is no easy task, considering the variety of force fields that have been developed to date. Comprehensive reviews discussing the available force fields for lipid membrane simulations have been published for example by A. P. Lyubartsev and A. L. Rabinovich in 2016 [277], as well as by A. Leonard et al. [278] or S. J. Marrink et al. [257] in 2019. Even though certain updates have been made in more recent years, e.g. to the CHARMM force field [262, 276], the force fields presented in these reviews are still widely used and implemented into common simulation software tools such as CHARMM [279], NAMD [280] and GROMACS [252–254]. In the context of the NMRlipids project (nmrlipids.blogspot.com), an open-science collaboration across several research groups, the advantages and disadvantages of the different well-known lipid force fields have been evaluated by comparison with experimental results. Notably, the comparison with e.g. NMR order parameters and form factors from x-ray scattering has shown that all these force fields have certain deficiencies [256, 281–284]. In other words, the best force field to be used may depend on membrane composition as well as the scientific question to be answered. Currently, efforts are being made to provide a robust solution to finding optimal force fields, utilizing a large communal databank of simulations and experiments [285].

The most widely used all-atom force fields for lipids can be sorted into the CHARMM, AMBER and OPLS families. Within these families, compatible force field para-

metrizations exist for various biomolecules and can be combined to model complex membranes. The method of force field parametrization varies somewhat between the families, resulting in unique force fields. For example, CHARMM force fields rely on parametrization via ab-initio quantum-mechanic calculations on small model compounds in the gas phase [278, 286, 287]. In practice, the selection of a force field will likely be based on the availability of a reliable parameter set for the target molecule, as well as personal taste.

Two force fields are described in more detail here: the CHARMM36 [287] and Slipids [288, 289] force fields. CHARMM36 belongs to the CHARMM family and represents a recent force field version that overcomes previous limitations to correctly reproduce the area-per-lipid in NPT ensembles. This force field is however still dependent on a cut-off scheme for the LJ potential, which is only addressed in more recent updates [261, 262, 276]. The bonded and non-bonded potentials used in the CHARMM36 force field are described by the equations given in section 4.1.1, using the Urey-Bradley angle potential. In addition, so-called improper dihedrals which are used to fix certain planar groups (e.g. aromatic rings) or maintain chiral centers, are included for the carbonyl groups connecting the glycerol backbone to the lipid tails. The improper dihedral potential thereby is a simple harmonic potential.

CHARMM36 is known to yield the most realistic order parameters for PC headgroups out of the commonly used lipid force fields [256]. It also reliably approximates the acyl chain ordering, area-per-lipid (apl) and x-ray scattering form factors [287], as well as NMR relaxation times [172]. However, it was found that area-per-lipid and chain ordering depend slightly on the simulation software used, as discussed by Lee et al. [290]. For example, GROMACS was found to result in slightly higher acyl tail ordering compared to the CHARMM or NAMD softwares, for which CHARMM36 was designed originally. Lee et al. argue that this is likely due to the manner in which cut-offs for long-range dispersion forces are treated in the different softwares. Using a PME algorithm for the LJ interactions, as implemented in the newer CHARMM modifications [261, 262, 276], should mitigate this problem. A comparison of simulation results obtained with and without the LJ-PME treatment in GROMACS is shown in Figure 4.2a. The use of LJ-PME results in slightly decreased acyl tail ordering which is reflected in slightly larger area-per-lipid and smaller thickness.

The Slipids force field is based on the CHARMM36 force field, but a number of changes have been made to the parameters [288]. Partial charges have been recalculated using the RESP scheme [291] based on quantum-mechanical calculations of the electrostatic potential around hexadecane molecules (for the acyl tails) or the DMPC headgroup (for the headgroup charges). As a result, the methylene carbons and protons in the lipid acyl tails each have a zero net charge, which is considerably different from the CHARMM36 partial charges. In addition, in the Slipids force

field the Coulomb interactions between atoms connected via exactly three bonds are scaled down by a "fudge" factor, $f_{QQ} = 0.8333$. This is considered via an additional term in the potential, written as

$$U_{\text{Coulomb},1-4} = f_{QQ} \sum_{1-4} \frac{q_i q_j}{4\pi\epsilon_0 r_{ij}} \quad . \tag{4.16}$$

These so-called 1-4 interactions are also considered in the CHARMM36 force field, albeit with $f_{QQ} = 1.0$. The same method of deriving the partial charges in the Slipids force field is also used in the AMBER family of force fields, and thus it is expected that Slipids can be combined with AMBER parametrizations of other (non-lipid) molecules in order to simulate complex biological membranes.

In addition to the partial charges, Slipids also uses slightly different parameters for the Lennard-Jones and torsional potentials along the lipid acyl tails. The LJ parameters were thereby derived by fitting experimental heats of vaporization and densities of different n-alkanes, and the LJ interactions between hydrogen atoms in the lipid tails were scaled according to

$$U_{\text{LJ},1-4} = f_{LJ} \sum_{1-4} 4\epsilon_{ij}((\frac{\sigma_{ij}}{r_{ij}})^{12} - (\frac{\sigma_{ij}}{r_{ij}})^{6}) \quad , \tag{4.17}$$

with $f_{LJ} = 0.5$. Torsional parameters were obtained from ab-initio calculations of the potential energy surface of octane. The resulting Slipids force field models the hydrophobic bilayer region very well, and reproduces experimental order parameters, bilayer thickness and form factors [288, 289]. However, there were slight deviations from experimental order parameters in the headgroup region [256], resulting in an update to the force field in 2020 [292]. As shown in Figure 4.2a, Slipids simulation results are somewhat different from CHARMM36 results. This observation, as well as the resulting consequences for n-alkane simulations, are discussed in detail in paper II.

4.2.2 Observables and block averaging

As described by equation 4.1, MD simulations yield time-averaged quantities. However, only quantities with correlation times that are short compared to the simulation time can be estimated reliably. Since lipid membrane systems usually contain around a hundred lipids or more, certain molecular properties can also be obtained via an ensemble average. In ergodic systems, the ensemble average then compliments the time average. For example, it is straightforward to obtain the C-H bond order parameters from atomistic simulations: One simply needs to determine the angles θ_{mn} (at every time point and for every lipid molecule) and evaluate equation 2.1. Figure 4.2a shows order parameters calculated in this manner for DPPC. The

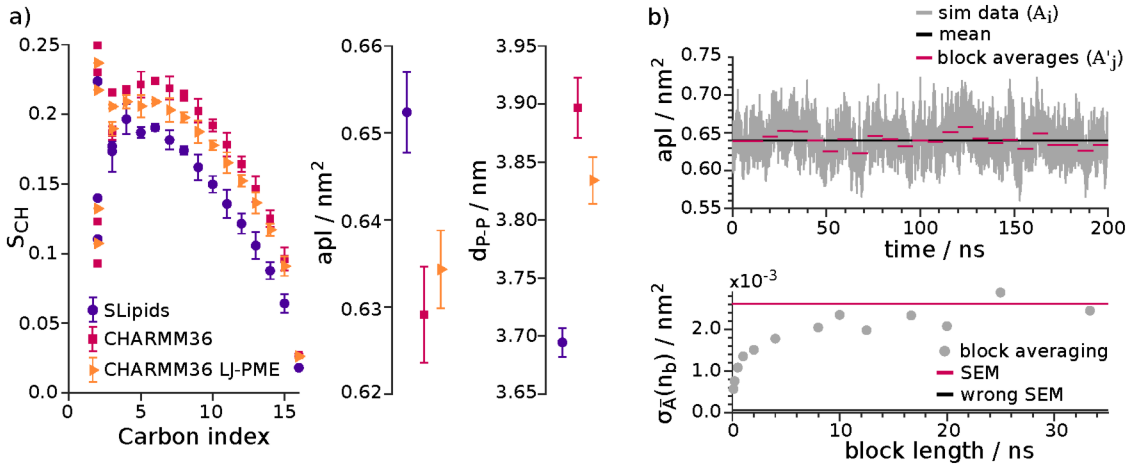

Figure 4.2: MD simulation results. a) Comparison of different lipid force fields. S_{CH}, area-per-lipid (apl) and bilayer thickness $d_{\mathrm{P-P}}$ of DPPC bilayers (72 lipid molecules) calculated from simulations with three force fields: Slipids, CHARMM36 (with force switch between 1.0 and 1.2 nm for the LJ potential), and CHARMM36 with LJ-PME. Simulations were conducted with GROMACS, at 60°C and with 19 water molecules per lipid, 100 ns run time. Error bars for S_{CH} show the standard deviation across equivalent C-H bonds, and for apl and $d_{\mathrm{P-P}}$ show the standard error of the mean (SEM) determined by block averaging. Experimental results for DPPC at 50°C are approx. 0.63 nm^2 and 3.8 nm for apl and $d_{\mathrm{P-P}}$, respectively [293]. b) Block-averaging. Top: Apl calculated for each frame of a CHARMM36 simulation of 72 DPPC molecules (70°C and 19 water molecules per lipid, 200ns with 100ns equilibration), as well as calculated mean over 200 ns (black) and over blocks of length 4 ns (pink). Bottom: SEM obtained from block averaging, as a function of block size (equations 4.18 and 4.19). The SEM obtained w/o block averaging, i.e. assuming the data to be uncorrelated, is shown for reference as a black line.

error bars thereby show the variation across equivalent C-H bonds (i.e. two bonds per acyl tail methylene, resulting in a total of four equivalent bonds from the two hydrocarbon tails of DPPC).

Other commonly evaluated parameters are the area-per-lipid (apl) and bilayer thickness ($d_{\mathrm{P-P}}$), also shown in Figure 4.2a. The area-per-lipid can be calculated from the size of the simulation box in the bilayer plane, i.e. by dividing the box area by the number of lipids per bilayer. Accordingly, $d_{\mathrm{P-P}}$ can be estimated by determining the average z-coordinates of the phosphorous atoms in the two bilayer leaflets and calculating the difference. Using such approaches, one observes that apl and $d_{\mathrm{P-P}}$ strongly fluctuate during the simulation (see Figure 4.2b). The mean value of this fluctuation is easily calculated, but in order to determine the standard error of this mean (SEM) it is necessary to make use of so-called block averaging techniques [294], also illustrated in Figure 4.2b. The procedure is explained as follows: The simulation data results in a time-series of n calculated values A_i with mean $\langle A \rangle \equiv \bar{A} = {}^1\!/_n \sum_{i=1}^{n} A_i$ (an approximation of the expectation value). In this time-series the individual observations A_i are not independent, which prohibits the use of standard equations for the SEM. However, one can divide the simulation into N_b

individual sets (i.e. blocks), containing n_b data points each. Then, we define the mean in block j as A'_j, $j = 1, 2, ..., N_b$. If the blocks are sufficiently large, the values A'_j should be uncorrelated and one can determine the standard error of the mean of A as a function of block size:

$$\sigma_{\bar{A}}(n_b) = \frac{\sigma_{A'}(n_b)}{\sqrt{N_b - 1}} \tag{4.18}$$

with

$$\sigma_{A'}(n_b) = \sqrt{\frac{1}{N_b - 1} \sum_{j=1}^{N_b} (A'_j - \bar{A})^2} \tag{4.19}$$

The plot of $\sigma_{\bar{A}}(n_b)$ vs. n_b should reach a plateau at larger values of n_b, as shown in the bottom plot of Figure 4.2b. Then, the plateau value is equal to the SEM of $\langle A \rangle$.

Chapter 5

Results

The aim of this thesis is the characterization of a model system for long, purely hydrophobic molecules inside lipid membranes. The miscibility, molecular arrangement and crystallizability of three different n-alkanes (lengths 10, 20 and 30 carbons) are studied in different lipid membranes, and the effects of hydrophobic chain length and sample hydration are discussed.

The experimental and simulated results of this thesis are summarized in three research articles, which were published previously as indicated. In this chapter, each article is reprinted with permission and briefly put into context. The most important findings and author contributions are listed. Overall conclusions derived from the results are presented in the combined summary in chapter 6.

5.1 Paper I: Filling the Gap with Long *n*-Alkanes: Incorporation of C20 and C30 into Phospholipid Membranes[1]

In the 1980's, Pope et al. [24, 25, 149] investigated the miscibility of *n*-alkanes up to 19 carbons in length with different phospholipid bilayers. For example, they monitored the existence of isotropic *n*-alkanes pools as function of *n*-alkane and lipid tail length by means of ^{2}H NMR. They observed that the miscibility of *n*-alkanes in DMPC and DPPC bilayers dropped notably and continuously when the *n*-alkane chain length increased beyond 12 carbons in length. Since then, the miscibility of longer *n*-alkanes (C20 or longer) with lipid bilayers has not been studied further.

In this paper, we build upon the findings presented by Pope et al. [25], and extend their miscibility study to include *n*-eicosane (C20) and *n*-triacontane (C30). The well characterized *n*-decane (C10) is thereby used as a reference for shorter *n*-alkanes. Lipid membranes consist of DMPC or DPPC, and two different levels of hydration are investigated (below and above the excess water limit of the lipid bilayers). Moreover, the effect of chain length on miscibility is evaluated in terms of *n*-alkane volume fraction. Using ^{2}H NMR, ^{31}P NMR, ^{1}H-^{13}C dipolar recoupling NMR, X-ray scattering, cryogenic electron microscopy and atomistic MD simulations, we show that C20 and C30 mix with the lipid membranes up to a critical alkane-to-acyl-chain volume fraction, ϕ_c. ϕ_c depends on *n*-alkane and lipid acyl tail length, as well as sample hydration. Lipid order parameters are not affected by the presence of *n*-alkanes in any sample. However, in the excess water regime the addition of very low amounts of *n*-alkanes results in a notable decrease in vesicle diameter, suggesting that unilamellar vesicles or alkane droplets are formed.

The author contributions to this article are as follows: AW and TMF designed and managed the project. AW and in part EP (as part of his Bachelor thesis project and supervised by AW) prepared the samples. AW performed and analyzed the NMR experiments and MD simulations with guidance from TMF. MO and AW performed and analyzed the X-ray scattering experiments. AM and FH prepared and performed the cryo-EM measurements. All authors interpreted and discussed the results. AW and TMF wrote the manuscript, with input from all authors.

[1]Reprinted with permission from: "Filling the Gap with Long *n*-Alkanes: Incorporation of C20 and C30 into Phospholipid Membranes", Anika Wurl, Maria Ott, Eric Plato, Annette Meister, Farzad Hamdi, Panagiotis L. Kastritis, Alfred Blume, and Tiago M. Ferreira. *Langmuir* 2022, 38, 28, 8595-8606. Copyright 2022 American Chemical Society [37]. The link to the article on the publisher website is https://doi.org/10.1021/acs.langmuir.2c00872 . No changes were made.

LANGMUIR

pubs.acs.org/Langmuir Article

Filling the Gap with Long *n*-Alkanes: Incorporation of C20 and C30 into Phospholipid Membranes

Anika Wurl,* Maria Ott, Eric Plato, Annette Meister, Farzad Hamdi, Panagiotis L. Kastritis, Alfred Blume, and Tiago M. Ferreira*

Cite This: *Langmuir* 2022, 38, 8595−8606 Read Online

ACCESS | Metrics & More | Article Recommendations | Supporting Information

ABSTRACT: Investigating how hydrophobic molecules mix with phospholipid bilayers and how they affect membrane properties is commonplace in biophysics. Despite this, a molecular-level empirical description of a membrane model as simple as a phospholipid bilayer with long linear hydrophobic chains incorporated is still missing. Here, we present an unprecedented molecular characterization of the incorporation of two long *n*-alkanes, *n*-eicosane (C20) and *n*-triacontane (C30) with 20 and 30 carbons, respectively, in phosphatidylcholine (PC) bilayers using a combination of experimental techniques (^{2}H NMR, ^{31}P NMR, ^{1}H−^{13}C dipolar recoupling solid-state NMR, X-ray scattering, and cryogenic electron microscopy) and atomistic molecular dynamics (MD) simulations. At low hydration, deuterated C20 and C30 yield ^{2}H NMR spectra evidencing anisotropic-motion, which demonstrates their miscibility in PC membranes up to a critical alkane-to-acyl-chain volume fraction, ϕ_c. The acquired ^{2}H NMR spectra of C20 and C30 have notably different lineshapes. At low alkane volume fractions below ϕ_c, CHARMM36 MD simulations predict such ^{2}H NMR spectra qualitatively and thus enable an atomistic-level interpretation of the spectra. Above ϕ_c, the ^{2}H NMR lineshapes become characteristic of motions in the intermediate-regime that, together with the MD simulation results, suggest the onset of immiscibility between the alkane molecules and the acyl chains. For all the systems investigated, the phospholipid molecular structure is unperturbed by the presence of the alkanes. However, at conditions of excess hydration and at surprisingly low alkane fractions below ϕ_c, a peak characteristic of isotropic motion is observed in both the ^{2}H spectra of the alkanes and ^{31}P spectra of the phospholipids, strongly indicating that the incorporation of the alkanes induces a reduction on the average radius of the lipid vesicles.

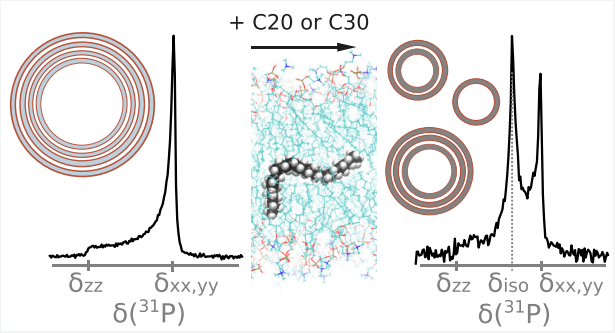

INTRODUCTION

Phospholipid membranes are the basis for cellular compartmentalization and a key element in cellular transport, energy storage, signaling, growth regulation, and possibly processes that are unknown at present.[1,2] Consequently, a great deal of molecular details from phospholipid membranes in biologically relevant conditions have been investigated. Prominent examples are the effects of cholesterol on membrane fluidity and phase behavior,[3−7] distinct mechanisms of interaction between amphiphilic peptides and membranes,[8−11] and from lipidomics.[12,13] However, a fundamental molecular-level description on how hydrophobic/amphiphilic molecules interact with lipid membranes and affect bilayer properties is only now emerging, enabled by the ongoing progress and combination of both experimental and molecular dynamics (MD) simulation techniques.[14−21] Such recent developments will hopefully help to better understand how cells operate on a membrane composition level but also how lipid-based systems used in applications such as drug delivery[22] or more recently mRNA-lipid nanoparticles[23] can be optimized.

Here, we focus on the case of incorporating hydrophobic linear chains in a lipid membrane, namely, the incorporation of long *n*-alkanes in phospholipid bilayers. The influence of *n*-alkanes on lipid membranes has been investigated for many decades due to their anesthetic properties,[24−27] but molecular principles are still under debate. An apparent cutoff of anesthetic potency was observed for *n*-alkanes with chain lengths longer than 8 carbons.[28] Such cutoff is controversial[29] and in contrast with the expectation that the anesthetic potency should increase with lipophilicity according to the Meyer−Overtone rule.[30]

The most recent and detailed studies on phospholipid/*n*-alkane systems were motivated by the *n*-alkanes' simple

Received: April 4, 2022
Revised: May 20, 2022
Published: July 5, 2022

https://doi.org/10.1021/acs.langmuir.2c00872
Langmuir 2022, 38, 8595−8606

chemical structure and the ease with which their hydrophobic chain length can be varied, making these molecules an ideal model for fundamental investigations of the effect of linear hydrophobic chains on phospholipid bilayers.[31−36]

Calorimetry measurements show that linear alkanes of different chain lengths affect the lipid phase behavior in distinct ways. Short-chain *n*-alkanes up to approximately 12 carbons in length decrease the gel-to-liquid crystalline phase transition temperature T_m of a number of biologically relevant phospholipids.[35,37−40] As the chain length of the *n*-alkanes approaches the acyl chain length of the lipids, the transition shifts to higher temperatures most likely due to a stabilization of the gel-phase as suggested by the strong increase of the bilayer bending rigidity below T_m.[35,41] The lipid headgroup structure further influences to what degree alkane addition affects the transition temperature.[31] Both the phase behavior and the mechanical properties of alkane-containing bilayers should depend on the exact location of the *n*-alkane chains with respect to the phospholipid molecules. The molecular arrangement of *n*-alkanes in lipid membranes has consequently been addressed in a variety of studies, with partly conflicting results. A number of studies indicated that short *n*-alkanes (less than 12 carbons) accumulate in the bilayer center, while *n*-alkanes with similar lengths to the lipid acyl chains either arrange parallel to the phospholipid acyl chains or are immiscible.[37−39,42,43] Opposing observations have recently been made by Usuda et al.,[35] suggesting that longer *n*-alkanes are preferentially located in the bilayer center, while short chains are dispersed throughout the membrane. Usuda et al. reasonably pointed out that such differences in findings may be related to variations of the amount of *n*-alkane actually mixed with the phospholipid bilayers, as theoretically predicted by Gruen et al.[44]

Surprisingly, neither experimental nor computational systematic investigations of the effect of long *n*-alkanes with different chain lengths under similar conditions, such as alkane-to-acyl-chain volume fraction, were reported to date. Here, we refer to long *n*-alkanes as those that have melting temperatures above the physiological temperature 37 °C which is the melting temperature of *n*-eicosane, the 20 carbon long linear alkane. A more complex behavior should be expected for these alkanes under physiological conditions due to the interplay between the enthalpic gain of crystallization and the entropy of mixing with the lipid acyl chains.

Previous works by Pope et al.[45] suggest that the mixing of long *n*-alkanes with lamellar phospholipid bilayers is unlikely, however, *n*-eicosane has been found to promote the formation of inverted hexagonal phases, similar to shorter *n*-alkanes.[46−48] More recently, coarse-grain MD simulation studies showed a tendency of long polymeric polyethylene chains (which were effectively a 80 carbon length *n*-alkane) to phase separate from the acyl chains as a lens-shaped oil droplet in between the bilayer leaflets.[49] As of now, there are no systematic experimental investigations or MD simulations on the incorporation of long *n*-alkanes with chain lengths between 20 and 80 carbons in lipid bilayers. Toward filling this gap, in this work, we investigate the behavior of two long linear alkanes — *n*-eicosane (C20) and *n*-triacontane (C30) with a length of 20 and 30 carbons, respectively — in contact with dimyristoylphosphatidylcholine (DMPC) and dipalmitoyl-phosphatidylcholine (DPPC) membranes with acyl tail lengths of 14 and 16 carbons, respectively. We do this at different levels of hydration, performing a detailed and unprecedented characterization of the molecular structure of C20 and C30 under such conditions and how they affect membrane properties. We expect that such an investigation is a good starting point for studying the effects of even longer chains, e.g. polymers, on cell and model membrane structure, which is relevant for biological applications and for understanding the effects of microplastic pollution on a microcopic level.

To characterize the systems with atomistic detail we use a combination of techniques, namely, ^{2}H NMR spectroscopy of deuterated C20 and C30, ^{31}P NMR and ^{1}H−^{13}C dipolar recoupling solid-state NMR of the phospholipid molecules, X-ray scattering, cryogenic electron microscopy, and all-atom MD simulations.

The ^{2}H NMR spectra presented demonstrate that both C20 and C30 incorporate in the phospholipid membranes. We present a molecular interpretation of such spectra based on the MD simulations performed and investigate the effects of the alkane chains on the properties of the membranes. A combined analysis of all the results obtained shows that, although the molecular structure of the phospholipids is not affected by the *n*-alkanes, a small amount of incorporated long *n*-alkane chains leads to a drastic change on the overall dimensions of the multilamellar vesicles at biologically relevant hydration levels.

METHODS

Sample Preparation. 1,2-Dipalmitoyl-*sn*-glycero-3-phosphocholine (DPPC) and 1,2-dimyristoyl-*sn*-glycero-3-phosphocholine (DMPC) were purchased from Avanti Polar Lipids. *n*-Decane, *n*-eicosane, and *n*-triacontane, as well as their perdeuterated counterparts, were obtained from Sigma-Aldrich. Chloroform was purchased from Carl Roth. All substances were used without further purification. The samples were prepared in different ways depending on the lipid/alkane system and the experimental technique used. In the following, we explain the preparation of samples investigated by NMR. Differences in sample preparation for the other experimental techniques are noted in the respective methods sections below.

MLVs with n-Decane. Samples containing *n*-decane were prepared by simply adding 10−40 vol % *n*-decane (alkane/lipid acyl chains) to powdered DPPC. The *n*-decane/lipid mixtures were then briefly mixed at room temperature with a thin metal rod before adding deionized water to achieve a water content of $n_w \approx 7$ (water molecules per lipid). Subsequently, the samples were repeatedly centrifuged and mixed by hand at 50 °C until homogeneous upon visual inspection.

MLVs with n-Eicosane and n-Triacontane. For preparing the samples with the long *n*-alkanes, lipid films were created by codissolving DMPC or DPPC and the desired amount of *n*-alkane (2.5−37 vol % and 2.5−5 vol % for *n*-eicosane and *n*-triacontane, respectively) in chloroform. The solvent was evaporated under a nitrogen stream, while simultaneously sonicating the solution in a heatbath above the melting temperatures of the individual components. Lipid films were then dried overnight at reduced pressure. Different methods for hydrating the samples were used. Excess hydration: For obtaining samples above the limit of water saturation (excess water), 200 wt % of deionized H_2O were added to the powder obtained from the lipid films. The mixtures were equilibrated for 1−3 h above the melting temperatures of lipid and *n*-alkane, with occasional mixing. The samples were then centrifuged and the resulting lipid pellet was used. Low hydration: For DMPC samples, the lipid films were placed in a desiccator of approximately 1 L volume at room temperature, containing about 2 mL of water. Samples were kept in the evacuated desiccator for at least 1 day, resulting in a homogeneous hydration of about 9−14 water molecules per lipid. For the DPPC films, hydration in a desiccator yielded a very low number of water molecules per lipid ($n_w \approx 4$) most likely because of the higher melting temperature of DPPC in comparison to DMPC. Therefore, the low hydration levels in DPPC samples were adjusted by weighting the appropriate water amounts, aiming for a water

https://doi.org/10.1021/acs.langmuir.2c00872
Langmuir 2022, 38, 8595−8606

content of 18 water molecules per lipid. This procedure resulted in hydration levels of n_w = 11−18. All samples were centrifuged into magic-angle-spinning (MAS) rotor inserts (Bruker) fitting approximately 20 mg. The final sample hydration of each sample was quantified by ^{1}H MAS NMR.

Solid-State NMR Experiments. Static ^{2}H NMR measurements were performed at a ^{2}H Larmor frequency of 61.40 MHz with a 5 mm broad-band probe. For ^{2}H, a quadrupole echo sequence[50] using a 90° pulse of 4.2 or 4.3 μs, a 40 μs delay, and a relaxation delay ≥0.5 s was employed. Between 8192 and 20480 scans were accumulated with a spectral width of 1 MHz. Free-induction decay (FID) signals were processed and Fourier-tranformed using Matlab, starting from the echo maximum.

Static ^{31}P NMR measurements were performed at a ^{31}P Larmor frequency of 162.08 MHz and consisted of single-pulse and Hahn-echo experiments with a 90° pulse duration of 4.4−4.7 μs, proton decoupling, and a recycle delay ≥5 s.

^{1}H and R-type proton detected local field (R-PDLF) experiments were conducted under 5 kHz MAS using a standard 4 mm double-resonance MAS probe. All measurements were conducted on a Bruker Avance III 400 spectrometer operating at a ^{1}H Larmor frequency of 399.92 MHz.

Single-scan ^{1}H spectra with a spectral width of 100 kHz were acquired at temperatures between 30 and 60 °C. FIDs were zero-filled to two times the original number of points. After Fourier transform, lipid and water peaks were fitted with Lorentzian lineshapes and the water content was calculated from the peak integrals.

R-PDLF experiments were conducted to quantify ^{1}H−^{13}C residual dipolar couplings. The R-PDLF sequence was combined with a refocused INEPT, as outlined in ref 51, and performed using recoupling blocks of type $R18_1^7$.[52] Sample heating due to the RF-pulses was monitored by observing the variation of the ^{1}H chemical shift of water and was ≤2 K. Dipolar splittings $\Delta\nu$ were obtained by 2D Fourier transform and relate to the C−H bond order parameter S_{CH} by

$$|S_{CH}| = \frac{d_{CH}}{d_{CH,s}} = \frac{\Delta\nu}{0.315 \cdot 21.5\ \text{kHz}} \quad (1)$$

where d_{CH} is the magnitude of the motion-averaged dipolar coupling of the given C−H bond, $d_{CH,s}$ is the magnitude of the static dipolar coupling of a C−H bond ($d_{CH,s} \approx 21.5$ kHz), and 0.315 is the effective scaling factor of the R-PDLF sequence.[51] An exemplary data set is shown in Figure 6 to illustrate the procedure. Peaks in the crowded spectral region between 29.4 and 31.0 ppm were assigned such that the order parameter profile resembled those known from literature.[6,53]

MD Simulations. Molecular dynamics simulations were performed with GROMACS.[54] Systems were each composed of one hydrated bilayer containing 72 DPPC molecules and varying numbers of *n*-alkane chains. Alkane concentrations ranged from 0 to 30 vol % for *n*-decane and *n*-eicosane, and from 0 to 5 vol % for *n*-triacontane. For *n*-triacontane, and 2.5 and 5 vol % *n*-eicosane, the systems were extended in the lateral dimension, using the GROMACS function *genconf*, to reach a total of 288 lipids per bilayer. This step was necessary to exclude interactions between different images of the same molecule[55] and to include a sizable number of alkane molecules in the simulation box. The number of water molecules was adjusted to match the experimental samples. An overview of all the simulations conducted is given in Table S1. This table also includes links to zenodo repositories which contain all the trajectories analyzed and files necessary to reproduce the simulations. The CHARMM36 force field[56,57] was used for both DPPC and *n*-alkanes. DPPC force-field and initial topology were copied from open access data made available by the NMRlipids project (nmrlipids.blogspot.fi),[58] and the acyl chain parameters were transferred to the alkanes. Alkane topologies were created using Molden.[59] Water molecules were described by the CHARMM TIP3P model.[60,61] The simulation procedure was as follows: First, systems of DPPC plus water and pure alkane systems were equilibrated separately, after which they were merged to create the desired alkane concentrations. For this, bulk alkane was placed between the two bilayer leaflets and the systems were re-equilibrated. The production runs of 300 ns were conducted in NPT ensembles, integrating the equations of motion based on the leapfrog algorithm. For long-range electrostatics, the particle mesh Ewald algorithm was used. Temperature was controlled by a modified Berendsen thermostat and a semi-isotropic pressure profile was realized with Parrinello−Rahman pressure coupling. Proton bonds were constrained using a fourth order LINCS correction. For details on these algorithms, see 62 and references therein.

Simulated trajectories were analyzed using Python's MDTraj library.[63] For every distinct C−H pair in DPPC and alkane molecules, time- and ensemble-averaged order parameters were calculated according to

$$S_{CH} = \frac{1}{2}\langle 3\cos^2\theta - 1\rangle \quad (2)$$

where θ is the angle between the bilayer normal and the C−H bond vector. To compare calculated values to the ^{2}H and R-PDLF NMR experiments, we consider only the magnitude of the order parameters, $|S_{CH}|$. Lipid structural quantities such as bilayer thickness and area-per-lipid were calculated for every simulated time frame. Afterward, the mean and standard deviation of these quantities were taken over the last 50 ns of the simulations.

X-ray Scattering. Only DPPC/C10 and DPPC/C20 mixtures up to 25 vol % alkane were subjected to X-ray diffraction measurements. Samples were prepared as described above, in excess water conditions, adding additional water to obtain sufficiently fluid mixtures (final lipid concentration around 150 mg/mL). Samples were vortexed and sealed in borosilicate glass capillaries from Hilgenberg (Maisfeld, Germany) with 1 mm outer diameter and 0.01 mm thickness. Wide angle X-ray scattering experiments were performed in transmission mode using a SAXSLAB laboratory setup (Retro-F) equipped with an AXO microfocus X-ray source, and an AXO multilayer X-ray optic (AXO Dresden GmbH, Dresden, Germany), used as a monochromator for Cu Kα radiation (λ = 0.154 nm). A two-dimensional detector (PILATUS3 R 300 K; DECTRIS, Baden, Switzerland) was used to record the 2D scattering patterns. The measurements were performed at 60 °C and corrected for background, transmission, and sample geometry. The intensities were angular-averaged and plotted versus the scattering angle q with subsequent normalization with respect to concentration and sample volume. The X-ray diffraction pattern of lamellar phases exhibit a set of Bragg reflections with reciprocal spacings in the characteristic ratios of $q_n = 2\pi n/d$ (Miller index n = 1, 2, 3, ...). The reflections were fitted by Gaussian functions and the lamellar repeat distance, d, was determined from the average of the repeat distances determined for each sample composition. Errors were calculated from the scatter of the results for the individual reflections, which was larger than the error of the fitted peak positions.

Cryogenic Transmission Electron Microscopy. A mixture of DMPC and 10 vol % C20 was prepared as described above, in the excess water regime, adding additional water to obtain a lipid concentration of 1.5 mg/mL. A sample of pure DMPC was prepared for comparison. The lipid suspensions were extruded (membrane pore size 100 nm) prior to measurement. For cryogenic transmission electron microscopy (cryo-EM), the Quantifoil R2/1 type holey carbon grids were first glow discharged in an easiGlow plasma treatment machine at 15 mA for 25 s in the negative polarity. The plasma-treated grids were mounted in a Leica Gridplunger GP2 with a chamber temperature of 30 °C and a relative humidity of more than 95%. A total of 5 μL of the samples were applied on both sides of the glow discharged grids and then blotted using a 595 ash-free filter paper for 12 s at a blotting force of zero. Then the grids were quickly plunged in liquified ethane at a temperature of −170 °C. The vitrified grids were consequently clipped in an autogrid assembly and loaded in a ThermoFisher Scientific Glacios 200 kV TEM under cryogenic conditions. The samples were studied under a low dose imaging regime using the ThermoFisher EPU software Version 2.11.1.11REL. On each region of interest (ROI), a series of movie frames were recorded, and then the frames were stacked, aligned, and summed

https://doi.org/10.1021/acs.langmuir.2c00872
Langmuir 2022, 38, 8595−8606

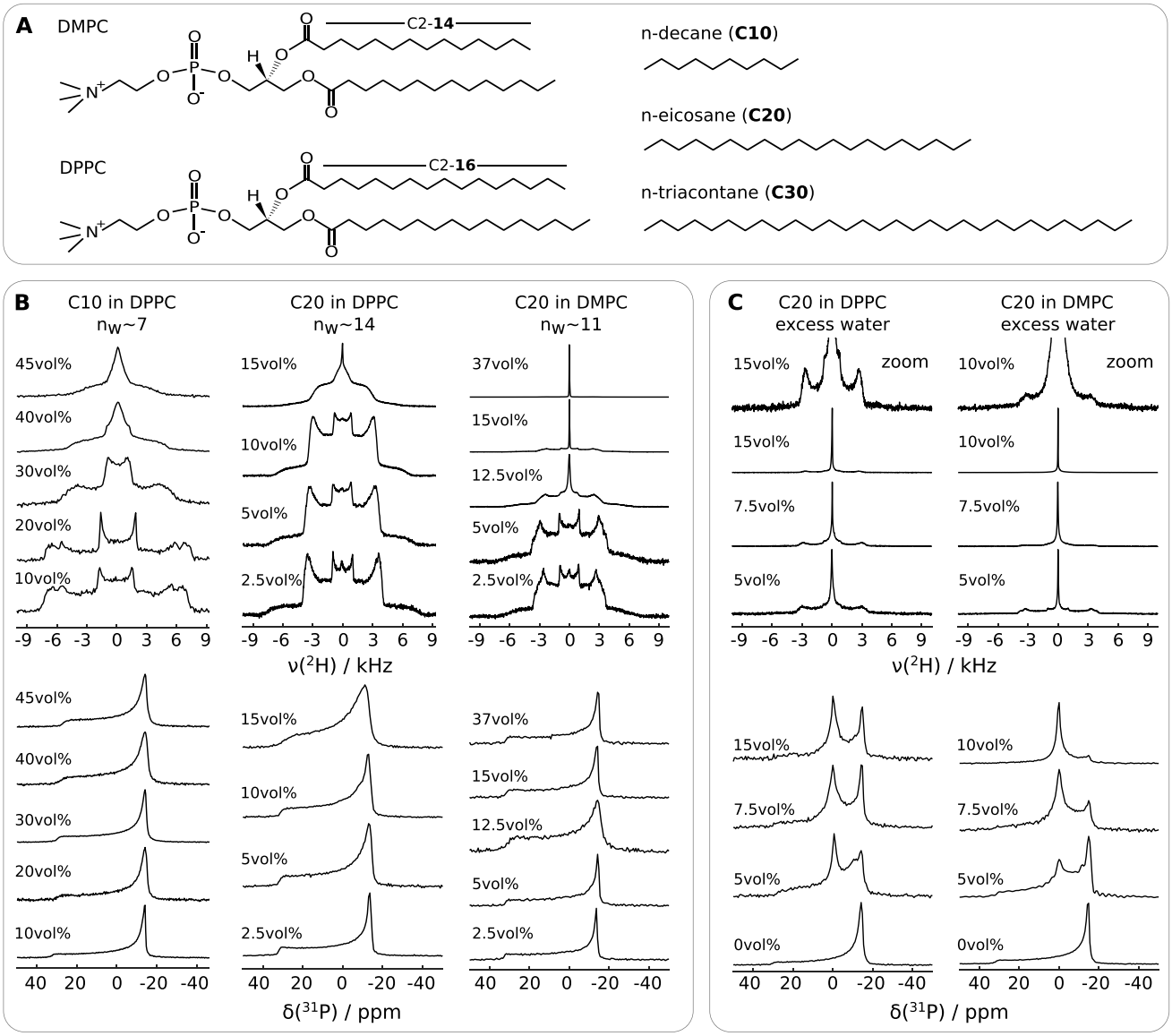

Figure 1. ^{2}H NMR spectra of alkanes (perdeuterated) mixed with DMPC and DPPC at a range of alkane-to-acyl-chain volume fractions and hydration levels, plus their effect on the ^{31}P NMR spectra of the phospholipids. (A) Chemical structures and carbon labels used for the lipids and alkanes used in this work. (B) Samples at low hydration. The number of water molecules per lipid n_w is indicated on the top of each column. Mixtures from left to right: decane-d_{22} in DPPC at 60 °C, eicosane-d_{42} in DPPC at 60 °C, and eicosane-d_{42} in DMPC at 50 °C. (C) Samples at excess hydration. Mixtures from left to right: eicosane-d_{42} in DPPC at 60 °C, and eicosane-d_{42} in DMPC at 40 °C. Pure lipid ^{31}P spectra at similar conditions are included as references.

into a single image using the on-flight frame alignment function of the EPU software.

RESULTS AND DISCUSSION

The ^{2}H and ^{31}P NMR spectra of samples consisting of C20d mixed with DPPC or DMPC in the liquid-crystalline phase under low and excess hydration are shown in Figure 1. Spectra from samples with perdeuterated *n*-decane in DPPC are also shown for comparison. We start by discussing the spectra acquired at low hydration (Figure 1B), and then we discuss the changes observed upon further hydration of these samples to conditions of excess water (Figure 1C).

C20d Molecules Mixed in DMPC and DPPC Membranes Display Anisotropic Motion at Low Hydration. At low hydration (Figure 1B) and low alkane volume fraction, all the acquired ^{2}H spectra are superpositions of Pake patterns. These spectral lineshapes imply that the perdeuterated alkane molecules have anisotropic motion during a time interval longer than 1 μs,[50] otherwise a single narrow line in the ^{2}H NMR spectrum would be observed (which is the case for neat alkanes in the liquid state). The spectral line shape and quadrupolar splittings measured do not vary significantly with alkane concentration up to a certain alkane-to-acyl-chain volume fraction (20, 10, and 5 vol % for the *n*-decane/DPPC, C20d/DPPC and C20d/DMPC systems, respectively). We can thus conclude that the *n*-decane and C20d molecules are fully mixed with the phospholipid acyl chains under these conditions.

For the alkane/DPPC systems, an increase of the volume fraction, ϕ, to above a certain critical alkane-to-acyl-chain

https://doi.org/10.1021/acs.langmuir.2c00872
Langmuir 2022, 38, 8595−8606

volume fraction, ϕ_c, results in strong broadening of the spectral lineshapes. This is observed at approximately 30 and 15 vol % for the C10d and C20d systems, respectively. These broad lineshapes are typical of exchange phenomena in the so-called intermediate motional regime.[64] One possible origin for this broadening is the formation of a slab of alkane or alkane droplets in between bilayer leaflets, where alkane molecules would undergo isotropic motion. In this case, the alkane molecules would continuously exchange between two rather distinct dynamical states, the anisotropic motion observed below ϕ_c (corresponding to alkane motion near the acyl chains) and the isotropic motion in the alkane slab formed between the bilayer leaflets. Such a phase separation would yield intermediate-regime lineshapes only if the exchange time, τ_{exc}, between the two distinct alkane dynamical states would be approximately the inverse of the splittings measured at low ϕ ($\tau_{exc} \approx 0.1-1$ ms). As it will be described in another section, we do observe the formation of an alkane slab at roughly the same alkane volume fraction for the C20/DPPC system in our MD simulations. However, based on these MD simulations, the exchange time of alkane molecules from the alkane slab to the acyl chain region is orders of magnitude faster than 0.1 ms. A more plausible origin for the broadening of the ^{2}H NMR spectra is a change of the morphology of the system with increasing alkane content, namely, a transition from the lamellar phase, L_α, to a liquid crystalline phase with a distinct symmetry or simply by a change of the curvature in the L_α phase, for example, from long-range stacks of flat membranes to a morphology closer to a multilamellar vesicle system. Such change in morphology would affect not only the orientations sampled by the alkane molecules during the ^{2}H NMR time-scale, but also the phospholipid orientations. Therefore, we measured the ^{31}P spectra from the phosholipid molecules to complement the ^{2}H NMR spectra. The measured ^{31}P spectra from the samples with low hydration are shown in Figure 1B and are characteristic of motionally averaged ^{31}P chemical shift anisotropy (CSA) tensors with an axial symmetry for all alkane concentrations, a clear signature of the lamellar phospholipid phase, L_α, where lipid molecules have fast uniaxial motion around the bilayer normal.[65−67] We can therefore rule out a transition from the lamellar liquid crystalline phase L_α to another phase. However, the ^{31}P spectra of the sample with C20d in DPPC above ϕ_c (i.e., for which an intermediate regime line shape is observed in the ^{2}H spectrum) shows considerable broadening. This indicates that, although such a ^{31}P spectrum is still evidence of a L_α phase, there is an increase of reorientations for the motionally averaged ^{31}P CSA tensor leading to T_2 broadening. Such an increase of reorientations is either due to an increase of the membrane curvature, an increase of phospholipid lateral diffusion, or a combination of both. We shall describe in the next section that further hydration of these systems induces a drastic effect on the ^{31}P spectra.

The spectra acquired from C20 in DMPC membranes at low hydration (right column in Figure 1B) also shows a superposition of Pake patterns at low ϕ. However, in contrast to the DPPC samples, the ^{2}H spectra display one additional narrow peak at ϕ greater than 5% which increases in intensity with increasing alkane content. Our interpretation is that such a peak originates from bulk C20d that did not mix with the phospholipid membranes, otherwise, an isotropic feature in the ^{31}P spectra would have been observed, which is not the case. It is important to note that in every lipid mixture prepared using organic solvents, a phase separation may also relate to different solubilities of the mixed components in the solvent used, leading to a sample that may not represent the true (i.e., long) thermodynamic equilibrium. We cannot ensure, therefore, that the phase separation of C20d observed in DMPC membranes at ϕ equal to 12.5 vol % is independent of the solvent used (chloroform) nor the solvent evaporation rate. In fact, as it will be also discussed in the next section, attaining a thermodynamical equilibrium for these mixtures is not a trivial task and depends on both the equilibration time and the sample preparation, as previously shown.[68]

C20d Incorporation Strongly Affects the ^{31}P Spectrum at Excess Hydration. Further hydration of the C20d/phospholipid samples discussed previously induces drastic changes in both the ^{2}H and ^{31}P NMR spectra. In addition to the anisotropic features described in the previous section, an extra peak characteristic of isotropic motion is observed in both the ^{2}H and the ^{31}P spectra of the fully hydrated samples, as shown in Figure 1C, that becomes prominent with an increase of alkane concentration. In this case, the appearance of an isotropic component in the ^{2}H spectra must therefore not be interpreted simply as a bulk alkane phase, as we did in the previous section for the C20d/DMPC system, but as a consequence of an overall change of morphology or dimensions of the multilamellar vesicles. Note that this is observed also at low alkane concentrations at which the samples at low hydration displayed only anisotropic spectral features.

Similar observations have been made by Sjoelund et al.,[47] who showed that water content has a noticeable effect on the formation of inverse hexagonal phases in different PC lipids and mentioned that adding C20 to DOPC resulted in the appearance of an isotropic component in the phosphorus spectra. Paz Ramos et al.[33] also investigated the effect of alkanes on the L_α-to-H_{II} phase transition in PE lipids and observed a small isotropic lipid phase coexisting with the inverse-hexagonal phase. ^{31}P spectra displaying isotropic components are typically observed in sonicated lipid suspensions consisting of small vesicles.[69] In such a case, complete motional averaging of the ^{31}P CSA tensor is achieved by a combination of vesicle tumbling and lateral diffusion of lipid molecules along the membrane.[65,66,70,71] In a biological context, it has been shown that different cells produce exosomes with different sizes,[72] potentially due to the effect of exosome composition on the bending rigidity of the membrane according to the thermodynamical treatement proposed by Huang et al.[73] It seems therefore reasonable to consider that the isotropic components in Figure 1C are originated by a reduction of bending rigidity and, consequently, a reduction of vesicle size induced by the incorporation of alkane in the multilamellar vesicles. This is in line with the recent observations made by Usuda et al. using neutron scattering experiments.[35] Alternative interpretations of the isotropic components are a transition from the L_α phase to a symmetric cubic phase (reverse or normal), to a non-symmetric sponge bicontinuous phase, to a dispersion of inverted micelles, or the simple formation of alkane droplets stabilized by interfacial phospholipid molecules. To investigate which of these options is more plausible, we performed cryogenic electron microscopy (cryo-EM) on a selected mixture.

The cryo-EM images acquired for a sample of 10 vol % C20 in DMPC (Figure 2 shows representative images) show lipid

https://doi.org/10.1021/acs.langmuir.2c00872
Langmuir 2022, 38, 8595−8606

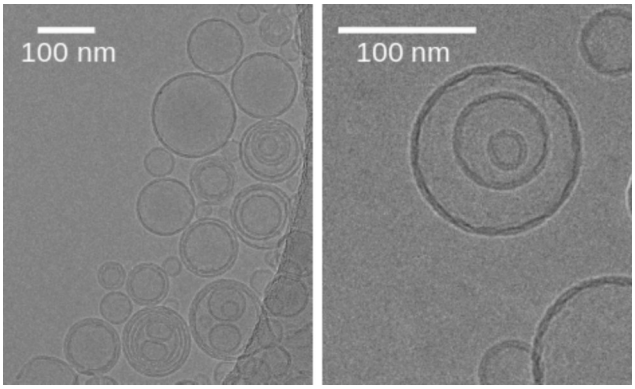

Figure 2. Cryo-EM images of extruded DMPC vesicles with 10 vol % C20. Vitrified samples were prepared above T_m at ∼30 °C.

vesicles of various sizes. Lipid droplets or other isotropic lipid structures, which, as described above, could be the origin of the isotropic component observed in the ^{31}P NMR spectra, could not be detected. Note that at this alkane volume fraction the isotropic component is the dominant contribution in the ^{31}P spectrum (Figure 1C). Therefore, the absence of these structures in the cryo-EM images indicates that the isotropic component in the ^{31}P spectrum most likely originates from a formation of smaller lipid vesicles induced by the incorporation of alkane. It would be of interest to determine and compare the vesicle size distribution of lipid systems with and without alkane. Such a determination is not possible with the used cryo-EM methodology since the multilamellar vesicles must follow an extrusion step to be imaged (membrane pore size of 100 nm), that is, the vesicle size distribution in the cryo-EM images does not correspond to the equilibrium distribution. Nevertheless, it is important to stress that the cryo-EM images do enable a direct observation of the samples after extrusion, indicating that lipid droplets (or similar structures) are absent, since small lipid droplets should also pass the 100 nm membrane pores. Because lipid droplets or similar structures are not observed, they cannot be the origin for the shape of the ^{31}P spectra at low alkane volume fraction.

In order to characterize further the size of the lipid vesicles, we performed ^{31}P Hahn echo measurements over a range of spin echo delays. Exemplary decay curves are shown in Figure 3, both for samples that did not display isotropic components

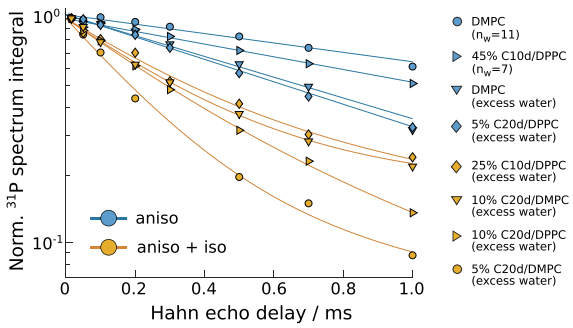

Figure 3. ^{31}P Hahn echo decays for different lipid-alkane mixtures. Blue data points are from samples with a purely anisotropic, lamellar phosphorus CSA pattern. Orange data points are from samples with an additional, isotropic peak in the ^{31}P spectrum. Exponential (blue) or biexponential (orange) fits to the data are added to guide the eye.

in the ^{31}P spectra (blue data) and samples with isotropic components (orange data). The ^{31}P Hahn echo signal decay of the samples without an isotropic component can be approximated by a single-exponential decay with T_2 relaxation times around 1.5 ms, in line with previous findings by Dufourc et al.[67] On the other hand, for samples containing an isotropic peak in the ^{31}P spectrum, the decay highly deviates from a single-exponential decay to a multiexponential decay containing significantly shorter T_2 components, characteristic of motions with time scales near the intermediate-regime. The theoretical vesicle diameter corresponding to the short T_2 limit can be estimated via the surface area that a lipid molecule can cover by lateral diffusion during a time interval approximately equal to the inverse of the motionaly averaged ^{31}P CSA magnitude. By doing so, we ignore the contribution of vesicle tumbling on the averaging of the ^{31}P CSA tensor. Using lipid self-diffusion coefficients of 22 μm^2/s (DPPC at 60 °C) and 9 μm^2/s (DMPC at 40 °C),[1] we estimate that the vesicle diameters corresponding to the intermediate motion regime are approximately 60 and 40 nm, for DPPC and DMPC, respectively, and thus suggest that vesicles of this size are present in samples that display an isotropic component in the ^{31}P spectrum. Moreover, as the concentration of alkane increases, an increasing fraction of the ^{31}P spectrum remains visible until long echo delays, indicating an increasing fraction of lipid vesicles that are much smaller than the sizes mentioned above and/or oil droplets for which the isotropic motional averaging reaches the fast limit.

We remark here that the spectra of the C20d/DPPC samples under excess water conditions shown in Figure 1 have been acquired a few months after sample preparation. For some samples, when they were first investigated within a few days of preparation, the ^{2}H quadrupolar splittings were significantly sharper and the isotropic peaks less prominent. To test for equilibration processes in the other mixtures, all samples were remeasured after several months. Over the course of approximately one year, no other changes in the ^{2}H spectra were observed, except for the high-concentration *n*-decane/DPPC samples, where the ^{2}H spectra became notably sharper (Figures S1 and S4). The different times needed to reach equilibrium for the *n*-decane and *n*-eicosane samples are most likely due to the distinct sample preparation used. While *n*-eicosane and *n*-triacontane samples were prepared by mixing the alkanes and lipids in chloroform, *n*-decane was mixed with the phospholipid powder directly without use of an organic solvent because decane would evaporate during the solvent evaporation step. Our results indicate that in such case the time to reach homogeneity of the alkane/phospholipid system becomes much longer.

C30d also Incorporates in Lipid Membranes and Induces an Isotropic Component in the ^{31}P Spectra. Exemplary ^{2}H spectra of perdeuterated *n*-triacontane (C30d) in DMPC and DPPC are shown in Figure 4. The ^{2}H spectra acquired from C30d in the presence of phospholipid membranes have much broader lineshapes than bulk C30d (the blue narrow peak in the top left plot of Figure 4), which demonstrates that the C30d chains undergo restricted anisotropic motion and are therefore incorporated in the membrane. This result is in contrast to the expectation from previous studies that such molecules would not be soluble in lipid membranes.[37] To the best of our knowledge, this is the longest alkane shown to be soluble in lipid membranes to date.

https://doi.org/10.1021/acs.langmuir.2c00872
Langmuir 2022, 38, 8595−8606

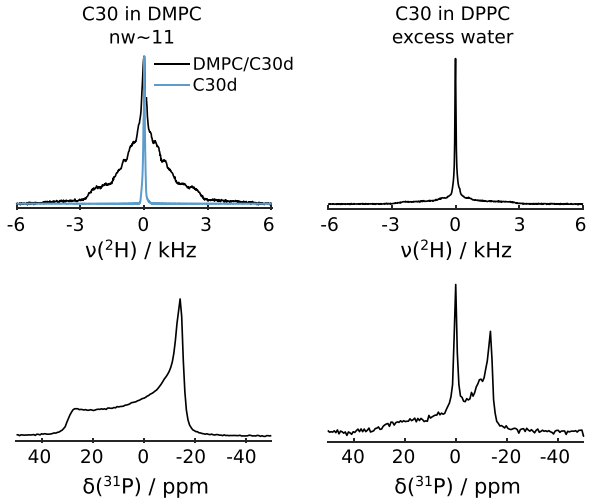

Figure 4. Static ^{2}H (upper row) and ^{31}P (lower row) spectra of 5 vol % perdeuterated *n*-triacontane (C30d) in DMPC (left column, n_w = 11, 70 °C) and in DPPC (right column, excess water, 70 °C). A ^{2}H spectrum of pure C30d at 70 °C is also shown for reference (blue, narrow peak in the top left spectrum).

Similar to the C20d/phospholipid systems described in the preceding sections, a hydration of the C30d/phospholipid systems up to excess water conditions leads to narrower spectral lineshapes with isotropic-motion features in the ^{2}H and ^{31}P spectra, evidence for isotropic motion of both the C30 and phospholipid molecules. This occurs at ϕ values as low as 2.5% and with equilibration times as short as 1 day.

As in the case of C20d in DMPC, at low hydration, an isotropic narrow peak shows up in the ^{2}H spectra, indicating phase-separated bulk C30d at a volume fraction of alkane-to-lipid-acyl-chain of 5 vol %. Again, this might be due to different solubilities of C30d and the phospholipids in the organic solvent used (chloroform) and consequent phase separation during the solvent evaporation process. We cannot exclude therefore that by using another organic solvent for mixing *n*-triacontane with the phospholipids one may reach systems with higher alkane-to-lipid-acyl-chain volume fractions.

At low hydration, the shape of the C30d ^{2}H spectrum is notably different from those of C20d in Figure 1B, missing clearly distinguishable splittings. The molecular details of such line shape become evident by comparison with the MD simulations performed in this work and are described in the next section.

All-Atom MD Simulations Enable to Predict the ^{2}H NMR Spectral Lineshapes Observed. To interpret the measured ^{2}H NMR spectra of the alkane molecules at low

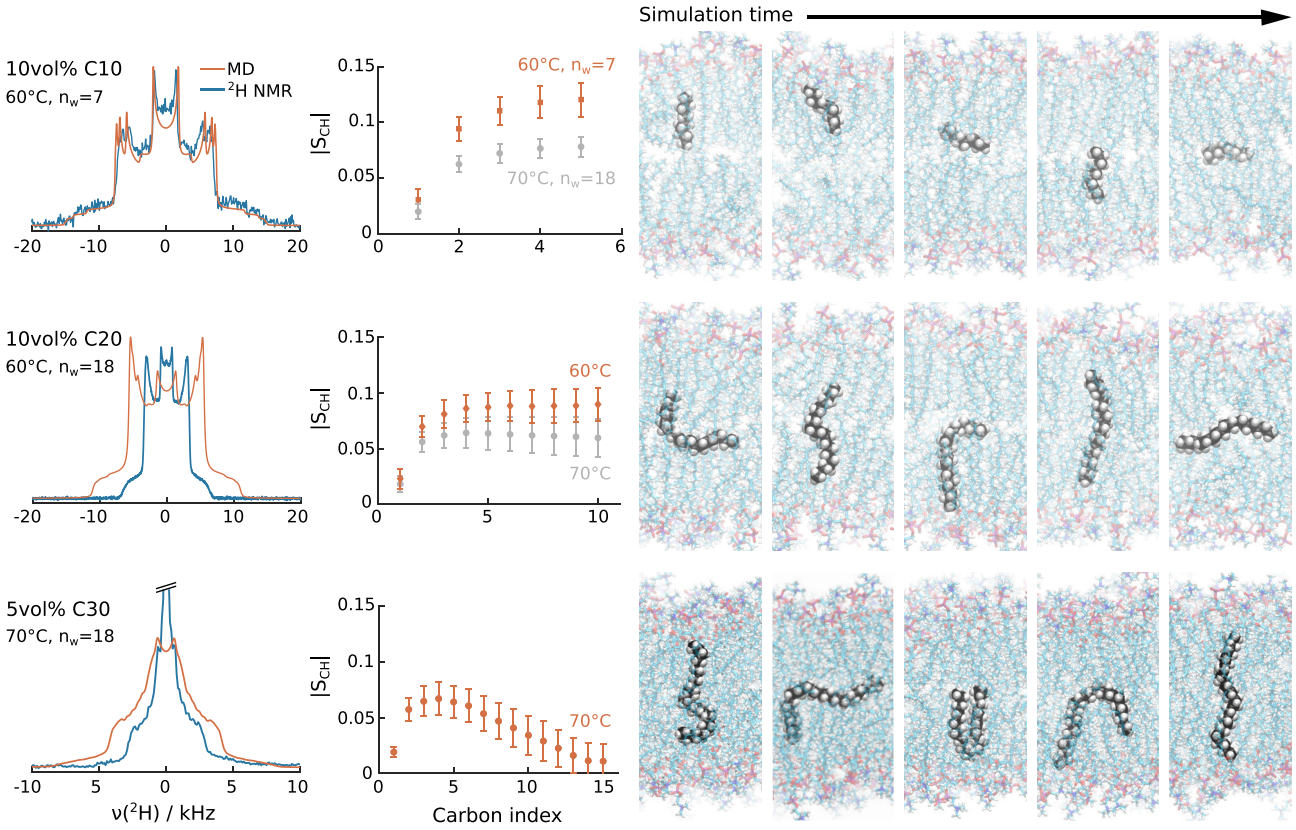

Figure 5. Simulated ^{2}H spectra of deuterated *n*-alkanes in DPPC calculated from the order parameter profiles determined from the MD simulations (red), and comparison with experimental data of equivalent systems (blue). The simulated order parameter profiles are plotted as mean ± standard deviation over all alkane chains. Order parameter profiles for 70 °C and n_w = 18 (gray) were added for C10 and C20 to facilitate a comparison between systems. The conformations of a selected alkane molecule at different times during a time interval of approximately 100 ns are shown on the right. Note that the additional alkane chains are omitted for clarity.

https://doi.org/10.1021/acs.langmuir.2c00872
Langmuir 2022, 38, 8595−8606

hydration in terms of molecular structure, we generated molecular models for a number of samples by performing (all-atom) CHARMM36 MD simulations. As mentioned previously, for systems above ϕ_c, the time-scale of the intermediate-regime motions that induces the drastic change of spectral lineshapes is near 0.1 ms, which is not accessible by our MD simulations. In this section, we therefore focus on alkane concentrations below ϕ_c, for which the time intervals simulated (up to 300 ns) should be enough to calculate a prediction of the experimental spectra. In Figure 5, exemplary ^{2}H NMR spectra are compared to spectra calculated from the alkane order parameter profiles determined from the MD simulation trajectories. The shapes of the simulated spectra match the experimental data reasonably well for all three systems with a nearly perfect match for the C10d case and a deviation to higher $|S_{CH}|$ for the C20d and C30d cases. The difference in width of the simulated and experimental ^{2}H spectra for C20d and C30d implies a higher ordering of *n*-alkanes in the MD simulations. The increased ordering observed in MD simulations may be due to force field imperfections related to the CH_2-CH_2 alkane-acyl chain interactions, which we simply defined to be equal to the CHARMM36 acyl chain Lennard–Jones interaction parameters. Consequently, the number of alkane chains reaching into the lipid tail region may be overestimated in the simulations due to a lipid–alkane interaction that is too attractive. Nevertheless, we assume that the models simulated are representative of our experimental samples and that the alkane molecular structures and orientations predicted are realistic (albeit only qualitatively) for the C20d and C30d cases.

The C–H bond order parameter profiles for C10d and C20d are rather different from the C30d profile. For the shorter alkanes, the highest, absolute order parameters are found in the middle of the alkane chain, while the middle region of C30d chains displays $|S_{CH}|$ values close to zero. This indicates that, in comparison to C10d and C20d, the C–H bonds in the middle segments of C30d sample a wider range of orientations close to an isotropic distribution. The number density profiles of C20 and C30 in DPPC obtained from MD simulations show that the overall alkane distribution in the bilayer is very similar for both alkanes at the same volume fraction (Figure S2).

The snapshots of individual alkane chains shown in Figure 5 illustrate that, rather than being confined to the bilayer center or a lipid leaflet, a single chain samples a variety of conformations and locations in the lipid bilayer over the course of approximately 100 ns. The alkane chains are continuously exchanging between regions of high and low density, the region close to the lipid–water interface and the middle of the bilayer, respectively (see, e.g., Figure S2). In the high density region the alkane methylene segments will have a tendency to adopt preferred orientations with respect to the ordered acyl chain segments, while in the middle of the bilayer (with higher free volume, i.e., lower density) alkane chain segments may adopt a wider range of orientations. This exchange is the reason for the reduced magnitude of alkane order parameters in comparison to typical lipid acyl chain order parameter profiles.[6]

Lipid Order Is Not Affected by Alkane Incorporation. Referring to Figure 1B,C, we note that the outer splittings of the C20d ^{2}H spectra, which correspond to the maximum absolute order parameter of those chains, are similar in DPPC and DMPC, and also at the different hydration levels. Decane $|S_{CH}|$ values are notably higher than for C20d. This could be due to the comparatively low water content in the decane samples since dehydration leads to acyl chain stretching,[74] which in turn should affect the alkane behavior.

In all mixtures, the magnitude of alkane order parameters remains fairly constant over the whole concentration range below ϕ_c, that is, below the alkane fraction at which the spectrum line shape starts to change. This is an indication that alkane chains do not affect the lipid acyl chain structure. To verify this interpretation, we performed R-PDLF NMR spectroscopy on all samples, allowing us to determine phospholipid order parameters and to quantify the effect of the alkane on the lipid molecular structure. Using R-PDLF NMR spectroscopy, we obtain site-specific $|S_{CH}|$ values of the lipid molecules, as shown in Figure 6. For each carbon site,

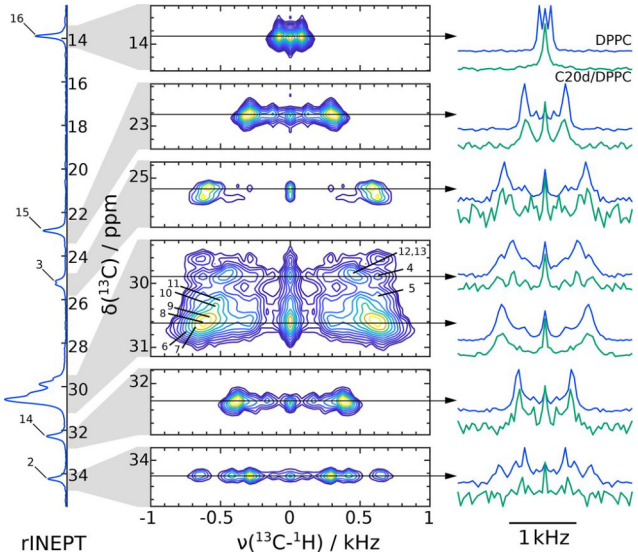

Figure 6. Comparison of R-PDLF measurements of pure DPPC (blue) and DPPC plus 25 vol % C20d (green) in excess water. (Left) Refocused INEPT ^{13}C intensities of the acyl tail region of pure DPPC, (middle) 2D spectrum showing the refocused dipolar couplings in the second dimension, and (right) dipolar slices at selected ^{13}C chemical shifts as indicated. Lipid acyl tail carbons were assigned as indicated.

that is, for each distinct peak in the ^{13}C spectrum, a splitting related to its recoupled ^{1}H–^{13}C dipolar coupling is obtained in the second (indirect) dimension. These splittings can then be used to calculate absolute C–H bond order parameters, as described in the Methods section.

Figure 6 compares the splittings of two samples, DPPC without alkane and DPPC with 25% of C20d both in excess water, showing no effect of the alkane on the lipid C–H bond order parameters. The complete order parameter profiles of these and other samples are given as Supporting Information in Figure S3. For all the samples investigated, the addition of C10d or C20d did not change the lipid tail ordering within experimental accuracy. Therefore, the anisotropic motion of the alkane molecules is dictated by the dynamics and structure of the acyl chains.

We note here that lipid order parameter measurements can also be used to identify nonlamellar lipid phases.[75] Dipolar couplings and thus C–H bond order parameters are influenced by motional averaging similar to the lipid headgroup ^{31}P CSA, for example, the ^{1}H–^{13}C dipolar couplings are reduced

https://doi.org/10.1021/acs.langmuir.2c00872
Langmuir 2022, 38, 8595–8606

approximately by half when comparing a hexagonal to a lamellar phase. In all of our R-PDLF measurements, including the samples showing an isotropic component in the ^{31}P spectrum, no contributions arising from an isotropic phase were measured. At first glance, this seems counterintuitive, but it is possible that in the intermediate regime, transverse relaxation is fast enough that nearly all signal from such structures gets lost during the refocused INEPT sequence.

MD Simulations and X-ray Scattering Experiments Also Evidence Immiscibility above a Critical Alkane Fraction. In addition, we characterized the influence of the alkane molecules on the bilayer dimensions by calculation of the area-per-lipid and bilayer thickness using the MD simulation trajectories at low water content. The bilayer thickness was defined as the average distance between the two phosphor planes. In Figure 7B, the results of such calculations are shown for C10 and C20. An increase of the alkane content is initially accompanied by an almost linear and significant enhancement of the area-per-lipid, whereas the increase of the bilayer thickness remains small, implying complete mixing of the alkane molecules with the lipid acyl chains. At a certain critical volume fraction ϕ_c the area-per-lipid reaches a plateau value. Above ϕ_c, the number of alkane molecules mixed with the acyl chains remains constant. The considerable increase of the bilayer thickness above ϕ_c, as seen in Figure 7B, indicates the tendency of the remaining alkane molecules to accumulate between the leaflets. This behavior is illustrated by snapshots of two systems, one below and one above ϕ_c, in Figure 7A. We note here that the vertical bars used in Figure 7B simply represent the fluctuations of bilayer thickness and area-per-lipid with time. Such fluctuations are inherent to lipid bilayers and not a measure of the average uncertainty due to averaging over a finite interval which is much smaller than the vertical bars plotted.

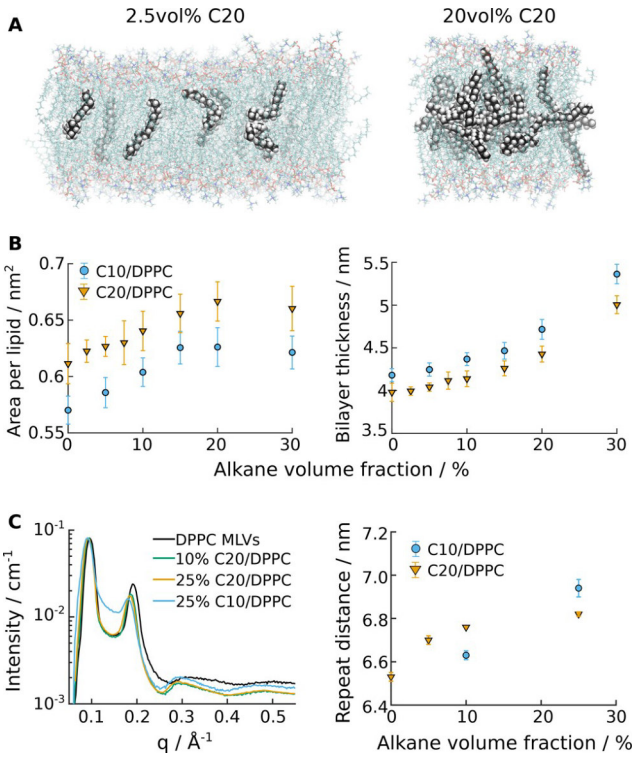

Figure 7. DPPC structural parameters obtained from MD simulations and X-ray diffraction experiments. (A) Selected snapshots from MD simulations. (B) Simulated area per lipid and ^{31}P–^{31}P distance of DPPC bilayers in the presence of varying amounts of *n*-alkane. Circles represent the mean thickness and the upper and lower limits are the ± standard deviation of the thickness fluctuations calculated from the final 50 ns of the simulated trajectories. The vertical bars therefore represent the fluctuations of bilayer thickness and area-per-lipid with time. Water content and temperature were as follows: C10/DPPC: n_w = 7, T = 60 °C; C20/DPPC: n_w = 19, T = 60 °C. (C) X-ray scattering intensity profiles for exemplary sample compositions (excess water, T = 60 °C) and average repeat distances calculated from the first two maxima observed. The error bars represent the variation range between values obtained from the different maxima and, in some cases, repeat measurements.

To investigate experimentally how the thickness of the bilayer changes with alkane incorporation we performed X-ray scattering experiments on MLVs in excess water. The intensity profiles and lamellar repeat distances of DPPC MLVs containing varying amounts of C10 and C20 are plotted in Figure 7C. The repeat distance encompasses the thickness of one bilayer plus one water layer in the MLVs and is therefore larger than the ^{31}P–^{31}P distance calculated from the MD simulations. Conducting the X-ray diffraction measurements on samples far above the excess water limit, however, guarantees that a change in the repeat distance directly translates to a change in bilayer thickness, as was previously demonstrated by McIntosh et al.[38] For DPPC MLVs containing C10, the repeat distance increases with the decane volume fraction in the investigated range of concentrations. This result agrees with previous studies,[35,37,38] as well as with our MD simulations. Upon adding C20, the DPPC bilayer repeat distance increases at first more strongly compared to C10, reaching a plateau at an alkane volume fraction between 10 and 20%. Notably, this happens at a similar volume fraction for which the NMR spectra started to display intermediate-motion lineshapes for the low hydration samples (see Figure 1B). This suggests that above the critical volume fraction of C20, unilamellar vesicles, alkane droplets or other structures that may not contribute to the Bragg peak pattern measured are formed. This implies that there are two types of structures in the system under excess water, one with a lower amount of alkane corresponding to membranes with dispersed alkanes and the other with alkane accumulations, for example, droplets as described by White and Thompson,[76] that might bud out from the MLVs and hence remain undetectable by X-ray scattering.

A direct comparison of the relative changes in bilayer thickness from MD simulations and repeat distance from scattering experiments (Figures 7) needs to be done with care since the hydration of the systems is different in the simulations and X-ray experiments. At an alkane volume fraction of 10%, the changes in bilayer thickness from simulations and experiments are similar (MD: +0.17 nm (C10 and C20), X-ray: +0.1 nm (C10), and +0.23 nm (C20)). However, the repeat distance for the C20 case in X-ray experiments has a stronger increase at low alkane fractions in comparison to the thickness profile in MD simulations (0–5 vol % thickness increase approximately 0.17 ± 0.04 nm (X-ray) and 0.014 nm (MD)). Again, this suggests that the MD simulation models overestimate the interaction of the alkane molecules with the lipid acyl chains, that is, an overestimation of alkane chains parallel to the acyl chains will lead to a higher increase of the area-per-lipid and consequently to a weaker dependence of the bilayer thickness on alkane concentration at

https://doi.org/10.1021/acs.langmuir.2c00872
Langmuir 2022, 38, 8595–8606

low alkane volume fractions. It remains to be investigated how the MD profiles in Figure 7B change as a function of hydration, that is, how ϕ_c depends on the number of water molecules per lipid, and to perform X-ray scattering measurements over smaller steps of alkane concentration to determine the accurate location of the inflection point as well as its dependence on lipid and alkane types.

CONCLUSIONS

In this work, we used all-atom MD simulations and solid-state NMR, X-ray diffraction and cryo-EM experiments to investigate the molecular arrangement of longer *n*-alkanes (C20 and C30) inside lipid bilayers and their effects.

^{2}H NMR spectroscopy of deuterated alkanes, X-ray diffraction experiments, and all-atom MD simulations indicate that, contrary to previous expectations, C20d and C30d can mix with saturated phospholipid acyl chains up to a considerable limiting fraction ϕ_c. At low hydration and above ϕ_c, the alkane forms an alkane slab or droplet between bilayer leaflets. At excess hydration above ϕ_c, either unilamellar vesicles with higher concentration of alkane or alkane droplets that may disperse through the aqueous media are formed.

The MD simulations enable to interpret qualitatively the ^{2}H NMR spectra measured at low hydration below ϕ_c, showing that the difference between the ^{2}H NMR spectra of C20d and C30d is due to their different order parameter profiles, with a maximum and a minimum absolute order parameter in the middle of the chain for C20d and C30d, respectively.

Sample hydration greatly influenced the ^{2}H and ^{31}P NMR spectra. In the excess hydration regime, the incorporation of alkane significantly changes the ^{31}P NMR spectra of the MLVs, even at very low alkane volume fractions, with the appearance of an isotropic spectral component that becomes prominent with an increase of alkane content. We hypothesize that this is due to a reduction of the membrane bending rigidity in the L_α phase and a consequent reduction of the average radius in the MLV system. Since this may be a general behavior of lipid membranes with physiological relevance, we believe that this hypothesis should motivate further experiments to directly measure the dependence of bending rigidity upon a minimal perturbation of the lipid membrane with a hydrophobic component.

The combination of NMR spectroscopy, X-ray scattering and MD simulations used in this work enabled us to describe the molecular structure of long *n*-alkanes in lipid bilayers with unprecedented detail and defines a starting point for future investigations regarding the fate of long hydrophobic chains inside model cellular membranes.

ASSOCIATED CONTENT

Supporting Information

The Supporting Information is available free of charge at https://pubs.acs.org/doi/10.1021/acs.langmuir.2c00872.

Details on simulated systems (Table S1), additional ^{2}H NMR spectra (Figure S1), density profiles for simulated systems (Figure S2), lipid order parameter profiles measured by R-PDLF NMR (Figure S3), and additional ^{31}P spectra (Figure S4) (PDF)

AUTHOR INFORMATION

Corresponding Authors

Anika Wurl − *NMR Group - Institute of Physics, Martin Luther University Halle-Wittenberg, 06099 Halle (Saale), Germany*; orcid.org/0000-0002-6785-9296; Email: anika.wurl@physik.uni-halle.de

Tiago M. Ferreira − *NMR Group - Institute of Physics, Martin Luther University Halle-Wittenberg, 06099 Halle (Saale), Germany*; Email: tiago.ferreira@physik.uni-halle.de

Authors

Maria Ott − *Department of Biotechnology and Biochemistry, Martin Luther University Halle-Wittenberg, 06099 Halle, Saale, Germany*; orcid.org/0000-0002-4686-9516

Eric Plato − *NMR Group - Institute of Physics, Martin Luther University Halle-Wittenberg, 06099 Halle (Saale), Germany*

Annette Meister − *Department of Biotechnology and Biochemistry, Martin Luther University Halle-Wittenberg, 06099 Halle, Saale, Germany*; orcid.org/0000-0003-1668-4382

Farzad Hamdi − *Department of Biotechnology and Biochemistry, Martin Luther University Halle-Wittenberg, 06099 Halle, Saale, Germany*

Panagiotis L. Kastritis − *Department of Biotechnology and Biochemistry, Martin Luther University Halle-Wittenberg, 06099 Halle, Saale, Germany*

Alfred Blume − *Insitute of Chemistry, Martin Luther University Halle-Wittenberg, 06099 Halle, Saale, Germany*; orcid.org/0000-0002-8416-7953

Complete contact information is available at: https://pubs.acs.org/10.1021/acs.langmuir.2c00872

Author Contributions

T.M.F. and A.W. designed the research project and managed its implementation. A.W. and E.P. prepared the samples. A.W. performed and analyzed the NMR experiments and MD simulations with guidance from T.M.F. M.O. and A.W. performed and analyzed the X-ray scattering experiments. A.M. and F.H. prepared and performed the cryo-EM measurements. All authors interpreted and discussed the results. A.W. and T.M.F. wrote the manuscript with input from all authors.

Notes

The authors declare no competing financial interest.

ACKNOWLEDGMENTS

This research study was funded by the German Research Foundation (Deutsche Forschungsgemeinschaft, DFG) [Project Number 189853844, TRR 102 (T.M.F. and A.W.)]. P.K.L. was supported by the Federal Ministry of Education and Research (BMBF, ZIK Program) [Grant Numbers 03Z22HN23 and 03Z22HI2 (to P.L.K.)] and the European Regional Development Fund for Saxony-Anhalt [Grant Number EFRE: ZS/2016/04/78115]. P.K.L. and A.M. also acknowledge the International Graduate School AGRIPOLY supported by the European Regional Development Fund (ERDF), the Federal State Saxony-Anhalt and the Martin-Luther University Halle-Wittenberg. T.M.F. greatly acknowledges financial support by the Ministry of Economics, Science and Digitalisation of the State of Saxony-Anhalt. T.M.F. and

A.W. gratefully acknowledge Kay Saalwächter and Alexey Krushelnitsky for their continuous support.

REFERENCES

(1) Marsh, D. *Handbook of Lipid Bilayers*; CRC Press: New York, 2013.
(2) Harayama, T.; Riezman, H. Understanding the diversity of membrane lipid composition. *Nat. Rev. Mol. Cell Biol.* **2018**, *19*, 281−296.
(3) Vist, M. R.; Davis, J. H. Phase equilibria of cholesterol dipalmitoylphosphatidylcholine mixtures: deuterium nuclear magnetic resonance and differential scanning calorimetry. *Biochemistry* **1990**, *29*, 451−464.
(4) Simons, K.; Ikonen, E. Cell biology - How cells handle cholesterol. *Science* **2000**, *290*, 1721−1726.
(5) Davis, J. H.; Clair, J. J.; Juhasz, J. Phase equilibria in DOPC/DPPC-d62/cholesterol mixtures. *Biophys. J.* **2009**, *96*, 521−539.
(6) Ferreira, T. M.; Coreta-Gomes, F.; Ollila, O H S.; Moreno, M. J.; Vaz, W L C.; Topgaard, D. Cholesterol and popc segmental order parameters in lipid membranes: solid state ^{1}H-^{13}C NMR and MD simulation studies. *Phys. Chem. Chem. Phys.* **2013**, *15*, 1976−1989.
(7) Andersson, J. M.; Grey, C.; Larsson, M.; Ferreira, T. M.; Sparr, E. Effect of cholesterol on the molecular structure and transitions in a clinical-grade lung surfactant extract. *Proc. Natl. Acad. Sci. U.S.A.* **2017**, *114*, E3592−E3601.
(8) Bechinger, B. The structure, dynamics and orientation of antimicrobial peptides in membranes by multidimensional solid-state NMR spectroscopy. *Biochimica et Biophysica Acta (BBA) - Biomembranes* **1999**, *1462*, 157−183.
(9) Bechinger, B.; Lohner, K. Detergent-like actions of linear amphipathic cationic antimicrobial peptides. *Biochimica et Biophysica Acta (BBA) - Biomembranes* **2006**, *1758*, 1529−1539.
(10) Lee, M. T.; Sun, T. L.; Hung, W. C.; Huang, H. W. Process of inducing pores in membranes by melittin. *Proc. Natl. Acad. Sci. U.S.A.* **2013**, *110*, 14243−14248.
(11) Strandberg, E.; Bentz, D.; Wadhwani, P.; Ulrich, A. S. Chiral supramolecular architecture of stable transmembrane pores formed by an alpha-helical antibiotic peptide in the presence of lysolipids. *Sci. Rep.* **2020**, *10*, 4710−4726, DOI: 10.1038/s41598-020-61526-w.
(12) Gross, R. W. The evolution of lipidomics through space and time. *Biochimica et Biophysica Acta (BBA) - Molecular and Cell Biology of Lipids* **2017**, *1862*, 731−739.
(13) Castellanos, D. B.; Martín-Jiménez, C. A.; Rojas-Rodríguez, F.; Barreto, G. E.; González, J. Brain lipidomics as a rising field in neurodegenerative contexts: Perspectives with machine learning approaches. *Frontiers in Neuroendocrinology* **2021**, *61*, 100899.
(14) Pabst, G.; Kučerka, N.; Nieh, M.-P.; Rheinstädter, M. C.; Katsaras, J. Applications of neutron and x-ray scattering to the study of biologically relevant model membranes. *Chem. Phys. Lipids* **2010**, *163*, 460−479.
(15) Leftin, A.; Brown, M. F. An NMR database for simulations of membrane dynamics. *Biochim. Biophys. Acta-Biomembr.* **2011**, *1808*, 818−839.
(16) Dimova, R. Recent developments in the field of bending rigidity measurements on membranes. *Adv. Colloid Interface Sci.* **2014**, *208*, 225−234.
(17) Reißer, S.; Strandberg, E.; Steinbrecher, T.; Elstner, M.; Ulrich, A. S. Best of two worlds? how MD simulations of amphiphilic helical peptides in membranes can complement data from oriented solid-state NMR. *J. Chem. Theory Comput.* **2018**, *14*, 6002−6014.
(18) Bacle, A.; Buslaev, P.; Garcia-Fandino, R.; Favela-Rosales, F.; Ferreira, T. M.; Fuchs, P F J.; Gushchin, I.; Javanainen, M.; Kiirikki, A. M.; Madsen, J. J.; Melcr, J.; Rodríguez, P Milán; Miettinen, M. S.; Ollila, O H S.; Papadopoulos, C. G.; Peón, A.; Piggot, T. J.; Piñeiro, A.; Virtanen, S. I. Inverse conformational selection in lipid−protein binding. *J. Am. Chem. Soc.* **2021**, *143*, 13701−13709.
(19) Antila, H. S.; Ferreira, T. M.; Ollila, O H S.; Miettinen, M. S. Using open data to rapidly benchmark biomolecular simulations: Phospholipid conformational dynamics. *J. Chem. Inf. Model.* **2021**, *61*, 938−949.
(20) Bochicchio, D.; Cantu, L.; Cadario, M. V.; Palchetti, L.; Natali, F.; Monticelli, L.; Rossi, G.; Del Favero, E. Polystyrene perturbs the structure, dynamics, and mechanical properties of DPPC membranes: An experimental and computational study. *J. Colloid Interface Sci.* **2022**, *605*, 110−119.
(21) De Mel, J. U.; Gupta, S.; Willner, L.; Allgaier, J.; Stingaciu, L. R.; Bleuel, M.; Schneider, G. J. Manipulating phospholipid vesicles at the nanoscale: A transformation from unilamellar to multilamellar by an n-alkyl-poly(ethylene oxide). *Langmuir* **2021**, *37*, 2362−2375.
(22) Large, D. E.; Abdelmessih, R. G.; Fink, E. A.; Auguste, D. T. Liposome composition in drug delivery design, synthesis, characterization, and clinical application. *Adv. Drug Delivery Rev.* **2021**, *176*, 113851.
(23) Hou, X.; Zaks, T.; Langer, R.; Dong, Y. Lipid nanoparticles for mRNA delivery. *Nat. Rev. Mater.* **2021**, *6*, 1078−1094.
(24) Fettiplace, R.; Andrews, D. M.; Haydon, D. A. The thickness, composition and structure of some lipid bilayers and natural membranes. *J. Membr. Biol.* **1971**, *5*, 277−296.
(25) Haydon, D. A.; Hendry, B. M.; Levinson, S. R.; Requena, J. Anaesthesia by the n-alkanes. a comparative study of nerve impulse blockage and the properties of black lipid bilayer membranes. *Biochimica et Biophysica Acta (BBA) - Biomembranes* **1977**, *470*, 17−34.
(26) Coster, H G L.; Laver, D. R. The effect of temperature on lipid-n-alkane interactions in lipid bilayers. *Biochimica et Biophysica Acta (BBA) - Biomembranes* **1986**, *857*, 95−104.
(27) Coster, H G L.; Laver, D. R. The effect of benzyl alcohol and cholesterol on the acyl chain order and alkane solubility of bimolecular phosphatidylcholine membranes. *Biochimica et Biophysica Acta (BBA) - Biomembranes* **1986**, *861*, 406−412.
(28) Haydon, D. A.; Hendry, B. M.; Levinson, S. R.; Requena, J. The molecular mechanisms of anaesthesia. *Nature* **1977**, *268*, 356−358.
(29) Liu, J.; Laster, M. J.; Taheri, S.; Eger, E. I.; Koblin, D. D.; Halsey, M. J. Is there a cutoff in anesthetic potency for the normal-alkanes. *Anesthesia and Analgesia* **1993**, *77*, 12−18.
(30) Missner, A.; Pohl, P. 110 years of the meyer-overton rule: predicting membrane permeability of gases and other small compounds. *ChemPhysChem* **2009**, *10*, 1405−1414.
(31) Hishida, M.; Endo, A.; Nakazawa, K.; Yamamura, Y.; Saito, K. Effect of n-alkanes on lipid bilayers depending on headgroups. *Chem. Phys. Lipids* **2015**, *188*, 61−67.
(32) Hishida, M.; Yanagisawa, R.; Yamamura, Y.; Saito, K. Phase separation of a ternary lipid vesicle including n-alkane: Rugged vesicle and bilayer flakes formed by separation between highly rigid and flexible domains. *J. Chem. Phys.* **2019**, *150*, 064904.
(33) Ramos, A. P.; Doroudgar, M.; Lafleur, M. Determination of n-alkane partitioning within phosphatidylethanolamine L-alpha/H-II phases. *BBA - Biomembranes* **2020**, *1862*, 183201.
(34) Usuda, H.; Hishida, M.; Yamamura, Y.; Saito, K. Common effects of incorporated n-alkane derivatives on molecular packing and phase behavior of DPPC bilayers. *Chem. Lett.* **2018**, *47*, 1512−1514.
(35) Usuda, H.; Hishida, M.; Kelley, E. G.; Yamamura, Y.; Nagao, M.; Saito, K. Interleaflet coupling of n-alkane incorporated bilayers. *Phys. Chem. Chem. Phys.* **2020**, *22*, 5418−5426.
(36) Zoni, V.; Campomanes, P.; Vanni, S. Investigating the structural properties of hydrophobic solvent-rich lipid bilayers. *Soft Matter* **2021**, *17*, 5329−5335.
(37) Pope, J. M.; Walker, L. W.; Dubro, D. On the ordering of n-alkane and n-alcohol solutes in phospholipid bilayer model membrane systems. *Chem. Phys. Lipids* **1984**, *35*, 259−277.
(38) McIntosh, T. J.; Simon, S. A.; MacDonald, R. C. The organization of n-alkanes in lipid bilayers. *Biochimica et Biophysica Acta (BBA) - Biomembranes* **1980**, *597*, 445−463.
(39) Lohner, K. Effects of small organic molecules on phospholipid phase transitions. *Chem. Phys. Lipids* **1991**, *57*, 341−362.

(40) Bothun, G. D.; Knutson, B. L.; Strobel, H. J.; Nokes, S. E. Liposome fluidization and melting point depression by compressed and liquid n-alkanes. *Colloids Surf., A* **2006**, *279*, 50−57.
(41) Hishida, M.; Yanagisawa, R.; Usuda, H.; Yamamura, Y.; Saito, K. Communication: Rigidification of a lipid bilayer by an incorporated n-alkane. *J. Chem. Phys.* **2016**, *144*, 041103.
(42) White, S. H.; King, G. I.; Cain, J. E. Location of hexane in lipid bilayers determined by neutron diffraction. *Nature* **1981**, *290*, 161−163.
(43) Lea, E J A. Effect of n-alkanes on membranes in lipid-water systems. *Int. J. Biol. Macromol.* **1979**, *1*, 185−187.
(44) Gruen, D. W.; Haydon, D. A. A mean-field model of the alkane-saturated lipid bilayer above its phase transition. ii. results and comparison with experiment. *Biophys. J.* **1981**, *33*, 167−187.
(45) Pope, J. M.; Littlemore, L. A.; Westerman, P. W. Chain-length dependence of n-alkane solubility in phosphatidylcholine bilayers: a 2h-nmr study. *Biochimica et Biophysica Acta (BBA) - Biomembranes* **1989**, *980*, 69−76.
(46) Chen, Z.; Rand, R. P. Comparative study of the effects of several n-alkanes on phospholipid hexagonal phases. *Biophys. J.* **1998**, *74*, 944−952.
(47) Sjölund, M.; Rilfors, L.; Lindblom, G. Reversed hexagonal phase formation in lecithin-alkane-water systems with different acyl chain unsaturation and alkane length. *Biochemistry* **1989**, *28*, 1323−1329.
(48) Epand, R. M. Diacylglycerols, lysolecithin, or hydrocarbons markedly alter the bilayer to hexagonal phase transition temperature of phosphatidylethanolamines. *Biochemistry* **1985**, *24*, 7092−7095.
(49) Bochicchio, D.; Panizon, E.; Monticelli, L.; Rossi, G. Interaction of hydrophobic polymers with model lipid bilayers. *Sci. Rep.* **2017**, *7*, 6357.
(50) Davis, J. H. The description of membrane lipid conformation, order and dynamics by ^{2}H NMR. *Biochimica et Biophysica Acta (BBA) - Reviews on Biomembranes* **1983**, *737*, 117−171.
(51) Dvinskikh, S. V.; Castro, V.; Sandström, D. Efficient solid-state NMR methods for measuring heteronuclear dipolar couplings in unoriented lipid membrane systems. *Phys. Chem. Chem. Phys.* **2005**, *7*, 607−613.
(52) Zhao, X.; Edén, M.; Levitt, M. H. Recoupling of heteronuclear dipolar interactions in solid-state NMR using symmetry-based pulse sequences. *Chem. Phys. Lett.* **2001**, *342*, 353−361.
(53) Seelig, A.; Seelig, J. Dynamic structure of fatty acyl chains in a phospholipid bilayer measured by deuterium magnetic resonance. *Biochemistry* **1974**, *13*, 4839−4845.
(54) Abraham, M. J.; Murtola, T.; Schulz, R.; Páll, S.; Smith, J. C.; Hess, B.; Lindahl, E. Gromacs: High performance molecular simulations through multi-level parallelism from laptops to supercomputers. *SoftwareX* **2015**, *1−2*, 19−25.
(55) Ryckaert, J.-P.; Bellemans, A. Molecular dynamics of liquid alkanes. *Faraday Discuss. Chem. Soc.* **1978**, *66*, 95−106.
(56) Klauda, J. B.; Venable, R. M.; Freites, J. A.; O'Connor, J. W.; Tobias, D. J.; Mondragon-Ramirez, C.; Vorobyov, I.; MacKerell, A. D.; Pastor, R. W. Update of the charmm all-atom additive force field for lipids: Validation on six lipid types. *J. Phys. Chem. B* **2010**, *114*, 7830−7843.
(57) Venable, R. M.; Luo, Y.; Gawrisch, K.; Roux, B.; Pastor, R. W. Simulations of anionic lipid membranes: Development of interaction-specific ion parameters and validation using nmr data. *J. Phys. Chem. B* **2013**, *117*, 10183−10192.
(58) Ollila, S.; Miettinen, M. MD simulation trajectory and related files for DPPC bilayer (CHARMM36, Gromacs 4.5). *Zenodo* **2015**, na.
(59) Schaftenaar, G.; Vlieg, E.; Vriend, G. Molden 2.0: quantum chemistry meets proteins. *Journal of Computer-Aided Molecular Design* **2017**, *31*, 789−800.
(60) Durell, S.; Brooks, B. R.; Ben-Naim, A. Solvent-induced forces between two hydrophilic groups. *J. Phys. Chem.* **1994**, *98*, 2198−2202.
(61) Jorgensen, W. L.; Chandrasekhar, J.; Madura, J. D.; Impey, R. W.; Klein, M. L. Comparison of simple potential functions for simulating liquid water. *J. Chem. Phys.* **1983**, *79*, 926−935.
(62) Abraham, M. J.; van der Spoel, D.; Lindahl, E. Gromacs user manual version, 2019, https://manual.gromacs.org/documentation/2019/manual-2019.pdf.
(63) McGibbon, R. T.; Beauchamp, K. A.; Harrigan, M. P.; Klein, C.; Swails, J. M.; Hernández, C. X.; Schwantes, C. R.; Wang, L.-P.; Lane, T. J.; Pande, V. S. Mdtraj: A modern open library for the analysis of molecular dynamics trajectories. *Biophys. J.* **2015**, *109*, 1528−1532.
(64) Vogelsberg, C. S.; Uribe-Romo, F. J.; Lipton, A. S.; Yang, S.; Houk, K. N.; Brown, S.; Garcia-Garibay, M. A. Ultrafast rotation in an amphidynamic crystalline metal organic framework. *Proc.Natl. Acad. Sci. USA* **2017**, *114*, 13613−13618.
(65) Seelig, J. 31p nuclear magnetic resonance and the head group structure of phospholipids in membranes. *Biochimica et Biophysica Acta (BBA) - Reviews on Biomembranes* **1978**, *515*, 105−140.
(66) Cullis, P. R.; De Kruijff, B. Lipid polymorphism and the functional roles of lipids in biological membranes. *Biochimica et Biophysica Acta (BBA) - Reviews on Biomembranes* **1979**, *559*, 399−420.
(67) Dufourc, E. J.; Mayer, C.; Stohrer, J.; Althoff, G.; Kothe, G. Dynamics of phosphate head groups in biomembranes. comprehensive analysis using phosphorus-31 nuclear magnetic resonance lineshape and relaxation time measurements. *Biophys. J.* **1992**, *61*, 42−57.
(68) Angelico, R.; Ceglie, A.; Colafemmina, G.; Delfine, F.; Olsson, U.; Palazzo, G. Phase behavior of the lecithin/water/isooctane and lecithin/water/decane systems. *Langmuir* **2004**, *20*, 619−631.
(69) Maulucci, G.; De Spirito, M.; Arcovito, G.; Boffi, F.; Castellano, A. C.; Briganti, G. Particle size distribution in dmpc vesicles solutions undergoing different sonication times. *Biophys. J.* **2005**, *88*, 3545−3550.
(70) Cullis, P. R. Lateral diffusion rates of phosphatidylcholine in vesicle membranes: Effects of cholesterol and hydrocarbon phase transitions. *FEBS Lett.* **1976**, *70*, 223−228.
(71) Pinheiro, T J T.; Watts, A. Lipid specificity in the interaction of cytochrome c with anionic phospholipid bilayers revealed by solid-state 31p nmr. *Biochemistry* **1994**, *33*, 2451−2458.
(72) Zhang, W.; Peng, P.; Kuang, Y.; Yang, J.; Cao, D.; You, Y.; Shen, K. Characterization of exosomes derived from ovarian cancer cells and normal ovarian epithelial cells by nanoparticle tracking analysis. *Tumor Biol.* **2016**, *37*, 4213−4221.
(73) Huang, C.; Quinn, D.; Sadovsky, Y.; Suresh, S.; Hsia, K. J. Formation and size distribution of self-assembled vesicles. *Proc. Nat. Acad. Sci.* **2017**, *114*, 2910−2915.
(74) Dvinskikh, S. V.; Castro, V.; Sandström, D. Probing segmental order in lipid bilayers at variable hydration levels by amplitude- and phase-modulated cross-polarization NMR. *Phys. Chem. Chem. Phys.* **2005**, *7*, 3255−3257.
(75) Ferreira, T. M.; Bernin, D.; Topgaard, D. *NMR Studies of Nonionic Surfactants*; Academic Press, 2013; Chapter 3, pp 73−127.
(76) White, S. H.; Thompson, T. E. Capacitance, area, and thickness variations in thin lipid films. *Biochimica et Biophysica Acta (BBA) - Biomembranes* **1973**, *323*, 7−22.

5.1.1 Paper I: Supporting Information

Additional tables and figures referred to in paper I, as published in reference [37]. No changes were made.

n-alkane	Number of alkane molecules	Number of DPPC molecules	Alkane volume fraction	Alkane mole fraction	Number of water molecules	n_w	T [K]	zenodo DOI
C10	0	72	0%	0%	504	7	333	10.5281/zenodo.6517496
C10	12	72	5%	14%	504	7	333	10.5281/zenodo.6517496
C10	26	72	10%	27%	504	7	333	10.5281/zenodo.6517496
C10	26	72	10%	27%	1357	19	343	10.5281/zenodo.6517496
C10	41	72	15%	36%	504	7	333	10.5281/zenodo.6517496
C10	58	72	20%	45%	504	7	333	10.5281/zenodo.6517496
C10	99	72	30%	58%	504	7	333	10.5281/zenodo.6517496
C20	0	72	0%	0%	1329	18.5	333	10.5281/zenodo.6524029
C20	12	288	2.5%	4%	5164	18	333	10.5281/zenodo.6524029
C20	24	288	5%	8%	5164	18	333	10.5281/zenodo.6524029
C20	9	72	7.5%	11%	1291	18	333	10.5281/zenodo.6524029
C20	12	72	10%	14%	1291	18	333	10.5281/zenodo.6524029
C20	12	72	10%	14%	1291	18	343	10.5281/zenodo.6524029
C20	20	72	15%	22%	1291	18	333	10.5281/zenodo.6524029
C20	29	72	20%	29%	1291	18	333	10.5281/zenodo.6524029
C20	49	72	30%	40%	1292	18	333	10.5281/zenodo.6524029
C30	8	288	2.5%	3%	5472	19	343	10.5281/zenodo.6539320
C30	16	288	5%	5%	5472	19	343	10.5281/zenodo.6539320

Table S1: Overview of the simulated systems. Alkane volume fraction is defined as the alkane-to-lipid acyl tail ratio, while the alkane mole fraction refers to the ratio of alkane to non-water (alkane and lipid) molecules. The zenodo DOIs can be used to access the simulation data stored in the zenodo repository.

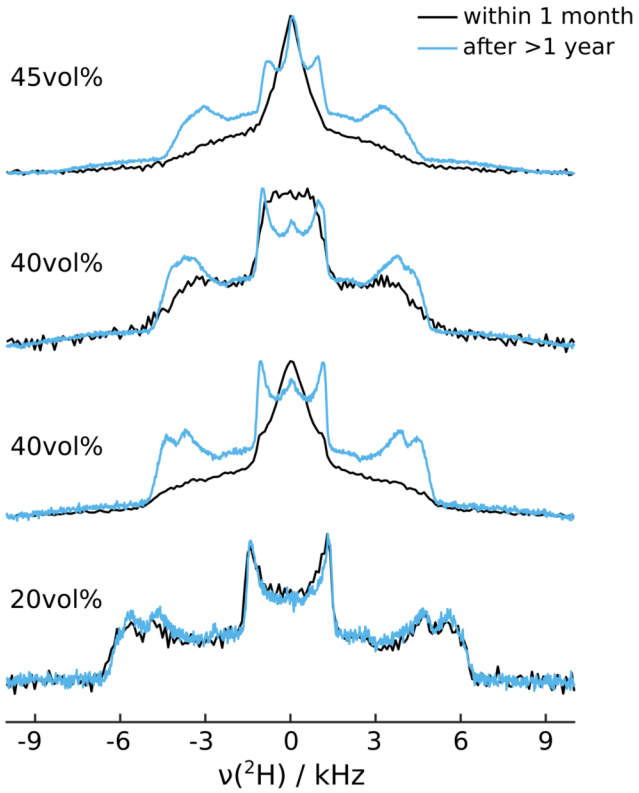

Figure S1: Static ^{2}H NMR spectra of decane-d22 in DPPC, n_w=7, T=60°C, measured at two different time points after sample preparation.

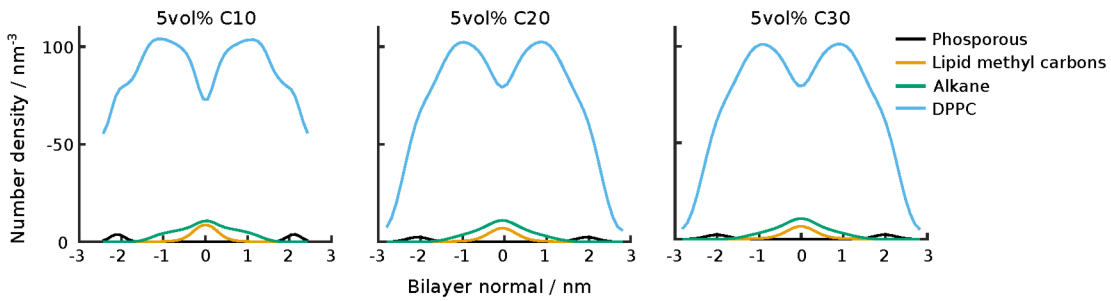

Figure S2: Number density profiles for selected atom groups of 5 vol% C10 (60°C,n_w=7), C20 (60°C) and C30 in DPPC (70°C), calculated from MD trajectories using *gmx density*.

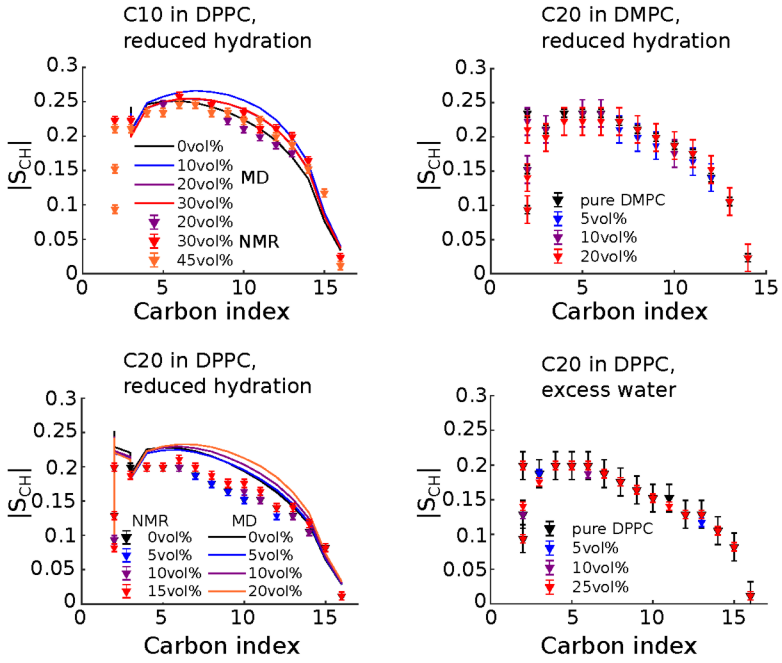

Figure S3: Lipid order parameter profiles obtained from R-PDLF measurements (triangles) and MD simulations (solid lines). The different alkane concentrations are noted in the legends. (a) DPPC plus *n*-decane, n_w=7-8, 60°C (b) DMPC plus *n*-eicosane, n_w=11-14, 40°C (c) DPPC plus *n*-eicosane, n_w=13-16, 60°C, (d) DPPC plus *n*-eicosane, excess water, 60°C.

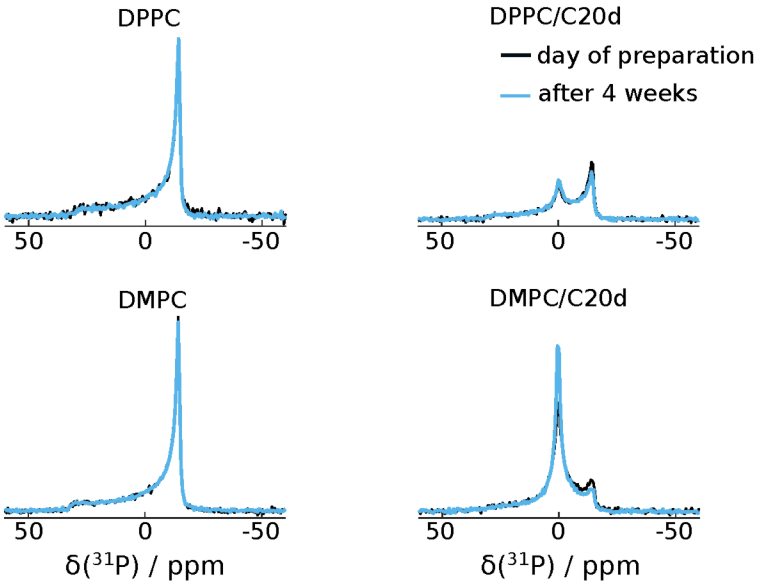

Figure S4: ^{31}P NMR spectra of DPPC or DMPC plus 10 vol% C20d in excess water conditions. Spectra shown in black were acquired on the day of preparation, while the blue spectra were taken 4 weeks later.

5.2 Paper II: Atomistic MD Simulations of *n*-Alkanes in a Phospholipid Bilayer: CHARMM36 versus Slipids[2]

In paper I [37] it was found that n-alkanes can be mixed with saturated lipid bilayers up to a certain volume fraction ϕ_c, which depends on n-alkane chain length. The corresponding MD simulations however showed no effect of chain length on ϕ_c (within the experimental uncertainty). It is possible that the experimentally determined value of ϕ_c is subject to the sample preparation protocol, i.e. the solvent used, and thus is lower than the value obtained from simulations. Importantly, in paper I, simulations with the CHARMM36 force field strongly overestimated n-alkane ordering for C20 and C30, possibly also invalidating the results for ϕ_c.

This paper systematically investigates n-alkane/lipid miscibility via MD simulations using two different force fields, namely CHARMM36 and Slipids. In particular, the effects of alkane chain length, sample hydration and simulation parameters are examined. As in paper I, the three n-alkanes C10, C20 and C30 are studied in DPPC membranes. The water content of the systems is either 7 or 19 water molecules per lipid, which is below the excess water limit and matches the experimental results presented in paper I. The results presented here clearly show that the Slipids force field produces much more realistic values for the n-alkane order parameters of C20 and C30, but not C10. This is explained by the fact that hydrocarbon chains modelled with Slipids are more flexible than their CHARMM36 counterparts. Chain flexibility can be adjusted via the electrostatic 1-4 interactions, and we show that the hydrocarbon charges in CHARMM36 can be tuned to provide a more realistic model for longer n-alkanes. With regards to miscibility, the Slipids simulations show indeed a significant dependence of ϕ_c on n-alkane length, which we explain by the interfacial energy penalty introduced by adding bulky, hydrophobic chains to the lipid membrane.

The author contributions to this article are as follows: AW and TMF designed the research project. AW and to a small part TMF performed and analyzed the MD simulations. AW and TMF wrote the manuscript.

[2]This article [Anika Wurl and Tiago M. Ferreira, *Macromol. Theory Simul.* **2023**, 2200078] [38] is an open access article published under the terms of the Creative Commons Attribution-NonCommercial-NoDerivs License, which permits use and distribution in any medium, provided the original work is properly cited, the use is non-commercial and no modifications or adaptations are made. The article can be found on the publishers (Wiley-VCH GmbH) website using the following link: https://doi.org/10.1002/mats.202200078 . No changes were made.

RESEARCH ARTICLE

Macromolecular Theory and Simulations
www.mts-journal.de

Atomistic MD Simulations of *n*-Alkanes in a Phospholipid Bilayer: CHARMM36 versus Slipids

Anika Wurl and Tiago M. Ferreira**

Linear alkanes (*n*-alkanes) are chemically the most simple linear hydrophobic molecules in nature. Studying the incorporation of *n*-alkanes into lipid membranes is therefore a good starting point toward understanding the behavior of hydrophobic molecules in lipid membranes and to assess how accurately molecular dynamics models describe such systems. Here, the miscibility and structure of different *n*-alkanes—*n*-decane (C10), *n*-eicosane (C20), and *n*-triacontane (C30)—in dipalmitoylphosphatidylcholine membranes are investigated using two of the most used force fields for lipid membrane molecular dynamics simulations (CHARMM36 and Slipids). The *n*-alkanes are miscible in the membrane up to a critical volume fraction, ϕ_c, that depends on the force field interaction parameters used. ϕ_c is dependent on alkane chain length only for the model with more disordered chains (Slipids). Below ϕ_c, a comparison with ^{2}H nuclear magnetic resonance (NMR) spectra indicates that a more realistic structure of the longer alkane molecules (C20 and C30) is obtained using the Slipids force field. On the other hand, for the shorter alkane (C10), Slipids simulations underestimate molecular order and CHARMM36 simulations enable a precise prediction of its experimental spectrum. The predicted ^{2}H NMR spectra are highly sensitive to 1–4 electrostatic interactions, and suggest that a reduction of the partial charges of the longer alkanes and acyl chains in CHARMM36 results in a better performance. The results presented indicate that lipid membranes with incorporated alkanes are highly valuable systems for the validation of force fields designed to perform lipid membrane simulations.

1. Introduction

Many biological processes related to the incorporation of hydrophobic molecules into cell membranes remain poorly understood at the molecular level. Examples include the anaesthetic effect of alkanes,[1–3] the formation of lipid droplets,[4–6] or the potential effect of microscale and nanoscale plastics on cell membrane structure.[7–10]

One important open question concerns the solubility of hydrophobic molecules in a membrane system. It is yet unclear how the chemistry, size, and shape of hydrophobic molecules affect their structure, dynamics, and partition in a lipid membrane.[11–13] Exploring these dependencies by systematic studies will help to understand their role in biological processes as well as to guide the development of lipid-based technologies.

Linear alkanes (*n*-alkanes) are the most simple hydrophobic chain-like molecules in nature for which extensive data has been collected. Therefore, *n*-alkanes are a suitable starting point to address the problems introduced above. The solubility of *n*-alkanes in many different solvents has been determined as a function of alkane chain length[14–16] as well as the enthalpy of mixing of various *n*-alkane binary mixtures.[17] The available data shows that at higher temperatures, the enthalpy of mixing of liquid *n*-alkanes with different chain length becomes negative, that is, there is complete miscibility.[18,19] The solubility of alkanes in phospholipid membranes, pertinent to the biophysical questions outlined above, is however more intricate since the lipid bilayer hydrophobic region is a nm-thick fluid possessing interfacial surface tension and a gradient of molecular order in the direction of the bilayer normal.[20–22] Depending on alkane chain length and concentration, the complete mixing of alkanes with the phospholipid acyl chains may imply a significant change of both the surface area and the molecular order of the system. Analogous to this problem, it is well known that the isotropic-to-nematic transition of a nematogenic solvent with dispersed flexible chains (including *n*-alkanes) induces phase separation, and that the concentration of the flexible chains in the nematic phase decreases with chain length.[23–25] In contrast to nematogens, the acyl chains in a lipid bilayer have a high degree of flexibility. Nevertheless, a similar dependence on *n*-alkane chain length may emerge due to the fact that longer alkanes have a stronger tendency to fold[26] and thus perturb the lipid membrane to a larger degree: Increased chain folding is expected to lead to a larger increase in local interfacial area-per-phospholipid

A. Wurl, T. M. Ferreira
NMR group - Institute for Physics
Martin Luther University Halle-Wittenberg
Betty-Heimann-Str. 7, 06120 Halle (Saale), Germany
E-mail: anika.wurl@physik.uni-halle.de; tiago.ferreira@physik.uni-halle.de

The ORCID identification number(s) for the author(s) of this article can be found under https://doi.org/10.1002/mats.202200078

DOI: 10.1002/mats.202200078

(APL) and therefore a higher increase of interfacial free energy.

The solubility of alkanes with different chain lengths in lipid bilayers has been investigated experimentally by different research groups with apparently contradicting results. Previous ^{2}H nuclear magnetic resonance (NMR) results reported by Pope et al.,[11,27,28] indicate that *n*-alkanes longer than the lipid acyl chains become immiscible. In contrast, we have recently demonstrated that *n*-eicosane (C20) and *n*-triacontane (C30), with chain lengths of 20 and 30 carbons, respectively, are miscible in dipalmitoylphosphatidylcholine (DPPC) membranes (acyl chain length of 16 carbons).[29] The origin of these contrasting observations is very likely the distinct sample preparation procedure used, which we have observed to heavily influence the time needed to attain thermodynamical equilibrium. In the previous work, we showed that with a standard mixing procedure [30]—dissolution of *n*-alkane and phospholipid in organic solvent, subsequent solvent evaporation, and hydration of the resulting lipid film—it is possible to mix C30 with DPPC lipid membranes up to an alkane-to-acyl chain volume ratio of ≈5%.[29] This is the longest *n*-alkane that has been directly observed in a lipid membrane to date. From our previous experimental results, it was apparent that the solubility of C30 in DPPC lipid membranes is significantly lower compared to the solubility of C20. However we cannot exclude an effect of the organic solvent used, that is, phase separation may occur during the evaporation of the organic solvent, due to the distinct solubilities of alkanes[15] and phosphatidylcholines,[31] leading to a lipid/alkane film with an inhomogeneous distribution of the two components.

Molecular dynamics (MD) simulations of alkanes in lipid membranes can be used to circumvent such sample preparation shortcomings since the initial arrangement of molecules is fully controlled. In a recent work, we used the CHARMM36 force field (ff)[32] for modeling DPPC bilayers containing *n*-alkanes, assuming equivalent interactions for both *n*-alkanes and acyl chains.[29] We had chosen CHARMM36 because of its generally good agreement with experimental NMR order parameters of phospholipids.[33] Such a description led to the observation of a critical *n*-alkane volume fraction ϕ_c, at which the bilayer APL reaches a maximum value, and above which alkane chains start to accumulate between the bilayer leaflets.[29] ϕ_c was identical for 10 and 20 carbon long *n*-alkanes in contrast to their experimental apparent solubility. Comparison of these simulations with ^{2}H NMR experimental results however showed that, while the CHARMM36 ff is suitable to model *n*-decane in a DPPC membrane, it significantly overestimates the ordering of longer *n*-alkanes (C20 or C30).[29] Ideally, to investigate the dependence of ϕ_c on longer alkane chain lengths, one should therefore use a more realistic model for these chains.

Another ff specifically designed to study lipid membranes is the Slipids ff.[34,35] The comparison of phospholipid order parameters with experimental data shows that the phospholipid headgroup structure is not as realistic as in CHARMM36.[33,36] However, since the Slipids ff was developed with particular focus on lipid acyl chains by using a parametrization based on DFT calculations on hexadecane (partial charges), high level ab initio calculations on octane (dihedral torsions) and a comparison with thermodynamical and dynamical properties of bulk alkanes, it is a suitable alternative to CHARMM36 for investigating the behavior of *n*-alkanes in phospholipid bilayers.

In this work, we perform a systematic investigation of alkanes with different chain lengths—*n*-decane (C10), *n*-eicosane (C20) and *n*-triacontane (C30)—incorporated into DPPC membranes, using both the CHARMM36 and the Slipids force fields. The simulations show that the Slipids ff gives indeed, as expected, more realistic estimates for C–H bond order parameters of the longer *n*-alkanes due to a higher configurational entropy of the chains. The main contribution for the different performance of the two ffs is the strength of the electrostatic 1–4 interactions and we demonstrate that by reducing the partial charges of the acyl chains in CHARMM36, a better agreement with the ^{2}H NMR spectra of C20 and C30 can be achieved. The dependence of ϕ_c on alkane chain length is also investigated for both force fields. ϕ_c is indeed dependent on alkane chain length but not as strongly as apparent from our previous experimental measurements. We believe that the results shown will motivate new experiments (exploring the use of different organic solvents) and should be taken as a valuable reference for future force field optimizations.

2. Results and Discussion

2.1. Slipids Simulations Predict the Structure of the Longer Alkanes More Accurately

In order to determine if the Slipids force field results in a more realistic structural behavior of the long *n*-alkane chains than CHARMM36, we simulated three *n*-alkanes with different chain length in a DPPC bilayer and calculated the alkane C–H bond order parameters. The comparison with experimental results is shown in **Figure 1**. For reference, we also present the phospholipid S_{CH} magnitudes of a pure DPPC membrane (Figure 1B), together with experimental values from our group and from Seelig et al.[37]

These profiles confirm that the CHARMM36 ff reproduces the phospholipid headgroup order parameters well. However, the absolute acyl tail order parameters are somewhat larger than the experimental values. This observation agrees with previous findings,[39] and is also indicated in the initial CHARMM36 publication:[32] While Klauda et al. achieve very good agreement with the ^{2}H NMR order parameters using a fixed APL of 0.64 nm^2 (NPAT ensemble, T = 50° C), their NPT simulation results in a slightly decreased area-per-lipid (62.9±0.3 nm^2), and consequently higher ordering of DPPC acyl chains. We note here that our order parameters were consistently larger than those obtained by Klauda et al.[32] (see Figure S1, Supporting Information). This is expected as we are using a simulation software different from the one used by Klauda et al. (GROMACS[40] vs CHARMM[41]) as shown previously,[42] possibly due to different switching functions implemented in the different programs. Recently, a particle-mesh Ewald algorithm has been implemented for the treatment of long-range dispersion eliminating the dependence on the cut-off switching function and is expected to improve the accuracy of lipid acyl chain order parameters[43,44] and liquid alkane properties.[45] However, we find that the alkane order parameters remain largely unaffected by slight variations of the simulation settings, or even the lipid order (see below), and

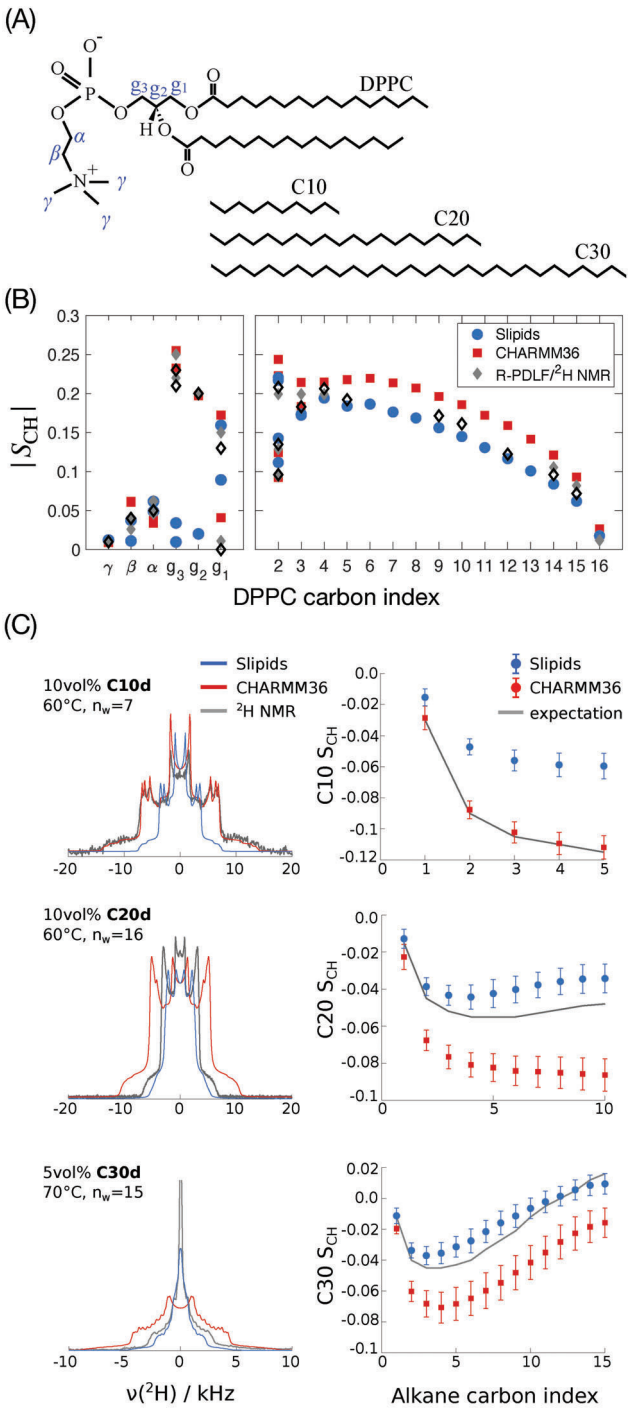

Figure 1. Comparison of simulated C–H order parameters calculated from CHARMM36 (red) and Slipids (blue) simulations with experimental observations. A) Chemical structures and labels for DPPC and the alkanes studied. B) Comparison of $|S_{CH}|$ values calculated from CHARMM36 and Slipids simulations of a pure DPPC bilayer (at excess hydration) with experimental values.[29,38] C) Simulated and experimental ^{2}H NMR spectra of the three *n*-alkanes and corresponding order parameter profiles. Expected order parameter profiles (gray) were estimated from the experimental ^{2}H NMR spectra (see Supporting Information for details). The temperature, hydration, and alkane volume fraction of the systems are shown on the top left corner of each spectra.

thus we simply used the default simulation settings provided by the CHARMM-GUI membrane builder.

Simulations with the Slipids ff result in a better agreement with the experimental DPPC acyl chain order parameters as expected,[34,39] but far worse order parameters for the headgroup and glycerol carbons (compared to CHARMM36), as also shown previously.[33] We note here that the updated (2020) version of the Slipids ff addresses the problem of the glycerol carbon order parameters.[35] However, we did not use that version as we are focusing solely on the hydrocarbon chains in this work. Furthermore, a test on the DPPC/*n*-alkane systems with the 2020 ff version yielded no improvement with regards to matching the experimental *n*-alkane order parameters.

With respect to the *n*-alkane order parameters, both CHARMM36 and Slipids only produce satisfactory results for certain alkane lengths. This is shown in Figure 1C, which compares simulated ^{2}H NMR spectra (calculated from the corresponding order parameter profiles) with experimental spectra from deuterated alkanes (C10d, C20d, and C30d). The manual fitting procedure used to obtain the experimental order parameter profiles is outlined in Figure S2, Supporting Information. The measurements were conducted at the same conditions (hydration, alkane volume fraction, and temperature) as the simulations. For C10, the spectrum predicted by the CHARMM36 simulation matches the experimental spectrum nearly perfectly, while the Slipids order parameters are closer to zero, resulting in a spectrum which is much too narrow. For C20 and C30 on the other hand, the quadrupolar splittings determined from the Slipids simulations match the experimental result well, while CHARMM36 significantly overestimates these splittings.

The observed chain-length dependent performance of the two force fields can be understood by looking more closely at the *n*-alkane order parameter profiles in Figure 1C. The maxima of the order parameter in the middle of the C20 and C30 chains are notably higher in Slipids than in CHARMM36 simulations. These maxima indicate that the alkane chains have a more disordered character and therefore fold more easily when using the Slipids ff compared to CHARMM36. The higher conformational freedom is confirmed by the consistently smaller trans-gauche ratio of the *n*-alkane carbon dihedrals in Slipids simulations, as shown in Figure 2 . Similar observations have been made by Hötgen et al.,[46] who point out that gauche conformations are under-represented in the CHARMM27 ff, a predecessor of CHARMM36.

We have also performed simulations of neat alkanes to understand how the trans-gauche ratios of the alkane chains vary from bulk to the lipid bilayer and for experimental comparisons. Experimentally it has been determined previously by Mengers and D'Angelo that the $^3J_{CC}$ of neat *n*-undecane at 25 °C in various solvents was equal to 3.6±0.1 Hz which translates to a trans-gauche ratio of 3.17 using a Karplus equation.[47] On the other hand, Casal et al. show that about 3.5 gauche conformers can be expected in a tridecane molecule at 30 °C, which equals a trans-gauche ratio of ≈2.4.[48] This value is similar to the trans-gauche ratios we obtained for bulk decane in CHARMM36 simulations, at the same temperature (see Figure S3, Supporting Information), but probably underestimates the amount of gauche conformers, according to the authors. Using CHARMM27, Klauda et al. previously calculated trans-gauche ratios of ≈2.0–2.5 for

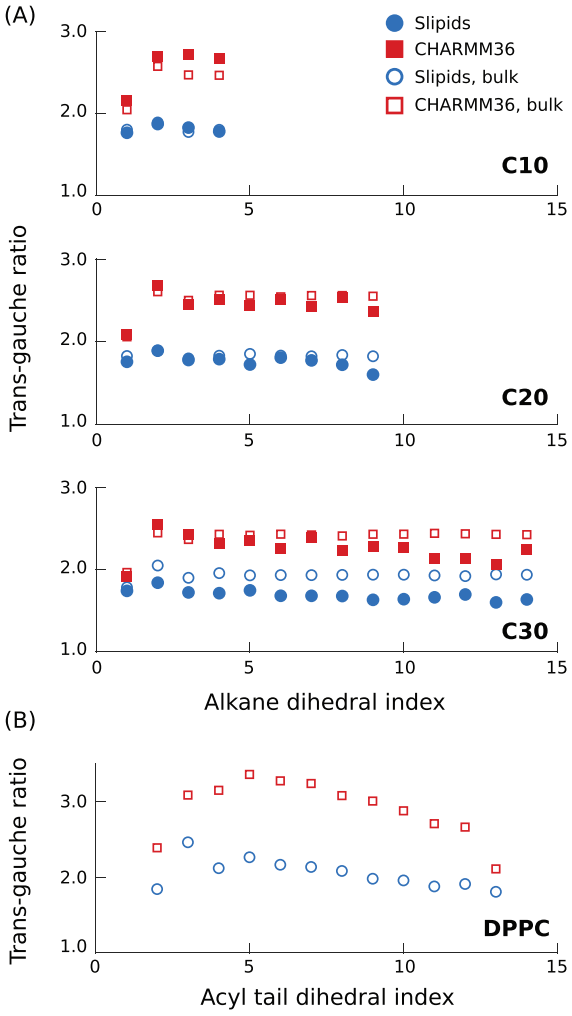

Figure 2. A) Trans-gauche ratios of the dihedrals along the alkane chains, calculated for the systems compared in Figure 1. Open symbols mark values obtained from bulk alkane simulations ($T = 50$ °C for C10, C20 and $T = 70$ °C for C30). B) Trans-gauche ratio along the DPPC acyl tails, w/o alkane ($T = 60$ °C, $n_w = 19$).

heptane,[49] while Thomas et al. observed higher amounts of trans conformers in Monte Carlo simulations of *n*-alkanes up to 12 carbons in length (trans-gauche ratios of ≈4.0).[50]

In our simulations, the trans-gauche ratio of alkane molecules calculated from bulk alkane systems is nearly the same as in the lipid bilayers, as shown in **Figure 2**. In addition, these trans-gauche are similar to those calculated for the lipid acyl tails, toward the end of the tail. This is in line with the previous observation that the phospholipid acyl tails in a lipid bilayer have a liquid like behavior very close to the behavior in bulk, as observed from experimental NMR spin-lattice relaxation rates and MD simulations.[51] We can thus conclude that the non-zero *n*-alkane order parameters of alkanes within these lipid membrane models are mainly a result of overall anisotropic orientation, rather than a combination of orientational and conformational effects.

We note that the simulations and experiments for C10, C20, and C30 were conducted at different conditions, such as a very low level of hydration for the C10 system. While the CHARMM36 ff was tested and shown to provide good results at such low water contents,[32,33,36] the Slipids ff was not yet tested in this context (to our knowledge). One could therefore suspect that the Slipids order parameters of C10 would agree better with the experiment at higher water contents. However, this is not the case, as shown in Figure S4, Supporting Information.

2.2. Reducing the Partial Charges of Alkyl Chains in CHARMM36 Enables to Reproduce the ^{2}H NMR Spectra of Long Alkanes

In this section we explore why the *n*-alkane chains behave differently in the CHARMM36 and Slipids simulations. The S_{CH} profile of saturated acyl chains is quantitatively related to the bilayer surface area as described in detail by Petrache et al.[52] An increase in surface area leads to more disordered acyl chains. Therefore, our initial hypothesis was that the reduction of *n*-alkane order parameters in Slipids simulations is a consequence of the larger area per lipid obtained for the Slipids ff in comparison to CHARMM36.[39] To test this hypothesis, we have performed NPAT simulations at fixed surface areas per phospholipid, equal to the average interfacial APL molecule, $\langle A \rangle$, determined from the simulations in the NPT for each force field. The results are shown in Figure S5, Supporting Information. By performing CHARMM36 simulations at a constant surface APL corresponding to the value determined from the Slipids simulations, $\langle A \rangle_{SL}$, a reduction of both the lipid and alkane order parameters was indeed observed. However, for the alkane, the reduced (absolute) order parameters were still notably larger than those obtained from NPT Slipids simulations. In addition, alkane ordering in Slipids simualtions was not significantly affected by the change in APL. This observation indicates that the reduced ordering of *n*-alkane molecules in the Slipids ff is a consequence of intramolecular interactions, rather than due to the different interfacial free energy minima of the bilayers.

To further investigate the main source of the differences between the two force fields, we generated hybrid force fields to describe acyl chains and alkanes by systematically replacing some of the force field parameters of Slipids by parameters from CHARMM36 and observe the effects on the alkane S_{CH} values. The results are shown as Supporting Information (Figure S6, Supporting Information) and can be summarized as follows: If the Slipids scaling factors for the 1–4 Coulombic interactions and for the 1–4 van der Waals (vdW) interactions are kept unchanged (0.8333 and 0.5, respectively), nearly no changes are observed in the S_{CH} profiles when substituting the Slipids ff parameters that describe the phospholipid acyl chains and alkanes with the parameters from CHARMM36, namely the parameters for dihedral torsions, Lennard–Jones (LJ) interactions, and partial charges. Nevertheless, in such conditions, certain trends can be detected. The substitutions of the partial charges (from zero to non-zero values in CHARMM36) and vdW parameters lead to an increase in alkane order, while the substitution of the dihedral torsion potentials has the opposite effect. If all these parameters are changed simultaneously there is no meaningful change of alkane order. In contrast, if in addition to the use of the CHARMM36 partial charges one takes the scaling factor for the 1–4 Coulombic interactions from CHARMM36 into account,

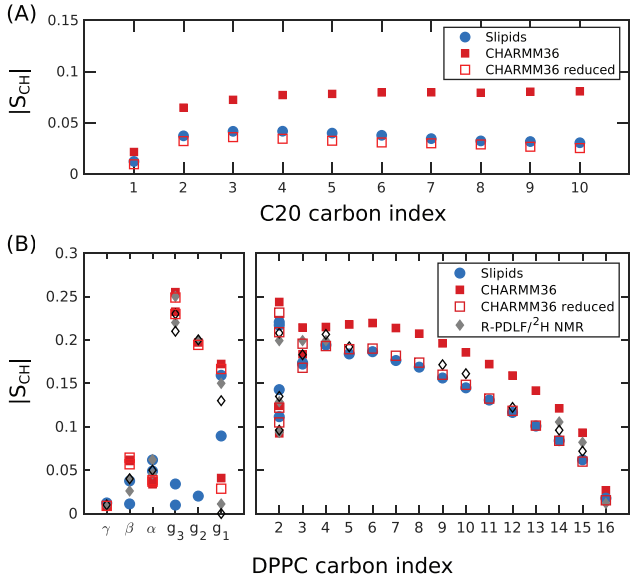

Figure 3. C–H bond order parameters A) for 10 vol% C20 in DPPC membranes and B) for pure DPPC membranes, calculated from MD simulations performed with the CHARMM36 and Slipids force fields, and by using CHARMM36 with the partial charges of acyl chains reduced by half (T = 60 °C, n_w = 18/19). The experimental order parameters were measured by R-PDLF (ref. [29], 60°C, n_w = 16) and ^{2}H NMR spectroscopy (ref. [37], 57 °C, excess hydration).

the increase of alkane order is greatly amplified, leading to S_{CH} magnitudes higher than for CHARMM36. This observation enables us to pinpoint the stronger 1–4 electrostatic interactions as the source of the higher order in CHARMM36. This result is in line with previous findings.[46] We have therefore performed CHARMM36 simulations with a reduction of partial charges for the alkanes and acyl chains. The results are shown in **Figure 3**. This reduction of partial charges results in both the long alkane and the acyl chain order parameter profiles becoming closer to the experimental ones. This suggests that by scaling the set of partial charges, it is possible to tune the force-field to yield a nearly perfect match between the simulated and the measured alkane ^{2}H NMR spectra. We refrain from doing this here.

It is not clear to us how the partial charges for acyl chains in the CHARMM36 ff were defined originally. They can be traced down as far as to the work by Feller and Mackerell in 2000,[53] but very likely they have been already defined in the first atomistic CHARMM force field in the early 1990s.[54] The Slipids force field uses partial charges averaged from DFT calculations performed on the most probable alkane structures from an iterative procedure using bulk MD simulations.[34] It is possible, as indicated by the results shown here, that a reduction of the partial charges in CHARMM36 leads to more realistic models. Such a hypothesis needs to be assessed by means of experimental observables other than the C–H bond order parameters. For instance, the validation of dynamics time-scales can be done by measuring NMR relaxation rates from these systems to enable comparisons with the MD predictions, as demonstrated previously.[32,36,55] Nevertheless, an important remark is that here the use of the alkane order parameters as target experimental observables (i.e., the fitting target) for tuning the CHARMM36 force field leads to a better match also for the DPPC acyl chain order parameters (which were not taken into account for the optimization) as can be seen in Figure 3B. The parametrizations of common lipid force fields have mostly been done by considering structural and thermodynamical observables from single component systems, or binary systems containing cholesterol.[56,57] We believe that for future ff optimizations, the use of experimental data from alkane/phospholipid mixtures should be taken as a valuable assessment tool, especially considering the chemical equivalence of alkanes to acyl chains, and the highly entropic (positional and conformational) nature of alkanes in a lipid bilayer in contrast to the rigid nature of cholesterol molecules.

2.3. The Effect of Alkane Chain Length on Alkane-Lipid Miscibility Depends on the Force Field Used

In order to investigate the effects of the alkanes on simple properties of the model lipid bilayers, and how such properties depend on chain length and interaction parameters, we conducted additional MD simulations at identical (NPT) conditions for the three n-alkanes for a range of alkane volume fractions (0–30 vol% of n-alkane each). We simulated two groups of systems, one group in a low hydration regime (n_w = 7) and a second group with a number of water molecules between bilayers closer to the excess water limit (n_w = 19). **Figure 4** shows the variation of bilayer thickness and APL on alkane volume fraction for all simulations. Every plot also shows the calculated values for the average quantity corresponding to the bilayer without alkane. From these values it is clear that by using the CHARMM36 interaction parameters, one predicts more ordered membranes (lower average area and higher thickness) than Slipids. As mentioned above, using the LJ-PME option could improve the accuracy of the APL obtained from CHARMM36 simulations. Rather than trying to use the optimal settings for CHARMM36 simulations, we here choose to use identical simulation settings for both the CHARMM36 and Slipids interaction sets, such that the differences observed between models depend only on interaction parameters. The simulation settings used for the CHARMM36 simulations were therefore the same as the settings described in **Table 1** for Slipids. No significant differences for the order parameters obtained with these settings have been found as shown in Figure S1, Supporting Information.

The bilayer thickness, here defined as the average distance between the phosphor planes of the two leaflets, increases in nearly exactly the same manner for the three n-alkanes, irrespective of the set of interaction parameters used and of the hydration state of the system. Generally, the thickness increase per added alkane becomes larger with increasing alkane content. This is in line with our previous results using the CHARMM36 ff.[29] The APL increases with alkane concentration for both hydration levels and force fields toward a maximum value that we define as ϕ_c. This observation is similar to what we found previously, and signals that the alkane molecules partition primarily into the acyl chain region below ϕ_c, while at higher concentrations the molecules accumulate more and more in the bilayer center.[29] At ϕ_c, the maximum APL is largest for C10 and smallest for C30 for both force fields. Taking the thickness dependence into account, this means that the bilayers with C10 and C30 have the lowest and

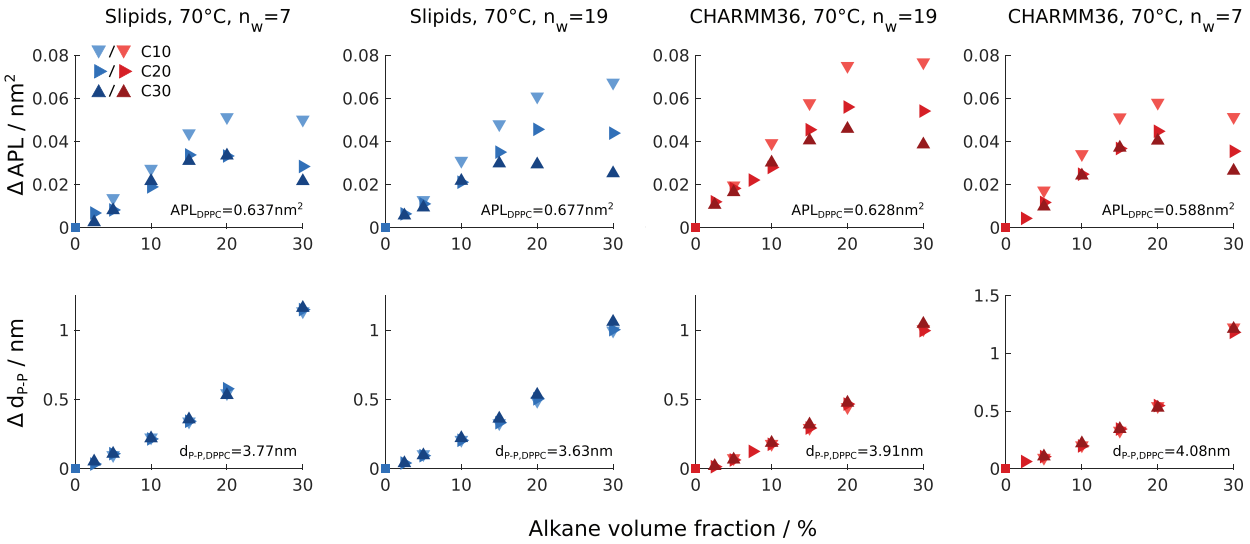

Figure 4. Variation of the simulated DPPC APL and bilayer P–P thickness relative to the value for pure DPPC, as a function of alkane concentration and for different alkane lengths. Results from using the CHARMM36 and Slipids interaction sets (using the same simulation conditions), and different levels of hydration (n_w = 7 and 19) are compared in the different columns. The temperature was set to 70 °C in all simulations. Errorbars are approximately the size of the symbols, but are not shown here for clarity.

Table 1. MD simulation settings used in this work, except for CHARMM36 simulations used to make Figure 4 and Figure S6, Supporting Information, which had the same simulation settings as for Slipids simulations..

Programs	CHARMM36	Slipids
Cutoff-scheme	Verlet	Verlet
vdw_modifier	Force-switch	None
rvdw [nm]	1.2	1.2
rvdw_switch [nm]	1.0	-
coulombtype	PME	PME
rcoulomb [nm]	1.2	1.4
tcoupl	Nose–Hoover	v-rescale
tau_t [ps]	1.0	0.1
pcoupl	Parrinello–Rahman	Parrinello–Rahman
tau_p [ps]	5.0	1.0

highest density, respectively. For simulations with CHARMM36, ϕ_c is independent of chain length and is ≈20 vol%. For simulations with Slipids, and at higher hydration, ϕ_c depends on alkane chain length with ϕ_c between 20 vol% and 30 vol% for C10, ϕ_c ≈20 vol% for C20, and to 15 vol% for C30. At lower hydration, the differences of ϕ_c for the distinct chain lengths obtained with Slipids are attenuated. Above ϕ_c, particularly for long alkanes and low water contents, the APL drops from 20 to 30 vol% of alkane.

Due to the pure hydrophobic nature of the alkanes, an increase of local area leads to more hydrophobic contacts between water molecules and the hydrophobic region. At ϕ_c, addition of decane results in the largest areas, that is, at the same volume fraction, smaller chains induce a higher increase of interfacial area. As the alkane gets longer, bulky U-shape conformations will occur that induce a higher fluctuation of the local area. Assuming a simple parabolic interfacial free energy,[20] the mixing of bulkier chains will therefore lead to a higher penalty of free energy which may disfavor such bulky conformations, leading to a lower average area for membranes with C30. The dependence of ϕ_c on chain length for the Slipids force field, in contrast to the results from CHARMM36, might also be directly related to the more disordered character of the alkane chains. The chains in Slipids have a higher propensity to fold, as shown in Figures 1 and 2, and this should lead to a stronger increase of local interfacial APL when the chain is located between acyl chains. The effect is however smaller than what is expected from experiments (ϕ_c ≈ 4–5 vol% for C30[29]). Nevertheless, such dependence of ϕ_c on alkane chain length is qualitatively predicted by the Slipids model. ϕ_c values calculated for C20 from both force fields are notably close to the apparent values from our previous experiments.[29]

ϕ_c should mainly result from the increase of interfacial free energy. If we assume the apparent experimental solubility of hydrophobic molecules in a lipid bilayer to be directly related to ϕ_c, the comparison of ϕ_c with solubility for different hydrophobic molecules becomes a highly valuable observable for validation of lipid membrane simulations. We must note here again that it is not clear to us if the experimental values for solubility that we previously measured depend on the sample preparation procedure. New experiments using a range of different sample preparation methods (e.g., different mixing temperature and organic solvents) need to be performed in this context. Several observables have been used to validate force fields for describing bulk alkanes[49,58–60] and phospholipid bilayers.[39,49,53,54,61] If the assumption that the apparent solubility observed in NMR experiments and ϕ_c are the same is indeed correct, a comparison of ϕ_c with solubility measurements would put the delicate balance of interactions that determines the surface tension described by a force field also to the test, as well as the transferability of interaction parameters from alkanes to acyl chains and vice-versa.

The description presented here concerns the behavior observed from computational models assuming an equivalent representation of the alkane chains irrespectively of their length. This seems to be a reasonable assumption for the longer *n*-alkanes such as C20 and C30, based on the C–D order parameter profiles calculated from the Slipids simulations which match well with all the experimental NMR values determined so far. Slipids however fails to describe the experimental order parameters of decane molecules which indicates that the assumption for equivalent representations of the alkane chains, starting from the shortest alkanes, may not be possible. This is in line with previous results from computational studies on bulk alkanes.[62]

3. Conclusions

In this manuscript, we compared two state-of-the-art lipid force fields with respect to their ability to describe *n*-alkanes of different lengths inside a lipid bilayer environment at different concentrations. Using ^{2}H NMR order parameters as the main validation observable, we show that the force field performance varies significantly with alkane chain length. CHARMM36 modeled only small concentrations of C10 in DPPC accurately, while Slipids reproduced the experimental order parameters of C20 and C30 well. By selectively modifying individual ff parameters, we identify the electrostatic 1–4 interactions as the main factor influencing alkyl chain ordering, at least within the parameter ranges used by the CHARMM36 and Slipids ffs. This is in line with previous observations.[46,62] In the Slipids ff, these 1–4 interactions are virtually absent since the partial charges of most carbons are zero, resulting in more flexible chains compared to CHARMM36. Because of the more disordered character of the alkyl chains in Slipids, the ^{2}H NMR data is well predicted for the longer alkanes with this force field. However, we also show that the CHARMM36 ff can be adapted to give order parameters similar to Slipids simulations, and to predict the ^{2}H NMR measurements, by reducing the partial charges of the alkanes and lipid acyl chains.

The two force fields predict a distinct dependence on alkane chain length for ϕ_c, the volume fraction at which the APL reaches a maximum with alkane incorporation. ϕ_c should be a consequence of the interfacial free energy and therefore of the delicate balance between the interactions modeled, and defines the solubility of alkanes in the acyl chain region. We believe that the combination of a large set of lipid membrane simulations, with a variety of alkane/phospholipid mixtures, with the measurement of experimental observables on the corresponding systems (alkane and phospholipid order parameters, X-ray scattering form factors, solubility measurements) would be an invaluable toolkit for force field optimization. The results shown here, particularly for the long alkanes are very encouraging.

The results and discussion presented here should be of general interest for the optimization of MD simulations of lipid membranes, and in particular for future investigations of hydrophobic macromolecules inside lipid bilayers, as well as for the re-emerging interest on the behavior of triglycerides inside lipid membranes in connection to lipid droplet formation in cellular membranes.

4. Experimental Section

Simulation Setup: Atomistic molecular dynamics simulations were performed using the GROMACS software[40] (version 2018.7). The investigated systems consisted of DPPC bilayers containing either C10, C20, or C30. The compositions used in this work are described in detail below and in Table S1, Supporting Information. Most DPPC/C10 and DPPC/C20 topologies were reused from a previous publication.[29] For the remaining systems the setup proceeded accordingly: the initial DPPC topology was downloaded from open access data made available by the NMRlipids project (nmrlipids.blogspot.fi)[63] and equilibrated. Alkane topologies were designed using Molden,[64] equilibrated in bulk, and the necessary number of alkane molecules was placed between the two bilayer leaflets. Then the mixtures were hydrated to the desired amount of water and re-equilibrated at the desired temperature. Several systems were expanded to a total of 288 lipids in order to improve the statistics for the analysis of alkane trajectories (for low alkane volume fractions), and to exclude interactions between different images of the same molecule[58] (for C30). For CHARMM36[32,65] simulations, the DPPC force field was also taken from the open data by Miettinen and Ollila.[63] Water molecules were described by the CHARMM TIP3P model.[66,67] For Slipids simulations, the DPPC parameters published as Supporting Information in the original Slipids publication were used.[34] In all simulations, alkane molecules were described by exactly the same force field parameters as the lipid acyl chains.

All simulations consisted of up to three runs (100 ns each), using a leap-frog integrator and 2 ps time steps. Most simulations were conducted in isothermic–isobaric (NPT) ensembles, except for two cases were the *x* and *y* box lengths were fixed (NPAT ensemble). Particle mesh Ewald was used for long-range electrostatics, and a fourth order LINCS correction for proton bond constraints. The detailed settings chosen for CHARMM36 and Slipids simulations are listed in Table 1. Details on the different algorithms used can be found in ref. [68] and references therein. CHARMM36 settings were based on the output of the CHARMM-GUI membrane builder.[41,42,69] The main simulation results are made available open source in the zenodo repository. These systems are summarized in Table S1, Supporting Information and can be accessed using the following DOI: https://doi.org/10.5281/zenodo.7572990. Additional systems discussed in the article include: 1) Pure, liquid *n*-alkanes C10, C20, and C30 (200 molecules per box), simulated at 298 K (C10), 323 K (C10 and C20), and 343 K (C30). Here, for both CHARMM36 and Slipids, the modified Berendsen thermostat ("v-rescale") with a time constant τ_t=0.1 ps, and the Parrinello–Rahman barostat with a time constant τ_p=1.0 ps were used. 2) 10 vol% C20 in an NPAT ensemble, at two different areas-per-phospholipid (0.642 and 0.682 nm^2, T = 60 °C, n_w = 18), simulated using both CHARMM36 and Slipids. 3) 10 vol% C20 and pure DPPC at T = 60 °C, n_w = 18, using CHARMM36 with the acyl chain charges of both alkane and lipid reduced by half. 4) A range of *n*-alkane simulations using identical conditions for CHARMM36 and Slipids (i.e., using the Slipids settings in Table 1 for CHARMM36 also). The investigated alkane concentrations were 0–30 vol% for C10, C20, and C30, at T = 70 °C and n_w = 7/19. This data is not included in the zenodo repository but can be made available upon request.

Analysis of MD Simulations: The first 100 ns of each simulation were excluded from the analysis, and only 10 ps time steps were considered. The simulated trajectories were processed using Python's MDTraj library.[70]

C–H bond order parameters S_{CH} were calculated according to

$$S_{CH} = \frac{1}{2}\langle 3\cos^2\theta - 1\rangle \quad (1)$$

where θ is the angle between the bilayer normal and the C–H bond vector, and angular brackets denote an average over simulation time and molecules. After calculating the order parameters for every carbon position along the *n*-alkanes, the corresponding ^{2}H NMR signals were calculated by summation of the individual signal contributions of the carbons (accounting for powder averaging and T_2 relaxation), and finally the ^{2}H NMR spectra were obtained by Fourier transform of the calculated NMR

signal. Trans-gauche ratios of the carbon dihedrals of the *n*-alkanes were calculated by determining the dihedral angles ϕ (values in [0,180]) and assigning $59° \leqslant \phi \leqslant 61°$ to the $g+$ and $g-$ configurations, and $179° \leqslant \phi$ to the *t* configuration. Trans-gauche ratios of equivalent dihedrals (both ends of the alkane molecules) were averaged. APL was defined as the time-averaged area of the simulation box divided by the number of lipids per leaflet, and the P–P bilayer thickness was calculated from the time- and ensemble-averaged distance between the two phosphor planes. The standard error of the mean of these time-averaged quantities was estimated via the block-averaging method.[71]

Experimental Data: The experimental data from ^{2}H and ^{1}H-^{13}C NMR measurements presented for comparison and assessment of the quality of the MD simulations was reused from a previous publication by our group.[29] Details on sample preparation and experimental setup can be found therein.

Supporting Information

Supporting Information is available from the Wiley Online Library or from the author.

Acknowledgements

This research study was funded by the German Research Foundation (Deutsche Forschungsgemeinschaft, DFG, project number 189853844, TRR 102). The authors acknowledge Wolfgang Paul, Jörg Kressler, and Markus Miettinen for useful discussions.

Open access funding enabled and organized by Projekt DEAL.

Conflict of Interest

The authors declare no conflict of interest.

Data Availability Statement

The data that support the findings of this study are available in the supplementary material of this article.

Keywords

alkanes, CHARMM36, lipid membranes, molecular dynamic simulations, Slipids

Received: December 8, 2022
Revised: January 31, 2023
Published online:

[1] D. A. Haydon, B. M. Hendry, S. R. Levinson, J. Requena, *Biochim. Biophys. Acta Biomembr.* **1977**, *470*, 17.
[2] R. S. Cantor, *Biophys. J.* **2001**, *80*, 2284.
[3] N. Kučerka, P. Hrubočák, E. Dushanov, T. Kondela, K. Kholmurodov, J. Gallová, P. Balgavý, *J. Mol. Liq.* **2019**, *276*, 624.
[4] S. Kim, J. M. Swanson, *Biophys. J.* **2020**, *119*, 1958.
[5] V. Zoni, R. Khaddaj, P. Campomanes, A. Thiam, R. Schneiter, S. Vanni, *eLife* **2021**, *10*, e62886.
[6] F. Hegaard, M. Klenow, A. Simonsen, *Langmuir* **2022**, *38*, 9247.
[7] D. Bochicchio, E. Panizon, L. Monticelli, G. Rossi, *Sci. Rep.* **2017**, *7*, 6357.
[8] Y. Guo, M. Werner, W. Li, J.-U. Sommer, V. A. Baulin, *Macromolecules* **2019**, *52*, 9578.
[9] D. Bochicchio, L. Cantu, M. Cadario, L. Palchetti, F. Natali, L. Monticelli, G. Rossi, E. Del Favero, *J. Colloid Interface Sci.* **2022**, *605*, 110.
[10] V. Yeh, A. Goode, D. Johnson, N. Cowieson, B. Bonev, *Langmuir* **2022**, *38*, 1348.
[11] J. M. Pope, L. A. Littlemore, P. W. Westerman, *Biochim. Biophys. Acta Biomembr.* **1989**, *980*, 69.
[12] J. Hamilton, *Biochemistry* **1989**, *28*, 2514.
[13] H. Khandelia, L. Duelund, K. Pakkanen, J. Ipsen, *PLoS One* **2010**, *5*, e12811.
[14] J. Patton, B. Stone, C. Papa, R. Abramowitz, S. Yalkowsky, *J. Lipid Res.* **1984**, *25*, 189.
[15] M. Haulait-Pirson, G. Huys, E. Vanstraelen, *Ind. Eng. Chem. Res.* **1987**, *26*, 447.
[16] K. Roberts, R. Rousseau, A. Teja, *J. Chem. Eng. Data* **1994**, *39*, 793.
[17] T. Holleman, *Physica* **1965**, *31*, 49.
[18] J. Friend, J. Larkin, A. Maroudas, M. McGlashan, *Nature* **1963**, *198*, 683.
[19] R. Orwoll, P. Flory, *J. Am. Chem Soc.* **1967**, *89*, 6822.
[20] J. Israelachvili, *Intermolecular and Surface Forces*, Academic Press, London **1991**.
[21] D. Evans, W. Wennerström, *The Colloidal Domain. Where Physics, Chemistry, Biology and Technology Meet*, Wiley-VCH, Hoboken, NJ **1999**.
[22] J. H. Davis, *Biochim. Biophys. Acta. Biomembr.* **1983**, *737*, 117.
[23] P. Flory, *Macromolecules* **1978**, *11*, 1138.
[24] B. Kronberg, I. Bassignana, D. Patterson, *J. Phys. Chem.* **1978**, *82*, 1714.
[25] H. Orendi, M. Ballauff, *Liq. Cryst.* **1989**, *6*, 497.
[26] J. Goodman, *J. Chem. Inf. Comput. Sci.* **1997**, *37*, 876.
[27] J. M. Pope, L. W. Walker, D. Dubro, *Chem. Phys. Lipids* **1984**, *35*, 259.
[28] J. M. Pope, D. W. Dubro, *Biochim. Biophys. Acta Biomembr.* **1986**, *858*, 243.
[29] A. Wurl, M. Ott, E. Plato, A. Meister, F. Hamdi, P. Kastritis, A. Blume, T. Ferreira, *Langmuir* **2022**, *38*, 8595.
[30] A. Bangham, M. Standish, J. Watkins, *J. Mol. Biol.* **1965**, *13*, 238.
[31] M. Okazaki, I. Hara, T. Fujiyama, *Chem. Phys. Lipids* **1976**, *17*, 28.
[32] J. B. Klauda, R. M. Venable, J. A. Freites, J. W. O'Connor, D. J. Tobias, C. Mondragon-Ramirez, I. Vorobyov, A. D. MacKerell, R. W. Pastor, *J. Phys. Chem. B* **2010**, *114*, 7830.
[33] A. Botan, F. Favela-Rosales, P. Fuchs, M. Javanainen, M. Kanduč, W. Kulig, A. Lamberg, C. Loison, A. Lyubartsev, M. Miettinen, L. Monticelli, J. Määttä, O. Ollila, M. Retegan, T. Rág, H. Santuz, J. Tynkkynen, *J. Phys. Chem. B* **2015**, *119*, 15075.
[34] J. Jämbeck, A. Lyubartsev, *J. Phys. Chem. B* **2012**, *116*, 3164.
[35] F. Grote, A. Lyubartsev, *J. Phys. Chem. B* **2020**, *124*, 8784.
[36] H. S. Antila, T. M. Ferreira, O. H. S. Ollila, M. S. Miettinen, *J. Chem. Inf. Model.* **2021**, *61*, 938.
[37] A. Seelig, J. Seelig, *Biochemistry* **1974**, *13*, 4839.
[38] J. Seelig, W. Niederberger, *J Am. Chem. Soc.* **1974**, *96*, 2069.
[39] K. Pluhackova, S. Kirsch, J. Han, L. Sun, Z. Jiang, T. Unruh, R. Böckmann, *J. Phys. Chem. B* **2016**, *120*, 3888.
[40] M. J. Abraham, T. Murtola, R. Schulz, S. Páll, J. C. Smith, B. Hess, E. Lindahl, *SoftwareX* **2015**, *1–2*, 19.
[41] B. R. Brooks, C. L. Brooks III, A. D. Mackerell Jr, L. Nilsson, R. J. Petrella, B. Roux, Y. Won, G. Archontis, C. Bartels, S. Boresch, A. Caflisch, L. Caves, Q. Cui, A. R. Dinner, M. Feig, S. Fischer, J. Gao, M. Hodoscek, W. Im, K. Kuczera, T. Lazaridis, J. Ma, V. Ovchinnikov, E. Paci, R. W. Pastor, C. B. Post, J. Z. Pu, M. Schaefer, B. Tidor, R. M. Venable, et al., *J. Comput. Chem.* **2009**, *30*, 1545.
[42] J. Lee, X. Cheng, J. M. Swails, M. S. Yeom, P. K. Eastman, J. A. Lemkul, S. Wei, J. Buckner, J. C. Jeong, Y. Qi, S. Jo, V. S. Pande, D. A. Case, C.

L. I. Brooks, A. D. J. MacKerell, J. B. Klauda, W. Im, *J. Chem. Theory Comput.* **2016**, *12*, 405.
[43] Y. Yu, A. Krömer, R. M. Venable, A. C. Simmonett, A. D. J. MacKerell, J. B. Klauda, R. W. Pastor, B. R. Brooks, *J. Chem. Theory Comput.* **2021**, *17*, 1562.
[44] Y. Yu, A. Krämer, R. M. Venable, B. R. Brooks, J. B. Klauda, R. W. Pastor, *J. Chem. Theory Comput.* **2021**, *17*, 1581.
[45] A. N. Leonard, A. C. Simmonett, F. C. I. Pickard, J. Huang, R. M. Venable, J. B. Klauda, B. R. Brooks, R. W. Pastor, *J. Chem. Theory Comput.* **2018**, *14*, 948.
[46] C. Högberg, A. Nikitin, A. Lyubartsev, *J. Comput. Chem.* **2008**, *29*, 2359.
[47] M. Karplus, *J. Chem. Phys.* **1959**, *30*, 11.
[48] H. Casal, R. McElhaney, *Biochemistry* **1990**, *29*, 5423.
[49] J. Klauda, B. Brooks, A. MacKerell, R. Venable, R. Pastor, *J. Phys. Chem. B* **2005**, *109*, 5300.
[50] L. Thomas, T. Christakis, W. Jorgensen, *J. Phys. Chem. B* **2006**, *110*, 21198.
[51] R. Venable, Y. Zhang, B. Hardy, R. Pastor, *Science* **1993**, *262*, 223.
[52] H. Petrache, S. Dodd, M. Brown, *Biophys. J.* **2000**, *79*, 3172.
[53] S. Feller, A. MacKerell, *J. Phys. Chem. B* **2000**, *104*, 7510.
[54] R. Pastor, A. MacKerell, *J. Phys. Chem. Lett.* **2011**, *2*, 1526.
[55] H. Antila, A. Wurl, O. Ollila, M. Miettinen, T. Ferreira, *Biophys. J.* **2022**, *121*, 68.
[56] A. Lyubartsev, A. Rabinovich, *Biochim. Biophys. Acta Biomembr.* **2016**, *1858*, 2483.
[57] A. Leonard, E. Wang, V. Monje-Galvan, J. Klauda, *Chem. Rev.* **2019**, *119*, 6227.
[58] J.-P. Ryckaert, A. Bellemans, *Faraday Discuss. Chem. Soc.* **1978**, *66*, 95.
[59] S. Burrows, I. Korotkin, S. Smoukov, E. Boek, S. Karabasov, *J. Phys. Chem. B* **2021**, *125*, 5145.
[60] M. Ghahremanpour, J. Tirado-Rives, W. Jorgensen, *J. Phys. Chem. B* **2022**, *126*, 5896.
[61] R. Sankararamakrishnan, H. Weinstein, *J. Phys. Chem. B* **2004**, *108*, 11802.
[62] X. Ye, S. Cui, V. de Almeida, B. Khomani, *J. Mol. Model.* **2013**, *19*, 1251.
[63] O. H. S. Ollila, M. Miettinen, MD simulation trajectory and related files for DPPC bilayer (CHARMM36, Gromacs 4.5), **2015**, https://doi.org/10.5281/zenodo.15549 (accessed: July 2019).
[64] G. Schaftenaar, E. Vlieg, G. Vriend, *J. Comput, Aided Mol. Des.* **2017**, *31*, 789.
[65] R. M. Venable, Y. Luo, K. Gawrisch, B. Roux, R. W. Pastor, *J. Phys. Chem. B* **2013**, *117*, 10183.
[66] S. . Durell, B. R. Brooks, A. Ben-Naim, *J. Phys. Chem.* **1994**, *98*, 2198.
[67] W. Jorgensen, J. Chandrasekhar, J. Madura, R. Impey, M. Klein, *J. Chem. Phys.* **1983**, *79*, 926.
[68] M. J. Abraham, D. van der Spoel, E. Lindahl, B. Hess, the GROMACS development team, "Gromacs user manual version 2019", https://manual.gromacs.org/documentation/2019/reference-manual/index.html (accessed: February 2023).
[69] S. Jo, T. Kim, V. G. Iyer, W. Im, *J. Comput. Chem.* **2008**, *29*, 1859.
[70] R. T. McGibbon, K. Beauchamp, M. Harrigan, C. Klein, J. Swails, C. Hernández, C. Schwantes, L.-P. Wang, T. Lane, V. Pande, *Biophys. J.* **2015**, *109*, 1528.
[71] H. Flyvbjerg, H. Petersen, *J. Chem. Phys.* **1989**, *91*, 461.

5.2.1 Paper II: Supporting Information

Additional tables and figures referred to in paper II, as published in reference [38]. No changes were made.

n-alkane	Number of alkane molecules	Number of DPPC molecules	Alkane volume fraction	Alkane mole fraction	Number of water molecules	n_w	T [K]	ff	simulated time [ns]
	0	72	0%	0%	2160	30	323.15	C36	100
	0	72	0%	0%	1329	18.5	333	C36	300
	0	72	0%	0%	1329	18.5	333	Slipids	300
C10	26	72	10%	27%	504	7	333	C36	300
C10	26	72	10%	27%	504	7	333	Slipids	300
C10	77	72	25%	52%	1362	19	333	C36	300
C10	77	72	25%	52%	1362	19	333	Slipids	300
C20	12	72	10%	14%	1153	16	333	C36	300
C20	12	72	10%	14%	1153	16	333	Slipids	300
C20	12	72	10%	14%	1291	18	333	C36	200
C20	12	72	10%	14%	1291	18	333	Slipids	300
C30	16	288	5%	5%	4321	15	343	C36	300
C30	16	288	5%	5%	4321	15	343	Slipids	300

Table S1: Overview of the simulated systems. Alkane volume fraction is defined as the alkane-to-lipid acyl tail ratio, while the alkane mole fraction refers to the ratio of alkane to non-water (alkane plus lipid) molecules.

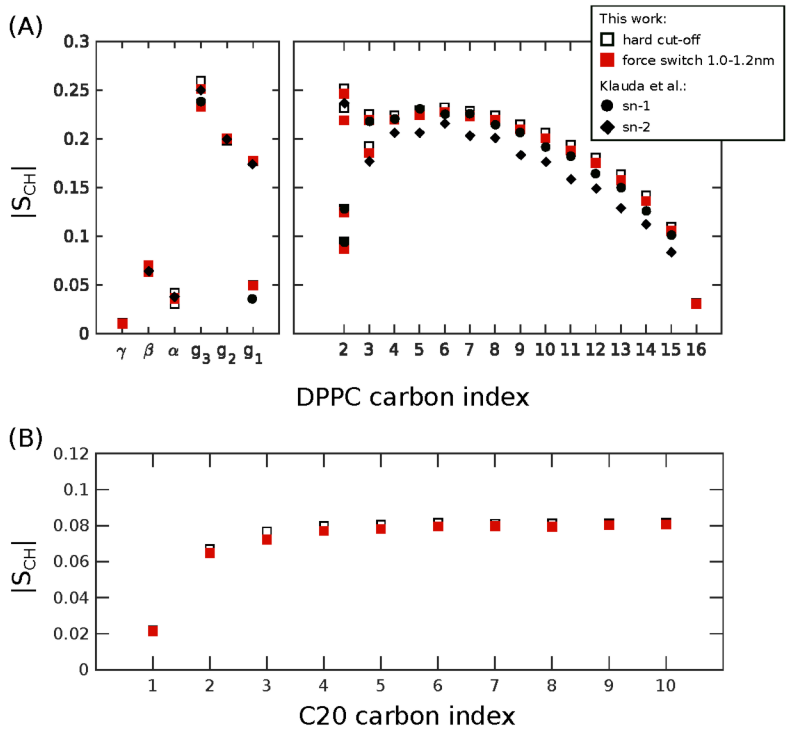

Figure S1: DPPC and *n*-eicosane order parameters obtained with different cut-off settings for the Lennard-Jones potential: hard cut-off at 1.2 nm (open squares) and using a force switch between 1.0 and 1.2 nm (filled red squares). (A) Pure DPPC at T=50°C, n_w=30, compared to results by Klauda et al. [287], at identical conditions. Note that the order parameters in this work are the average of the *sn*-1 and *sn*-2 chains. The area-per-phospholipid in our simulations was calculated to 60.8±0.3 nm^2, while Klauda et al. achieve 62.9±0.3 nm^2. Using a force switch range of 0.8-1.2 nm did not improve the agreement, so we refrained from including these datapoints in the plot. (B) 10 vol% C20 in DPPC, T=60°C, n_w=19.

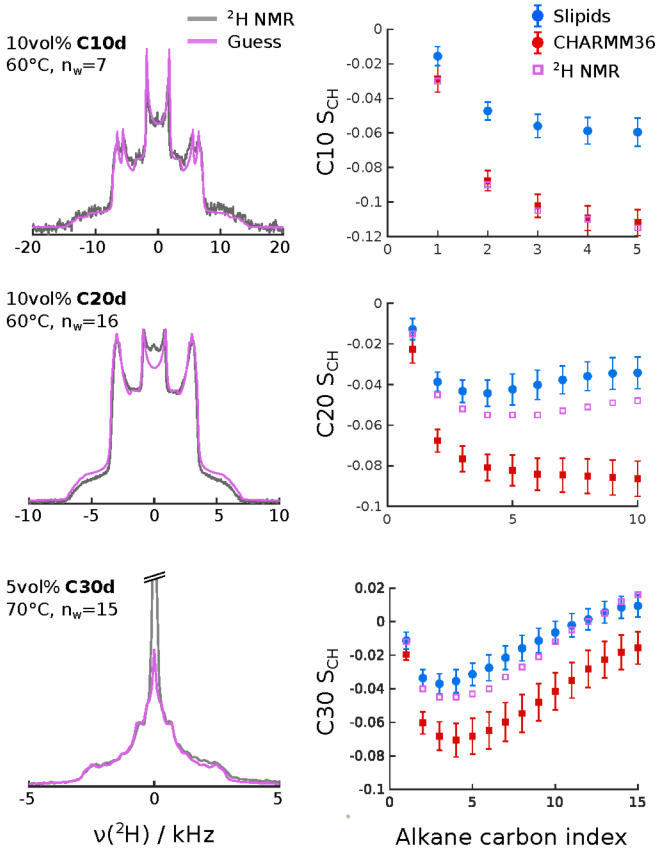

Figure S2: Estimation of $|S_{CH}|$ profiles from the experimental ^{2}H NMR spectra measured previously [37]. The ^{2}H NMR spectra (grey, left column) were manually fitted by guessing the C-H bond order parameter profile of the alkane chains (pink, right column) and summing-up the individual signal contributions (including a powder average and a relaxation time of T_2=2 ms.). The assignment of the individual order parameters to the carbon indices was based on the shape of the profiles obtained from the MD simulations. The agreement between the manual fit and the experimental ^{2}H spectra was very sensitive to slight changes in order parameter magnitude (of the order of 0.002), thus the fitted profile should be reasonably correct.

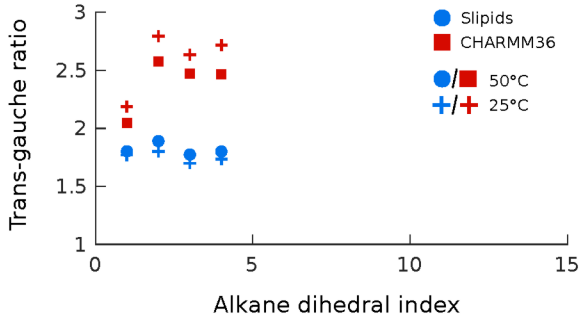

Figure S3: Trans-gauche ratios determined from *n*-decane molecules simulated as a neat liquid at two different temperatures, using CHARMM36 (red) and Slipids (blue).

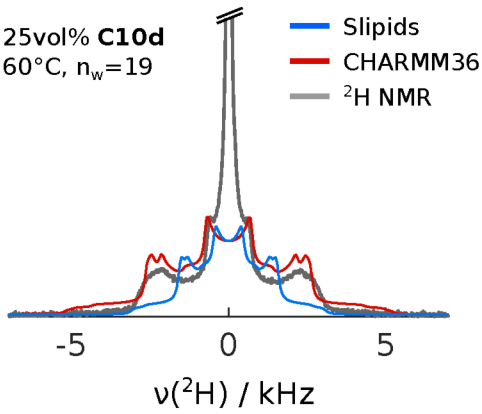

Figure S4: Comparison of experimental [37] and simulated ^{2}H NMR spectra of 25 vol% C10d in DPPC at a higher hydration level (experiment: excess water, simulation: n_w=19). The center peak in the experimental spectrum is most likely due to vesicles that are small enough for isotropic averaging of the ^{2}H quadrupolar couplings.

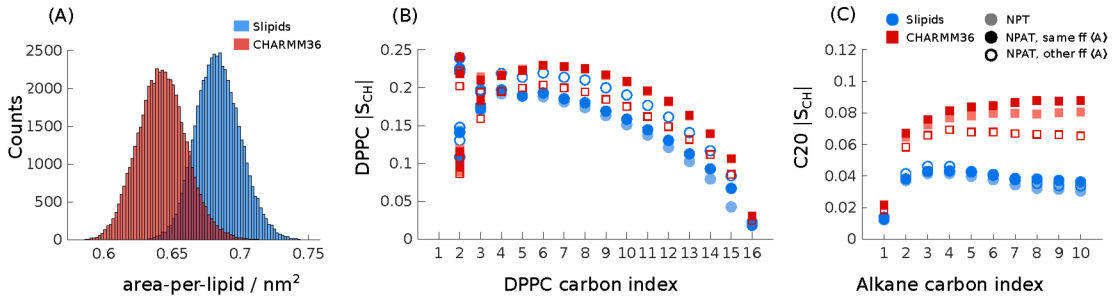

Figure S5: Effect of using a constant area-per-lipid in CHARMM36 and Slipids simulations of 10 vol% C20 in DPPC. (A) Distribution of area-per-lipid values in the "standard" *NPT* simulations. (B) DPPC $|S_{CH}|$ profiles from CHARMM36 or Slipids simulations calculated from the *NPT* simulation ("variable area"), and from *NPAT* simulations at two different areas: area-per-phospholipid $\langle A \rangle_{SL}$ =0.682 nm^2 and $\langle A \rangle_{C36}$ =0.642 nm^2, roughly equal to the maxima of the distributions shown in (A). Open symbols represent results obtained from using the *other forcefield's* area-per-lipid. (C) The same as (B), but for *n*-eicosane order parameters.

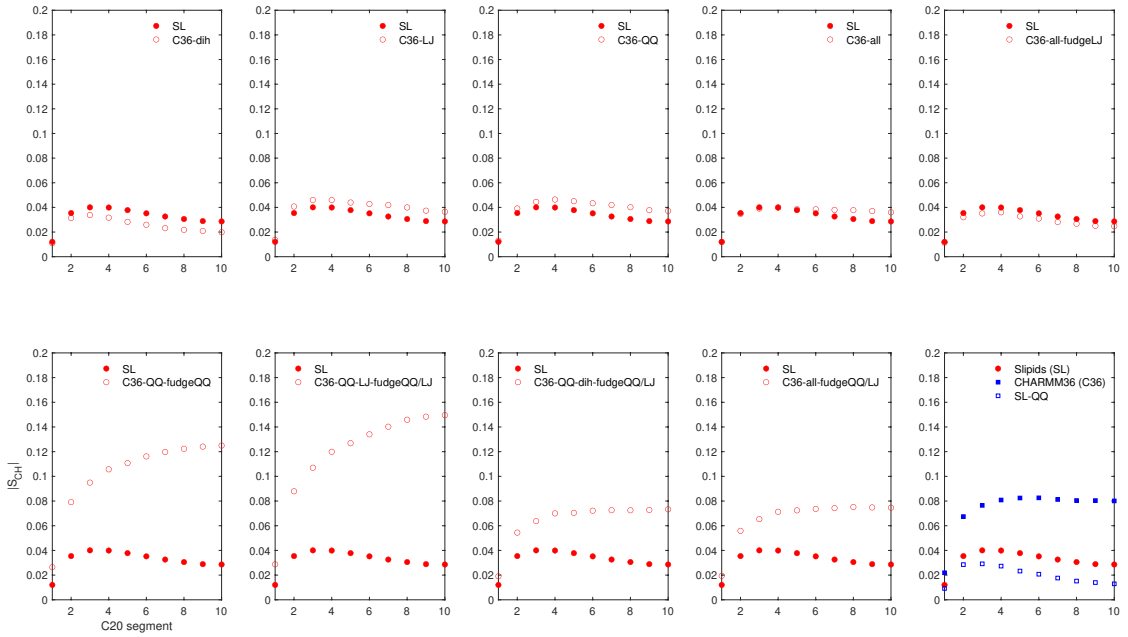

Figure S6: The variation of the C20 $|S_{CH}|$ profile induced by modifications of ff parameters in Slipids and CHARMM36 simulations of DPPC/C20 bilayers. The filled circles and squares denote simulations performed with the original Slipids and CHARMM36 ffs, respectively.
Modifications to Slipids (open circles): **C36-dih** - denotes that all the acyl chain dihedral torsion potentials were replaced by the CHARMM36 potentials; **C36-LJ** - denotes that all the non-bonded Lennard Jones interaction parameters of atoms in the acyl chains were replaced by CHARMM36 parameters; **C36-QQ** - denotes that all the partial charges in the acyl chains were replaced by the values used in CHARMM36; **C36-all** - all the dih, LJ and QQ modifications previously described were done; **C36-all-fudgeLJ** - the same as C36-all but not using the Slipids scale factor for the 1-4 vdW interactions; **C36-QQ-fudgeQQ** - the same as C36-QQ but not using the Slipids scale factor for the 1-4 electrostatic interactions; **C36-QQ-LJ-fudgeQQ/LJ** - combining C36-QQ-fudgeQQ with C36-LJ using no scalling factor for the 1-4 vdW interactions; **C36-QQ-dih-fudgeQQ/LJ** - combining C36-QQ-fudgeQQ with C36-dih using no scalling factor for the 1-4 vdW interactions; **C36-all-fudgeQQ/LJ** - the same as C36-all but not using scaling factors for 1-4 interactions.
Modifications to CHARMM36 (open square) - CHARMM36 with replacing all the partial charges in the acyl chains by the ones in Slipids. Note that the CHARMM36 simulations performed for this plot were done using the same settings as for Slipids, similarly to the simulations used in Figure 4 of the main text.

5.3 Paper III: Crystallization of *n*-alkanes under anisotropic nanoconfinement in lipid bilayers[3]

In papers I [37] and II [38] it was shown that C20 and C30 can indeed be incorporated into phospholipid bilayers, up to a certain amount. However, *n*-alkane/lipid mixtures had only been studied at temperatures above the melting temperatures of the respective *n*-alkanes and lipids. Since these temperatures are generally higher than room- or body temperature, it is of interest to examine the behaviour of these systems at lower temperatures. Consequently, the question arises whether *n*-alkanes will crystallize inside the lipid membranes once the experimental temperature is lowered below the crystallization temperature. Other possible scenarios include the inhibition of crystallization, or the expulsion of *n*-alkanes from the lipid bilayers.

The following paper answers this question for the *n*-alkanes C20 and C30 by means of ^{2}H and ^{1}H NMR spectroscopy, differential scanning calorimetry, and X-ray scattering. Saturated (DMPC and DPPC) and unsaturated (DOPC and POPC) lipid membranes are studied. We show for the first time that hydrophobic chains such as C20 and C30 can indeed crystallize inside lipid membranes, under certain conditions. C30 crystallizes in DMPC and POPC bilayers, while C20 only crystallizes in an unsaturead lipid bilayer with lower phase-transition temperature. In DMPC on the other hand, C20 molecules become trapped in the lipid gel-phase upon cooling and do not crystallize. Further investigation of C30 in DMPC showed that when 5 vol% of C30 are added to the membrane, about 64-72% of *n*-alkane molecules crystallize inside the membrane. The mixed chains exhibit slightly reduced phase transition temperatures. In the membrane, the formation of the rotator phase upon crystallization occurs via a two-step process: Pre-organized *n*-alkane chains assemble in rotator-phase crystallites just as fast as bulk C30, but further addition of molecules to the rotator-phase crystal is slowed significantly. An intermediate crystal form is shown to persist in the membrane for longer times, compared to bulk C30.

The author contributions to this article are as follows: AW and TMF designed and managed the project. AW prepared the samples and performed and analyzed the NMR measurements. MO and AW performed and analyzed the X-ray scattering experiments. AW performed and analyzed the DSC experiments with guidance from CS. All authors interpreted and discussed the results. AW and in part TMF wrote the manuscript, with input from MO and CS.

[3]This article [Anika Wurl, Maria Ott, Christian Schwieger and Tiago M. Ferreira, DOI: 10.26434/chemrxiv-2023-ljjt7 (2023)] [39] is a preprint article published on ChemRxiv under the terms of the Creative Commons Attribution 4.0 License, which permits use and distribution in any medium, provided the original work is properly cited. The article can be accessed on the preprint server using the following link: https://doi.org/10.26434/chemrxiv-2023-ljjt7 . No changes were made.

Crystallization of *n*-alkanes under anisotropic nano-confinement in lipid bilayers

Anika Wurl,[1,*] Maria Ott,[2] Christian Schwieger,[3] and Tiago M. Ferreira[1,†]

[1]*NMR group - Institute for Physics, Martin Luther University Halle-Wittenberg*
[2]*Department of Biotechnology and Biochemistry, Martin Luther University Halle-Wittenberg*
[3]*Institute of Chemistry, Martin Luther University Halle-Wittenberg*

(Dated: December 19, 2023)

Understanding crystallization behaviour is integral to the design of pharmaceutical compounds for which the pharmacological properties depend on the crystal forms achieved. Very often, these crystals are based on hydrophobic molecules. One method for delivering crystal-forming hydrophobic drugs is by means of lipid nanoparticle carriers. However, so far, a characterization of the potential crystallization of fully hydrophobic molecules in a lipid environment has never been reported. In this work we investigate the crystallization behaviour of two model hydrophobic chains, *n*-eicosane (C20) and *n*-triacontane (C30), in phospholipid bilayers. We combine static ^{2}H nuclear magnetic resonance (NMR) spectroscopy and differential scanning calorimetry (DSC) and show that C30 can indeed crystallize inside DMPC and POPC bilayers. The phase transition temperatures of C30 are slightly reduced inside DMPC, and rotator phase formation becomes a two-step process: Pre-organized *n*-alkane chains assemble in rotator-phase crystallites just as fast as bulk C30, but further addition of molecules is notably slower. Under the same isothermal conditions, different crystal forms can be obtained by crystallization in the membrane and in bulk. In excess water conditions, homogeneous nucleation of C30 is observed. The initial anisotropic molecular arrangement of C30 molecules in the membrane is readily recovered upon reheating, showing reversibility. The shorter C20 molecules on the other hand become trapped in the DMPC membrane gel-phase upon cooling and do not crystallize. This work marks the first observation of the crystallization of hydrophobic chains inside a lipid bilayer environment. As such, it defines a fundamental starting point for studying the crystallization characteristics of various hydrophobic molecules in lipid membranes.

INTRODUCTION

From a biophysical perspective, the interactions between hydrophobic molecules and cell membranes are integral to a variety of open questions, such as lipid droplet formation [1–3], the effect of micro- and nanoplastic pollution on living cells [4, 5] or nanoparticle design for drug delivery [6–9]. Various drugs show crystal polymorphism and the crystal properties are often related to stability and performance [10]. Moreover, such drugs can potentially crystallize inside their carrier nanoparticles [10–12] or in a biological environment [13]. It is therefore essential to understand the crystallization behaviour in detail, such that one may control it. However, we still lack understanding of allegedly simple scenarios. For example, to our knowledge, the potential crystallization of purely hydrophobic, chain-like molecules inside a lipid membrane has never been reported.

The nano-confinement realized by lipid bilayers presents a unique system that is of fundamental interest for crystallization studies, since the lipid membrane resembles an anisotropic solution featuring a gradient of molecular order. This type of confinement is substantially different from the confinement in emulsion droplets, nanoparticles or porous materials. The interaction of purely hydrophobic molecules with lipid membranes has been addressed in a number of simulation studies, many of which were inspired by the increasing accumulation of nanoplastics in the environment [14–19]. However, there is a lack of experimental studies related to this topic, partly due to the fact that such systems are challenging to prepare experimentally. In contrast to the partial insertion of amphiphilic or polyphilic molecules, the addition of purely hydrophobic polymers often leads to pore formation in the membrane, or phase separation of the components [20]. The first experimental studies date back to the 1980s with the work of Pope and coworkers on the inclusion of *n*-alkanes in lipid membranes. These studies suggested that *n*-alkanes with chain lengths higher than 18 carbons are nearly immiscible with the lipid acyl tails. Later, squalane has been found to incorporate in the bilayer center of DOPC/DOPG membranes [21] and Bochicchio et al. demonstrated the effect of polystyrene 25-mers on DPPC membrane dynamics, thermal and mechanical properties using calorimetry, X-ray and neutron scattering [5]. Very recently, we showed with ^{2}H NMR that about 3-5vol% of *n*-triacontane (C30) can be incorporated into dipalmitoylphosphatidylcholine (DPPC) or dimirystoylphosphatidylcholine (DMPC) membranes [22]. This system is a perfect starting point for investigating the crystallization of hydrophobic, chain-like molecules inside lipid membranes.

The crystallization behaviour of bulk *n*-alkane itself is notable due to the existence of the so-called rotator phases, which may be formed prior to the crystalline phase upon cooling [23, 24]. These rotator phases are defined by a rotational freedom along the long axis of the molecules, while the positional long range order is retained along all dimensions. Consequently, the rotator phases are similar to the lipid gel phases that are formed between the liquid-crystalline and crystalline phases in lipid bilayers [25]. The occurence, stability and nature of the rotator phases strongly depends on the length of the *n*-alkanes, as has been reviewed in detail by a number of authors [23, 24, 26]. *n*-Alkanes with stable rotator phases crystallize via rotator phase nuclei, before transforming into the

low-temperature crystal form [27, 28]. C30 in particular exhibits two stable rotator phases, namely RIII and RIV, which are characterized by different chain tilt directions and triclinic and monoclinic lattices, respectively [24, 29, 30].

The crystallization of *n*-alkanes has been investigated in a number of confinement geometries [24, 31, 32]. The confinement in nanopores or microcapsules results in a stabilization of rotator phases in general, and transient or metastable rotator phases in particular [31, 33–36]. The same studies showed that *n*-alkane phase transition temperatures are reduced inside nanopores. In *n*-alkane mixtures, both alkanes only co-crystallize if one alkane is no more than 22% longer than the other [37]. If one *n*-alkane is much shorter and acts as a solvent for the other, the crystallization temperature of the longer alkane has been found to be significantly reduced [38]. While there are numerous studies investigating the organization of shorter *n*-alkanes in lipid membranes [39–44], we are not aware of any studies reporting on the crystallization of *n*-alkanes (or other purely hydrophobic molecules) inside lipid membranes. Filling this obvious gap will be beneficial for better understanding more complex biological problems such as the crystallization of drugs in lipid/polymer nanoparticles or the role of triglycerides in lipid-droplet formation.

In this work we study two *n*-alkanes, *n*-eicosane (C20) and *n*-triacontane (C30) inside different phospholipid membrane. We show in which mixtures crystallization of the *n*-alkanes occurs, and highlight the differences between crystallization in bulk and inside the lipid membrane for C30.

METHODS

Sample preparation

1,2-dimyristoyl-*sn*-glycero-3-phosphocholine (DMPC), DMPC with perdeuterated acyl tails (DMPC-d54), 1,2-dipalmitoyl-*sn*-glycero-3-phosphocholine (DPPC), DPPC-d62, 1-palmitoyl-2-oleoyl-*sn*-glycero-3-phosphocholine (POPC) and 1,2-dioleoyl-*sn*-glycero-3-phosphocholine (DOPC) were obtained from Avanti Polar Lipids. Hydrogenated and perdeuterated *n*-eicosane (C20/C20d) and *n*-triacontane (C30/C30d), methanol and chloroform were obtained from Sigma Aldrich. Multilamellar vesicles (MLVs) of phospholipids containing *n*-eicosane or *n*-triacontane were prepared by first co-dissolving the lipid and 10 and 5 vol% of *n*-alkane (for C20 and C30, respectively) in chloroform. Here, the volume fraction refers to the number of alkane carbons per total number of carbons in alkane plus lipid acyl tails. The solvent was then evaporated under a nitrogen gas stream to produce a dry lipid film. During evaporation, the solution was simultaneously subjected to sonication in a heatbath that was kept at a temperature above the bulk *n*-alkane melting and the lipid bilayer melting temperatures. The resulting lipid films were kept at reduced pressure over night to remove any remaining solvent. Samples containing DMPC, POPC or DOPC were rehydrated in a high humidity atmosphere: Lipid films and about 2 ml of water were placed in a desiccator. The desiccator was then evacuated by briefly attaching it to a vacuum pump, until the water had de-gased. Time spent in the evacuated desiccator varied between four hours and one day for the different samples. This technique resulted in homogeneous hydration of about 9-20 water molecules per lipid (values determined by ^{1}H MAS NMR were typically lower by 5 water molecules per lipid, compared to the weighted amounts). For the DPPC-based films, the desiccator method only resulted in about 4 water molecules per lipid. Therefore, water content in DPPC samples was adjusted by weighting the appropriate water amounts, aiming for a water content of 18 water molecules per lipid. This procedure resulted in hydration levels of n_w=11-18, as determined by ^{1}H MAS NMR. All samples were frozen before and between measurements. For NMR, samples were centrifuged into magic-angle-spinning (MAS) rotor inserts (Bruker) fitting approximately 20 mg.

Solid-State NMR Experiments

All measurements were conducted on a Bruker Avance III 400 spectrometer operating at a ^{1}H Larmor frequency of 399.92 MHz (equal to a ^{2}H Larmor frequency of 61.40 MHz). Data processing was conducted in Matlab. Temperature-dependent measurements were performed in between 10 and 85°C (the exact range being determined by the main phase transition temperatures of the sample components). Sample temperature was thereby based on setup-specific calibrations with ethylene glycol, and samples were heated and cooled at constant rates (realized by the Bruker software), usually 1 or 2 K/min. ^{1}H MAS measurements were conducted at 5 kHz MAS using a standard 4 mm double-resonance MAS probe. Single-scan ^{1}H spectra had a spectral width of 100 kHz. Free-induction decays (FIDs) were zero-filled, Fourier-transformed, and the lipid and water peaks were fitted with Lorentzian lineshapes to calculate the water content from the peak integrals. A 5 mm broad-band probe was used for static ^{2}H NMR experiments, employing a quadrupole echo sequence [25]. The echo delay was 40 μs, the relaxation delay was 1 s (or 50 s in a select case), and the 90° pulse width was around 4.3 or 6.0 μs. Dependent on sample composition and temperature/quadrupolar coupling strength, 1024 to 81920 scans with a spectral width of 1 MHz were acquired for each spectrum. The FIDs were processed and Fourier-transformed using Matlab, starting from the echo maximum.

Wide-angle X-ray scattering (WAXS)

WAXS measurements were performed on two samples of C20 in DPPC (10 and 25 vol% of *n*-alkane), and a DPPC reference sample. Additional water was added to the samples subjected to WAXS, resulting in a final lipid concentration of about 150 $\frac{\text{mg}}{\text{ml}}$. The dispersions were vortexed and filled into borosilicate glass capillaries (from Hilgenberg (Maisfeld, Germany); 1 mm outer diameter and 0.01 mm thickness). The experimental setup is described in detail in our previous publication and is not repeated here [22]. Scattering profiles were measured at 22 °C and corrected for background, transmission and sample geometry. The scattering intensities were angular-averaged and plotted versus the scattering vector q before normalization with respect to concentration and sample volume.

Differential Scanning Calorimetry

DSC measurements were conducted on a PerkinElmer DSC 8000. Samples subjected to DSC measurements were limited to hydrated DMPC/C30d, hydrated DMPC, and pure C30d. Temperature sweeps

were performed with heating/cooling rates of 1 and 2 °C/min, respectively. Samples were allowed to equilibrate for 5 or 10 min at the starting temperature before each run. Isothermal crystallization experiments were performed by cooling the sample from the highest temperatures to the desired crystallization temperature at 40 °C/min. Once the crystallization temperature was reached, the heat flow was monitored for a certain time (total duration ranging from 1 to 30 or 60 min). From the temperature scans, heat capacities were calculated using the pyris software (after subtracting baseline heat flows measured with empty pans), and the data was normalized to sample mass. In the mixtures, the mass of each component in the DSC sample was calculated from the amounts weighted into the mixture during preparation, assuming that no water was lost due to evaporation prior to the measurement. During the isothermal measurements, even in the absence of thermal transitions, the heat flow as a function of time only reached a constant baseline after 0.5-1 min. Therefore, such measurements were used as baselines to subtract the non-constant heat flow recorded at short times from the data. Then, relative transition enthalpies were calculated by integrating the heat flow up to different crystallization times t_c, and normalizing to the total integral. This method could only be used for bulk C30d, since in the mixtures the amount of *n*-alkane, and therefore the heat flow related to the transition events, was very small. Instead, the total duration of the crystallization step was varied, and the respective enthalpies were determined from a consecutive heating run, similar to the method used by e.g. Alamo et al. [45, 46]. Using a Malvern MicroCal VP-DSC instrument, heating/cooling runs were acquired for an additional sample of 5 vol% C30d in DMPC, and a DMPC reference sample, prepared with increased amounts of water. The sample preparation was the same as described above, except for adding additional water until a lipid concentration of 10 $\frac{\text{mg}}{\text{ml}}$ was reached, and vortexing and sonicating the dispersion prior to measuring. Scan rates were 1 °C/min in both heating and cooling scans ranging from 5/20 - 80 °C. Prescan equlibration times of 10 min were used. The reference cell was filled with pure de-gased water and a water/water baseline was subtracted from each sample scan.

RESULTS AND DISCUSSION

This work is organized in the following way. First, we employ static ^{2}H nuclear magnetic resonance (NMR) to determine under which conditions C20d and C30d can crystallize in phospholipid membranes. In general, the shape of the ^{2}H NMR spectrum depends on the dynamics and geometry of a C-D bonds motion [25]. Fast, isotropic motions result in a single, narrow peak. This is the case for liquid *n*-alkanes [22]. Anisotropic motions, such as those of *n*-alkanes inside lipid bilayers, produce broader spectra [22, 42]. As will be seen, liquid (an)isotropic, rotator, or crystal phases result in very distinct spectral shapes and thus ^{2}H NMR is a powerful tool to determine the presence and phase of *n*-alkanes inside lipid membranes. We then examine the crystallization properties of C30 in a DMPC bilayer in more detail by comparing temperature-dependent NMR measurements with differential scanning calorimetry (DSC). We also remark on the effect of sample hydration and compare the crystallization kinetics of C30 in the membrane environment with bulk *n*-alkane.

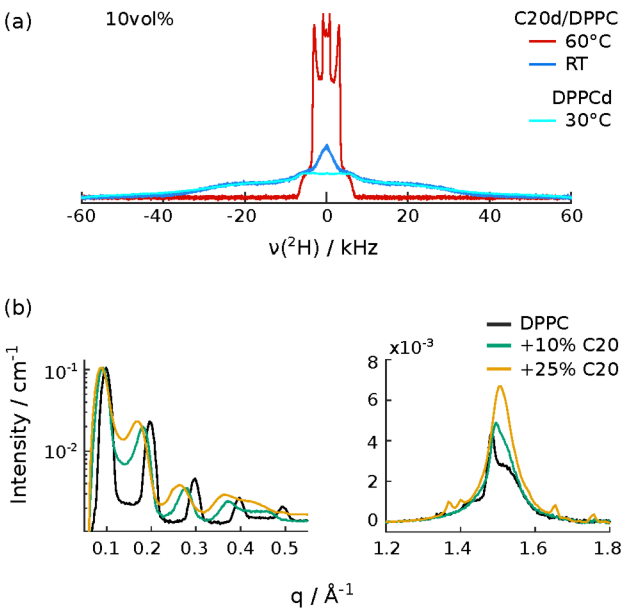

FIG. 1. Organization of C20 in DPPC membranes at different temperatures. (a) ^{2}H NMR spectra of 10 vol% C20d in DPPC (0.18 C20d molecules per DPPC) at a reduced hydration of n_w=16, and pure DPPC-d62. The intensity of the DPPC-d62 spectrum is scaled to match the intensity of the C20d/DPPC spectra. At room temperature (approx. 25°C), the spectral shape of C20d in DPPC resembles that of gel-phase DPPC-d62. (b) X-ray scattering profiles for fully hydrated DPPC MLV's (at excess water) containing 0, 10 and 25 vol% of C20, measured at 22°C.

C20 is incorporated into the lipid gel phase and does not crystallize

Since shorter *n*-alkanes can be incorporated into lipid membranes to larger amounts, we first investigated systems with *n*-eicosane-d42 (C20d). ^{2}H NMR spectra of 10 vol% C20d in a DPPC bilayer at different temperatures are shown in Figure 1a. Above the lipid and alkane melting temperatures (e.g. 60°C), a spectral line shape corresponding to an anisotropic arrangement of liquid molecules is observed [22, 25]. This proves that the C20d molecules are indeed dispersed throughout the lipid membrane. Upon cooling below the crystallization temperature of bulk C20d (about 33°C [47]), the spectrum broadens considerably. However, instead of a ^{2}H spectrum displaying crystal-like features, the spectrum strongly resembles the ^{2}H NMR spectra of phospholipid gel phases [48–51]. A spectrum of perdeuterated DPPC at 30°C, a temperature close to the DPPC gel-to-rippled phase transition [48, 52], is shown in Figure 1a for comparison. This observation indicates that C20d adopts a gel-like state at room temperature, most likely because the C20d molecules are built into the DPPC gel structure owing to their chemical similarity with the lipid acyl tails. This is reasonable since the main transition temperature of DPPC (above 42°C due to reduced hydration

levels [53] and alkane addition [39, 54, 55]) is higher than the crystallization temperature of the alkane. Then, upon cooling, the liquid-to-gel phase transition of DPPC occurs before reaching the crystallization temperature of the alkane, and the C20d molecules become trapped in the lipid gel phase. This prevents them from crystallizing. Similar observations have previously been made for shorter *n*-alkanes in different lipid membranes [41].

To confirm that the C20d molecules are incorporated into the gel phase, we have performed X-ray scattering experiments on DPPC multi-lamellar vesicles with C20 concentrations ranging from 0 to 25 vol% at a temperature below the lipid main transition. These experiments show that the presence of C20 increases the lamellar repeat distance of the bilayers in the gel phase from 63.8±0.3 $Å^{-1}$ (pure DPPC) to 72.5±1.8 $Å^{-1}$ (25 vol% C20), as seen by a continuous shift of the low-q Bragg reflections to smaller reciprocal distances (Figure 1b). In addition, C20 affects the lateral ordering of the lipid acyl tails, as evidenced by the disappearance of the shoulder of the peak at q=1.5 $Å^{-1}$. Similar observations have previously been explained by an overall denser packing and the removal of acyl chain tilt [40, 56–58]. We therefore conclude that C20 is built into the DPPC L'_β phase, transforming it into an L_β (untilted gel) phase. The formation of the L_β phase is often observed in mixtures of lipids with different acyl tail lengths [56], or for lipids with smaller head/tail volume ratio [59]. Since C20 inside a bilayer of DPPC with 16-carbon long tails represents a similar system, the formation of an untilted gel in this case is not surprising.

The situation appears similar for C20d in DMPC membranes (Figure S1). In this system, the DMPC gel-to-liquid transition should occur at a lower temperature than the crystallization temperature for bulk C20d. Still, at 30°C, below the crystallization temperature of the alkane and above the DMPC gel-to-liquid transition, the ^{2}H spectrum of C20d does not show any sign of crystallization, retaining the shape characteristic of anisotropic, liquid hydrocarbon chains. Only a slight broadening is observed which is a natural consequence of the decrease in temperature, since temperature strongly affects alkane order parameters in lipid membranes [42, 43]. Similar to DPPC, both reduced hydration [43, 60] and addition of long-chain *n*-alkanes [39, 40, 43] will increase the DMPC main transition temperature. However, it is clearly not elevated above the bulk C20d transition temperature in this sample; otherwise the 30°C spectrum would also show gel-like features. This indicates that the crystallization temperature of C20d is reduced inside the membrane environment, similarly to what happens in mixtures composed of short and long alkanes. This is also observed in the ^{2}H NMR spectra of 10 vol% C20d in DOPC (Figure S2), which still shows anisotropic-fluid characteristics at 25 °C. However, the DOPC/C20d sample contains a large amount of bulk *n*-alkane, making further analysis difficult. We therefore mostly concentrated our efforts on C30d, having a melting temperature well above the main transition temperatures of DMPC and DPPC. In the following sections we demonstrate that C30d can crystallize within a lipid membrane environment.

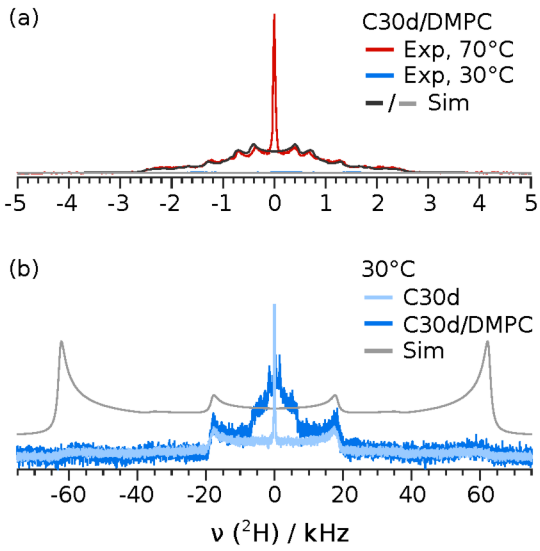

FIG. 2. ^{2}H NMR spectra of 5 vol% C30d inside DMPC membranes at reduced hydration, using a quadrupole echo technique and a short recycle delay of 1 s. (a)/(b): spectrum ranges chosen to best visualize liquid-anisotropic/solid *n*-alkane signals, respectively. Simulated spectra are included for comparison. The simulated 70°C spectrum was calculated by guessing the order parameter profile and summing up the resulting Pake patterns according to the procedure in our previous work [61]. Transversal relaxation was set to T_2=5 ms to best approximate the experimental spectrum. The crystalline spectrum was calculated based on C-D bond order parameters of 0.29 and 1.0 for methyl and methylene bonds, respectively. The overall intensity was matched to the intensity of the 70°C spectrum, and T_2=0.2 ms was used.

C30 crystallizes inside DMPC and POPC membranes

The static ^{2}H NMR spectra measured from membranes containing 5 vol% of C30d in DMPC are shown in Fig. 2. The high-temperature spectrum was acquired above the melting point of C30d (approx. 62°C [47]) and originates from a superposition of Pake patterns. In the middle of this spectrum a narrow peak is visible. This peak likely originates from a separate, isotropic *n*-alkane phase, i.e. C30d that didn't enter the lipid membrane. A quantification of this alkane fraction will be provided only in the following section. Upon cooling the mixtures to 30°C the complete signal seems to vanish. However, closer inspection reveals that the spectrum broadens considerably (Figure 2b). For comparison, the spectrum of crystalline bulk C30d obtained at 30°C is included in the figure. The spectra of both C30d in DMPC and bulk C30d feature horns at about ±17-18 kHz and ±60 kHz. Comparison with a simulated spectrum shows that both these horns represent the quadrupolar splittings for a 90°orientation of C30d crystallites with respect to the main magnetic field. The

position of the outer splittings indeed corresponds to a rigid quadrupolar coupling of 167 kHz, as expected for the static limit [25]. Similar splittings have been measured in short *n*-alkane solids [62]. Therefore, at 30°C, C30d molecules that were mixed with the acyl chains at high temperature must (mostly) be part of a crystalline structure. We have also performed experiments on samples containing C30d in POPC bilayers and the ^{2}H spectra obtained mirror the results for C30d in DMPC (Fig. S4).

For both the POPC and DMPC samples containing crystallized alkane, re-heating of the samples to above the *n*-alkane melting temperature leads to a recovery of the initial ^{2}H spectrum within the first few scans after temperature equilibration. This observation suggests that C30 crystals are small and most likely located inside the lipid bilayers. Only then, the *n*-alkane molecules are able to quickly disperse throughout the membrane upon melting.

The outer shoulders of the simulated spectrum are much more prominent than in the experimental spectra. Figure S3 indicates that this is because the spectra in Figure 2b were acquired using a too short recycle delay of 1 s. While such a short delay is suitable for liquid *n*-alkanes [63, 64], it is clearly insufficient for the higher quadrupolar couplings of the solid methylene groups [50]. However, since the crystalline component can still be identified using the short recycle delay, and long recycle delays increase the measurement time beyond what is practical, we continued using a recycle delay of 1 s in this work. The inner horns of the low-temperature spectra originate from the methyl groups of crystalline C30d. At 30°C, the quadrupolar coupling of the methyl C-D bonds is decreased to one third of the rigid coupling. Such a reduction is expected for the rotation of the methyl group around its symmetry axis [25, 62, 65], showing that the methyl groups rotate with correlation times much faster than μs at the chosen temperature.

An additional component is observed in the center of the low-temperature C30d spectra in bulk and in the membrane. For the bulk sample, this component appears as a very narrow peak, indicating an isotropic (liquid) *n*-alkane component, likely due to shorter *n*-alkane molecules present in the sample. For C30d in DMPC, this component appears broader, and may originate from non-crystallized molecules. A more detailed discussion of this feature and the temperature dependence of the ^{2}H spectrum of C30d is provided in the following section.

In summary, our ^{2}H NMR measurements show that *n*-alkanes crystallize inside lipid membranes only if the *n*-alkane melting point lies sufficiently far above the main transition temperature of the lipid membranes. If the temperature difference between the two transitions is too small, upon cooling the *n*-alkane molecules become trapped in the lipid gel phase and do not crystallize. We observe this at very low cooling rates since the ^{2}H NMR experiments performed at each temperature had a duration of 1 hour or more. These results suggest that the crystallization temperature of *n*-alkanes is decreased inside a lipid membrane environment similarly to what happens when chains are dispersed in a non-structured solvent.

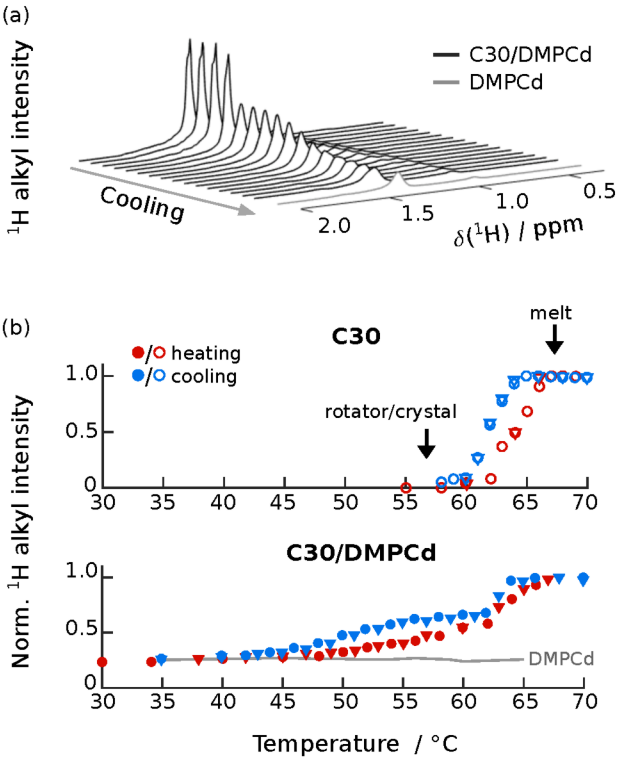

FIG. 3. ^{1}H intensity in the alkyl chain spectral region of C30 as a function of temperature. (a) Alkyl spectral region of C30 in DMPC-d54 during cooling at 1K/min. Even though the lipid is perdeuterated, some signal can be detected even when no alkane is present. (b) Normalized intensities calculated by summing all spectrum points in the ppm range displayed in (a). Upper row: bulk C30, Lower row: 5 vol% C30 in DMPCd, and pure DMPCd for reference. The different symbol shapes mark different heating/cooling runs.

In order to investigate this in more detail, we performed ^{1}H NMR and DSC experiments on the system C30/DMPC which are evaluated in the following section.

The crystallization temperature of C30 decreases inside DMPC bilayers

In order to study the temperature dependence of the crystallization process of C30d inside DMPC membranes, we first performed ^{1}H NMR measurements on mixtures of non-deuterated C30 and DMPC with per-deuterated acyl tails (DMPC-d54). The measurements were performed under MAS at a spinning rate of 5 kHz. This allowed us to record the ^{1}H NMR signal of the *n*-alkane alkyl protons during a temperature sweep. At the MAS frequency used, the ^{1}H alkyl peaks can only be resolved if the alkane is in a liquid state; in the crystalline and rotator phase the peaks are broadened beyond detection due to significantly reduced chain mobility and consequent increase of the ^{1}H homonuclear dipolar cou-

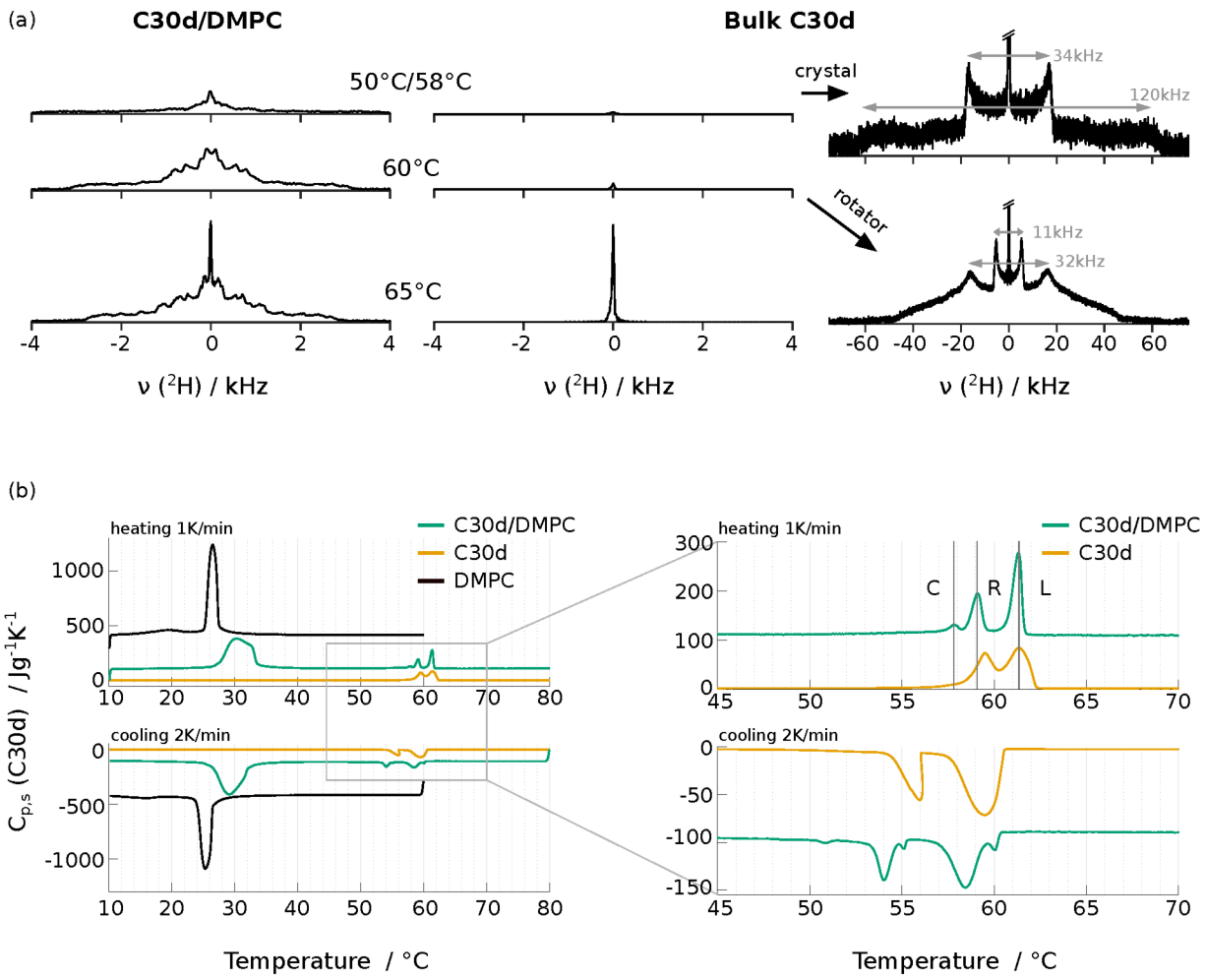

FIG. 4. Temperature-dependent phase behaviour of C30d in DMPC and in bulk. (a) ^{2}H NMR spectra of 5 vol% C30d in DMPC, at reduced hydration and for three selected temperatures, compared to bulk C30d spectra (Measurement time per spectrum 35 and 17 min in the membrane and in bulk, respectively). (b) DSC heat capacities of 5 vol% C30d in DMPC, at reduced hydration, compared to DMPC (at comparable hydration) and bulk C30d. The heating rate was 1K/min and the cooling rate was 2K/min. Right: Zoom into the *n*-alkane phase transition region. Heat capacities are given in JK^{-1} per gram C30d and were shifted vertically to facilitate visualization. The heat capacity of DMPC/water was normalized to result in the same energy per number of DMPC molecules in the C30d/DMPC mixture.

plings. For the rotator phase, this observation is similar to lipid gel-phases, where reduced mobility results in increased dipole-dipole interactions and T_2 relaxation rates [66, 67]. Figure 3 shows the results of such measurements. In Figure 3a, the alkyl chain region of the ^{1}H spectrum is plotted with decreasing temperature, and the low-temperature spectrum of DMPC-d54/water is included for comparison. The normalized spectrum integrals upon heating/cooling of C30 in bulk and in the membrane are plotted in Figure 3b. The melting of bulk C30 is indicated by a strong signal increase between 64 and 67°C, which corresponds to the expected melting temperature of about 65°C (from the rotator to the liquid phase) [29, 30, 68]. In the subsequent cooling runs, the signal intensity decreases between approx. 65 and 60°C. According to Sirota et al., the liquid-to-rotator transition of C30 is similar to, but slightly below, it's melting temperature [29, 68]. More precisely, since they also found a transition between the RIV and RIII rotator phases at 63.9-64.4°C, the liquid-to-rotator transition of C30 should lie between 64 and 65°C. We'd like to note here that, since the ^{1}H NMR experiments were conducted under MAS, a temperature gradient of a few degrees exists within the samples. This gradient broadens the observed transitions and obstructs a more accurate comparison with literature values. Still, Figure 3 shows that C30 in a DMPC-d54 membrane behaves notably different from bulk C30: The apparent melting process starts earlier, at approx. 50°C, and continues until about 62°C, after which the signal increases sharply. This two-step process becomes even more

evident in the cooling runs, were we first observe a fast decay similar to the bulk sample, followed by a second process between 55 and 45°C. Based on these results alone, there are two possible explanations for this two-step melting/crystallization process. One is that it is possible that the initial, fast drop of ^{1}H intensity upon cooling corresponds to bulk C30 that is not incorporated into the lipid membranes; the slower drop of intensity (at lower temperatures) would then correspond to crystallization of alkane molecules incorporated in the lipid bilayers. An alternative explanation is that both transitions relate to mixed C30, where one component behaves similar to bulk alkane while the other is more strongly associated with the lipid. In fact, this lipid-associated component may not even crystallize, but only adopt a rotator phase/gel-like state in combination with the lipid acyl tails.

In order to identify the alkane phases during the melting and crystallization process, we acquired ^{2}H NMR spectra of C30d in bulk and in DMPC membranes in the relevant temperature range. Selected results are shown in figure 4a. For bulk C30d, we can clearly distinguish the crystal, rotator and liquid phase. The crystalline signal features two sets of horns/shoulders, separated by approx. 34 and 120 kHz, as explained in the first part of this manuscript. The rotator phase resembles spectra of gel-phase lipids [48–51], while the liquid *n*-alkane results in a single peak. We obtain transition temperatures of about 60.0-60.5°C and 62.5-64.0°C for the crystal-to-rotator and rotator-to-liquid transition of bulk C30d upon heating, respectively. Upon cooling, the rotator-to-crystal transition temperature was between 60 and 58°C. These results are in line with previous works [29, 47, 68, 69] and the DSC results that are described below (Figure 4b). In contrast to the bulk C30d case, it is more difficult to identify exact phase transition temperatures for the C30d/phospholipid mixture. Still, the observations match the ^{1}H NMR results shown in Figure 3: The intensity of the ^{2}H NMR spectra in the region between ±4kHz gradually increases from about 45 to 60°C. In this temperature range, the spectral shape of the signal reveals the presence of alkane molecules with anisotropic motion in the membrane environment. Additionally, at 65°C and above, a central, narrow peak becomes visible in the ^{2}H NMR spectra. Since the temperature range in which this peak is observed roughly matches the temperature interval in which bulk C30d is liquid, it seems reasonable to assign this narrow signal to phase-separated bulk alkane.

In order to detect alkane crystallization, we acquired ^{2}H spectra in the relevant temperature range with a much larger number of scans (up to 81920, Figure S5). A close look at these spectra reveals the co-existence of liquid and crystalline (58 and 53°C) or liquid and rotator phase alkane (61.0, 60.5 and 59.5°C) in the transition range of bulk C30d.

Analysis of the ^{2}H NMR spectra enabled us to determine the fraction of C30d molecules located in different environments in our samples. An upper limit to the amount of bulk alkane, i.e. C30d molecules that did not enter the lipid membranes, can be estimated by a subtraction method [70, 71]. The spectrum of pure C30d in the melt is fitted, and then a fraction of the resulting Lorentzian line shape is subtracted from the C30d/DMPC spectrum until an intensity of nearly zero is reached in the center of the spectrum (Figure S6). The difference between the original and the reduced spectrum then corresponds to an upper limit for the bulk alkane fraction, and is 10-15 %. We determined that this small amount of bulk C30d is not sufficient to account for the crystalline signal observed at e.g. 55°C. This was done by comparing the ^{2}H signal intensities across different temperatures, as described in more detail in the SI (Figure S7). From these calculations we obtain that, at 55°C, more than nearly 70 % of the molecules that comprise the crystals must have been dispersed inside the DMPC membranes prior to crystallization. We conclude therefore that our samples contain not only two, but three different types of C30d molecules: Phase-separated bulk alkane, and chains incorporated in the membrane that can be divided into those that crystallize at similar temperatures to bulk C30d, and those that remain in a liquid state at temperatures much lower than the bulk crystallization temperature.

These findings are supported by DSC heating/cooling runs shown in Figure 4b. For bulk C30d, two peaks are observed in the heat capacity upon heating and cooling, corresponding to the crystal-rotator and rotator-liquid transitions at lower and higher temperature, respectively. Inside DMPC membranes, the crystal-to-rotator transition temperature of C30d upon heating is decreased by only 0.4°C, while the rotator-to-liquid transition temperature is hardly affected at all. The transition peaks become more narrow and an additional peak is visible at 57.8°C, prior to the original crystal-to-rotator transition. Upon cooling, the shift in the phase transitions upon mixing with DMPC is more evident: the liquid-to-rotator transition is lowered by approx. 1°C, and the rotator-to-crystal transition by 1.5-2.0°C. Small features remain visible close to the bulk transition temperatures. Regarding the properties of the DMPC membranes, the main transition is broadened and shifted to higher temperatures upon addition of C30d, and the pretransition can no longer be observed in the mixture. Notably, the DSC results show no indication of a broad transition in the 45-55°C interval, proving that no crystallization occurs in this temperature range.

Combined, our ^{2}H NMR and DSC results can be interpreted in the following way. As described in the first part of this manuscript, at high temperatures ($T \leq 62$°C), the C30d/DMPC sample contains *n*-alkane mixed with the lipid, but also roughly 10 % of bulk alkane. If the sample is cooled, bulk C30d crystallizes first, followed soon after by a fraction of the C30d molecules inside the DMPC membrane as shown by the DSC curves. The fraction of crystallizing chains can be determined by comparing the DSC transition enthalpies of the mixture with the bulk transition enthalpies. By integrating the (rotator-to-liquid) melting peak we find that the melting enthalpy of C30d in DMPC amounts to roughly 81±3% of the bulk C30d melting enthalpy. Therefore, 19±3% of C30d molecules do not crystallize in the mixture. These non-crystallizing chains will be discussed further below.

Before the actual crystallization, both bulk C30d and the

C30d molecules incorporated into the lipid membranes transition through a rotator phase. According to literature, the high-temperature peak in the heat capacity should signify the transition from liquid to the RIV rotator phase [29, 30, 68]. The RIV phase is then expected to transform into the RIII phase if the sample is cooled further. However, we do not see any indication of a rotator-rotator transition in bulk C30d. This is not unexpected, since the latent heat involved in this transition would be very small [30, 68, 72]. Consequently, we cannot determine which rotator phase is adopted at any given temperature, and whether both rotator phases can be formed in the lipid membrane.

Upon further cooling, at about 54°C (according to DSC), the C30d molecules that had initially anisotropic motions in the lipid membrane, and that formed a rotator phase, crystallize. Notably, this transition happens at a different temperature than for bulk C30d. With ^{2}H NMR, the crystallization is already observed at 58°C (Fig. S5). This discrepancy between DSC and NMR is easily explained by the acquisition time needed for the ^{2}H NMR spectra presented in Figure S5, ranging from 14 to 24 hours, resulting in a very small, effective cooling rate. DSC scans however were conducted at cooling rates of 2 °C/min and thus the DSC transition temperatures can be expected to be lower than those obtained from ^{2}H NMR [73, 74]. Furthermore, our ^{2}H NMR results have a relatively low temperature resolution (about ±1°C). This makes it difficult to detect slight shifts of the crystallization temperature such as the one between bulk and incorporated C30.

If C30d inside DMPC membranes crystallizes at only slightly lower temperatures than bulk C30d, the anisotropic liquid C30d component which is observed between approx. 45 and 60°C in the ^{2}H spectra must originate from *n*-alkane molecules inside the membrane which do not crystallize. We suspect that these non-crystallizing *n*-alkane molecules are build into the DMPC phase, similar to C20 in DMPC. Such a co-association of alkane and lipid is supported by the increased main transition temperature of DMPC in the presence of C30d. As mentioned previously, a shift of the lipid main transition temperature is expected when adding longer *n*-alkanes to saturated phospholipid bilayers. The loss of the pretransition temperature has also been observed previously in mixtures of C12 or C14 with DPPC [40, 58]. It should however be noted that, while the DMPC and C30d/DMPC samples compared in figure 4b were prepared in an identical manner, hydration somewhat differs between the samples. After preparation, the samples contained 22.5 and 12.5 water molecules per lipid for DMPC and C30d/DMPC, respectively. Since lipid acyl chain ordering increases with decreasing water content below approx. 25-30 water molecules per lipid [75], the shift of the DMPC main transition partially relates to a decrease in hydration. However, at the estimated water concentration, we would not expect such a large shift of the main transition temperature, and the pretransition should still exist (in the absence of alkane) [60, 76]. Therefore, we are convinced that the shift of the lipid main transition demonstrates an association between alkane and lipid molecules.

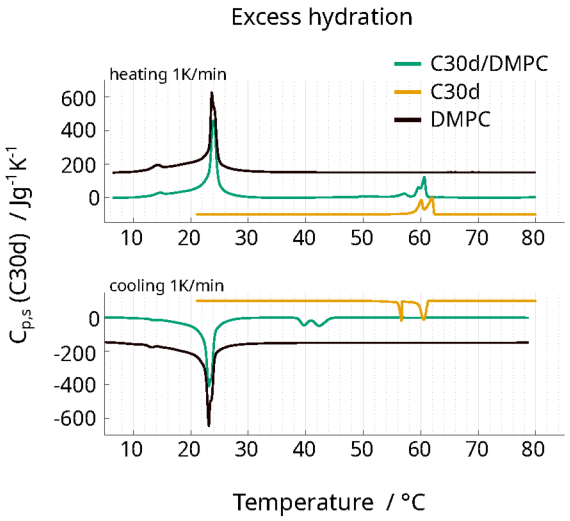

FIG. 5. DSC heat capacities in excess water conditions. Heating and cooling runs (1K/min) of 5 vol% C30d in DMPC (lipid concentration 10 mg/ml) are compared to DMPC (at comparable hydration) and bulk C30d. Heat capacities are given in JK^{-1} per gram C30d and were shifted along y to not overlap. The heat capacity of DMPC/water was normalized to result in the same energy per number of DMPC molecules in the C30d/DMPC mixture.

Our interpretation so far does not fully explain the continuous NMR signal decrease between 60 and 45°C (Figures 3 and 4a). This signal decrease must be related to the non-crystallizing C30d in the membrane, since all other *n*-alkane molecules should already be crystalline at this point. However, the associated lipid/alkane gel transition does not happen until about 35°C. Generally, lipid ordering decreases with increasing temperature even in the liquid-crystalline phase [56], and lipid dynamics are also affected irrespective of phase transitions [77]. It is possible that changing lipid dynamics affect the *n*-alkane NMR relaxation rates sufficiently to result in intermediate-motion lineshapes and signal loss even before the actual phase transition.

An increase of membrane hydration leads to homogeneous nucleation

Finally, we have investigated whether the crystallization of C30d inside DMPC is affected by the low amount of water in our systems. Figure 5 shows DSC heating and cooling runs of 5 vol% C30d in DMPC in excess water conditions. There are two important differences compared to the reduced hydration sample: First, the DMPC main transition is not at all affected by the presence of C30d. Second, the cooling transitions of C30d are shifted to much lower temperatures: the liquid-to-rotator and rotator-to-crystal transition occur at 19.5 and 20.5°C below the bulk C30d melting

temperatures, respectively. Such a strong hysteresis between heating and cooling transitions is evidence for homogeneous nucleation of C30d [28, 78–81]. We previously showed that under excess water conditions, *n*-alkanes induce the formation of smaller lipid structures (vesicles or maybe micelles with alkane droplets) [22]. Confinement in such small structures could explain why homogeneous nucleation is possible in this system. Furthermore, the unaffected lipid transition supports this interpretation, since the alkane would be spatially separated from most of the lipid in this scenario.

It is interesting that we still observe two peaks in the DSC cooling runs, showing that a rotator phase is adopted prior to crystallization of C30d. Previously, the role of the rotator phase upon homogeneous nucleation was not clear [28]. Rotator phases were observed in droplets of odd *n*-alkanes between 15 and 19 carbons, and both the liquid-to-rotator and rotator-to-crystal transition temperatures were decreased notably. However, the liquid-to-rotator transition temperature was affected more strongly, reducing the interval in which the rotator phase could be observed [79, 82]. For odd and even *n*-alkanes between C20 and C32, rotator phases were observed during heating, but not upon cooling [78, 79, 81, 83]. Consequently, it was argued that these *n*-alkanes crystallize directly, without transitioning through a rotator phase, upon homogeneous crystallization. It has also been found that the interface between *n*-alkane and the confining material (e.g. surfactant or polymer microcapsules) can induce surface heterogeneous nucleation [12, 84–87]. In such systems the freezing temperatures are not reduced as much as in the case of homogeneous nucleation, and rotator phases occur if the surfactant hydrocarbon tails are of similar length as the alkane [84, 85]. Our measurements show a rotator phase even during cooling, as well as significant undercoolings for both the liquid-to-rotator and rotator-to-crystal transition. It seems reasonable that the lipid acyl tails can induce surface heterogeneous nucleation similar to the surfactants mentioned above. Weidinger et al. argue that such nucleation does not necessarily have to result in smaller undercoolings, since the number of molecules exposed to the surface, and therefore available for nucleation, is comparatively small [82]. Possibly, the liquid-to-rotator transition of C30d in our samples is indeed heterogeneous, and therefore still visible in the DSC scans. Only the rotator-to-crystal transition might be truly homogeneous, similar to mixtures of C18/C19 investigated by Jiang et al. [86] or observations by Kovacik et al. on C16 in surfactant emulsion droplets [88].

Crystallization kinetics of C30d are slower in the membrane environment

In order to compare the crystallization kinetics of C30d in the membrane and in bulk, we performed DSC isothermal crystallization experiments. The heat flow recorded during isothermal crystallization for C30d and C30d/DMPC samples is plotted in Figure 6a,c. For bulk C30d, one or two transition

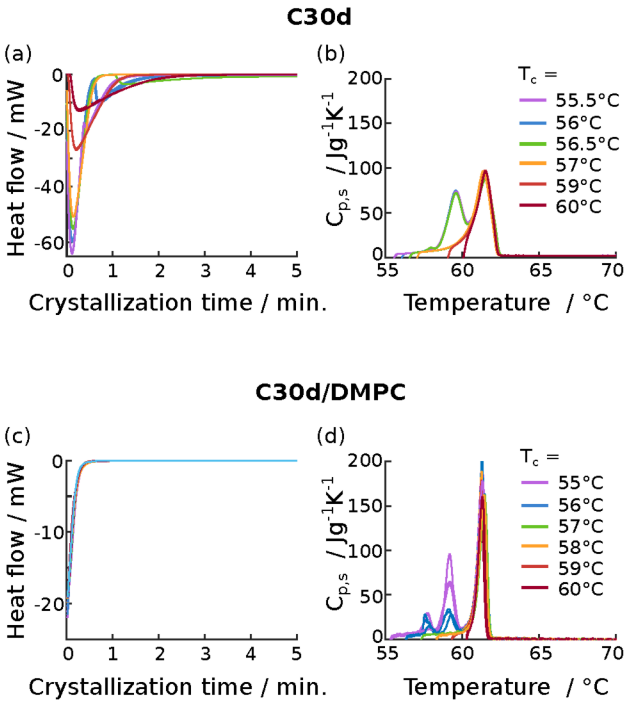

FIG. 6. Isothermal crystallization of bulk C30d and of C30d mixed with DMPC membranes. (a) Corrected heat flow during isothermal crystallization of C30d at different crystallization temperatures T_c. (b) Heat capacity of C30d during heating directly after the isothermal crystallization step shown in (a). Heating rate 1 K/min. (c),(d) The same as in (a) and (b) but for 5 vol% C30d in DMPC. Due to the low amount of alkane in the mixture, the artifact at very short crystallization times could not be subtracted reliably, causing the heat flow during isothermal crystallization to look the same for all measurements.

events can be identified per temperature. For C30d in DMPC however, the heat flow curves look nearly identical for all temperatures. The initial increase in heat flow observed for this sample is not a transition event but simply the stabilization of the heat flow after cooling. This artifact could not be removed reliably, since the amount of *n*-alkane in the sample was very small. However, alkane crystallization clearly takes place in the C30d/DMPC mixture since melting peaks are observed when the sample is heated again, directly after the crystallization step (Figure 6d). For isothermal processes above 56.5°C, both bulk and mixed C30d show a similar behaviour upon re-melting: Only a single peak at 61.5/61.3°C is observed. The presence of only one peak in the heat capacity profile upon heating shows that C30d remains in the rotator phase at these temperatures and does not crystallize. At lower temperatures, crystallization does take place after some time, as expected. In this case, the heat capacity profiles show distinct behavior for bulk C30d and C30d in DMPC membranes. For bulk C30d only two peaks are observed upon heating, while for C30d molecules in DMPC membranes three distinct melting peaks are observed.

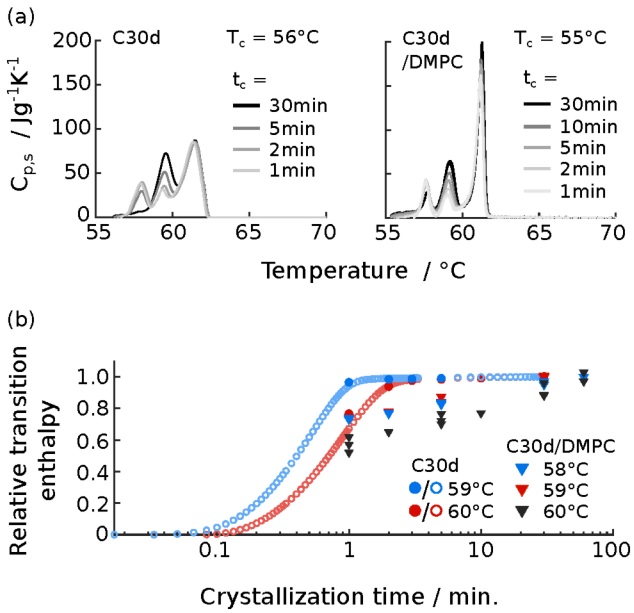

FIG. 7. Effect of varying the duration t_c of the isothermal process for both bulk C30d and C30d mixed with DMPC membranes. (a) Heat capacity of C30d during heating runs conducted directly after isothermal crystallization at temperature T_c. (b) Relative transition enthalpy of the liquid-to-rotator transition as a function of crystallization time. For bulk C30d, values were obtained directly during isothermal crystallization (open symbols) and by varying the crystallization time and comparing the subsequent melting enthalpies (filled symbols). For bulk C30d, the relative enthalpy is calculated with respect to the enthalpy after 30 minutes of crystallization. For C30d in DMPC, the relative enthalpy is calculated with respect to the integrated enthalpy after 60 minutes of crystallization. For the mixture, the liquid-to-rotator transition temperature of C30d is 1°C below the transition in bulk, which is considered in the color-coding.

Since the heat flow of C30d in DMPC could not be measured during the isothermal crystallization itself, we varied the duration of the isothermal step between 1 and 60 minutes. Then, we heated the samples again and compared the heat capacities and transition enthalpies upon melting for various crystallization durations. Figure 7a shows the effect of variable crystallization time on the heat capacities during melting for bulk and mixed C30d. Similar to the heating/cooling runs shown in Figure 4b, mixing of C30d with DMPC results in a third peak upon melting. Interestingly, if shorter crystallization times are used, this additional peak is also observed in bulk C30d (at 57.9-58.0°C). For both samples, the intensity of this peak decreases with crystallization time. Simultaneously, the peak at approx. 59°C increases in intensity. This observation confirms that the additional peak corresponds to the melting of an intermediate crystal phase which is formed during the transition from the rotator to the low-temperature crystal phase. To our knowledge, C30 is not known to have multiple crystal phases [23, 30], and we did not see any indication of an additional transition in the standard DSC cooling runs (Figure 4b). However, Alamo et al. previously explained a similar observation in $C_{168}H_{338}$ by a crystal-thickening process [45, 46]. Indeed, it was proposed that *n*-alkanes as short as C25 may first crystallize with non-aligned chain ends [28, 89, 90], effectively reducing the crystal thickness until the crystal-perfecting process is complete. Such thin crystals would be expected to melt at lower temperatures, possibly explaining the additional peak. Irrespective of its nature, this intermediate crystal form seems to be stabilized in DMPC membranes.

Variation of the duration of the isotherm process was also used to determine the speed of the liquid-to-rotator transition. Figure 7b shows the relative transition enthalpies obtained from integrating the heat capacity on re-heating after isothermal crystallization (for different total crystallization times). These relative transition enthalpies represent the fraction of *n*-alkane molecules in the rotator phase at a given time. For bulk C30d, the transition enthalpies obtained from integrating the heatflow during the long isothermal crystallization steps are plotted as a reference, and show that both methods are in good agreement. In bulk both the liquid-to-rotator and rotator-to-crystal transition occur faster at lower crystallization temperatures (see also Figure S8). Consequently, *n*-alkane diffusion coefficients should be of low relevance in this system. For C30d in DMPC, our data is not precise enough to make such a claim. However, the formation of the rotator phase appears to be a two-step process: Initial "gelation" of pre-organized *n*-alkane chains occurs as fast as in bulk, as evidenced by the high relative transition enthalpy after only one minute of crystallization. The following slow increase in melting enthalpy suggest that additional molecules are added to the rotator-phase nuclei with time. Notably, the transition enthalpy measured in the mixture would also include some bulk alkane, as described above. By subtracting a fixed fraction of the bulk transition enthalpy at each time point, the relative transition enthalpy of only the mixed alkane can be estimated. Evidently (Figure S9), assuming 20% of bulk C30d in the sample, the relative transition enthalpy still reaches a value of 0.66 after one minute, confirming that initial formation of the rotator phase is indeed very fast.

CONCLUSIONS

We have investigated the crystallizability of *n*-eicosane and *n*-triacontane in phospholipid bilayers. Our results suggest that there is a relation between the difference in bulk melting temperatures (alkane and lipid) and the crystallizability of the *n*-alkane. In DMPC and DPPC, C20 co-associated with the lipid acyl tails and therefore transitioned to a gel-like phase together with the lipid. C20 did appear to crystallize in DOPC bilayers, however due to the large fraction of bulk alkane in this sample it was impossible to validate our findings in the same manner as for the other investigated mixtures. C30 was able to crystallize inside DMPC and POPC bilayers. In a sample containing 5 vol% of C30 in DMPC, and only low amounts

of water, about 85-90 % of the alkane molecules were incorporated into the bilayer. The remaining chains did not mix with the lipid at all. Of the incorporated *n*-alkane, approximately 75-80 % crystallized at temperatures slightly below the bulk crystallization temperature. The non-crystallizing chains were instead built into the lipid phase, similar to C20. Inside the bilayer, C30 also crystallized via at least one rotator phase, and an intermediate crystal phase was stabilized compared to the bulk sample. With regards to crystallization kinetics, the formation of the rotator phase was observed to consist of two steps in the membrane: First, pre-organized *n*-alkane chains transitioned as fast as in bulk, but further addition of molecules to the rotator-phase crystal was slowed significantly. This finding suggests that the molecular arrangement of the *n*-alkane in the lipid bilayer strongly influences the crystallization process.

In excess water conditions, we instead observed a strong reduction of transition temperatures upon cooling, suggesting that C30d is confined to smaller droplets and crystallizes homogeneously.

This work marks the first observation of crystallization of purely hydrophobic molecules inside the hydrophobic core of lipid membranes. While the investigated *n*-alkanes are still far shorter than actual polymers, this study provides a first impression of what to expect from the crystallization of long hydrophobic chains inside lipid bilayers. Furthermore, our results motivate studying more biologically relevant systems such as crystallizable drugs or triglycerides inside model cell membranes.

ACKNOWLEDGEMENTS

This research study was funded by the German Research Foundation (Deutsche Forschungsgemeinschaft,DFG) [project number 189853844, TRR 102 (T.M.F. and A.W.)]. T.M.F. greatly acknowledges financial support by the Ministry of Economics, Science and Digitalisation of the State of Saxony-Anhalt. A.W. and T.M.F. gratefully thank K. Herfurt for her help regarding DSC measurements, and K. Busse, A. Krushelnitzky and K. Saalwächter for helpful discussions and their continued support.

* anika.wurl@physik.uni-halle.de
† tiago.ferreira@physik.uni-halle.de

[1] Siyoung Kim and Jessica M.J. Swanson, "The surface and hydration properties of lipid droplets," Biophysical Journal **119**, 1958–1969 (2020).
[2] Valeria Zoni, Rasha Khaddaj, Pablo Campomanes, Abdou Rachid Thiam, Roger Schneiter, and Stefano Vanni, "Pre-existing bilayer stresses modulate triglyceride accumulation in the er versus lipid droplets," eLife **10**, e62886 (2021).
[3] Frederik Viktor Hegaard, Martin Berg Klenow, and Adam Cohen Simonsen, "Lens nucleation and droplet budding in a membrane model for lipid droplet biogenesis," Langmuir **38**, 9247–9256 (2022).
[4] Hans Bouwmeester, Peter C. H. Hollman, and Ruud J. B. Peters, "Potential health impact of environmentally released micro- and nanoplastics in the human food production chain: Experiences from nanotoxicology," Environmental Science & Technology **49**, 8932–8947 (2015).
[5] Davide Bochicchio, Laura Cantu, Maria Vittoria Cadario, Leonardo Palchetti, Francesca Natali, Luca Monticelli, Giulia Rossi, and Elena Del Favero, "Polystyrene perturbs the structure, dynamics, and mechanical properties of dppc membranes: An experimental and computational study," Journal of Colloid and Interface Science **605**, 110–119 (2022).
[6] Linde Schoenmaker, Dominik Witzigmann, Jayesh A. Kulkarni, Rein Verbeke, Gideon Kersten, Wim Jiskoot, and Daan J.A. Crommelin, "mrna-lipid nanoparticle covid-19 vaccines: Structure and stability," International Journal of Pharmaceutics **601**, 120586 (2021).
[7] Letao Xu, Xing Wang, Yun Liu, Guangze Yang, Robert J. Falconer, and Chun-Xia Zhao, "Lipid nanoparticles for drug delivery," Advanced NanoBiomed Research **2**, 2100109 (2022).
[8] Matthias Schulz and Wolfgang H. Binder, "Mixed hybrid lipid/polymer vesicles as a novel membrane platform," Macromolecular Rapid Communications **36**, 2031–2041 (2015).
[9] Archana Khosa, Satish Reddi, and Ranendra N. Saha, "Nanostructured lipid carriers for site-specific drug delivery," Biomedicine & Pharmacotherapy **103**, 598–613 (2018).
[10] B.Yu Shekunov and P York, "Crystallization processes in pharmaceutical technology and drug delivery design," Journal of Crystal Growth **211**, 122–136 (2000).
[11] Karin M. Rosenblatt and Heike Bunjes, "Evaluation of the drug loading capacity of different lipid nanoparticle dispersions by passive drug loading," European Journal of Pharmaceutics and Biopharmaceutics **117**, 49–59 (2017).
[12] David Julian McClements, "Crystals and crystallization in oil-in-water emulsions: Implications for emulsion-based delivery systems," Advances in Colloid and Interface Science **174**, 1–30 (2012).
[13] Choon Fu Goh, Ben J. Boyd, Duncan Q. M. Craig, and Majella E. Lane, "Profiling of drug crystallization in the skin," Expert Opinion on Drug Delivery **17**, 1321–1334 (2020).
[14] Marco Werner, Jens-Uwe Sommer, and Vladimir A. Baulin, "Homo-polymers with balanced hydrophobicity translocate through lipid bilayers and enhance local solvent permeability," Soft Matter **8**, 11714–11722 (2012).
[15] Wen-de Tian, Kang Chen, and Yu-qiang Ma, "Interaction of fullerene chains and a lipid membrane via computer simulations," RSC Adv. **4**, 30215–30220 (2014).
[16] D Bochicchio, E Panizon, L Monticelli, and G Rossi, "Interaction of hydrophobic polymers with model lipid bilayers," Scientific reports **7**, 6357 (2017).
[17] Mihaela Drenscko and Sharon M. Loverde, "Molecular dynamics simulations of the interaction of phospholipid bilayers with polycaprolactone," Molecular Simulation **45**, 859–867 (2019).
[18] Oldamur Hollóczki and Sascha Gehrke, "Can nanoplastics alter cell membranes?" ChemPhysChem **21**, 9–12 (2020).
[19] S. Zenak, S.A. Sabeur, and J.J. López-Cascales, "Study of the insertion of a small symmetric star polymer into different phospholipid bilayers," Journal of Molecular Structure **1222**, 128888 (2020).
[20] Matthias Schulz, Adekunle Olubummo, and Wolfgang H. Binder, "Beyond the lipid-bilayer: interaction of polymers and nanoparticles with membranes," Soft Matter **8**, 4849–4864 (2012).

[21] Thomas Hauß, Silvia Dante, Norbert A Dencher, and Thomas H Haines, "Squalane is in the midplane of the lipid bilayer: implications for its function as a proton permeability barrier," Biochimica et Biophysica Acta (BBA) - Bioenergetics **1556**, 149–154 (2002).
[22] Anika Wurl, Maria Ott, Eric Plato, Annette Meister, Farzad Hamdi, Panagiotis L. Kastritis, Alfred Blume, and Tiago M. Ferreira, "Filling the gap with long n-alkanes: Incorporation of c20 and c30 into phospholipid membranes," Langmuir **38**, 8595–8606 (2022).
[23] Michel Dirand, Mohammed Bouroukba, Virginie Chevallier, Dominique Petitjean, Emmanuel Behar, and Véronique Ruffier-Meray, "Normal alkanes, multialkane synthetic model mixtures, and real petroleum waxes: Crystallographic structures, thermodynamic properties, and crystallization," Journal of Chemical & Engineering Data **47**, 115–143 (2002).
[24] Diana Cholakova and Nikolai Denkov, "Rotator phases in alkane systems: In bulk, surface layers and micro/nanoconfinements," Advances in Colloid and Interface Science **269**, 7–42 (2019).
[25] J H Davis, "The description of membrane lipid conformation, order and dynamics by 2h-nmr," Biochimica et Biophysica Acta (BBA) - Reviews on Biomembranes **737**, 117–171 (1983).
[26] Prabir K. Mukherjee, "Phase transitions among the rotator phases of the normal alkanes: A review," Physics Reports **588**, 1–54 (2015).
[27] E. B. Sirota and A. B. Herhold, "Transient Phase-Induced Nucleation," Science **283**, 529–532 (1999).
[28] H. Kraack, M. Deutsch, and E. B. Sirota, "n-alkane homogeneous nucleation: Crossover to polymer behavior," Macromolecules **33**, 6174–6184 (2000).
[29] E. B. Sirota, Jr. King, H. E., D. M. Singer, and Henry H. Shao, "Rotator phases of the normal alkanes: An x-ray scattering study," The Journal of Chemical Physics **98**, 5809–5824 (1993).
[30] J. Doucet, I. Denicolò, A. F. Craievich, and C. Germain, "X-ray study of the rotator phase of paraffins (IV): C27H56, C28H58, C29H6, C3H62, C32H66, and C34H7," The Journal of Chemical Physics **80**, 1647–1651 (1984).
[31] Yunlan Su, Guoming Liu, Baoquan Xie, Dongsheng Fu, and Dujin Wang, "Crystallization features of normal alkanes in confined geometry," Accounts of Chemical Research **47**, 192–201 (2014).
[32] Nobuo Maeda, Mika M. Kohonen, and Hugo K. Christenson, "Phase behavior of long-chain n-alkanes at one and between two mica surfaces," The Journal of Physical Chemistry B **105**, 5906–5913 (2001).
[33] Li Ping Wang, Jian Sui, Min Zhai, Fang Tian, and Xiao Zheng Lan, "Physical control of phase behavior of hexadecane in nanopores," The Journal of Physical Chemistry C **119**, 18697–18706 (2015).
[34] P. Huber, V. P. Soprunyuk, and K. Knorr, "Structural transformations of even-numbered n-alkanes confined in mesopores," Phys. Rev. E **74**, 031610 (2006).
[35] P. Huber, D. Wallacher, J. Albers, and K. Knorr, "Quenching of lamellar ordering in an n-alkane embedded in nanopores," Europhysics Letters **65**, 351–357 (2004).
[36] Baoquan Xie, Haifeng Shi, Shichun Jiang, Ying Zhao, Charles C. Han, Duanfu Xu, and Dujin Wang, "Crystallization behaviors of n-nonadecane in confined space: Observation of metastable phase induced by surface freezing," The Journal of Physical Chemistry B **110**, 14279–14282 (2006).
[37] Robert R. Matheson and Paul Smith, "A simple thermodynamic analysis of solid-solution formation in binary systems of homologous extended-chain alkanes," Polymer **26**, 288–292 (1985).
[38] Michael Senra, Ekarit Panacharoensawad, Kriangkrai Kraiwattanawong, Probjot Singh, and H. Scott Fogler, "Role of n-alkane polydispersity on the crystallization of n-alkanes from solution," Energy & Fuels **22**, 545–555 (2008).
[39] K. Lohner, "Effects of small organic molecules on phospholidpid phase transitions," Chemistry and Physics of Lipids **57**, 341–362 (1991).
[40] T J McIntosh, S A Simon, and R C MacDonald, "The organization of n-alkanes in lipid bilayers," Biochimica et Biophysica Acta (BBA) - Biomembranes **597**, 445–463 (1980).
[41] Mafumi Hishida, Asami Endo, Koyomi Nakazawa, Yasuhisa Yamamura, and Kazuya Saito, "Effect of n-alkanes on lipid bilayers depending on headgroups," Chemistry and Physics of Lipids **188**, 61–67 (2015).
[42] J.M. Pope, L.W. Walker, and D. Dubro, "On the ordering of n-alkane and n-alcohol solutes in phospholipid bilayer model membrane systems," Chemistry and Physics of Lipids **35**, 259–277 (1984).
[43] J.M. Pope and D.W. Dubro, "The interaction of n-alkanes and n-alcohols with lipid bilayer membranes: a 2h-nmr study," Biochimica et Biophysica Acta (BBA) - Biomembranes **858**, 243–253 (1986).
[44] J.M. Pope, L.a. Littlemore, and P.W. Westerman, "Chain-length dependence of n-alkane solubility in phosphatidylcholine bilayers: a 2h-nmr study," Biochimica et Biophysica Acta (BBA) - Biomembranes **980**, 69–76 (1989).
[45] RG Alamo, L Mandelkern, GM Stack, C Kröhnke, and Gerhard Wegner, "Isothermal thickening of crystals of high-molecular-weight n-alkanes," Macromolecules **26**, 2743–2753 (1993).
[46] RG Alamo, L Mandelkern, GM Stack, C Krohnke, and Gerhard Wegner, "Crystallization kinetics of long-chain n-alkanes from the melt and from solution," Macromolecules **27**, 147–156 (1994).
[47] Douglas L Dorset, Herbert L Strauss, and Robert G Snyder, "Chain-length dependence of the melting point difference between hydrogenated and deuterated crystalline n-alkanes," The Journal of Physical Chemistry **95**, 938–940 (1991).
[48] J.H. Davis, "Deuterium magnetic resonance study of the gel and liquid crystalline phases of dipalmitoyl phosphatidylcholine," Biophysical Journal **27**, 339–358 (1979).
[49] A. Léonard and E.J. Dufourc, "Interactions of cholesterol with the membrane lipid matrix. a solid state nmr approach," Biochimie **73**, 1295–1302 (1991).
[50] Neville Boden, Leslie D. Clark, Sean M. Hanlon, and Michael Mortimer, "Deuterium nuclear magnetic resonance spin echo spectroscopy in molecular crystals," Faraday Symp. Chem. Soc. **13**, 109–123 (1978).
[51] Margus R Vist and James H Davis, "Phase equilibria of cholesterol/dipalmitoylphosphatidylcholine mixtures: deuterium nuclear magnetic resonance and differential scanning calorimetry," Biochemistry **29**, 451–464 (1990).
[52] Frank M. Linseisen, Sybille Bayerl, and Thomas M. Bayerl, "2h-nmr and dsc study of dppc-dodab mixtures," Chemistry and Physics of Lipids **83**, 9–23 (1996).
[53] Michiko Kodama, Mika Kuwabara, and Syûzô Seki, "Successive phase-transition phenomena and phase diagram of the phosphatidylcholine-water system as revealed by differential scanning calorimetry," Biochimica et Biophysica Acta (BBA) - Biomembranes **689**, 567–570 (1982).
[54] Susan Mabrey and Julian M. Sturtevant, "Incorporation of saturated fatty acids into phosphatidylcholine bilayers," Biochimica et Biophysica Acta (BBA) - Lipids and Lipid Metabolism **486**,

444–450 (1977).
[55] Joan M. Boggs, Godha Rangaraj, and Kalavelil M. Koshy, "Effect of hydrogen-bonding and non-hydrogen-bonding long chain compounds on the phase transitin temperatures of phospholipids," Chemistry and Physics of Lipids **40**, 23–34 (1986).
[56] A Tardieu, V Luzzati, and F C Reman, "Structure and polymorphism of the hydrocarbon chains of lipids: A study of lecithin-water phases," Journal of Molecular Biology **75**, 711–733 (1973).
[57] Thalia T Mills, Juyang Huang, Gerald W Feigenson, and John F Nagle, "Effects of cholesterol and unsaturated dopc lipid on chain packing of saturated gel-phase dppc bilayers," General physiology and biophysics **28**, 126–139 (2009).
[58] Hatsuho Usuda, Mafumi Hishida, Yasuhisa Yamamura, and Kazuya Saito, "Common effects of incorporated n-alkane derivatives on molecular packing and phase behavior of dppc bilayers," Chemistry Letters **47**, 1512–1514 (2018).
[59] R.N. Lewis and R.N. McElhaney, "Calorimetric and spectroscopic studies of the polymorphic phase behavior of a homologous series of n-saturated 1,2-diacyl phosphatidylethanolamines," Biophysical Journal **64**, 1081–1096 (1993).
[60] M J Janiak, D M Small, and G G Shipley, "Temperature and compositional dependence of the structure of hydrated dimyristoyl lecithin." Journal of Biological Chemistry **254**, 6068–6078 (1979).
[61] Anika Wurl and Tiago M. Ferreira, "Atomistic md simulations of n-alkanes in a phospholipid bilayer: Charmm36 versus slipids," Macromolecular Theory and Simulations **32**, 2200078 (2023).
[62] L. J. Burnett and B. H. Muller, "Deuteron Quadrupole Coupling Constants in Three Solid Deuterated Paraffin Hydrocarbons: C2D6, C4D10, C6D14," The Journal of Chemical Physics **55**, 5829–5831 (2003).
[63] Russell E Jacobs and Stephen H White, "Behavior of hexane dissolved in dimyristoylphosphatidylcholine bilayers: an nmr and calorimetric study," Journal of the American Chemical Society **106**, 915–920 (1984).
[64] Adrian Paz Ramos, Mahmoudreza Doroudgar, and Michel Lafleur, "Determination of n-alkane partitioning within phosphatidylethanolamine lα/hii phases," Biochimica et Biophysica Acta (BBA) - Biomembranes **1862**, 183201 (2020).
[65] Michael R Paddy, FW Dahlquist, James H Davis, and Myer Bloom, "Dynamical and temperature-dependent effects of lipid-protein interactions. application of deuterium nuclear magnetic resonance and electron paramagnetic resonance spectroscopy to the same reconstitutions of cytochrome c oxidase," Biochemistry **20**, 3152–3162 (1981).
[66] D. Chapman, E. Oldfield, D. Doskočilová, and B. Schneider, "Nmr of gel and liquid crystalline phospholipids spinning at the 'magic angle'," FEBS Letters **25**, 261–264 (1972).
[67] Jeffrey Forbes, Cynthia Husted, and Eric Oldfield, "High-field, high-resolution proton" magic-angle" sample-spinning nuclear magnetic resonance spectroscopic studies of gel and liquid crystalline lipid bilayers and the effects of cholesterol," Journal of the American Chemical Society **110**, 1059–1065 (1988).
[68] E. B. Sirota and D. M. Singer, "Phase transitions among the rotator phases of the normal alkanes," The Journal of Chemical Physics **101**, 10873–10882 (1994).
[69] Douglas L Dorset, "Structural interactions between n-paraffins and their perdeuterated analogues: binary compositions with identical chain lengths," Macromolecules **24**, 6521–6526 (1991).
[70] JC Huschilt, RS Hodges, and JH Davis, "Phase equilibria in an amphiphilic peptide-phospholipid model membrane by deuterium nuclear magnetic resonance difference spectroscopy," Biochemistry **24**, 1377–1386 (1985).
[71] James H. Davis, Jesse James Clair, and Janos Juhasz, "Phase equilibria in dopc/dppc-d62/cholesterol mixtures," Biophysical Journal **96**, 521–539 (2009).
[72] S. Paoloni, F. Mercuri, U. Zammit, J. Leys, C. Glorieux, and J. Thoen, "Analysis of rotator phase transitions in the linear alkanes hexacosane to triacontane by adiabatic scanning calorimetry and by photopyroelectric calorimetry," The Journal of Chemical Physics **148**, 094503 (2018).
[73] Hans Hagen Fueldner, "Characterization of a third phase transition in multilamellar dipalmitoyllecithin liposomes," Biochemistry **20**, 5707–5710 (1981).
[74] S C Chen, J M Sturtevant, and B J Gaffney, "Scanning calorimetric evidence for a third phase transition in phosphatidylcholine bilayers." Proceedings of the National Academy of Sciences **77**, 5060–5063 (1980).
[75] Sergey V. Dvinskikh, Vasco Castro, and Dick Sandström, "Probing segmental order in lipid bilayers at variable hydration levels by amplitude- and phase-modulated cross-polarization nmr," Phys. Chem. Chem. Phys. **7**, 3255–3257 (2005).
[76] Martin J Janiak, Donald M Small, and G Graham Shipley, "Nature of the thermal pretransition of synthetic phospholipids: dimyristoyl-and dipalmitoyllecithin," Biochemistry **15**, 4575–4580 (1976).
[77] Erick J Dufourc, Chr Mayer, Jurgen Stohrer, Gerhard Althoff, and Gerd Kothe, "Dynamics of phosphate head groups in biomembranes. comprehensive analysis using phosphorus-31 nuclear magnetic resonance lineshape and relaxation time measurements," Biophysical journal **61**, 42–57 (1992).
[78] David Turnbull and Robert L Cormia, "Kinetics of crystal nucleation in some normal alkane liquids," The Journal of Chemical Physics **34**, 820–831 (1961).
[79] Rivelino Montenegro and Katharina Landfester, "Metastable and stable morphologies during crystallization of alkanes in miniemulsion droplets," Langmuir **19**, 5996–6003 (2003).
[80] D. R. Uhlmann, G. Kritchevsky, R. Straff, and G. Scherer, "Crystal nucleation in normal alkane liquids," The Journal of Chemical Physics **62**, 4896–4903 (1975).
[81] M.J. Oliver and P.D. Calvert, "Homogeneous nucleation of n-alkanes measured by differential scanning calorimetry," Journal of Crystal Growth **30**, 343–351 (1975).
[82] I. Weidinger, J. Klein, P. Stöckel, H. Baumgärtel, and T. Leisner, "Nucleation behavior of n-alkane microdroplets in an electrodynamic balance," The Journal of Physical Chemistry B **107**, 3636–3643 (2003).
[83] LW Phipps, "Heterogeneous and homogeneous nucleation in supercooled triglycerides and n-paraffins," Transactions of the Faraday Society **60**, 1873–1883 (1964).
[84] Yuya Shinohara, Tadashi Takamizawa, Satoru Ueno, Kiyotaka Sato, Isao Kobayashi, Mitsutoshi Nakajima, and Yoshiyuki Amemiya, "Microbeam x-ray diffraction analysis of interfacial heterogeneous nucleation of n-hexadecane inside oil-in-water emulsion droplets," Crystal Growth & Design **8**, 3123–3126 (2008).
[85] Diana Cholakova, Desislava Glushkova, Zhulieta Valkova, Sonya Tsibranska-Gyoreva, Krastina Tsvetkova, Slavka Tcholakova, and Nikolai Denkov, "Rotator phases in hexadecane emulsion drops revealed by x-ray synchrotron techniques," Journal of Colloid and Interface Science **604**, 260–271 (2021).
[86] Kai Jiang, Yunlan Su, Baoquan Xie, Shichun Jiang, Ying Zhao, and Dujin Wang, "Effect of geometrical confinement on the nu-

cleation and crystallization behavior of n-alkane mixtures," The Journal of Physical Chemistry B **112**, 16485–16489 (2008), pMID: 19367940.

[87] Burkard Spiegel, Alexander Käfer, and Matthias Kind, "Crystallization behavior and nucleation kinetics of organic melt droplets in a microfluidic device," Crystal Growth & Design **18**, 3307–3316 (2018).

[88] Filip Kovacik, Halil I. Okur, Nikolay Smolentsev, Rüdiger Scheu, and Sylvie Roke, "Hydration mediated interfacial transitions on mixed hydrophobic/hydrophilic nanodroplet interfaces," The Journal of Chemical Physics **149**, 234704 (2018).

[89] W. P. Zhang and D. L. Dorset, "Phase transformation and structure of n-c50h102/n-c60h122 solid solutions formed from the vapor phase," Journal of Polymer Science Part B: Polymer Physics **28**, 1223–1232 (1990).

[90] Peng Yi and Gregory C. Rutledge, "Molecular simulation of bundle-like crystal nucleation from n-eicosane melts," The Journal of Chemical Physics **135**, 024903 (2011).

5.3.1 Paper III: Supporting Information

Additional tables and figures referred to in paper III, as published in reference [39]. No changes were made.

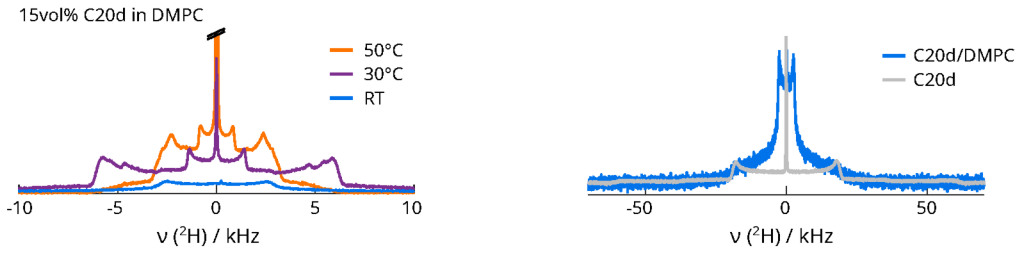

Figure S1: ^{2}H NMR spectra of 15 vol% C20d in DMPC (reduced hydration). Left: Temperature series. Spectra acquired at 50°C (above $T_{m,\mathrm{DMPC}}$ and $T_{m,\mathrm{C20d}}$), 30°C (above $T_{m,\mathrm{DMPC}}$ but below $T_{m,\mathrm{C20d}}$) and at room temperature (around $T_{m,\mathrm{DMPC}}$). Spectra are scaled to the same number of scans. Right: comparison of the 23°C spectrum to crystalline bulk C20d at the same temperature (bulk intensity scaled to match the mixture).

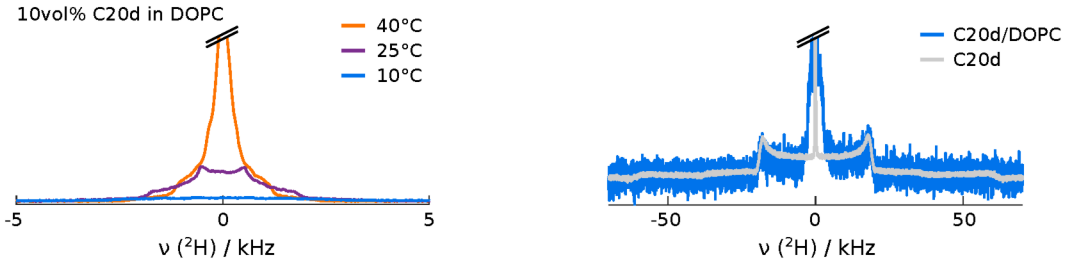

Figure S2: ^{2}H NMR spectra of 10 vol% C20d in DOPC (reduced hydration). Left: spectra acquired above (40°C), below (25°C) and far below (10°C) the crystallization temperature of bulk C20d. Spectra scaled to the same number of scans. Right: comparison of the 10°C spectrum to crystalline bulk C20d at 23°C (bulk intensity scaled to match the mixture).

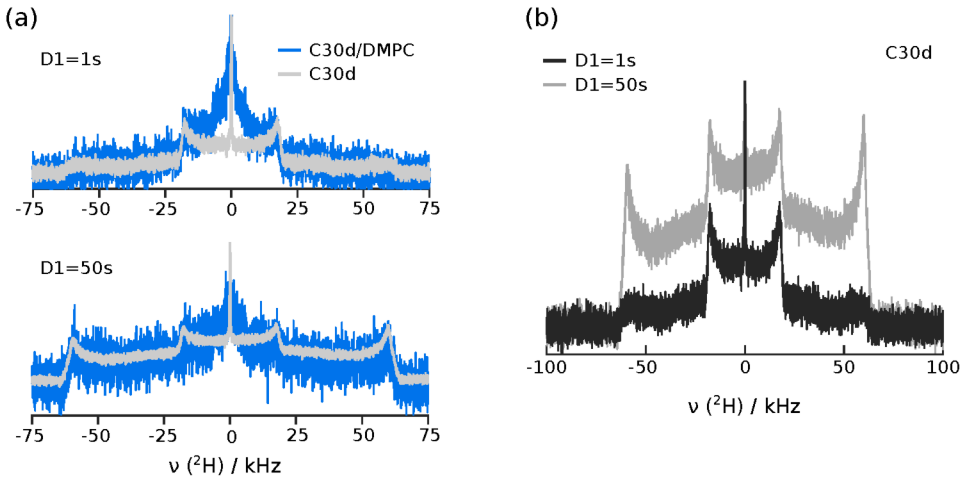

Figure S3: Effect or recycle delay on the ^{2}H spectral shape. (a) Spectra of 5 vol% C30d in DMPC and bulk C30d, comparing long and short recycle delays (D1=1s and 50s). (b) Sspectra of bulk C30d acquired using different recycle delays D1 (but otherwise identical experimental settings).

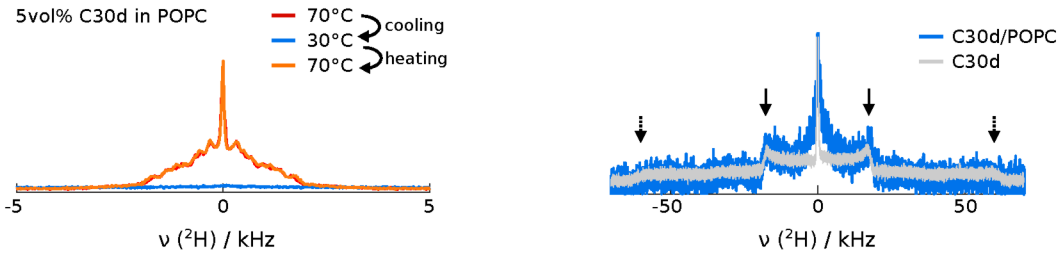

Figure S4: ^{2}H NMR spectra of 5 vol% C30d in POPC (reduced hydration). Left: Temperature series; 70°C (above the melting temperature of C30d), then cooled to 30°C (far below the crystallization temperature of C30d), and heated again to 70°C. Spectra scaled to the same number of scans. Right: comparison of the 30°C spectrum to crystalline bulk C30d at the same temperature.

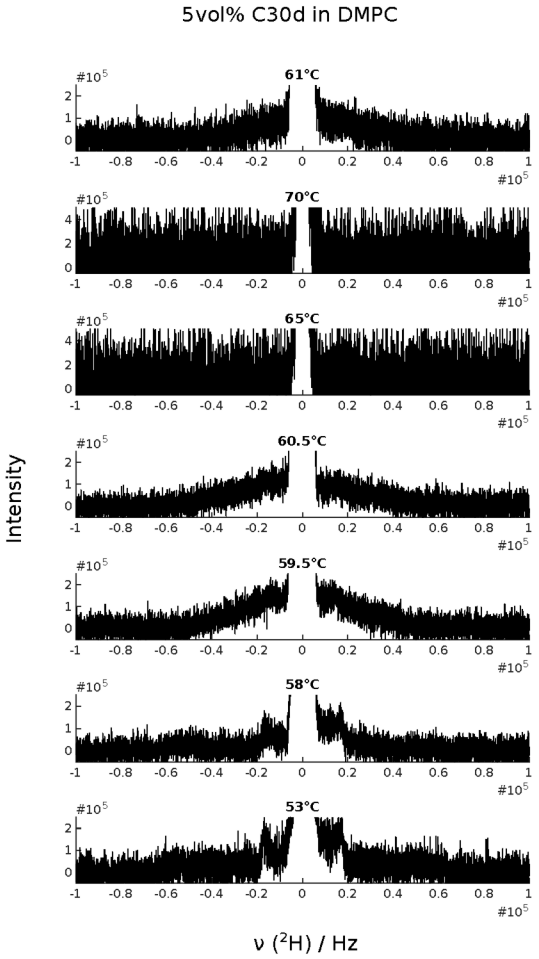

Figure S5: Broad signal component of the ^{2}H NMR spectra of 5 vol% C30d in DMPC, at different temperatures. Spectra were acquired sequentially, from top to bottom, and are scaled to the same number of scans (NS=2048), such that the intensities are comparable.

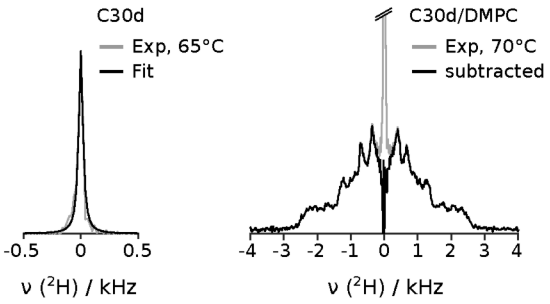

Figure S6: Subtraction method for determining the bulk alkane fraction in C30d/DMPC samples. Left: Fit of the bulk C30d signal with a single Lorentzian. Right: Subtraction of the scaled, fitted bulk signal from the C30d/DMPC spectrum.

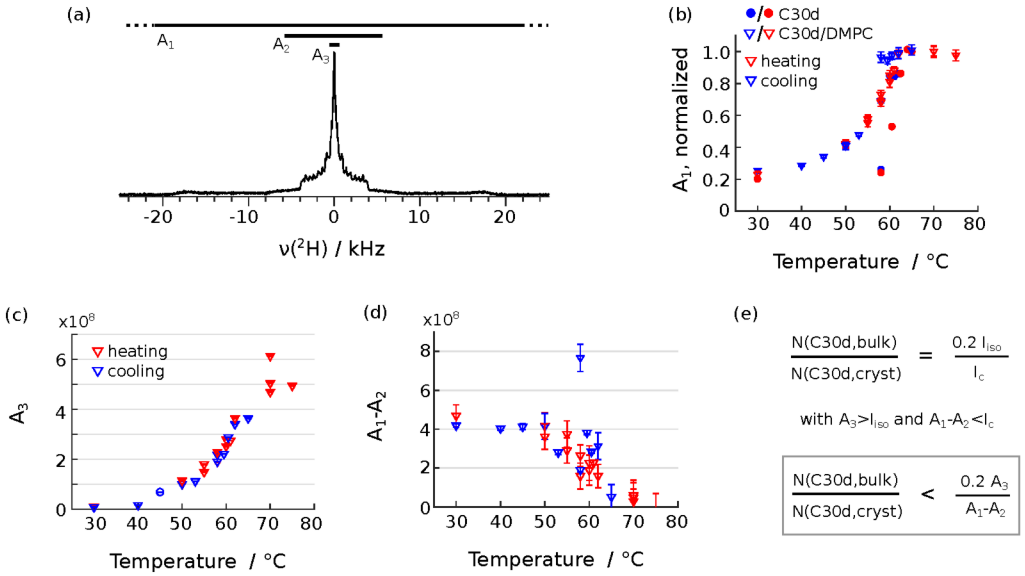

Figure S7: Areas of ^{2}H NMR spectra, A_i, calculated by summation of spectrum points in the intervals [-100kHz,100kHz] (A_1), [-6kHz,6kHz] (A_2) and [-100Hz,100Hz] (A_3), as functions of temperature. Only spectra acquired with a relaxation delay of 1 s were considered. (a) Exemplary spectrum acquired at 50°C. (b) Normalized areas of the full spectra, including crystalline, rotator and liquid C30d chains. When only crystalline chains are present (30°C), the area is only 20 % of area at 65-75°C due to significant relaxation effects for the higher couplings. (c),(d) Areas used to estimate the amount of bulk C30d molecules relative to all crystallizing molecules. An upper limit of 31±6 % was calculated, using the formulas and approximations shown in (e). The factor 0.2 is due to the effects of relaxation on the measured areas, see (b). A_3 will always be larger than the bulk signal intensity I_{iso}, since there will be a non-zero intensity in the center of the spectrum, even if no bulk alkane is present. Similarly, A_1-A_2 will always be smaller than the total crystalline intensity I_c, since part of the crystalline component is also cut off when subtracting A_2. We used A_3(T=70°C), when all bulk alkane is liquid, and A_1-A_2(T=55°), when all crystallizing molecules should be crystalline. While this is a fairly rough estimate, it clearly shows that bulk alkane alone is not sufficient to account for the broad spectral components shown in figure S5.

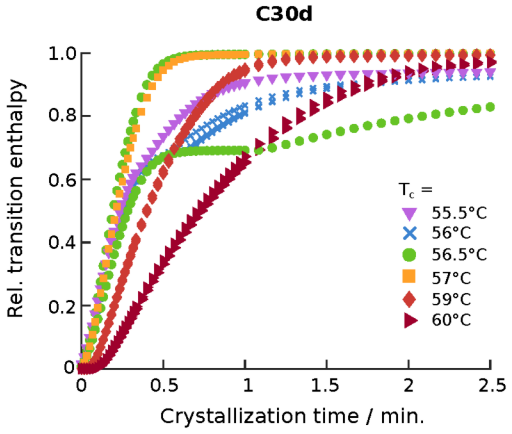

Figure S8: Relative transition enthalpy of C30d during isothermal crystallization, obtained by integrating the heat flow data and normalizing to the total integral (up to 30 min).

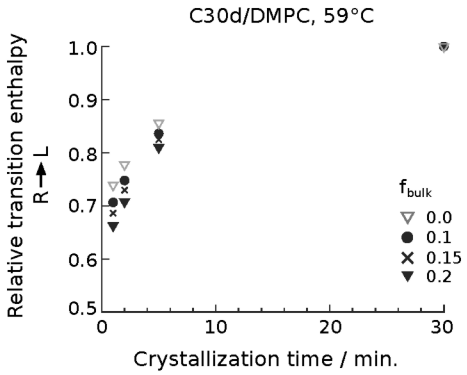

Figure S9: Rotator-to-liquid transition enthalpy of C30d in DMPC, corrected for bulk alkane. Assuming a constant fraction of bulk C30d, f_{bulk}, the measured transition enthalpy was reduced based on the bulk transition enthalpy at the same crystallization temperature/time.

Chapter 6

Summary

This thesis presents a systematic investigation of the behaviour of n-alkanes with different chain lengths inside simple phospholipid bilayers. Importantly, this work extends previous studies on n-alkane organization in lipids to longer n-alkanes, allowing not only the investigation of n-alkane crystallization in the membrane but also providing an important starting point for understanding the interactions between lipid membranes and long, hydrophobic molecules. This thesis discusses various aspects of n-alkane/lipid mixtures such as miscibility, alkane and lipid molecular structure, n-alkane crystallizability, and the effect of sample hydration. By combining solid-state NMR, X-ray scattering, cryo-TEM and DSC with atomistic MD simulations, the investigated mixtures are described with a high level of molecular detail. The findings described in this thesis, and their scientific relevance, can be summarized as follows.

It is shown for the first time that the two longer n-alkanes C20 and C30 can be incorporated to a significant amount into bilayers consisting of saturated phospholipids. Static ^{2}H and ^{31}P NMR measurements show distinct mixing behaviour depending on n-alkane- and lipid acyl tail length, as well as sample hydration. At low hydration, high alkane concentrations result in the accumulation of n-alkanes between bilayer leaflets. The limiting alkane volume fraction above which this observation is made decreases with n-alkane length. At the same time, lipid order parameters are not affected by alkane addition, showing a strong resistance of the lipid bilayer to perturbations by long, purely hydrophobic chains. At high, biologically relevant hydration levels on the other hand, alkane addition promotes the formation of smaller lipid structures. Such finding provides a possible indication as to how lipid droplet formation could be aided by the presence of triglycerides.

The molecular structure of n-alkanes inside lipid membranes is confirmed using MD simulations. The simulations successfully reproduce experimental order parameters and show that n-alkanes are highly mobile inside the hydrophobic region of a

lipid bilayer. More precisely, longer *n*-alkanes are able to adopt disordered conformations inside a lipid membrane, while short chains are generally more extended. This chain-length dependent behaviour has a pronounced impact on how accurately common lipid force fields reproduce experimental order parameters. It is therefore recommended to take alkane or lipid acyl tail length into account when selecting a force field. Moreover, it is shown how chain ordering in simulations can be tuned by scaling the charges on the hydrocarbon atoms. This result provides an example for how to optimize force field parameters for long, hydrophobic molecules in a lipid membrane environment and should be of general interest to the MD simulation community.

This thesis also, for the first time, reports on the crystallization of purely hydrophobic chains inside lipid bilayers. Using static ^{2}H NMR it is shown that the *n*-alkanes C20 and C30 can crystallize inside lipid membranes, provided the *n*-alkane melting point lies sufficiently far above the lipid main transition temperature. If the two transition temperatures are similar, however, *n*-alkanes and lipid acyl tails co-associate to form a gel-like phase at lower temperatures. Due to the presence of a partially ordered "solvent" (i.e. the lipid acyl tails), the one-dimensional confinement in lipid membranes presents a unique confinement geometry that is fundamentally interesting and may be used for the design of lipid-based materials. The crystallization of C30 in DMPC is studied in more detail using a combination of NMR and DSC. Again, sample hydration (and the structural differences resulting from it) play an important role in determining the crystallization characteristics. At low hydration, crystallization in the membrane occurs via at least one rotator phase, and the transition temperatures are only slightly reduced compared to bulk alkane. Rotator phase formation in the membrane is shown to be a two-step process consisting of fast initial gelation of pre-associated *n*-alkane molecules, and slow addition of further molecules to those crystals. Furthermore, an intermediate crystal phase of C30 is stabilized inside the lipid membrane, highlighting the importance of such investigations for crystallizable, hydrophobic drugs where crystal structure often determines the biological effect.

In summary, the results presented in this thesis provide insight into the fundamental behaviour of hydrophobic chains inside lipid membranes and therefore present an important basis for the study of more complex systems such as triglycerides, hydrophobic drugs or polymers in cellular membranes.

Bibliography

[1] L. Xu et al., *Advanced NanoBiomed Research* **2022**, *2*, 2100109.

[2] P. Yingchoncharoen, D. S. Kalinowski, D. R. Richardson, *Pharmacological Reviews* **2016**, *68*, 701–787.

[3] A. Khosa, S. Reddi, R. N. Saha, *Biomedicine & Pharmacotherapy* **2018**, *103*, 598–613.

[4] S. Kim, J. M. Swanson, *Biophysical Journal* **2020**, *119*, 1958–1969.

[5] V. Zoni et al., *eLife* **2021**, *10*, e62886.

[6] F. V. Hegaard, M. B. Klenow, A. C. Simonsen, *Langmuir* **2022**, *38*, 9247–9256.

[7] H. Bouwmeester, P. C. H. Hollman, R. J. B. Peters, *Environmental Science & Technology* **2015**, *49*, 8932–8947.

[8] P. D. Dissanayake et al., *Environmental Research* **2022**, *209*, 112734.

[9] T. Gouin, *Environmental Toxicology and Chemistry* **2020**, *39*, 1119–1137.

[10] E. Guzzetti et al., *Environmental Toxicology and Pharmacology* **2018**, *64*, 164–171.

[11] M. A. Browne et al., *Environmental Science & Technology* **2008**, *42*, 5026–5031.

[12] K. Mattsson et al., *Environmental Science & Technology* **2015**, *49*, 553–561.

[13] E. Bergami et al., *Ecotoxicology and Environmental Safety* **2016**, *123*, 18–25.

[14] N. M. Hall et al., *Marine Biology* **2015**, *162*, 725–732.

[15] D. Bochicchio et al., *Scientific reports* **2017**, *7*, 6357.

[16] M. Drenscko, S. M. Loverde, *Molecular Simulation* **2019**, *45*, 859–867.

[17] O. Hollóczki, S. Gehrke, *ChemPhysChem.* **2020**, *21*, 9–12.

[18] S. Zenak, S. Sabeur, J. López-Cascales, *Journal of Molecular Structure* **2020**, *1222*, 128888.

[19] D. Bochicchio et al., *Journal of Colloid and Interface Science* **2022**, *605*, 110–119.

[20] M. Werner, J.-U. Sommer, V. A. Baulin, *Soft Matter* **2012**, *8*, 11714–11722.

[21] W.-d. Tian, K. Chen, Y.-q. Ma, *RSC Adv.* **2014**, *4*, 30215–30220.

[22] T. Hauß et al., *Biochimica et Biophysica Acta (BBA) - Bioenergetics* **2002**, *1556*, 149–154.

[23] M. Schulz, A. Olubummo, W. H. Binder, *Soft Matter* **2012**, *8*, 4849–4864.

[24] J. Pope, D. Dubro, *Biochimica et Biophysica Acta (BBA) - Biomembranes* **1986**, *858*, 243–253.

[25] J. Pope, L. Littlemore, P. Westerman, *Biochimica et Biophysica Acta (BBA) - Biomembranes* **1989**, *980*, 69–76.

[26] P. Flory, *Macromolecules* **1978**, *11*, 1138–1141.

[27] B. Kronberg, I. Bassignana, D. Patterson, *J. Phys. Chem.* **1978**, *82*, 1714–1719.

[28] H. Orendi, M. Ballauff, *Liquid Crystals* **1989**, *6*, 497–500.

[29] R. M. Michell, A. J. Müller, *Progress in Polymer Science* **2016**, *54-55*, 183–213.

[30] G. Liu, A. J. Müller, D. Wang, *Accounts of Chemical Research* **2021**, *54*, 3028–3038.

[31] M. V. Massa, K. Dalnoki-Veress, *Phys. Rev. Lett.* **2004**, *92*, 255509.

[32] J. M. Carr et al., *Journal of Materials Research* **2012**, *27*, 1326–1350.

[33] B. Shekunov, P. York, *Journal of Crystal Growth* **2000**, *211*, 122–136.

[34] K. M. Rosenblatt, H. Bunjes, *European Journal of Pharmaceutics and Biopharmaceutics* **2017**, *117*, 49–59.

[35] D. J. McClements, *Advances in Colloid and Interface Science* **2012**, *174*, 1–30.

[36] C. F. Goh et al., *Expert Opinion on Drug Delivery* **2020**, *17*, 1321–1334.

[37] A. Wurl et al., *Langmuir* **2022**, *38*, 8595–8606.

[38] A. Wurl, T. M. Ferreira, *Macromolecular Theory and Simulations* **2023**, *32*, 2200078.

[39] A. Wurl et al., „Crystallization of n-alkanes under anisotropic nano-confinement in lipid bilayers“, Preprint on ChemRxiv at https://doi.org/10.26434/chemrxiv-2023-ljjt7, **2023**.

[40] A. G. Lee, *Biochimica et Biophysica Acta (BBA) - Biomembranes* **2004**, *1666*, 62–87.

[41] G. van Meer, D. R. Voelkner, G. W. Feigenson, *Nature Reviews Molecular Cell Biology* **2008**, *9*, 112–124.

[42] H. Palsdottir, C. Hunte, *Biochimica et Biophysica Acta (BBA) - Biomembranes* **2004**, *1666*, 2–18.

[43] M. P. Muller et al., *Chemical Reviews* **2019**, *119*, 6086–6161.

[44] C. U. Mårtensson, K. N. Doan, T. Becker, *Biochimica et Biophysica Acta (BBA) - Molecular and Cell Biology of Lipids* **2017**, *1862*, 102–113.

[45] G. Paradies et al., *Biochimica et Biophysica Acta (BBA) - Bioenergetics* **2014**, *1837*, 408–417.

[46] D. Marsh, *Handbook of Lipid Bilayers*, CRC press, New York, **2013**.

[47] T. Harayama, H. Riezman, *Nature Reviews Molecular Cell Biology* **2018**, *19*, 281–296.

[48] G. Daum, *Biochimica et Biophysica Acta (BBA) - Reviews on Biomembranes* **1985**, *822*, 1–42.

[49] J. Israelachvili, *Intermolecular and Surface Forces*, 3rd ed., Academic Press/ Elsevier Inc., **2011**.

[50] H. Matsuki et al., *International Journal of Molecular Sciences* **2013**, *14*, 2282–2302.

[51] J. N. Israelachvili, D. J. Mitchell, B. W. Ninham, *J. Chem. Soc., Faraday Trans. 2* **1976**, *72*, 1525–1568.

[52] J. N. Israelachvili, D. Mitchell, B. W. Ninham, *Biochimica et Biophysica Acta (BBA) - Biomembranes* **1977**, *470*, 185–201.

[53] C. Tanford, *Proceedings of the National Academy of Sciences* **1974**, *71*, 1811–1815.

[54] P. Fromherz, *Chemical Physics Letters* **1983**, *94*, 259–266.

[55] D. D. Lasic, *Biochemical Journal* **1988**, *256*, 1–11.

[56] K. M. Taylor, R. M. Morris, *Thermochimica Acta* **1995**, *248*, 289–301.

[57] D. E. Large et al., *Adv. Drug Deliv. Rev.* **2021**, *176*, 113851.

[58] J. Seelig, *Biochimica et Biophysica Acta (BBA) - Reviews on Biomembranes* **1978**, *515*, 105–140.

[59] A. Tardieu, V. Luzzati, F. C. Reman, *Journal of Molecular Biology* **1973**, *75*, 711–733.

[60] M. Kodama, M. Kuwabara, S. Seki, *Biochimica et Biophysica Acta (BBA) - Biomembranes* **1982**, *689*, 567–570.

[61] M. J. Janiak, D. M. Small, G. G. Shipley, *Journal of Biological Chemistry* **1979**, *254*, 6068–6078.

[62] M. J. Ruocco, G. Graham Shipley, *Biochimica et Biophysica Acta (BBA) - Biomembranes* **1982**, *684*, 59–66.

[63] J. Stümpel, H. Eibl, A. Nicksch, *Biochimica et Biophysica Acta (BBA) - Biomembranes* **1983**, *727*, 246–254.

[64] J. Katsaras et al., *Biochemistry* **1995**, *34*, 4684–4688.

[65] J. Katsaras, *The Journal of Physical Chemistry* **1995**, *99*, 4141–4147.

[66] M. J. Janiak, D. M. Small, G. G. Shipley, *Biochemistry* **1976**, *15*, 4575–4580.

[67] S. Tristram-Nagle et al., *Biophysical Journal* **1993**, *64*, 1097–1109.

[68] G. S. Smith et al., *The Journal of Chemical Physics* **1990**, *92*, 4519–4529.

[69] W. J. Sun et al., *Proceedings of the National Academy of Sciences* **1996**, *93*, 7008–7012.

[70] D. Chapman, R. Williams, B. Ladbrooke, *Chemistry and Physics of Lipids* **1967**, *1*, 445–475.

[71] H. Ellens, J. Bentz, F. C. Szoka, *Biochemistry* **1986**, *25*, 285–294.

[72] D. Siegel, R. Epand, *Biophysical Journal* **1997**, *73*, 3089–3111.

[73] S. M. Gruner, *Proceedings of the National Academy of Sciences* **1985**, *82*, 3665–3669.

[74] A. P. Ramos, M. Doroudgar, M. Lafleur, *Biochimica et Biophysica Acta (BBA) - Biomembranes* **2020**, *1862*, 183201.

[75] P. F. Almeida, *Biochimica et Biophysica Acta (BBA) - Biomembranes* **2009**, *1788*, 72–85.

[76] H.-Y. Wang, D. Bharti, I. Levental, *Frontiers in Cell and Developmental Biology* **2020**, *8*.

[77] E. Sezgin et al., *Nature Reviews Molecular Cell Biology* **2017**, *18*, 361–374.

[78] G. Enkavi et al., *Chemical Reviews* **2019**, *119*, 5607–5774.

[79] D. Marsh, *Biochimica et Biophysica Acta (BBA) - Biomembranes* **2009**, *1788*, 2114–2123.

[80] J. Juhasz, F. J. Sharom, J. H. Davis, *Biochimica et Biophysica Acta (BBA) - Biomembranes* **2009**, *1788*, 2541–2552.

[81] L. Löser, K. Saalwächter, T. Mendes Ferreira, *Phys. Chem. Chem. Phys.* **2018**, *20*, 9751–9754.

[82] A. Seelig, J. Seelig, *Biochemistry* **1974**, *13*, 4839–4845.

[83] S. V. Dvinskikh, V. Castro, D. Sandström, *Phys. Chem. Chem. Phys.* **2005**, *7*, 3255–3257.

[84] J. H. Davis, J. J. Clair, J. Juhasz, *Biophysical Journal* **2009**, *96*, 521–539.

[85] A. Léonard, E. Dufourc, *Biochimie* **1991**, *73*, 1295–1302.

[86] J. Seelig, A. Seelig, *Biochemical and Biophysical Research Communications* **1974**, *57*, 406–411.

[87] M. Dirand et al., *Journal of Chemical & Engineering Data* **2002**, *47*, 115–143.

[88] M. G. Broadhurst, *Journal of research of the National Bureau of Standards. Section A Physics and chemistry* **1962**, *66A*, 241–249.

[89] J. Doucet et al., *The Journal of Chemical Physics* **1984**, *80*, 1647–1651.

[90] E. B. Sirota et al., *The Journal of Chemical Physics* **1993**, *98*, 5809–5824.

[91] E. B. Sirota, D. M. Singer, *The Journal of Chemical Physics* **1994**, *101*, 10873–10882.

[92] D. Cholakova, N. Denkov, *Advances in Colloid and Interface Science* **2019**, *269*, 7–42.

[93] E. B. Sirota, *Langmuir* **1998**, *14*, 3133–3136.

[94] E. B. Sirota, A. B. Herhold, *Science* **1999**, *283*, 529–532.

[95] D. L. Dorset, H. L. Strauss, R. G. Snyder, *The Journal of Physical Chemistry* **1991**, *95*, 938–940.

[96] J. C. Earnshaw, C. J. Hughes, *Phys. Rev. A* **1992**, *46*, R4494–R4496.

[97] X. Z. Wu et al., *Phys. Rev. Lett.* **1993**, *70*, 958–961.

[98] X. Z. Wu et al., *Science* **1993**, *261*, 1018–1021.

[99] B. M. Ocko et al., *Phys. Rev. E* **1997**, *55*, 3164–3182.

[100] A. Weinstein, S. A. Safran, *Phys. Rev. E* **1996**, *53*, R45–R48.

[101] D. Turnbull, J. C. Fisher, *The Journal of Chemical Physics* **2004**, *17*, 71–73.

[102] W. R. Turner, *Industrial & Engineering Chemistry Product Research and Development* **1971**, *10*, 238–260.

[103] H. Kraack, M. Deutsch, E. B. Sirota, *Macromolecules* **2000**, *33*, 6174–6184.

[104] D. Turnbull, R. L. Cormia, *The Journal of Chemical Physics* **1961**, *34*, 820–831.

[105] R. Montenegro, K. Landfester, *Langmuir* **2003**, *19*, 5996–6003.

[106] D. R. Uhlmann et al., *The Journal of Chemical Physics* **1975**, *62*, 4896–4903.

[107] W. P. Zhang, D. L. Dorset, *Journal of Polymer Science Part B: Polymer Physics* **1990**, *28*, 1223–1232.

[108] P. Yi, G. C. Rutledge, *The Journal of Chemical Physics* **2011**, *135*, 024903.

[109] G. Ungar, A. Keller, *Colloid and Polymer Science* **1979**, *257*, 90–94.

[110] R. Alamo et al., *Macromolecules* **1993**, *26*, 2743–2753.

[111] H. Schollmeyer, B. Struth, H. Riegler, *Langmuir* **2003**, *19*, 5042–5051.

[112] N. Maeda, M. M. Kohonen, H. K. Christenson, *The Journal of Physical Chemistry B* **2001**, *105*, 5906–5913.

[113] K. Nanjundiah, A. Dhinojwala, *Phys. Rev. Lett.* **2005**, *95*, 154301.

[114] T. Shimizu, T. Yamamoto, *The Journal of Chemical Physics* **2000**, *113*, 3351–3359.

[115] M. Bai et al., *Europhysics Letters* **2007**, *79*, 26003.

[116] P. Huber et al., *Europhysics Letters* **2004**, *65*, 351–357.

[117] P. Huber, V. P. Soprunyuk, K. Knorr, *Phys. Rev. E* **2006**, *74*, 031610.

[118] A. Henschel et al., *Phys. Rev. E* **2007**, *75*, 021607.

[119] W. Wang et al., *Phys. Chem. Chem. Phys.* **2013**, *15*, 14390–14395.

[120] L. P. Wang et al., *The Journal of Physical Chemistry C* **2014**, *118*, 18177–18186.

[121] L. P. Wang et al., *The Journal of Physical Chemistry C* **2015**, *119*, 18697–18706.

[122] X. Wang et al., *Thermochimica Acta* **2020**, *690*, 178687.

[123] I. Weidinger et al., *The Journal of Physical Chemistry B* **2003**, *107*, 3636–3643.

[124] Y. Shinohara et al., *Crystal Growth & Design* **2008**, *8*, 3123–3126.

[125] B. Spiegel, A. Käfer, M. Kind, *Crystal Growth & Design* **2018**, *18*, 3307–3316.

[126] D. Cholakova et al., *Journal of Colloid and Interface Science* **2021**, *604*, 260–271.

[127] K. Jiang et al., *The Journal of Physical Chemistry B* **2008**, *112*, 16485–16489.

[128] Y. Su et al., *Accounts of Chemical Research* **2014**, *47*, 192–201.

[129] M. Masnadi, S. G. Urquhart, *Langmuir* **2012**, *28*, 12493–12501.

[130] X. Z. Wu et al., *MRS Proceedings* **1994**, *366*, 15.

[131] G. P. Harp et al., *Macromolecules* **2006**, *39*, 7464–7466.

[132] L. Phipps, *Transactions of the Faraday Society* **1964**, *60*, 1873–1883.

[133] M. Oliver, P. Calvert, *Journal of Crystal Growth* **1975**, *30*, 343–351.

[134] R. Montenegro et al., *The Journal of Physical Chemistry B* **2003**, *107*, 5088–5094.

[135] B. Xie et al., *The Journal of Physical Chemistry B* **2006**, *110*, 14279–14282.

[136] D. A. Haydon et al., *Biochimica et Biophysica Acta (BBA) - Biomembranes* **1977**, *470*, 17–34.

[137] T. J. McIntosh, S. A. Simon, R. C. MacDonald, *Biochimica et Biophysica Acta (BBA) - Biomembranes* **1980**, *597*, 445–463.

[138] H. G. L. Coster, D. R. Laver, *Biochimica et Biophysica Acta (BBA) - Biomembranes* **1986**, *857*, 95–104.

[139] H. G. L. Coster, D. R. Laver, *Biochimica et Biophysica Acta (BBA) - Biomembranes* **1986**, *861*, 406–412.

[140] K. Lohner, *Chemistry and Physics of Lipids* **1991**, *57*, 341–362.

[141] D. A. Haydon et al., *Nature* **1977**, *268*, 356–358.

[142] N. Kučerka et al., *J. Mol. Liq.* **2019**, *276*, 624–629.

[143] M. Hishida et al., *Chemistry and Physics of Lipids* **2015**, *188*, 61–67.

[144] M. Hishida et al., *The Journal of Chemical Physics* **2019**, *150*, 064904.

[145] A. P. Ramos, M. Doroudgar, M. Lafleur, *Biochimica et Biophysica Acta (BBA) - Biomembranes* **2020**, *1862*, 183201.

[146] H. Usuda et al., *Chemistry Letters* **2018**, *47*, 1512–1514.

[147] H. Usuda et al., *Phys. Chem. Chem. Phys.* **2020**, *22*, 5418–5426.

[148] V. Zoni, P. Campomanes, S. Vanni, *Soft Matter* **2021**, *17*, 5329–5335.

[149] J. Pope, L. Walker, D. Dubro, *Chemistry and Physics of Lipids* **1984**, *35*, 259–277.

[150] R. E. Jacobs, S. H. White, *Journal of the American Chemical Society* **1984**, *106*, 915–920.

[151] R. E. Jacobs, S. H. White, *Journal of the American Chemical Society* **1984**, *106*, 6909–6912.

[152] G. D. Bothun et al., *Colloids and Surfaces A: Physicochemical and Engineering Aspects* **2006**, *279*, 50–57.

[153] J. Douliez, A. Léonard, E. Dufourc, *Biophysical Journal* **1995**, *68*, 1727–1739.

[154] L. Ebihara et al., *Biophysical Journal* **1979**, *28*, 185–196.

[155] M. Hishida et al., *J. Chem. Phys.* **2016**, *144*, 041103.

[156] E. J. A. Lea, *International Journal of Biological Macromolecules* **1979**, *1*, 185–187.

[157] D. W. Gruen, D. A. Haydon, *Biophysical Journal* **1981**, *33*, 167–187.

[158] R. M. Epand, *Biochemistry* **1985**, *24*, 7092–7095.

[159] D. P. Siegel, J. Banschbach, P. L. Yeagle, *Biochemistry* **1989**, *28*, 5010–5019.

[160] D. C. Turner, S. M. Gruner, J. S. Huang, *Biochemistry* **1992**, *31*, 1356–1363.

[161] Z. Chen, R. Rand, *Biophysical Journal* **1998**, *74*, 944–952.

[162] M. Sjölund et al., *Biophysical Journal* **1987**, *52*, 145–153.

[163] M. Sjölund, L. Rilfors, G. Lindblom, *Biochemistry* **1989**, *28*, 1323–1329.

[164] M. H. Levitt, *Spin dynamics: basics of nuclear magnetic resonance*, John Wiley & Sons, **2008**.

[165] M. J. Duer, *Introduction to Solid-State NMR Spectroscopy*, Blackwell Publishing, **2004**.

[166] J. Keeler, *Understanding NMR Spectroscopy*, University of Cambridge Repository, **2004**.

[167] H. Friebolin, *Ein-und zweidimensionale NMR-Spektroskopie: eine Einführung*, John Wiley & Sons, **2013**.

[168] R. Bärenwald et al., *Polymers* **2016**, *8*, 439.

[169] J. Herzfeld, R. G. Griffin, R. A. Haberkorn, *Biochemistry* **1978**, *17*, 2711–2718.

[170] C. Tilcock, P. Cullis, S. Gruner, *Chemistry and Physics of Lipids* **1986**, *40*, 47–56.

[171] P. Cullis, B. de Kruyff, *Biochimica et Biophysica Acta (BBA) - Biomembranes* **1976**, *436*, 523–540.

[172] H. S. Antila et al., *Biophysical Journal* **2022**, *121*, 68–78.

[173] P. Cullis, B. De Kruyff, R. Richards, *Biochimica et Biophysica Acta (BBA) - Biomembranes* **1976**, *426*, 433–446.

[174] B. De Kruijff, P. Cullis, G. Radda, *Biochimica et Biophysica Acta (BBA) - Biomembranes* **1975**, *406*, 6–20.

[175] E. J. Dufourc et al., *Biophysical Journal* **1992**, *61*, 42–57.

[176] A. McLaughlin et al., *Journal of Magnetic Resonance (1969)* **1975**, *20*, 146–165.

[177] P. Cullis, *FEBS Letters* **1976**, *70*, 223–228.

[178] J. Berden et al., *FEBS Letters* **1974**, *46*, 55–58.

[179] J. A. Berden, R. W. Barker, G. K. Radda, *Biochimica et Biophysica Acta (BBA) - Biomembranes* **1975**, *375*, 186–208.

[180] E. Oldfield, D. Chapman, W. Derbyshire, *Chemistry and Physics of Lipids* **1972**, *9*, 69–81.

[181] J. Seelig, W. Niederberger, *Journal of the American Chemical Society* **1974**, *96*, 2069–2072.

[182] A. Seelig, J. Seelig, *Biochimica et Biophysica Acta (BBA) - Biomembranes* **1975**, *406*, 1–5.

[183] G. W. Stockton et al., *Biochemistry* **1976**, *15*, 954–966.

[184] J. H. Davis, *Biochimica et Biophysica Acta (BBA) - Reviews on Biomembranes* **1983**, *737*, 117–171.

[185] A. Abragam, *The Principles of Nuclear Magnetism*, Oxford University Press, **1961**.

[186] J. R. Hoyland, *Journal of the American Chemical Society* **1968**, *90*, 2227–2232.

[187] L. Burnett, B. Muller, *The Journal of Chemical Physics* **1971**, *55*, 5829–5831.

[188] J. Davis, *Biophysical Journal* **1979**, *27*, 339–358.

[189] M. R. Vist, J. H. Davis, *Biochemistry* **1990**, *29*, 451–464.

[190] T. M. Ferreira, D. Bernin, D. Topgaard in, Annual Reports on NMR Spectroscopy, Academic Press, **2013**, pp. 73–127.

[191] J. Forbes et al., *J. Chem. Soc., Faraday Trans. 1* **1988**, *84*, 3821–3849.

[192] D. Chapman et al., *FEBS Letters* **1972**, *25*, 261–264.

[193] J. Forbes, C. Husted, E. Oldfield, *Journal of the American Chemical Society* **1988**, *110*, 1059–1065.

[194] R. Bärenwald, PhD thesis, Martin-Luther-Universität Halle-Wittenberg, **2018**.

[195] A. E. Bennett et al., *The Journal of Chemical Physics* **1995**, *103*, 6951–6958.

[196] K. Takegoshi, J. Mizokami, T. Terao, *Chemical Physics Letters* **2001**, *341*, 540–544.

[197] B. Fung, A. Khitrin, K. Ermolaev, *Journal of Magnetic Resonance* **2000**, *142*, 97–101.

[198] D. Burum, R. Ernst, *Journal of Magnetic Resonance (1969)* **1980**, *39*, 163–168.

[199] S. R. Hartmann, E. L. Hahn, *Phys. Rev.* **1962**, *128*, 2042–2053.

[200] A. Nowacka et al., *Langmuir* **2010**, *26*, 16848–16856.

[201] A. Nowacka et al., *Journal of Magnetic Resonance* **2013**, *230*, 165–175.

[202] J. D. Gross, D. E. Warschawski, R. G. Griffin, *Journal of the American Chemical Society* **1997**, *119*, 796–802.

[203] X. Zhao, M. Edén, M. H. Levitt, *Chemical Physics Letters* **2001**, *342*, 353–361.

[204] S. V. Dvinskikh et al., *Journal of Magnetic Resonance* **2004**, *168*, 194–201.

[205] S. V. Dvinskikh, V. Castro, D. Sandström, *Phys. Chem. Chem. Phys.* **2005**, *7*, 607–613.

[206] M. Hong et al., *Journal of Magnetic Resonance* **1997**, *129*, 85–92.

[207] M. F. Cobo et al., *Journal of Magnetic Resonance* **2012**, *221*, 85–96.

[208] A. Wurl, K. Saalwächter, T. Mendes Ferreira, *Magnetic Resonance* **2023**, *4*, 115–127.

[209] A. Gansmüller, J.-P. Simorre, S. Hediger, *Journal of Magnetic Resonance* **2013**, *234*, 154–164.

[210] S. Fridolf et al., *Phys. Chem. Chem. Phys.* **2022**, *24*, 25588–25601.

[211] J. Lindon, A. Ferrige, *Progress in Nuclear Magnetic Resonance Spectroscopy* **1980**, *14*, 27–66.

[212] Z. Tošner et al., *Journal of Magnetic Resonance* **2017**, *284*, 20–32.

[213] W. H. de Jeu, *Basic X-Ray Scattering for Soft Matter*, Oxford University Press, **2016**.

[214] J. F. Nagle, S. Tristram-Nagle, *Biochimica et Biophysica Acta (BBA) - Reviews on Biomembranes* **2000**, *1469*, 159–195.

[215] M. Wiener, R. Suter, J. Nagle, *Biophysical Journal* **1989**, *55*, 315–325.

[216] R. Zhang, R. M. Suter, J. F. Nagle, *Phys. Rev. E* **1994**, *50*, 5047–5060.

[217] J. Nagle et al., *Biophysical Journal* **1996**, *70*, 1419–1431.

[218] W. Lesslauer, J. E. Cain, J. K. Blasie, *Proceedings of the National Academy of Sciences* **1972**, *69*, 1499–1503.

[219] J. Torbet, M. Wilkins, *Journal of Theoretical Biology* **1976**, *62*, 447–458.

[220] G. Pabst et al., *Phys. Rev. E* **2000**, *62*, 4000–4009.

[221] W. Sun et al., *Biophysical Journal* **1996**, *71*, 885–891.

[222] T. T. Mills et al., *General physiology and biophysics* **2009**, *28*, 126–139.

[223] Y. Levine, *Progress in Surface Science* **1973**, *3*, 279–352.

[224] A. Meister, A. Blume, *Polymers* **2017**, *9*, 521.

[225] L. A. Earl et al., *Current Opinion in Structural Biology* **2017**, *46*, 71–78.

[226] K. Mio, C. Sato, *Biophysical Reviews* **2018**, *10*, 307–316.

[227] R. Nygaard, J. Kim, F. Mancia, *Current Opinion in Structural Biology* **2020**, *64*, 26–33.

[228] R. G. Efremov, C. Gatsogiannis, S. Raunser in *A Structure-Function Toolbox for Membrane Transporter and Channels*, Methods in Enzymology, Academic Press, **2017**, pp. 1–30.

[229] W. Jiang, L. Tang, *Current Opinion in Structural Biology* **2017**, *46*, 122–129.

[230] G. H. Michler, *Electron Microscopy of Polymers*, Springer, Berlin Heidelberg, **2008**.

[231] J. Lepault, F. Pattus, N. Martin, *Biochimica et Biophysica Acta (BBA) - Biomembranes* **1985**, *820*, 315–318.

[232] Y. Tahara, Y. Fujiyoshi, *Micron* **1994**, *25*, 141–149.

[233] M. Andersson, L. Hammarstroem, K. Edwards, *The Journal of Physical Chemistry* **1995**, *99*, 14531–14538.

[234] M. J. Dobro et al. in *Cryo-EM Part A Sample Preparation and Data Collection*, Methods in Enzymology, Academic Press, **2010**, pp. 63–82.

[235] M. Adrian et al., *Nature* **1984**, *308*, 32–36.

[236] J. Dubochet, A. McDowall, *Journal of Microscopy* **1981**, *124*, 3–4.

[237] C. Lopez et al., *Food Research International* **2020**, *138*, 109770.

[238] H. H. Fueldner, *Biochemistry* **1981**, *20*, 5707–5710.

[239] J. M. Boggs, G. Rangaraj, K. M. Koshy, *Chemistry and Physics of Lipids* **1986**, *40*, 23–34.

[240] B. Wunderlich, *Thermal analysis of polymeric materials*, Springer Science & Business Media, **2005**.

[241] A. J. Müller, R. M. Michell in *Polymer Morphology*, John Wiley & Sons, Ltd, **2016**, Chapter 5, pp. 72–99.

[242] G. W. H. Höhne, W. F. Hemminger, H.-J. Flammersheim, *Differential Scanning Calorimetry*, Springer Berlin, Heidelberg, **2003**.

[243] S. C. Chen, J. M. Sturtevant, B. J. Gaffney, *Proceedings of the National Academy of Sciences* **1980**, *77*, 5060–5063.

[244] A. J. Müller, R. M. Michell, A. T. Lorenzo in *Polymer Morphology*, John Wiley & Sons, Ltd, **2016**, Chapter 11, pp. 181–203.

[245] M. Karplus, J. A. McCammon, *Nature Structural Biology* **2002**, *9*, 646–652.

[246] M. M. Seibert et al., *Journal of Molecular Biology* **2005**, *354*, 173–183.

[247] H. Geng et al., *Computational and Structural Biotechnology Journal* **2019**, *17*, 1162–1170.

[248] P. S. Georgoulia, N. M. Glykos, *Archives of Biochemistry and Biophysics* **2019**, *664*, 76–88.

[249] J. M. Haile, *Molecular Dynamics Simulations: Elementary Methods*, John Wiley & Sons, Inc., **1992**.

[250] M. P. Allen in *Computational Soft Matter: From Synthetic Polymers to Proteins, Lecture Notes, Vol. 28*, Norbert Attig, Kurt Binder, Helmut Grubmüller, Kurt Kremer (Eds.), John von Neumann Institute for Computing, Jülich, NIC Series, **2004**, pp. 1–28.

[251] P. Bauer, B. Hess, E. Lindahl, GROMACS 2022.6 Manual, version 2022.6, **2023**.

[252] H. Berendsen, D. van der Spoel, R. van Drunen, *Computer Physics Communications* **1995**, *91*, 43–56.

[253] D. Van Der Spoel et al., *Journal of Computational Chemistry* **2005**, *26*, 1701–1718.

[254] M. J. Abraham et al., *SoftwareX* **2015**, *1-2*, 19–25.

[255] H. Antila et al., *The Journal of Physical Chemistry B* **2019**, *123*, 9066–9079.

[256] A. Botan et al., *J. Phys. Chem. B* **2015**, *119*, 15075–15088.

[257] S. J. Marrink et al., *Chemical Reviews* **2019**, *119*, 6184–6226.

[258] V. Knecht, A. E. Mark, S.-J. Marrink, *Journal of the American Chemical Society* **2006**, *128*, 2030–2034.

[259] C. L. Wennberg et al., *Journal of Chemical Theory and Computation* **2013**, *9*, 3527–3537.

[260] C. L. Wennberg et al., *Journal of Chemical Theory and Computation* **2015**, *11*, 5737–5746.

[261] A. N. Leonard et al., *Journal of Chemical Theory and Computation* **2018**, *14*, 948–958.

[262] Y. Yu et al., *Journal of Chemical Theory and Computation* **2021**, *17*, 1562–1580.

[263] D. M. York, T. A. Darden, L. G. Pedersen, *The Journal of Chemical Physics* **1993**, *99*, 8345–8348.

[264] U. Essmann et al., *The Journal of Chemical Physics* **1995**, *103*, 8577–8593.

[265] J. W. Ponder et al., *The Journal of Physical Chemistry B* **2010**, *114*, 2549–2564.

[266] K. Vanommeslaeghe, A. MacKerell, *Biochimica et Biophysica Acta (BBA) - General Subjects* **2015**, *1850*, 861–871.

[267] H. J. C. Berendsen et al., *The Journal of Chemical Physics* **1984**, *81*, 3684–3690.

[268] G. Bussi, D. Donadio, M. Parrinello, *The Journal of Chemical Physics* **2007**, *126*, 014101.

[269] S. Nosé, *Molecular Physics* **1984**, *52*, 255–268.

[270] W. G. Hoover, *Phys. Rev. A* **1985**, *31*, 1695–1697.

[271] M. Parrinello, A. Rahman, *Journal of Applied Physics* **1981**, *52*, 7182–7190.

[272] S. Nosé, M. Klein, *Molecular Physics* **1983**, *50*, 1055–1076.

[273] J.-P. Ryckaert, G. Ciccotti, H. J. Berendsen, *Journal of Computational Physics* **1977**, *23*, 327–341.

[274] S. Miyamoto, P. A. Kollman, *Journal of Computational Chemistry* **1992**, *13*, 952–962.

[275] B. Hess et al., *Journal of Computational Chemistry* **1997**, *18*, 1463–1472.

[276] M.-K. Hsieh, Y. Yu, J. B. Klauda, *Langmuir* **2022**, *38*, 3–17.

[277] A. P. Lyubartsev, A. L. Rabinovich, *Biochimica et Biophysica Acta (BBA) - Biomembranes* **2016**, *1858*, 2483–2497.

[278] A. N. Leonard et al., *Chemical Reviews* **2019**, *119*, 6227–6269.

[279] B. R. Brooks et al., *Journal of Computational Chemistry* **2009**, *30*, 1545–1614.

[280] L. Kalé et al., *Journal of Computational Physics* **1999**, *151*, 283–312.

[281] O. S. Ollila, G. Pabst, *Biochimica et Biophysica Acta (BBA) - Biomembranes* **2016**, *1858*, 2512–2528.

[282] M. Javanainen et al., *Journal of Chemical Theory and Computation* **2023**, *19*, 6342–6352.

[283] T. J. Piggot, Á. Piñeiro, S. Khalid, *Journal of Chemical Theory and Computation* **2012**, *8*, 4593–4609.

[284] T. J. Piggot, Á. Piñeiro, S. Khalid, *Journal of Chemical Theory and Computation* **2017**, *13*, 1862–1865.

[285] A. M. Kiirikki et al., *Nature Communications* **2024**, *15*, 1136.

[286] J. B. Klauda et al., *The Journal of Physical Chemistry B* **2005**, *109*, 5300–5311.

[287] J. B. Klauda et al., *The Journal of Physical Chemistry B* **2010**, *114*, 7830–7843.

[288] J. P. M. Jämbeck, A. P. Lyubartsev, *The Journal of Physical Chemistry B* **2012**, *116*, 3164–3179.

[289] J. P. M. Jämbeck, A. P. Lyubartsev, *Journal of Chemical Theory and Computation* **2012**, *8*, 2938–2948.

[290] J. Lee et al., *Journal of Chemical Theory and Computation* **2016**, *12*, 405–413.

[291] C. I. Bayly et al., *The Journal of Physical Chemistry* **1993**, *97*, 10269–10280.

[292] F. Grote, A. P. Lyubartsev, *The Journal of Physical Chemistry B* **2020**, *124*, 8784–8793.

[293] N. Kučerka et al., *Biophysical Journal* **2008**, *95*, 2356–2367.

[294] H. Flyvbjerg, H. Petersen, *J. Chem. Phys.* **1989**, *91*, 461–466.

Acknowledgements

I am extremely grateful to everyone who supported me during my doctoral studies. Many thanks to my colleagues in the NMR group, fellow PhD students in the iRTG, my family and friends for being a part of my PhD journey. In particular, I'd like to thank:

- Tiago Mendes Ferreira for giving me the opportunity to be part of a number of exciting research projects, and for being a great supervisor.
- Alfred Blume for being my mentor and providing extremely valuable advice for my thesis project.
- Kay Saalwächter for motivating me to join the NMR group, and for always being available for advice and discussions.
- Alexey Krushelnitsky and Günter Hempel for much-appreciated explanations regarding NMR theory, as well as their invaluable technical assistance with the NMR spectrometers. Also Mareen Schaller for introducing me to the "inner workings" of the NMR group.
- Lucas Löser and David Haselberger for helpful discussions and for creating a lively office atmosphere.
- Markus S. Miettinen and Tobias Rindfleisch for a fun and productive research stay in Bergen.
- The co-authors of the papers, especially Maria Ott, Annette Meister and Christian Schwieger, for the fruitful collaborations and for introducing me to new techniques. Also Karsten Busse, Yu Qiang and Katrin Herfurt for their advice and help with DSC measurements.
- Ann-Kristin Flieger, Beate Horn and Thomas Michael for the organization of many interesting SFB events and workshops. The funding of my PhD project within the SFB/TRR 102 by the DFG is highly appreciated.

Curriculum Vitae

Persönliche Informationen

Name: Anika Wurl

Ausbildung

Seit 12/2018:	Doktorandin, Institut f. Physik, MLU Halle-Wittenberg Betreuer: Tiago M. Ferreira
10/2016 – 11/2018:	M.Sc. Medizinische Physik, MLU Halle-Wittenberg
10/2013 – 09/2016:	B.Sc. Medizinische Physik, MLU Halle-Wittenberg
08/2004 – 07/2012:	Schulische Ausbildung, Ratsgymnasium Wolfsburg

Halle (Saale), den

Anika Wurl

Publikationen

1. Hanne S. Antila, Anika Wurl, O.H. Samuli Ollila, Markus S. Miettinen, and Tiago M. Ferreira: "Rotational decoupling between the hydrophilic and hydrophobic regions in lipid membranes", *Biophysical Journal* 2022, 121, 68-78.

2. Anika Wurl, Maria Ott, Eric Plato, Annette Meister, Farzad Hamdi, Panagiotis L. Kastritis, Alfred Blume, and Tiago M. Ferreira:"Filling the Gap with Long *n*-Alkanes: Incorporation of C20 and C30 into Phospholipid Membranes", *Langmuir* 2022, 38, 8595-8606.

3. Anika Wurl and Tiago M. Ferreira: "Atomistic MD Simulations of *n*-Alkanes in a Phospholipid Bilayer: CHARMM36 versus Slipids", *Macromol. Theory Simul.* 2023, 2200078.

4. Anika Wurl, Kay Saalwächter, and Tiago M. Ferreira: "Time-domain proton-detected local-field NMR for molecular structure determination in complex lipid membranes", *Magn. Reson.* 2023, 4, 115-127.

5. Anika Wurl, Maria Ott, Christian Schwieger, and Tiago M. Ferreira: "Crystallization of *n*-alkanes under anisotropic nano-confinement in lipid bilayers", *ChemRxiv*, 2023, doi:10.26434/chemrxiv-2023-ljjt7.

Erklärung

Hiermit versichere ich, die vorliegende Arbeit selbstständig und ohne fremde Hilfe verfasst und keine anderen als die von mir angegeben Quellen und Hilfsmittel verwendet zu haben. Die den benutzten Werken wörtlich oder inhaltlich entnommenen Stellen habe ich als solche kenntlich gemacht. Ich erkläre, keine anderweitigen Promotionsversuche unternommen und die vorliegende Dissertation weder in der jetzigen noch in einer anderen Fassung einer anderen wissenschaftlichen Einrichtung vorgelegt zu haben.

Halle (Saale), den

Anika Wurl